

**A STUDY OF EXCLUSIVE NONLEPTONIC DECAYS OF  $B$  MESONS  
INTO FINAL STATES OF STRANGE MESONS AND  $1S$  OR  $2S$   
CHARMONIA**

**by**

**Andreas T. Warburton**

A thesis submitted in conformity with the requirements  
for the degree of Doctor of Philosophy,  
Graduate Department of Physics,  
in the University of Toronto



## Abstract

Bound states of heavy quarks can serve as a laboratory for inquiry into the behaviour of the fundamental strong and electroweak interactions. This thesis examines observations of  $B^0$ ,  $\overline{B}^0$ , and  $B^\pm$  mesons produced in proton-antiproton collisions at centre-of-mass energies of  $\sqrt{s} = 1.8$  TeV. The  $B$ -meson decay products are recorded using the Collider Detector at Fermilab (CDF) located on the Tevatron collider at the Fermi National Accelerator Laboratory in Batavia, Illinois, USA.

Four  $B$ -meson decays and their charge conjugates are studied:  $B^+ \rightarrow J/\psi K^+$ ,  $B^0 \rightarrow J/\psi K^*(892)^0$ ,  $B^+ \rightarrow \psi(2S) K^+$ , and  $B^0 \rightarrow \psi(2S) K^*(892)^0$ . Using a data sample corresponding to  $\int \mathcal{L} dt = (109 \pm 7) \text{ pb}^{-1}$ , statistically significant signals are observed in all the channels. Topological similarities between the  $B$  decays are exploited to measure the six relative branching fractions ( $\mathcal{B}$ ) of each channel with respect to the other channels. The ratios involving the  $B^+ \rightarrow J/\psi K^+$  mode are

$$\begin{aligned} \frac{\mathcal{B}(B^0 \rightarrow J/\psi K^*(892)^0)}{\mathcal{B}(B^+ \rightarrow J/\psi K^+)} &= 1.76 \pm 0.14[\text{stat}] \pm 0.15[\text{syst}] \\ \frac{\mathcal{B}(B^+ \rightarrow \psi(2S) K^+)}{\mathcal{B}(B^+ \rightarrow J/\psi K^+)} &= 0.558 \pm 0.082[\text{stat}] \pm 0.056[\text{syst}] \\ \frac{\mathcal{B}(B^0 \rightarrow \psi(2S) K^*(892)^0)}{\mathcal{B}(B^+ \rightarrow J/\psi K^+)} &= 0.908 \pm 0.194[\text{stat}] \pm 0.100[\text{syst}]. \end{aligned}$$

The indicated uncertainties are statistical and systematic, respectively. In ratios involving unlike  $B$ -meson species, equal production rates for  $B^+$  and  $B^0$  mesons have been assumed.

Absolute branching fractions are extracted by normalizing the above ratio measurements to the world-average value,  $\mathcal{B}(B^+ \rightarrow J/\psi K^+) = (1.01 \pm 0.14) \times 10^{-3}$ :

$$\begin{aligned} \mathcal{B}(B^0 \rightarrow J/\psi K^*(892)^0) &= (1.78 \pm 0.14[\text{stat}] \pm 0.29[\text{syst}]) \times 10^{-3} \\ \mathcal{B}(B^+ \rightarrow \psi(2S) K^+) &= (0.56 \pm 0.08[\text{stat}] \pm 0.10[\text{syst}]) \times 10^{-3} \\ \mathcal{B}(B^0 \rightarrow \psi(2S) K^*(892)^0) &= (0.92 \pm 0.20[\text{stat}] \pm 0.16[\text{syst}]) \times 10^{-3}. \end{aligned}$$

The  $B^+ \rightarrow \psi(2S) K^+$  and  $B^0 \rightarrow \psi(2S) K^*(892)^0$  reconstructions are the first observations of these processes at a hadron collider. The branching-fraction ratio measurements are consistent with phenomenological predictions that employ the factorization *Ansatz*, and

the absolute branching-fraction measurements are consistent with previous world-average limits and values from  $e^+ e^-$  colliders. The measured branching fractions that involve  $\psi(2S)$  final states constitute the world's most precise measurements of these quantities.

## Acknowledgments

It is impossible to convey the extent of my gratitude to Pekka Sinervo, my mentor and graduate advisor. I have been fortunate to have benefited from Pekka's profound generosity of spirit, superlative physics expertise, and professional but compassionate approach to all things.

There are literally hundreds of people who deserve acknowledgment for their part in making this study possible. Appendix D lists the Run 1 CDF collaboration, whose immeasurable hard work over several years resulted in the successful construction and operation of the CDF detector. Not listed in Appendix D are the hundreds of technicians, engineers, and other support personnel who were vital to the outcome of the physics programme.

I owe Andreas Hölscher my thanks for introducing me to the topic of exclusive  $B$  decays into charmonium. George Sganos, who pioneered many of the techniques used in this dissertation, provided me with an abundance of computer code and energetic advice about the *modus operandi* required to advance through a personal physics analysis effort while completing service responsibilities for the Collaboration. My other immediate colleagues at Toronto, Robert Cropp, Szymon Gadomski, Björn “quantum chromodynamics” Hinrichsen, Andrew Robinson, and Wendy Taylor, were always helpful and supportive, even when I was too preoccupied to reciprocate.

I would like to thank William Trischuk for his much appreciated good humour, support, and valuable advice. I also am grateful to Michael Luke and Bob Orr for their encouragement and helpful contributions to this work.

Thank you to my companion in the trenches, Hyunsoo Kim, for his friendship, help, and willingness to endure my ramblings at any hour of the day. I also thank my CDF colleagues Bill Ashmanskas, Kostas Kordas, Petar Maksimović, and Benn Tannenbaum for friendship and good times in Chicago.

I gratefully acknowledge the financial support of the Natural Sciences and Engineering Research Council of Canada, the W. C. Sumner Memorial Foundation, and the University of Toronto. I thank the officers of Massey College for electing me as a Junior Fellow; my membership in the Massey community has yielded several social and intellectual opportunities beyond the world of physics.

I am grateful to Nicole Schulman for her patience and camaraderie, especially in waging the War of the Squirrels. Thank you to Marc Ozon for his unconditional friendship, perennial generosity, and help of all kinds. Words cannot describe my gratitude to Colleen Flood for her love and forbearance and to my dear family, Rennie, Ruth, Mark, and Rolf, who have always tolerated and supported me in my endeavours. *Ein besonderes Dankeschön meinem Grossmueti, Hedi Eichenberger-Wiederkehr, für sein mutiges Korrekturlese-Angebot!*

Andreas

# Contents

<b>Abstract</b>	<b>iii</b>
<b>Acknowledgments</b>	<b>v</b>
<b>1 Introduction</b>	<b>1</b>
1.1 The Fifth Quark . . . . .	2
1.1.1 Discovery . . . . .	4
1.1.2 Electroweak Interactions . . . . .	5
1.1.3 Hadroproduction . . . . .	7
1.2 The $B$ Meson . . . . .	10
1.2.1 Hadronization . . . . .	11
1.2.2 Nonleptonic $B$ -Meson Decays . . . . .	12
1.2.3 The Factorization <i>Ansatz</i> . . . . .	14
1.2.4 Theoretical Predictions . . . . .	16
1.3 Dissertation Overview . . . . .	17
<b>2 Experimental Apparatus</b>	<b>21</b>
2.1 The Fermilab Tevatron $p\bar{p}$ Collider . . . . .	21
2.2 An Overview of the CDF Detector . . . . .	24
2.3 The Tracking Systems . . . . .	26
2.3.1 The Silicon Microstrip Vertex Detector . . . . .	26
2.3.2 The Vertex Time Projection Chamber . . . . .	30
2.3.3 The Central Tracking Chamber . . . . .	31
2.3.4 The Central Drift Tube Array . . . . .	34

2.4	The Muon Chambers . . . . .	35
2.4.1	The Central Muon Detector . . . . .	35
2.4.2	The Central Muon Upgrade Detector . . . . .	39
2.4.3	The Central Muon Extension . . . . .	39
2.5	The Trigger Systems . . . . .	42
2.5.1	Level 1 . . . . .	42
2.5.2	Level 2 . . . . .	44
2.5.3	Level 3 . . . . .	46
2.6	The Data Acquisition System . . . . .	47
<b>3</b>	<b>Selection of Candidate Events</b>	<b>51</b>
3.1	The Data Sample . . . . .	51
3.2	The Data Reduction Procedure . . . . .	52
3.3	Magnetic Field Considerations . . . . .	54
3.4	Primary Vertex Considerations . . . . .	55
3.5	Track Quality Criteria . . . . .	56
3.6	Optimizing the Kinematic Selection Criteria . . . . .	58
3.7	Muon Candidate Selection . . . . .	59
3.8	Charmonium Reconstruction . . . . .	60
3.8.1	Dimuon Charmonium Decays . . . . .	60
3.8.2	Hadronic Cascade $\psi(2S)$ Decays . . . . .	61
3.9	$B$ -Meson Candidate Reconstruction . . . . .	61
3.9.1	Kaon Candidate Selection Criteria . . . . .	62
3.9.2	$B$ -Meson Candidate Selection Criteria . . . . .	63
3.9.3	Multiple Invariant Mass Combinations . . . . .	64
<b>4</b>	<b>Geometric and Kinematic Acceptance</b>	<b>69</b>
4.1	The Monte Carlo Generation of $B$ Mesons . . . . .	69
4.2	The Monte Carlo Decay of $B$ Mesons . . . . .	70
4.2.1	The $\psi(2S) \rightarrow J/\psi \pi^+ \pi^-$ Monte Carlo Matrix Element . . . . .	70
4.3	Simulation of the Detector Response . . . . .	73
4.4	Simulation of the Level 1 and 2 Triggers . . . . .	73



4.5	The Acceptance Calculations . . . . .	76
4.5.1	Differential Production Cross Section of Generated $b$ Quarks . . . . .	77
4.5.2	Trigger Effects . . . . .	77
4.5.3	Helicity Distributions . . . . .	80
<b>5</b>	<b>Efficiency Corrections</b>	<b>82</b>
5.1	Constrained Fit Confidence Level Criteria . . . . .	82
5.1.1	Dimuon $CL(\chi^2)$ Criteria . . . . .	82
5.1.2	Dipion $CL(\chi^2)$ Criteria . . . . .	88
5.1.3	$B$ -Meson $CL(\chi^2)$ Criteria . . . . .	91
5.2	Tracking Efficiencies . . . . .	91
5.3	Proper Decay Length Criteria . . . . .	92
5.4	$B$ -Candidate Isolation Criterion . . . . .	94
5.5	Daughter Branching Fractions . . . . .	96
<b>6</b>	<b>Branching Fraction Measurements</b>	<b>97</b>
6.1	$B$ -Meson Candidate Event Yields . . . . .	97
6.2	Sample Branching-Fraction Ratio Calculation . . . . .	100
6.3	Branching-Fraction Ratio Results . . . . .	101
6.4	Derived Absolute Branching-Fraction Results . . . . .	105
<b>7</b>	<b>Conclusions</b>	<b>109</b>
7.1	Branching Fraction Measurements . . . . .	110
7.2	Future Prospects . . . . .	111
<b>A</b>	<b>Level 2 Dimuon Triggers</b>	<b>113</b>
A.1	Run 1A Level 2 Dimuon Triggers . . . . .	113
A.2	Run 1B Level 2 Dimuon Triggers . . . . .	113
<b>B</b>	<b>CDF Track Characterization</b>	<b>115</b>
B.1	Global Coordinates from the Track Helix . . . . .	115
B.2	Helix from Momentum and Point of Origin . . . . .	117

<b>C</b>	<b>Pattern Recognition Efficiencies</b>	<b>119</b>
C.1	Data Sample . . . . .	119
C.2	Track Embedding Procedure . . . . .	119
C.3	Definition of a “Found” Track or Track Pair . . . . .	123
C.4	Pattern Recognition Efficiency . . . . .	126
C.4.1	Definition . . . . .	126
C.4.2	Efficiency Dependence on Kinematic Observables . . . . .	127
C.4.3	Efficiency Dependence on Occupancy-Related Observables . . . . .	128
C.4.4	Time-Dependent Effects . . . . .	129
C.4.5	Stereo Efficiency . . . . .	133
C.5	Results . . . . .	134
C.6	Conclusions . . . . .	135
<b>D</b>	<b>The CDF Collaboration</b>	<b>140</b>
	<b>Bibliography</b>	<b>145</b>

# List of Tables

1.1	Cross sections for $b\bar{b}$ production at various colliders. . . . .	10
1.2	Theoretical branching-fraction predictions. . . . .	17
1.3	Branching-fraction ratios measured in the analysis. . . . .	20
2.1	Properties of the CDF calorimeters. . . . .	27
3.1	Monte Carlo constraints on $K$ - $\pi$ mass assignment combinations. . . . .	68
4.1	Absolute products of the geometric and kinematic acceptances. . . . .	76
4.2	Relative products of the geometric and kinematic acceptances. . . . .	77
4.3	Systematic uncertainty on acceptance due to variations in the differential production cross section of generated $b$ quarks. . . . .	78
4.4	Systematic uncertainty on acceptance due to trigger requirement. . . . .	79
4.5	Summary of trigger parameterization shift effects on relative acceptance. . .	80
4.6	Systematic uncertainty on acceptance due to variations in the longitudinal polarization fractions of those decays with vector-vector final states. . . . .	81
5.1	Dimuon $CL(\chi^2)$ criterion efficiencies. . . . .	88
5.2	Dipion $CL(\chi^2)$ criterion efficiencies. . . . .	91
5.3	Proper decay length resolutions for $B^+$ candidates. . . . .	93
5.4	Proper decay length resolutions for $B^0$ candidates. . . . .	93
5.5	Measured $c\tau_B$ cut efficiencies in the $B^+$ and $B^0$ decay modes. . . . .	94
5.6	Measured isolation criterion efficiencies in the $B^+$ and $B^0$ decay modes. . .	95
5.7	Branching fractions of the daughter meson decay modes. . . . .	96
6.1	Summary of $B$ -meson candidate event yields. . . . .	100

6.2	Numbers entering into sample calculation of $R_{J/\psi K^*(892)^0}^{\psi(2S) K^+}$ . . . . .	102
6.3	Branching-fraction ratio results. . . . .	103
6.4	Derived absolute branching-fraction results. . . . .	107
C.1	Run list for pattern recognition efficiency embedding study. . . . .	120
C.2	Wire efficiencies used in the embedding process. . . . .	123
C.3	3-D pattern recognition efficiencies for tracks with $r_{\text{CTC}}^{\text{exit}} > 110$ cm. . . . .	136
C.4	2-D pattern recognition efficiencies for tracks with $r_{\text{CTC}}^{\text{exit}} > 110$ cm. . . . .	136
C.5	Aggregate Run 1 efficiencies for tracks with $r_{\text{CTC}}^{\text{exit}} > 110$ cm. . . . .	136
C.6	3-D pattern recognition efficiencies for tracks with $r_{\text{CTC}}^{\text{exit}} > 132$ cm. . . . .	136
C.7	2-D pattern recognition efficiencies for tracks with $r_{\text{CTC}}^{\text{exit}} > 132$ cm. . . . .	137
C.8	Aggregate Run 1 efficiencies for tracks with $r_{\text{CTC}}^{\text{exit}} > 132$ cm. . . . .	137

# List of Figures

1.1	Feynman diagrams for $\mathcal{O}(\alpha_s^2) b\bar{b}$ hadroproduction. . . . .	9
1.2	Feynman diagrams for $\mathcal{O}(\alpha_s^3) b\bar{b}$ hadroproduction. . . . .	9
1.3	Feynman diagram of an exclusive colour-suppressed $B$ -meson decay. . . . .	13
1.4	Schematic diagrams of the $B^+$ decay modes. . . . .	18
1.5	Schematic diagrams of the $B^0$ decay modes. . . . .	18
2.1	Schematic diagram of the Tevatron collider and its affiliated accelerators. . . . .	23
2.2	Isometric view of the CDF detector. . . . .	25
2.3	Schematic elevation view of the CDF detector. . . . .	26
2.4	Isometric view of one of the two SVX barrels. . . . .	28
2.5	Layout of an SVX ladder module. . . . .	29
2.6	Event display of the vertex time projection chamber (VTX). . . . .	32
2.7	A central tracking chamber (CTC) endplate. . . . .	33
2.8	Central muon $\eta$ - $\varphi$ coverage map. . . . .	36
2.9	Layout of a central muon (CMU) wedge on a central calorimeter wedge. . . . .	37
2.10	Layout of a central muon detector (CMU) module. . . . .	38
2.11	Layout of a central muon detector (CMU) drift cell. . . . .	38
2.12	Schematic of a CMP or CMX proportional drift cell. . . . .	40
2.13	Cell layout in a central muon extension (CMX) module. . . . .	41
2.14	Schematic diagram of the data acquisition pipeline. . . . .	49
3.1	Distribution of the $B$ -meson isolation variable, $I_B$ . . . . .	65
3.2	Event-display diagram of an observed candidate $B^+$ decay. . . . .	66
4.1	Dipion invariant mass distributions using two Monte Carlo models. . . . .	71

4.2	Dipion invariant mass distribution observed in $\psi(2S) \rightarrow J/\psi \pi^+ \pi^-$ candidate decays. . . . .	72
4.3	Level 1 low- $p_T$ CMU and CMX trigger efficiency parameterizations. . . . .	75
4.4	Level 2 low- $p_T$ CMU and CMX trigger efficiency parameterizations. . . . .	75
5.1	$CL(\chi^2)$ distribution for vertex-constrained $J/\psi$ dimuon fit. . . . .	84
5.2	$CL(\chi^2)$ distribution for vertex-constrained $\psi(2S)$ dimuon fit. . . . .	84
5.3	$CL(\chi^2)$ distribution for vertex-plus-mass-constrained $J/\psi$ dimuon fit. . . . .	85
5.4	$CL(\chi^2)$ distribution for vertex-plus-mass-constrained $\psi(2S)$ dimuon fit. . . . .	85
5.5	$J/\psi$ dimuon invariant mass distribution and the effect of a vertex-constraint criterion. . . . .	86
5.6	$\psi(2S)$ dimuon invariant mass distribution and the effect of a vertex-constraint criterion. . . . .	86
5.7	$J/\psi$ dimuon normalized invariant mass distribution and the effect of a vertex-constraint criterion. . . . .	87
5.8	$\psi(2S)$ dimuon normalized invariant mass distribution and the effect of a vertex-constraint criterion. . . . .	87
5.9	$CL(\chi^2)$ distribution for vertex-constrained $\pi^+ \pi^-$ fit. . . . .	89
5.10	$J/\psi \pi^+ \pi^-$ invariant mass distribution and the effect of a $\pi^+ \pi^-$ vertex-constraint criterion. . . . .	90
5.11	$J/\psi \pi^+ \pi^-$ normalized invariant mass distribution and the effect of a $\pi^+ \pi^-$ vertex-constraint criterion. . . . .	90
6.1	The $J/\psi K^+$ invariant mass distribution. . . . .	98
6.2	The $\psi(2S) K^+$ invariant mass distributions using the $\psi(2S) \rightarrow \mu^+ \mu^-$ and $\psi(2S) \rightarrow J/\psi \pi^+ \pi^-$ modes. . . . .	98
6.3	The $J/\psi K^*(892)^0$ invariant mass distribution. . . . .	99
6.4	The $\psi(2S) K^*(892)^0$ invariant mass distributions using the $\psi(2S) \rightarrow \mu^+ \mu^-$ and $\psi(2S) \rightarrow J/\psi \pi^+ \pi^-$ modes. . . . .	99
6.5	Comparison of measured branching-fraction ratios with theoretical predictions. . . . .	104
6.6	Comparison with $e^+ e^-$ absolute branching fractions for the $\psi(2S)$ modes. . . . .	106
6.7	Comparison with theoretical predictions for the $\psi(2S)$ final-state modes. . . . .	108

C.1	Instantaneous luminosity profiles of the data and embedded samples. . . . .	120
C.2	Profile of mean number of used hits per axial superlayer. . . . .	122
C.3	Profile of mean number of used hits per stereo superlayer. . . . .	122
C.4	Minimum matching $\chi^2$ vs. next-to-minimum matching $\chi^2$ . . . . .	125
C.5	Minimum matching $\chi^2$ vs. the embedded transverse momentum. . . . .	125
C.6	Pattern recognition efficiency dependence on CTC exit radius. . . . .	127
C.7	Pattern recognition efficiency dependence on transverse momentum. . . . .	128
C.8	Pattern recognition efficiency dependence on instantaneous luminosity. . . . .	130
C.9	Pattern recognition efficiency dependence on primary vertex multiplicity. . . . .	130
C.10	Pattern recognition efficiency dependence on CTC-track multiplicity. . . . .	131
C.11	Two-track efficiency correlations. . . . .	132
C.12	Dipion pattern recognition efficiency dependence on run number. . . . .	133
C.13	Kinematic dependencies of the stereo pattern recognition efficiency. . . . .	134
C.14	Occupancy dependencies of the stereo pattern recognition efficiency. . . . .	135

# Chapter 1

## Introduction

At the high-energy frontier of experimental particle physics, the last quarter of this century has seen the discovery of a new generation of heavy and (apparently) fundamental constituents of matter, the bottom and top quarks. This dissertation describes a study of some of the properties of the bottom-quark member of this new generation, properties that can aid in the understanding of matter and the fundamental forces that act upon it. The present chapter opens with a chronology of experimental results that puts into context and motivates the study of exclusive nonleptonic decays of  $B$  mesons, composite particles that consist of a bottom quark and a light antiquark.

An understanding of the properties of all types of matter, be it particulate or astronomical in scale, appears to require the existence of agents, or forces, to mediate its interactions. Unlike the infinite-range forces of quotidian experience, namely electromagnetism and gravity, the ‘weak’ and ‘strong’ nuclear interactions did not receive recognition until the decades near the turn of this century. Fifteen years before Rutherford reported evidence for the atomic nucleus in 1911 [1], Becquerel demonstrated the existence of spontaneous radioactivity emitted by phosphorescent substances [2], a harbinger of a hitherto unknown ‘weak’ force. The ‘strong’ force, the first evidence of which was reported by Chadwick and Bieler in studies of  $\alpha$ -particle collisions with hydrogen nuclei [3], was postulated to bind together the known baryons (protons [4] and neutrons [5]) into atomic nuclei. The concept of the ‘meson’ was introduced by Yukawa in 1935 as a hypothetical mediator of the strong nuclear force experienced between proximate nucleons [6]. Yukawa’s meson, called the pion ( $\pi$ ), was eventually discovered in cosmic rays in 1947 [7] after having been mistaken for the muon,



the first evidence of which was reported a decade earlier [8]. By the 1950s, the evolution of cosmic-ray experimental techniques and the advent of the modern particle accelerator made possible the study of a more massive type of matter in the form of ‘strange’ mesons and baryons. Whereas the production of the new strange matter was thought to involve the strong interaction, the long lifetime of the strange particles ( $\sim 10^{-10}$  s) indicated that the weak interaction played a primary rôle in their decay [9]. The subsequent “explosion” of new particle discoveries during the 1960s and 1970s hinted that two large classes of particles, the mesons and baryons, were composite, just as the multitude of different atomic elements foretold the existence of subatomic structure in the early years of this century.

## 1.1 The Fifth Quark

The notion of quarks found its origins in the early 1960s in the course of searches for an organizing principle to describe the proliferation of hadronic particles and resonances observed by the experiments of that time [10]. To this end, Gell-Mann [11] and, independently, Ne’eman [12] refined an application of the SU(3) representation<sup>1</sup>, which was originally formulated in terms of “fundamental”  $p$ ,  $n$ , and  $\Lambda$  baryons [13], to introduce an organizational framework of the known baryons and mesons. The SU(3) approximate-symmetry interpretation was further extended by Gell-Mann [14] and, independently, Zweig [15] with a hypothesis that hadrons consisted of ‘quarks’. Gell-Mann and Zweig hypothesized three ‘flavours’ of quarks: up ( $u$ ), down ( $d$ ), and strange ( $s$ ).

Although the quark idea met with immediate success by explaining the taxonomy of the experimentally observed particles and resonances, evidence for quarks as dynamical objects was to come from future experiments. Studies of the deep inelastic scattering of electrons by protons, where the incoming electron scatters off the target proton to produce a massive hadronic recoil system, were able to probe the structure of nucleons with measurements of the differential scattering cross section as a function of the recoiling hadronic invariant mass for different values of four-momentum transfer between the electron and proton. In the recoil invariant mass region beyond the resonances, the cross section exhibited only a weak dependence on the momentum transfer between the electron and the hadronic state [16].

---

<sup>1</sup> SU(3) denotes the ‘special unitary’ group in three dimensions, where the matrix operator that effects transitions between members of this group is unitary and has determinant +1 (special).

This observation, which was called ‘scale invariance’ because the cross section appeared to be independent of the momentum transfer and to depend on a dimensionless quantity that related the momentum of the recoiling hadronic system to the incident proton momentum, gave credence to quark parton models of nucleon structure advanced by Bjorken [17] and Feynman [18], which predicted this scaling behaviour. Further confirmation of this parton picture was supplied six years later by observations of azimuthal asymmetries in the production of hadrons using electron-positron annihilation [19].

In spite of the parton model’s successful description of deep inelastic scattering results, the quark idea suffered from a theoretical deficiency when used to classify, for example, the  $\Delta^{++}$  baryon<sup>2</sup> resonance [20]. The  $\Delta^{++}$  baryon, thought in the quark model to be made up of three  $u$  quarks, each in the same state, appeared to be symmetric under the interchange of any of the constituent quarks, thereby violating the Pauli principle [21, 22]. An exact SU(3) symmetry, that of a new quantum degree of freedom for quarks, termed ‘colour’, was hypothesized [23] to resolve the conflict with Fermi statistics by rendering the  $\Delta^{++}$  wave function antisymmetric. With this new colour symmetry, there also emerged a theory of the strong force called quantum chromodynamics, or QCD, which described the strong interactions as being between spin-1/2 quarks and mediated by spin-1 gluons [24, 25, 26]. It was postulated that all flavours of quarks and antiquarks were each endowed with one of three colours and anticolours, respectively. Unlike photons, which do not carry electric charge, the gluon mediators carried colour and were thought to form a colour SU(3) octet.

QCD also postulated that all naturally occurring particles are colour SU(3) singlets. This was motivated largely by the inability of the experiments to produce isolated quarks. In QCD, since gluons are themselves colour sources, they are self-interacting; this property incites the QCD coupling to grow in strength as the separation between two colour sources increases. If two quarks within a hadron or a pair of hadrons are made to recede from each other in an energetic process (*e.g.*, in a particle accelerator), the potential energy accrued by the increased interquark separation will make it energetically favourable for pairs of quarks to be produced from the vacuum and to interact with the receding particles and with each other. This process continues until all the quarks are once again confined inside hadrons

---

<sup>2</sup>In this dissertation, references to specific charge states imply the additional charge-conjugate state, unless obviated by context or noted otherwise.

producing ‘jets’ of particles. Evidence of such jets arising from energetic quarks was first reported in 1975 in  $e^+ e^-$  annihilation studies [27]. As predicted by QCD, jets due to gluon *Bremsstrahlung* in processes like  $e^+ e^- \rightarrow \gamma^* \rightarrow q \bar{q} g$  were subsequently discovered at higher centre-of-mass energies [28].

An explanation of the revolutionary and largely unexpected 1974 discovery of the  $J/\psi$  meson in  $e^+ e^-$  annihilation and  $p$ - $Be$  fixed-target experiments [29] proved to be one of the quark parton model’s greatest achievements. The unusually high mass and long lifetime [30] of the  $J/\psi$  meson indicated the presence of fundamentally new physics; in turn, the quark parton model established the observation as a manifestation of a fourth quark, charm ( $c$ ), in a bound state with its antiquark to form the  $J/\psi$  meson.

The interpretation of the  $J/\psi$  meson as a  $c\bar{c}$  bound state was buttressed by the discovery of the  $\psi'$ , or  $\psi(2S)$ , meson in its  $e^+ e^-$  decay channel [31], a resonance that was identified immediately as a radial excitation of the  $J/\psi$  state. Quite analogously to electrodynamic explanations of the states of positronium observed two decades previous, QCD was able to predict the charmonium  $c\bar{c}$  bound states and their narrow widths. The subsequent experimental observation of the decay  $\psi(2S) \rightarrow J/\psi \pi^+ \pi^-$  [32] served to complement the dilepton channels in clarifying the spectroscopy of the charmonium system.

The discovery of charm brought the count of known fundamental fermions to four quarks and four leptons (the electron,  $e^-$ , and muon,  $\mu^-$ , and their associated neutrinos) in two generations, thereby vindicating theoretical prejudice toward a lepton-quark symmetry [33]. This symmetry was temporarily broken by the discovery of the  $\tau^-$  lepton in  $e^+ e^-$  collisions [34], setting the stage for a third generation of fundamental fermions.

### 1.1.1 Discovery

Evidence for the  $b$  quark, often referred to as the ‘bottom’ or ‘beauty’ quark, was initially obtained with techniques analogous to those used in the discovery of charmonium. In 1977, a significant excess in the rate of dimuon production was observed in 400-GeV proton-nucleus collisions by a fixed-target experiment at Fermilab [35]. The original enhancement, observed near  $9.5 \text{ GeV}/c^2$ , was interpreted as arising due to decays of bottomonium, a  $b\bar{b}$  bound state ( $\Upsilon$ ), and was rapidly confirmed and resolved into two resonances, namely the  $\Upsilon(1S)$  and  $\Upsilon(2S)$  mesons [36].

Extensions of nonrelativistic potential models tuned on the  $c\bar{c}$  system were used to calculate the dielectronic partial width of the  $\Upsilon$  state,  $\Gamma(\Upsilon \rightarrow e^+ e^-)$ , which depended on the electric charge carried by the  $b$  and  $\bar{b}$  quarks. Comparisons of the calculated  $\Gamma(\Upsilon \rightarrow e^+ e^-)$  with the area under the observed  $\Upsilon$  line shape suggested that the  $b$  quark would join its  $d$  and  $s$ -quark counterparts in possessing an electric charge of  $-1/3$ . The emerging pattern of generations implied by the properties of the observed quarks<sup>3</sup> helped presage the 1995 discovery of a sixth quark, top ( $t$ ), observed in 1.8-TeV  $p\bar{p}$  collisions [38, 39, 40].

### 1.1.2 Electroweak Interactions

Whereas the weak interactions of leptons have been observed to be strictly intragenerational [41], quarks in their mass-eigenstate generations,

$$\begin{pmatrix} u \\ d \end{pmatrix} \begin{pmatrix} c \\ s \end{pmatrix} \begin{pmatrix} t \\ b \end{pmatrix}, \quad (1.1)$$

may interact weakly with quarks in generations other than their own. The typical notation used to describe the degree of this ‘mixing’ is the Cabibbo-Kobayashi-Maskawa (CKM) matrix [42, 43],

$$\begin{pmatrix} d' \\ s' \\ b' \end{pmatrix} = \begin{pmatrix} V_{ud} & V_{us} & V_{ub} \\ V_{cd} & V_{cs} & V_{cb} \\ V_{td} & V_{ts} & V_{tb} \end{pmatrix} \begin{pmatrix} d \\ s \\ b \end{pmatrix}, \quad (1.2)$$

which, by convention, leaves the  $+2/3$ -charged quarks unmixed; the states  $(d', s', b')$  are the weak eigenstates. Under the constraints that there be three quark generations and that the CKM matrix be unitary, the mixing can be parameterized with three angles and one complex phase. The pursuit of measurements [30] to constrain the CKM matrix and observe the charge-parity<sup>4</sup> ( $CP$ ) violation in the  $b$ -quark system (a result of a non-zero complex phase) constitutes a major component of many experimental programmes at modern particle accelerators [45].

Contemporary understanding of the weak interactions has its foundations in Fermi’s field theory of  $\beta$  decay, introduced in 1934 [46]. The idea of the four-fermion interaction

<sup>3</sup>Analogous to the need for the charm quark in the second quark generation to cancel out unobserved strangeness-changing neutral currents in the electroweak theory (GIM mechanism [33]), the lack of observed flavour-changing neutral currents (*e.g.*,  $B^0 \rightarrow \mu^+ \mu^-$ ) in the  $b$ -quark system inferred the existence of a weak isospin partner to the third-generation  $b$  quark. Moreover, the weak isospin of the  $b$  quark was measured, via angular asymmetries in  $e^+ e^- \rightarrow b\bar{b}$  production, to be  $T_3 = -1/2$  [37], suggesting a doublet structure similar to that for the lighter generations.

<sup>4</sup>‘Parity’ refers to the quantum mechanical operator that inverts a spatial displacement vector, *i.e.*,  $\mathbf{r} \rightarrow -\mathbf{r}$ . Parity violation was first observed in studies of  $\beta$  decay in polarized  $\text{Co}^{60}$  atoms [44].

was retained for several years before Sakurai introduced the universal  $V - A$  (vector and axial-vector current) modification [47] to accommodate the experimentally observed parity violation. Unfortunately, the  $V - A$  Fermi theory had the shortcomings of unitarity violation (the nonconservation of probability in predicted cross sections that grew quadratically as a function of centre-of-mass momentum) and nonrenormalizability<sup>5</sup> in its predictions of cross sections at high energies. The ‘standard model’ of electroweak interactions, developed primarily by Glashow, Weinberg, and Salam in the 1960s [49] and based on the gauge group  $SU(2) \times U(1)$ , hypothesized four intermediate gauge fields to avoid these difficulties: the  $W^+$ ,  $W^-$ ,  $Z^0$ , and  $\gamma$  bosons. The first three of these were thought to be endowed with mass via the Higgs mechanism [50]; the fourth ( $\gamma$ ) boson was the massless photon of the electromagnetic interaction. The weak and electromagnetic forces were thence consolidated into a single theory. Soon after the Glashow-Weinberg-Salam standard model had been proven to be renormalizable [51], neutral weak-current interactions, predicted by the existence of the  $Z^0$  boson in the theory, were discovered in a neutrino-antineutrino experiment using the Gargamelle bubble chamber at CERN in 1973 [52]. Complete confirmation of the electroweak theory, however, came a decade later with the discovery of the  $W^\pm$  and  $Z^0$  intermediate vector bosons [53].

The term in the standard-model electroweak Lagrangian that plays a large rôle in the  $b$ -quark decays investigated in this dissertation represents the charged-current weak interaction between the fermion fields [30]:

$$\mathcal{L}_{CC} = -\frac{g}{2\sqrt{2}} \sum_i \bar{\xi}_i \gamma^\mu (1 - \gamma^5) (T^+ W_\mu^+ + T^- W_\mu^-) \xi_i, \quad (1.3)$$

where  $g$  is the  $SU(2)$  gauge coupling constant,  $\gamma^\mu(1 - \gamma^5)$  are the Dirac  $\gamma$  matrices representing the  $V - A$  current,  $T^+$  and  $T^-$  are the weak-isospin raising and lowering operators, respectively,  $W_\mu^\pm$  are the massive weak charged boson fields, and the index  $i$  represents the fermion families. In charged-current weak interactions of the  $b$  quark, the fermion fields,  $\xi_i$ , are either left-handed  $SU(2)$  doublets,  $\xi_3 = \begin{pmatrix} t \\ b' \end{pmatrix}_L$ , or right-handed  $SU(2)$  singlets,  $\xi_3 = (b')_R$ , where  $b'$  is the weak eigenstate defined in Equation 1.2.

---

<sup>5</sup>A theory is renormalizable if the predicted amplitudes of physical processes remain finite at all energies and for all powers of the coupling constant, often at the expense of the introduction of a finite number of arbitrary experimentally-determined parameters [48].

### 1.1.3 Hadroproduction

In the present study,  $b$  and  $\bar{b}$  quarks were produced in 1.8-TeV collisions of protons ( $p$ ) and antiprotons ( $\bar{p}$ ) by way of the inclusive process

$$p(k_p) + \bar{p}(k_{\bar{p}}) \rightarrow b(k_b) + \bar{b}(k_{\bar{b}}) + X, \quad (1.4)$$

where  $X$  denotes the ‘underlying event’ and  $k_p$  and  $k_{\bar{p}}$  ( $k_b$  and  $k_{\bar{b}}$ ) are the momenta of the baryons ( $b$  quarks). Note that the  $p$  ( $\bar{p}$ ) baryons each comprise several partons: the  $uud$  ( $\bar{u}\bar{u}\bar{d}$ ) ‘valence’ quarks, gluons, and many ‘sea’ quark-antiquark pairs<sup>6</sup>.

A perturbative QCD formula for the invariant differential hadroproduction cross section of a  $b$  quark with energy  $E_b$  and mass  $m_b$  can be expressed by convolving the partonic cross section ( $\hat{\sigma}$ ) with the parton distribution functions of the two hadron reactants in the form [54]

$$\frac{E_b d^3\sigma}{d^3k_b} = \sum_{i,j} \int_0^1 dx_1 \int_0^1 dx_2 \left[ \frac{E_b d^3\hat{\sigma}_{ij}}{d^3k_b}(x_1 k_p, x_2 k_{\bar{p}}, k_b; m_b, \mu, \Lambda) \right] F_i^p(x_1, Q^2) F_j^{\bar{p}}(x_2, Q^2), \quad (1.5)$$

where  $x_1 k_p$  and  $x_2 k_{\bar{p}}$  are the momenta of the incoming partons,  $F_{i,j}^{p,\bar{p}}$  are the parton distribution functions for the  $i^{\text{th}}$  and  $j^{\text{th}}$  parton in the  $p$  and  $\bar{p}$  baryons, respectively, and  $Q^2$  is the square of the four-momentum transfer. The parameter  $\mu$  represents the energy scale of the process and, by assumption,  $|Q| \equiv \mu$ . The quantity  $\Lambda$  is an experimentally-determined parameter used in the description of the dependence of the strong coupling constant,  $\alpha_s$ , on the energy scale,  $\mu$ .

Integrating Equation 1.5 over the momentum  $k_b$  yields the total cross section for the production of a  $b$  quark,

$$\sigma(s) = \sum_{i,j} \int_0^1 dx_1 \int_0^1 dx_2 \hat{\sigma}_{ij}(x_1 x_2 s; m_b, \mu, \Lambda) F_i^p(x_1, \mu^2) F_j^{\bar{p}}(x_2, \mu^2), \quad (1.6)$$

where  $s$  is the square of the centre-of-mass energy of the colliding proton and antiproton. The threshold condition for  $b\bar{b}$  production is met when the square of the parton-parton centre-of-mass energy,  $\hat{s} \equiv x_1 x_2 s$ , satisfies the condition  $\hat{s} = 4m_b^2$ .

The heavy mass of the  $b$  quark makes possible QCD calculations of  $\hat{\sigma}_{ij}$  as a perturbation series in powers of the running strong coupling constant,  $\alpha_s$ . The first terms in the series

---

<sup>6</sup>The ‘underlying event’ refers to the aggregate product of lower-energy interactions between those partons not directly involved in the ‘hard’ scattering part of Equation 1.4.

that contribute to the cross section are  $\mathcal{O}(\alpha_s^2)$  quark-antiquark annihilation or gluon-gluon fusion processes:

$$\begin{aligned} q + \bar{q} &\rightarrow b + \bar{b} \\ g + g &\rightarrow b + \bar{b}. \end{aligned} \tag{1.7}$$

Figure 1.1 depicts Feynman diagrams of these lowest-order  $b\bar{b}$  production mechanisms [55].

The next-to-leading  $\mathcal{O}(\alpha_s^3)$  terms in the perturbative series arise from processes [55] like

$$\begin{aligned} q + \bar{q} &\rightarrow b + \bar{b} + g \\ g + g &\rightarrow b + \bar{b} + g \\ g + q &\rightarrow b + \bar{b} + q \\ g + \bar{q} &\rightarrow b + \bar{b} + \bar{q}, \end{aligned} \tag{1.8}$$

some examples of which are illustrated with Feynman diagrams in Figure 1.2. Due to interference with diagrams containing virtual gluons, the two processes in Equation 1.7 can also contribute at  $\mathcal{O}(\alpha_s^3)$ . For high energies, *i.e.*, when  $k_T(b) \gg m_b$ , where  $k_T(b)$  is the momentum of the  $b$  quark projected onto a plane perpendicular to the axis of the two incoming partons, some of the next-to-leading order  $\mathcal{O}(\alpha_s^3)$  mechanisms can contribute to the cross section by amounts comparable to the  $\mathcal{O}(\alpha_s^2)$  contributions [54].

In Equations 1.5 and 1.6, there is a degree of arbitrariness in the value of the renormalization scale,  $\mu$ , that contributes a relatively large uncertainty to QCD predictions of  $b$ -quark production because they are not calculated to all orders in  $\alpha_s$ . The value of  $\mu$  is typically assigned to be near a physical scale, such as  $m_b$  or  $\sqrt{m_b^2 + k_T^2(b)}$ ; however, these choices of  $\mu$  are “bootstrapped” because the fact that  $b$  quarks are confined inside hadrons requires that extractions of  $m_b$  depend on the renormalization scheme used, model-specific definitions of  $m_b$ , and the value of  $\mu$  itself [30, 56].

Nason, Dawson, and Ellis (NDE) have calculated  $\frac{d^2\sigma}{dy_b dk_T^2(b)}$ , the inclusive differential  $b$ -quark production cross section, as a function of rapidity,  $y_b$ , and  $k_T(b)$  [54]. Rapidity is a measure of the polar angle of a particle’s trajectory, usually with respect to the collision axis, and is defined for a  $b$  quark as

$$y_b \equiv \frac{1}{2} \ln \left[ \frac{E_b + k_z(b)}{E_b - k_z(b)} \right], \tag{1.9}$$

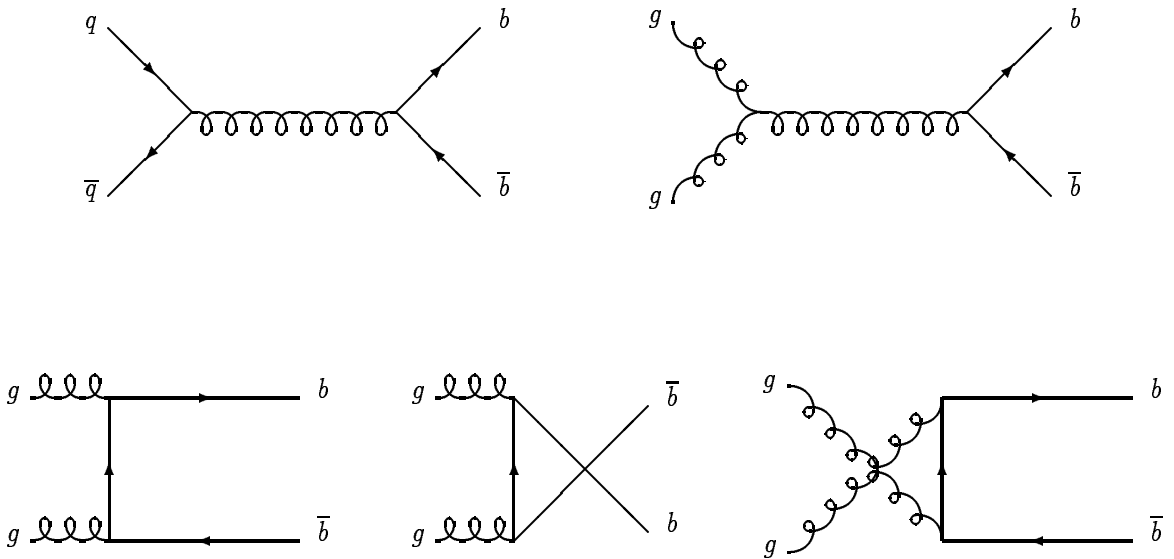


Figure 1.1: Feynman diagrams for the lowest-order ( $\mathcal{O}(\alpha_s^2)$ ) mechanisms of  $b\bar{b}$  hadroproduction.

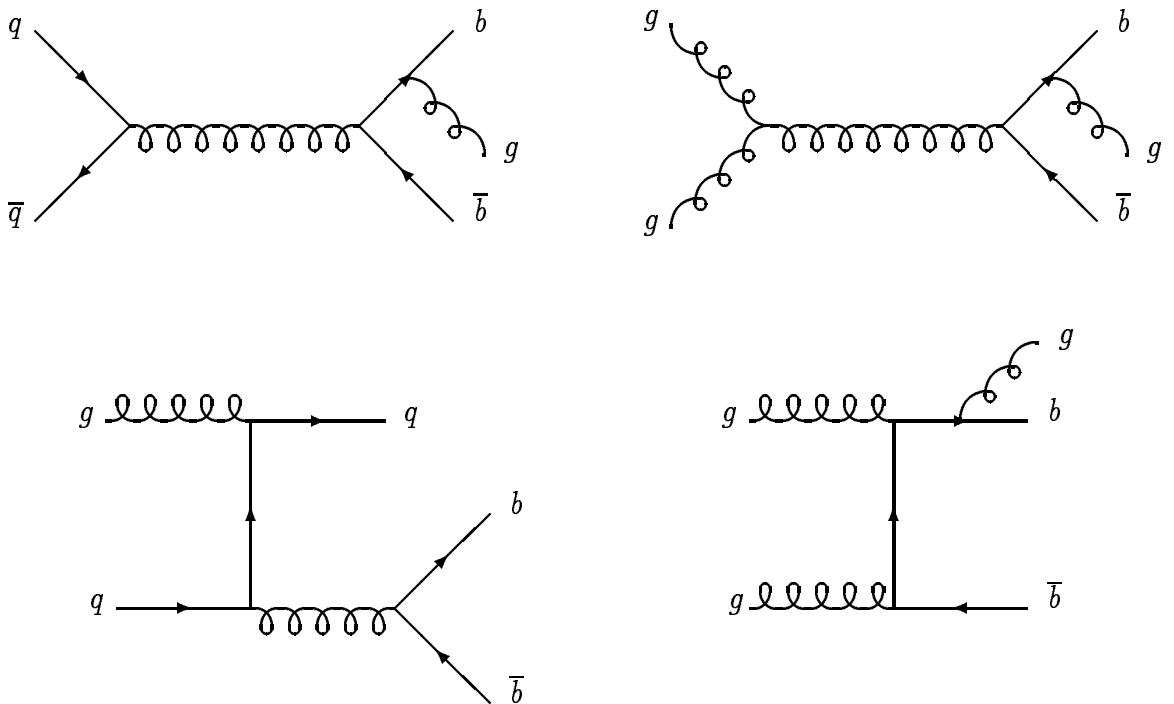


Figure 1.2: Examples of some of the Feynman diagrams for the next-to-leading order ( $\mathcal{O}(\alpha_s^3)$ ) mechanisms of  $b\bar{b}$  hadroproduction.



Collision Type	$p\bar{p}$	$pp$	$e^+e^-$	
Accelerator	Tevatron	LHC	CESR	LEP, SLC
$\sqrt{s}$ [GeV]	1 800	14 000	10.58	92
$\sigma_{b\bar{b}}^{\max}$ [ $\mu\text{b}$ ]	20–40	$\sim 200$	$\sim 1.1 \times 10^{-3}$	$\sim 9 \times 10^{-3}$
$\sigma_{b\bar{b}}/\sigma_{\text{tot}}$	$4 \times 10^{-4}$	$2 \times 10^{-3}$	0.25–0.33	$\sim 0.2$

Table 1.1: Comparison of hadroproduction and lepto-production cross sections for  $b\bar{b}$  production at various centre-of-mass energies [57]. The parameters of the five accelerators are summarized in Reference [30].

where  $k_z(b)$  is the projection of the  $b$ -quark momentum onto the beam axis. The rapidity variable is useful to descriptions of high-energy particle production because the shape of the particle-multiplicity distribution,  $dN/dy_b$ , is Lorentz-invariant; reference frame transformations amount to linear shifts in the origin of  $y_b$  [30].

Table 1.1 compares the maximum  $b$ -quark production cross section ( $\sigma_{b\bar{b}}^{\max}$ ) applicable to the present study (Tevatron) with that in other collision types at different energies. Although the rates of  $b\bar{b}$  hadroproduction exceed those of lepto-production by three orders of magnitude, they constitute a significantly smaller fraction ( $\sigma_{b\bar{b}}/\sigma_{\text{tot}}$ ) of the total cross section ( $\sigma_{\text{tot}}$ ) than do the analogous  $b\bar{b}$  lepto-production fractions. The consequentially low signal-to-background ratios for  $b$ -quark production at hadron colliders pose experimental challenges that must be overcome.

## 1.2 The $B$ Meson

Analogously to studies of the charm sector, the discovery of the bottomonium states lead naturally to the expectation that, at masses somewhat greater than those of the lowest-lying  $\Upsilon$  resonances, “open” bottom meson production would occur in the form of bare  $B^+$  ( $\bar{b}u$ ) and  $B^0$  ( $\bar{b}d$ ) mesons. First evidence for  $B$ -meson production, reported in 1981 by the CLEO collaboration [58], was obtained through observations of increases in the single electron and muon inclusive cross sections in  $e^+e^-$  collisions. The enhancements were attributed to inclusive semileptonic decays of  $B$  mesons via the processes  $B \rightarrow X \ell \nu_\ell$ , where  $\ell$  denotes either the  $e$  or  $\mu$  lepton flavour and  $X$  represents the remaining hadronic system.

Prior to the first evidence for the existence of  $B$  mesons, however, Fritzsche argued that “... the only realistic method to discover the  $B$  mesons” was through the reconstruction of their decays to charmonium states [59]. Fritzsche’s assertion, which launched a considerable amount of theoretical work on the subject (see, for example, References [60]), was motivated by the following points:  $c\bar{c}$  mesons are readily produced in weak  $B$ -meson decays; the  $\mu^+ \mu^-$  and  $e^+ e^-$  decay modes of the  $c\bar{c}$  states can be identified easily, most notably in hadronic collision environments with their sizeable backgrounds; and the relative heaviness of the charmonium states forces the remaining hadronic system in each  $B$  decay to be relatively simple because of the attendant restricted multiparticle phase space [59]. In spite of theoretical expectations that  $B$  mesons would first be reconstructed in their charmonium final states, it is interesting to note that the first full reconstruction of  $B$  decays was achieved using final states containing  $D^0$  and  $D^*(2010)^+$  mesons, such as  $B^- \rightarrow D^0 \pi^-$  and  $B^- \rightarrow D^*(2010)^+ \pi^- \pi^-$  [61]. More mention of the mechanism of charmonium production in  $B$ -meson decays, which is the subject of this investigation, is given in Section 1.2.2 and thereafter.

### 1.2.1 Hadronization

The ‘fragmentation’ of a  $b$  quark into a colour-singlet hadron, in this case a  $B$  meson, is a long-distance, nonperturbative QCD process. Models of fragmentation typically employ a parameter  $z_f$ , where  $z_f \equiv \frac{E_B + p_{\parallel}(B)}{E_b + k(b)}$  [62], which represents the fraction of available energy-momentum carried by the  $B$  meson. The symbols  $E_B$  and  $p_{\parallel}(B)$ , respectively, represent the hadronized  $B$ -meson energy and the momentum component parallel to the direction of fragmentation. Simple kinematical arguments support the claim that functions describing  $b \rightarrow Bq$  processes, where  $q$  is the light-quark counterpart to the  $\bar{q}$  quark in the  $B$  meson, peak at high values of  $z_f$  due to the expectation that the majority of the  $b$ -quark momentum is transferred to the  $B$  meson [63, 64]. Peterson *et al.* noted that the quantum mechanical amplitude describing fragmentation would be inversely proportional to the energy transfer of the process,  $\Delta E \equiv E_B + E_q - E_b$  [65]. Assuming  $m_b \approx m_B$ , then

$$\Delta E = \sqrt{m_b^2 + z_f^2 k(b)^2} + \sqrt{m_q^2 + (1 - z_f)^2 k(b)^2} - \sqrt{m_b^2 + k(b)^2}. \quad (1.10)$$

The fragmentation function,  $D_b^B(z_f)$ , was estimated from Equation 1.10 with the expression

$$D_b^B(z_f) \propto \frac{1}{z_f (\Delta E)^2} = \frac{1}{z_f \left[1 - \frac{1}{z_f} - \frac{\epsilon_b}{1-z_f}\right]^2}, \quad (1.11)$$

where the factor of  $z_f$  in the denominator arose from longitudinal phase space and the quantity  $\epsilon_b \sim m_q^2/m_b^2$  was the ‘‘Peterson parameter’’ [65].

The Peterson parameterization benefits from its dependence on a single experimentally determined parameter ( $\epsilon_b$ ). Chrin has estimated a value of  $\epsilon_b = 0.006 \pm 0.002$ , which is based on a survey of several experimental  $e^+ e^-$  observations [62]. The search continues for a better understanding of  $b$ -quark fragmentation and its sensitivity to the type of collision environment in which the  $b$  quark was produced and the flavour(s) of the non- $b$  quark(s) constituting the final-state hadrons.

### 1.2.2 Nonleptonic $B$ -Meson Decays

Nonleptonic decays of  $B$  mesons feature a rich interplay of the weak and strong interactions. Knowledge of  $B$ -meson decay rates may be used to obtain angle and phase information in the CKM matrix (Equation 1.2) by way of the charged-current electroweak interaction described in Equation 1.3. The practical extraction of information about the weak processes, however, is confounded by the fact that quarks are necessarily confined inside bound colour-singlet states, requiring the invocation of quantum chromodynamics to complete the description. The relatively heavy mass of the  $b$  quark, nominally 4.1 to 4.5 GeV/ $c^2$  [30] or about 5 times the mass of a proton, is such that QCD descriptions can be decoupled into ‘short’ and ‘long-distance’ dynamical regimes [66] (see Section 1.2.3). Short-distance effects exploit the asymptotic-freedom property of QCD, which enables the perturbative calculation of corrections to the electroweak Hamiltonian due to exchanges of hard gluons [67]. In the context of nonleptonic decays of  $B$  mesons, long-distance QCD effects generally involve the hadronization of the decay products and include the exchange of soft gluons, the creation of  $q\bar{q}$  pairs from the vacuum, and interactions of the hadrons in the final state. That long-distance QCD processes are nonperturbative has so far thwarted calculations of these effects from first principles; nevertheless, the separation of the decay mechanism into short and long-distance components is currently the most successful approach to understanding many  $B$ -meson decay processes. Experimental measurements of  $B$ -meson decay properties are

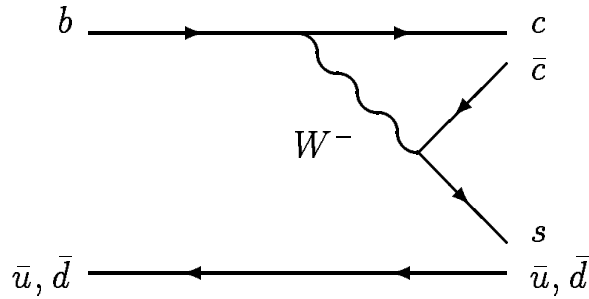


Figure 1.3: Feynman diagram of the ‘spectator-internal’ weak decay mechanism for a  $B$  meson (here either a  $b\bar{u}$  ( $B^-$ ) or  $b\bar{d}$  ( $\overline{B^0}$ ) state) decaying to charmonium ( $J/\psi$  or  $\psi(2S)$ ) and a strange meson ( $K^-$  or  $\overline{K^*}(892)^0$ ). The decay is colour-suppressed because it only occurs when the  $c\bar{s}$  pair, itself a colour singlet, conspires with the  $c$  quark and the  $\bar{u}$  or  $\bar{d}$  quark to form colour-singlet  $c\bar{c}$  and  $s\bar{u}$  or  $s\bar{d}$  mesons. In this mechanism, the  $\bar{u}$  or  $\bar{d}$  quark is assumed to be a ‘spectator’ of the weak process.

clearly essential to the pursuit of an understanding of the dynamical complexities of the underlying phenomena.

This dissertation concerns the experimental study of exclusive nonleptonic decays of  $B$  mesons into  $J/\psi$  or  $\psi(2S)$  vector-meson and  $K^+$  pseudoscalar-meson or  $K^*(892)^0$  vector-meson<sup>7</sup> final states. Figure 1.3 exhibits the weak-interaction aspect of these decays, which are categorized as ‘spectator-internal’ processes by virtue of two assumptions: (i) the light-quark (spectator) constituent of the  $B$  meson fails to participate in any process before hadronization and final-state interactions occur and (ii) the quark with which the spectator forms a colour singlet in the final state derives from an “internally produced”  $W$  boson. These decays are considered to be colour-suppressed because they can only occur when the  $W$  bosons’ hadronic decay products, themselves constituting colour singlets, conspire with the charm quarks from the flavour-changing decays and the spectator quarks to form colour-singlet charmonium and strange mesons, respectively. Finally, these processes are CKM-favoured, as their rates depend upon  $|V_{cb}|^2$  (refer to Equation 1.2), where  $|V_{cb}| = 0.041 \pm 0.003$  [30].

Gourdin, Kamal, and Pham state that “it is generally believed that the best place to study the importance of colour-suppressed processes in  $B$ -meson decay is to look at final states involving a charmonium and a strange meson” [70]. Precise measurements

<sup>7</sup>The  $K^*(892)^0$  vector meson was the first meson resonance to be observed [68, 69].

of properties of this class of decays can improve knowledge of wave functions in the  $B$  system [71], the same wave functions that are involved in, *e.g.*, the rare processes  $B^0 \rightarrow K^*(892)^0 \gamma$  and  $B \rightarrow K e^+ e^-$  [71, 72]. Experimental observations of  $B \rightarrow \psi K$  decays also provide input to and tests of theoretical and phenomenological methodologies and hypotheses. Some of these issues are discussed in Section 1.2.3.

### 1.2.3 The Factorization *Ansatz*

The factorization *Ansatz* model was first used by Bauer, Stech, and Wirbel (BSW) to describe exclusive semileptonic decays of heavy mesons [73]. The techniques were subsequently extended to encompass nonleptonic heavy-flavoured meson decays [74]. A fundamental assumption in the BSW model is the distinction, noted in Section 1.2.2, between two disparate time (or distance) scales in the decay dynamics. In the nonleptonic weak decay of a  $B$  meson, the  $b$  quark decays with a time scale of  $\tau \sim 1/M_W \sim 10^{-26}$  s. It is assumed that all other partons in the system (including the spectator quark, sea quarks, and soft gluons) suspend any interaction until the longer QCD time scale,  $\tau \sim 1/\Lambda_{\text{QCD}} \sim 10^{-23}$  s, indicating the time when confinement forces become important, takes effect.

Using the mode  $B^+ \rightarrow J/\psi K^+$  as an example, the amplitude of the decay ( $\mathcal{M}$ ) can be expressed as a superposition of local operators,  $O_i$ , with scale-dependent short-distance Wilson coefficients,  $C_i(\mu)$ , in the form

$$\begin{aligned} \mathcal{M}(B^+ \rightarrow J/\psi K^+) &= \langle J/\psi, K^+ | \mathcal{H}_{\text{eff}} | B^+ \rangle \\ &= -\frac{G_F}{\sqrt{2}} \sum_i C_i(\mu) \langle J/\psi, K^+ | O_i | B^+ \rangle, \end{aligned} \quad (1.12)$$

where  $G_F$  is the Fermi coupling constant and  $\mathcal{H}_{\text{eff}}$  is the effective Hamiltonian embodying the  $\mathcal{O}(\alpha_s)$  hard-gluon corrections to the weak decay of the  $b$  quark [75]:

$$\mathcal{H}_{\text{eff}} \equiv -\frac{G_F}{\sqrt{2}} V_{cb} \{ C_1(\mu) [(\bar{c}b)^\alpha (\bar{s}'c)_\alpha] + C_2(\mu) [(\bar{s}'b)^\alpha (\bar{c}c)_\alpha] \}. \quad (1.13)$$

The primed fields represent weak eigenstates, which were defined in Equation 1.2. Similar to the form of Equation 1.3, Equation 1.13 uses the notation

$$(\bar{q}_2 q_1)^\alpha \equiv \sum_\lambda \bar{q}_{2\lambda} \gamma^\alpha (1 - \gamma^5) q_{1\lambda} \quad (1.14)$$

for the current terms, where  $\lambda$  is the colour index. Currents proportional to the Wilson coefficient  $C_1(\mu)$  are charged, as exemplified in Figure 1.3, and currents proportional to

$C_2(\mu)$  are effectively neutral. In principle, gluonic penguin<sup>8</sup> interactions can also contribute to Equation 1.13; however, these are highly suppressed due to the fact that the production of a  $J/\psi$  meson from gluons necessarily involves no less than three gluons [76].

The factorization *Ansatz* is an approximation whereby one of the currents in the (current)  $\times$  (current) form expressed in Equation 1.13 is assumed to be asymptotic, thereby enabling the factorization of the amplitude in terms of hadronic ( $H$ ) currents instead of quark currents [74, 77]:

$$\mathcal{M}(B^+ \rightarrow J/\psi K^+) = -\frac{G_F}{\sqrt{2}} a_2 V_{cb} \left\{ \langle J/\psi | (\bar{c}c)_\alpha^H | 0 \rangle \cdot \langle K^+ | (\bar{s}'b)_H^\alpha | B^+ \rangle \right\}, \quad (1.15)$$

where the quantity  $a_2$  is a new scale-independent coefficient native to spectator-internal mechanisms (see Figure 1.3) and constructed via a linear combination of the Wilson coefficients evaluated at a scale defined by  $\mu \simeq m_b$ ,

$$a_2 \simeq C_2(m_b) + \xi C_1(m_b). \quad (1.16)$$

The new parameter  $\xi$  is an *ad hoc* colour factor, often taken naïvely to be  $\sim 1/3$  due to the three degrees of colour freedom<sup>9</sup>. Since the colour structure in Equation 1.16 can easily be destroyed by long-distance soft-gluon dynamics,  $a_2$  is typically treated as a free parameter [74, 75]. Equation 1.15 suggests that a knowledge of the  $B \rightarrow \psi K$  decay rates can furnish estimates of the magnitude of the  $a_2$  parameter [78, 79].

The asymptotic  $\langle J/\psi | (\bar{c}c)_\mu^H | 0 \rangle$  single-particle matrix element in Equation 1.15 is proportional to the  $J/\psi$  decay constant, thus reducing the amplitude calculation to a determination of the hadronic form factors constituting the  $\langle K^+ | (\bar{s}'b)_H^\mu | B^+ \rangle$  matrix element. Several different approaches to modeling the hadronic form factors, which typically employ measurements from experiments involving semileptonic decays, exist in the literature and will not be discussed here in detail. One elegant and successful method has been to exploit the heavy-quark symmetries that arise in the  $m_b \rightarrow \infty$  limit [80]. The application of heavy-quark symmetries to the determination of  $B \rightarrow K$  form factors, however, is hampered by

<sup>8</sup>Penguin decays have the characteristic that the  $W$  boson is reabsorbed by the quark line from which it was emitted, yielding an effective net flavour-changing neutral current process. A photon, gluon, or  $Z^0$  boson is emitted from the resulting loop.

<sup>9</sup>As the choice of the notation  $a_2$  suggests, there is another scale-independent coefficient,  $a_1$ , defined by  $a_1 \simeq C_1(m_b) + \xi C_2(m_b)$ , which represents a separate ‘spectator-external’ class of  $B$ -meson decays.

the relative lightness of the  $s$  quark. Moreover, the observed absence of tree-level flavour-changing neutral-current decays complicates the use of experimental inputs in estimates of  $B \rightarrow K$  form factors. Highly model-dependent *Ansätze* have been used to estimate  $B \rightarrow K$  form factors from, *e.g.*,  $D \rightarrow K^{(*)} \ell \nu$  semileptonic decay measurements [81, 82]. Two principal sources of significant theoretical uncertainty are present in all these estimations: the uncertainties in the numerical values of the form factors at zero momentum transfer between the  $B$  parent and the  $K$  daughter ( $q^2 = 0$ ) and the uncertainties in the assumed parameterizations of their  $q^2$  extrapolations [83].

It is important to point out that, unlike for semileptonic decays where the amplitude can be decomposed into leptonic and hadronic currents, there is no theoretical justification for the application of the factorization *Ansatz* to colour-suppressed  $B \rightarrow \psi K$  decay modes [84, 82]. Tests of the validity of factorization for  $B \rightarrow \psi K$  decays are challenged by the difficulty in isolating factorization effects from form-factor effects. Part of the ambiguity can be removed by confronting the data with calculated observables that involve *ratios* of form factors, thereby purging some reliance on the absolute values of the form factors, but nevertheless retaining a dependence on assumptions about their  $q^2$  extrapolations [85]. Tests of factorization have consisted of requiring that the models reconcile ratio-of-branching-fraction measurements (*e.g.*,  $\mathcal{B}(B \rightarrow J/\psi K)/\mathcal{B}(B \rightarrow \psi(2S) K)$ ) with measurements of longitudinal polarization fractions (*e.g.*,  $\frac{\Gamma_L}{\Gamma}(B^0 \rightarrow J/\psi K^*(892)^0)$ ). Factorization models have been shown to be unable to account simultaneously for measurements of these two observables [70, 82]. While inadequacies in the form-factor approximations are clearly possible, it has been suggested that the discrepancies may be due to nonfactorizable contributions to the decay amplitudes [86, 87, 88, 89, 90].

#### 1.2.4 Theoretical Predictions

The foregoing synopsis of factorization techniques points out some of the difficulties and uncertainties in constructing a reliable theoretical and phenomenological picture of exclusive  $B$ -meson decays to charmonium and strange-meson final states. Although the present tendency is for the experimental data to drive phenomenological investigations of form-factor assumptions and nonfactorizable contributions to the  $a_1$  and  $a_2$  parameters, there nevertheless exist some recent branching-fraction predictions in the literature.

Decay Channel	Branching-Fraction Predictions ( $\mathcal{B}$ ) [ $\times 10^{-3}$ ]		
	Deshpande [71]	Deandrea [81]	Cheng [86]
$B^+ \rightarrow J/\psi K^+$	0.84	$1.1 \pm 0.6$	n/a
$B^0 \rightarrow J/\psi K^*(892)^0$	1.63	$1.6 \pm 0.5$	n/a
$B^+ \rightarrow \psi(2S) K^+$	0.33	$0.37 \pm 0.19$	0.52
$B^0 \rightarrow \psi(2S) K^*(892)^0$	1.27	$0.74 \pm 0.23$	0.76
Year Published	1990	1993	1997

Table 1.2: Theoretical branching-fraction predictions, based on the factorization *Ansatz*, of the decay modes under study. The Deandrea *et al.* predictions assumed  $B$ -meson lifetimes of  $\tau_{B^+} = \tau_{B^0} = 1.4 \times 10^{-12}$  s and the Cheng *et al.* predictions used the world-average [30] measured lifetimes:  $\tau_{B^+} = 1.62 \times 10^{-12}$  s and  $\tau_{B^0} = 1.56 \times 10^{-12}$  s.

The three sets of factorization predictions considered in Table 1.2 were selected because they all included treatments of the  $\psi(2S)$  final states. The Deshpande *et al.* results [71] made use of form factors from BSW, who calculated solutions to a relativistic harmonic oscillator potential model and assumed a single-pole<sup>10</sup>  $q^2$  dependence [73, 74]. The Deandrea *et al.* calculations employed form factors that were derived from experimental exclusive semileptonic  $D$ -meson decay measurements and that were also taken to possess a monopole  $q^2$  dependence [81]. The Cheng *et al.* predictions<sup>11</sup> for the  $\psi(2S)$  final states were based both on an  $a_2$  parameter that was computed from experimental measurements of the analogous  $J/\psi$  modes and on form factors that were calculated explicitly over the entire physical  $q^2$  range [86].

### 1.3 Dissertation Overview

This dissertation describes searches for the decay channels listed in Table 1.2 and relates details of their full reconstruction and branching-fraction ( $\mathcal{B}$ ) measurements, as observed in 1.8-TeV proton-antiproton collisions. Figures 1.4 and 1.5 schematically illustrate the topologies considered in the analysis of  $B^+$  and  $B^0$  mesons, respectively. Both species of charmonium meson are sought in their dimuon modes, and the  $\psi(2S)$  meson is supplemen-

<sup>10</sup>The generic monopole form-factor formula is  $F(q^2) = F(0)/(1 - q^2/m^2)$ , where  $m$  represents the pole mass [73, 81].

<sup>11</sup>Note that the Cheng *et al.* predictions were compared in Reference [86] with preliminary versions [91] of the measurements described in this dissertation.



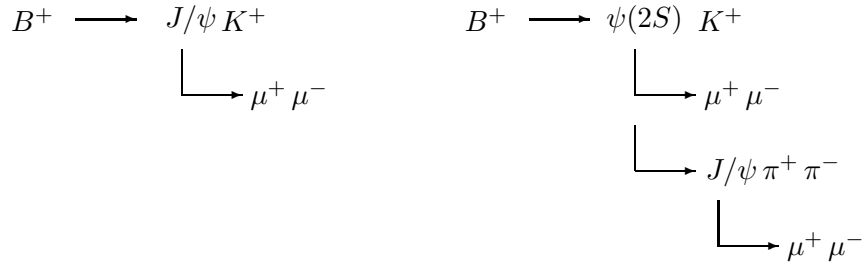


Figure 1.4: Schematic diagrams of the  $B^+$  decay modes reconstructed in this study.

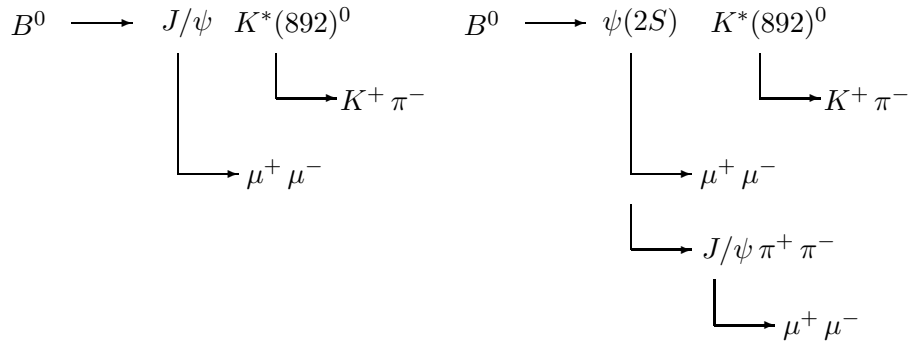


Figure 1.5: Schematic diagrams of the  $B^0$  decay modes reconstructed in this study.

tally reconstructed in its hadronic-cascade  $\psi(2S) \rightarrow J/\psi \pi^+ \pi^-$  mode (refer to Section 1.1).

Just as the examination of relative, as opposed to absolute, branching fractions can simplify theoretical approaches to  $B$ -meson decay ([85] and Section 1.2.3), the use of candidate event yields to compute ratios of branching fractions can have several benefits on the experimental side. Consider an expression describing the requisite ingredients to measure the experimental absolute branching fraction of, for example, the decay  $B^\pm \rightarrow \psi(2S) K^\pm$ , where the  $\psi(2S)$  meson decays in its  $\psi(2S) \rightarrow J/\psi \pi^+ \pi^-$  channel:

$$\mathcal{B}(B^\pm \rightarrow \psi(2S) K^\pm) = \frac{N(B^\pm \rightarrow \psi(2S) K^\pm)}{2\varepsilon \mathcal{A} f_u \cdot \sigma(p\bar{p} \rightarrow b(\bar{b}) X) \cdot \int \mathcal{L} dt \cdot \mathcal{B}(\psi(2S) \rightarrow J/\psi \pi^+ \pi^-) \cdot \mathcal{B}(J/\psi \rightarrow \mu^+ \mu^-)}, \quad (1.17)$$

where  $N(B^\pm \rightarrow \psi(2S) K^\pm)$  denotes the yield of candidate decays reconstructed,  $\varepsilon$  repre-

sents the product of several reconstruction efficiencies (Chapter 5),  $\mathcal{A}$  is the geometric and kinematic acceptance correction factor (Chapter 4),  $f_u$  is the fragmentation fraction, or the probability that a  $b$  quark will hadronize with a  $u$  quark into a  $B^\pm$  meson,  $\sigma(p\bar{p} \rightarrow b(\bar{b})X)$  is the  $b$ -quark hadroproduction cross section ( $X$  denotes the underlying event),  $\int \mathcal{L} dt$  signifies the time-integrated luminosity of the data sample, and  $\mathcal{B}(\psi(2S) \rightarrow J/\psi \pi^+ \pi^-)$  and  $\mathcal{B}(J/\psi \rightarrow \mu^+ \mu^-)$  are charmonium branching fractions. The factor of two in the denominator of Equation 1.17 accounts for the fact that both  $B^+$  and  $B^-$  meson candidates are reconstructed.

As the schematic decay chains in Figures 1.4 and 1.5 connote, several topological similarities exist amongst the decays under scrutiny. The construction of ratios of branching fractions like the one expressed in Equation 1.17 can therefore exploit these congruities by accommodating the cancelation of several common reconstruction efficiencies and systematic uncertainties. Moreover, other quantities with sizeable measurement uncertainties concomitantly divide to unity in these ratios. Since the data sample (Section 3.1) is common to modes in both the numerator and denominator of a ratio of branching fractions, the  $\int \mathcal{L} dt$  factors are no longer important. Depending on which modes make up a given ratio, some of the charmonium and  $K^*(892)^0$  branching-fraction factors can divide out of the expression, thereby reducing the overall systematic uncertainty. The cancelation of the  $\sigma(p\bar{p} \rightarrow b(\bar{b})X)$  factors is expected to be especially beneficial, as theoretical models (Section 4.1) and experimental measurements of the  $b$ -quark differential hadroproduction cross section versus  $p_T$ , both of which rely on some assumptions, have been observed to have consistent shapes but only marginally consistent normalizations [92].

An example of a branching-fraction ratio to be measured in this study is given by extending Equation 1.17 to the expression

$$\frac{\mathcal{B}(B^+ \rightarrow \psi(2S) K^+)}{\mathcal{B}(B^0 \rightarrow J/\psi K^*(892)^0)} = \frac{N(B^+ \rightarrow \psi(2S) K^+)}{N(B^0 \rightarrow J/\psi K^*(892)^0)} \cdot \frac{\varepsilon'_R \mathcal{A}'}{\varepsilon_R \mathcal{A}} \cdot \frac{f_d}{f_u} \cdot \frac{\mathcal{B}(K^*(892)^0 \rightarrow K^+ \pi^-)}{\mathcal{B}(\psi(2S) \rightarrow J/\psi \pi^+ \pi^-)}, \quad (1.18)$$

where the primed quantities refer to the  $B^0 \rightarrow J/\psi K^*(892)^0$  reconstruction, the subscripts  $R$  indicate that the efficiency products have been reduced from their absolute values due to the cancelation of common factors in the ratio, and  $f_d$  is the fragmentation fraction for the  $b \rightarrow B^0$  hadronization process. Direct measurements of branching-fraction ratios such

$R_j^i \equiv \mathcal{B}(i)/\mathcal{B}(j)$	$B^+ \rightarrow J/\psi K^+$	$B^0 \rightarrow J/\psi K^*(892)^0$	$B^+ \rightarrow \psi(2S) K^+$
$B^0 \rightarrow J/\psi K^*(892)^0$	$R_{J/\psi K^+}^{J/\psi K^*(892)^0}$		
$B^+ \rightarrow \psi(2S) K^+$	$R_{J/\psi K^+}^{\psi(2S) K^+}$	$R_{J/\psi K^*(892)^0}^{\psi(2S) K^+}$	
$B^0 \rightarrow \psi(2S) K^*(892)^0$	$R_{J/\psi K^+}^{\psi(2S) K^*(892)^0}$	$R_{J/\psi K^*(892)^0}^{\psi(2S) K^*(892)^0}$	$R_{\psi(2S) K^+}^{\psi(2S) K^*(892)^0}$

Table 1.3: The branching-fraction ratios measured for the various  $B$ -meson final states. The ratio  $R_j^i$  is located in the  $i^{\text{th}}$  row and the  $j^{\text{th}}$  column, and the  $i$  and  $j$  indices refer to the numerators and denominators of the ratios, respectively. Note that the ratios containing  $\psi(2S)$  mesons are composed of contributions from two separate  $B$ -meson reconstructions.

as that in Equation 1.18 may be made with the assumption that  $f_u = f_d$ . Measurements of  $f_u/f_d$  that assumed isospin symmetry have confirmed this hypothesis in  $p\bar{p}$  collisions, up to an uncertainty of 21% [93]. Reference [30] also assumes  $f_u = f_d$  on the grounds that the  $B^+$  and  $B^0$  meson masses are nearly equal and that the CLEO collaboration has measured  $f_u/f_d = 1.13 \pm 0.20$  [94]. Finally, the world-average [30]  $B^+ \rightarrow J/\psi K^+$  branching fraction will be used to extract measurements of those absolute branching fractions listed in Table 1.2 from the appropriate measured ratios of branching fractions.

Table 1.3 lists the branching-fraction ratios investigated. Numerators and denominators containing  $\psi(2S)$  mesons are composed of contributions from two separate  $B$ -meson reconstructions, namely those involving the  $\psi(2S) \rightarrow \mu^+ \mu^-$  and  $\psi(2S) \rightarrow J/\psi \pi^+ \pi^-$  decay modes.

Chapter 2 describes the acceleration and detection apparatus used to produce  $B$  mesons and record their decays, respectively. Techniques invoked to reconstruct  $B$ -meson candidates and reject background processes are discussed in Chapter 3, whereas Monte Carlo methods employed to determine the geometric and kinematic acceptance corrections receive treatment in Chapter 4. Chapter 5 traces the reckoning of several efficiencies and their associated systematic uncertainties, both of which are used in Chapter 6 to calculate ratios of branching fractions from the observed yields of the decays under study. The implications of the measurements are discussed further in Chapter 6 and conclusions are offered in Chapter 7.

## Chapter 2

# Experimental Apparatus

The apparatus employed in this study resides at the Fermi National Accelerator Laboratory (FNAL) in Batavia, Illinois, USA. The laboratory, which is commonly known as Fermilab, is owned by the United States Department of Energy and is operated under a contract with the Universities Research Association, Incorporated. Section 2.1 in this chapter briefly describes the sequence of accelerators, culminating in the Tevatron synchrotron, that ultimately accelerate and collide beams of protons against those of antiprotons at centre-of-mass energies of 1.8 TeV.

In this study, observation of the ensuing collision products was achieved through the use of one of two general-purpose particle detectors situated at different interaction regions on the Tevatron collider ring. The Collider Detector at Fermilab (CDF detector) is an azimuthally and forward-backward symmetric device that consists of several tracking, calorimeter, and muon subsystems. Section 2.2 provides an overview of the CDF detector and Sections 2.3 through 2.6 describe those subsystems apposite to the present analysis: the tracking, muon, trigger, and data acquisition systems.

### 2.1 The Fermilab Tevatron $p\bar{p}$ Collider

The acceleration of protons and antiprotons to energies of 900 GeV is accomplished at Fermilab by a synergism of six particle accelerators. The Cockroft-Walton [95] pulsed ion source begins the sequence by converting gaseous  $H_2$  molecules to  $H^-$  ions, which are subsequently subjected to a 750-keV electric potential. The  $H^-$  ions then enter a 150-m linear accelerator, or Linac, where they are accelerated to energies of 400 MeV by a sequence

of drift-tube induced oscillating electric fields [96, 97]. Refer to Figure 2.1 for a schematic diagram that depicts the Linac and the other accelerators.

At the end of the Linac stage, the  $H^-$  ions are guided into the Booster, an alternating gradient synchrotron [98] with a circumference of  $\sim 470$  m, in which they make  $\sim 16\,000$  revolutions and acquire an energy of 8 GeV. During injection into the Booster, both electrons are stripped from the  $H^-$  ions by passing the ions through a carbon foil. The 8-GeV protons are injected from the Booster into the  $\sim 6.28$ -km circumference Main Ring proton synchrotron where they are accelerated to typical energies of  $\sim 150$  GeV under the guidance of 1014 conventional copper-coiled dipole and quadrupole magnets [96]. Please refer to Figure 2.1.

The Tevatron, located directly below and in the same tunnel as the Main Ring, is another synchrotron, but one that is distinct from the others in that it has magnet coils consisting of superconducting niobium-titanium (Nb-Ti) alloy filaments embedded in copper instead of the conventional copper coils used in the Booster and Main Ring magnets [99, 100]. The increased magnetic fields produced by the Nb-Ti magnets enable the Tevatron to accelerate protons to energies of nearly 1 TeV.

Antiprotons are produced using 120-GeV protons that are extracted from the Main Ring and are made to strike a 7-cm thick nickel or copper target. A liquid lithium lens focuses the antiprotons and directs them to the Debuncher, which is a ring 520-m in circumference where the antiproton beam aperture and energy distribution are reduced by means of stochastic cooling [101] and debunching [102] techniques, respectively. The antiprotons are then transferred to the Accumulator ring, which is concentric with the Debuncher, for storage and further cooling. Once enough antiprotons have been accumulated and the Tevatron has already been filled with 150-GeV proton bunches, antiprotons in the Accumulator are ‘shot’ into the Main Ring, boosted to 150 GeV, injected into the Tevatron in counter-rotation to the proton bunches, and then accelerated along with the protons to 900 GeV. The counter-rotating beams are made to collide at interaction regions such as  $B\bar{O}$  (shown in Figure 2.1) where 1.8-TeV collisions occur near the geometric centre of the CDF detector.

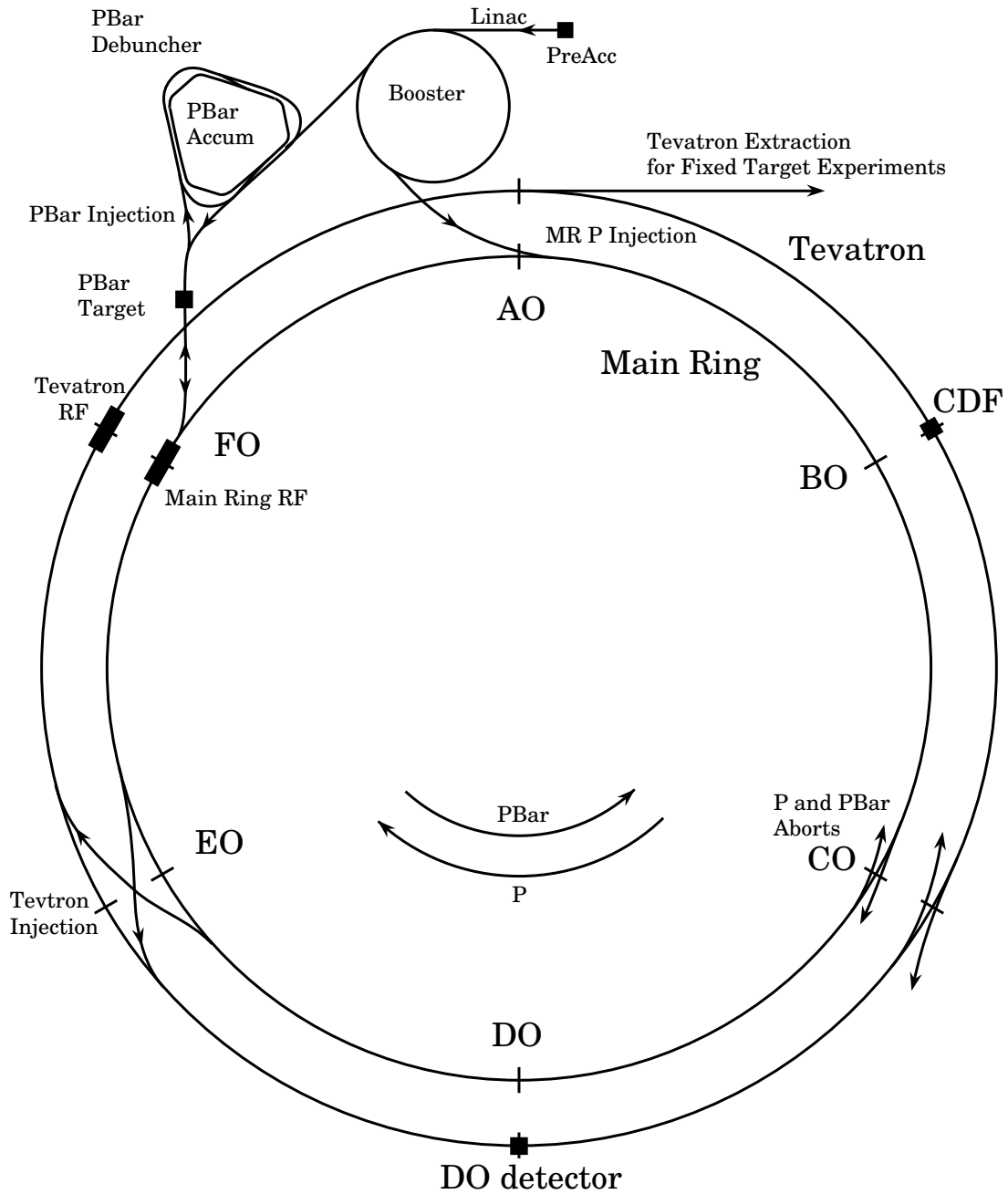


Figure 2.1: Schematic diagram of the  $\sim 6.28$ -km circumference Tevatron  $p\bar{p}$  collider and its affiliated accelerators. For simplicity, the Main Ring and Tevatron are diagrammed as coplanar. This figure is not drawn to scale.

## 2.2 An Overview of the CDF Detector

The Collider Detector at Fermilab (CDF detector) is a general-purpose device designed to study the physics of  $p\bar{p}$  collisions at centre-of-mass energies near 2.0 TeV. A comprehensive description of the CDF detector and its subsystems is given in References [103, 104, 105, 106, 38, 107] and citations therein.

The basic design goals of the CDF detector, pictured in Figure 2.2, were to identify leptons and measure the momenta and energies of particles originating from the  $B\bar{O}$  interaction region. Since the phase space for high energy hadronic collisions is typically described by rapidity (refer to Section 1.1.3), transverse momentum, and azimuthal angle, it is natural that the CDF detector components have an approximately cylindrical symmetry and uniform segmentation in pseudorapidity and azimuthal angle<sup>1</sup>. Tracking detectors, which detect charged particles and measure their momenta, reside nearest the interaction region and inside a  $\sim 1.4$ -T magnetic field. The field is generated by a large electromagnet that consists of 1 164 turns of Nb-Ti/Cu superconductor that constitute a solenoid 4.8-m in length, 1.5-m in radius, and 0.85 radiation lengths in radial thickness. The tracking systems surround an evacuated beryllium beam pipe that is 3.8-cm in diameter, has walls 0.5-mm thick, and forms part of the Tevatron. Section 2.3 describes the CDF tracking systems in some detail.

The detector is divided into a central region ( $|\eta| < 1.1$ ), two end plug regions ( $1.1 < |\eta| < 2.4$ ), and two forward-backward regions ( $2.2 < |\eta| < 4.2$ ). Refer to Figure 2.3 for a schematic elevation-view of one quadrant of the CDF detector. The tracking volume and solenoid are surrounded by sampling calorimeters that measure electromagnetic and hadronic energy flow from the collision point for particles with  $|\eta| < 4.2$ . The calorimeter systems are segmented into projective  $\eta$ - $\varphi$  ‘towers’, each of which points back towards the nominal interaction region and has an electromagnetic shower counter in front of a corresponding hadronic calorimeter cell. In high energy  $p\bar{p}$  collisions, such a projective tower geometry is motivated by the importance of reconstructing jets, which are defined as

---

<sup>1</sup>The CDF coordinate system is right-handed with  $x$  pointing out of the Tevatron ring,  $y$  vertical, and  $z$  in the proton beam direction. The polar angle,  $\theta$ , is measured with respect to the proton direction; the pseudorapidity,  $\eta$ , is defined by  $\eta \equiv -\ln(\tan(\theta/2))$ , with  $\theta$  measured assuming a  $z$ -vertex position of zero; the azimuthal angle is represented by  $\varphi$  and defined with respect to the plane of the Tevatron; and the transverse displacement coordinate is denoted by  $r$ .

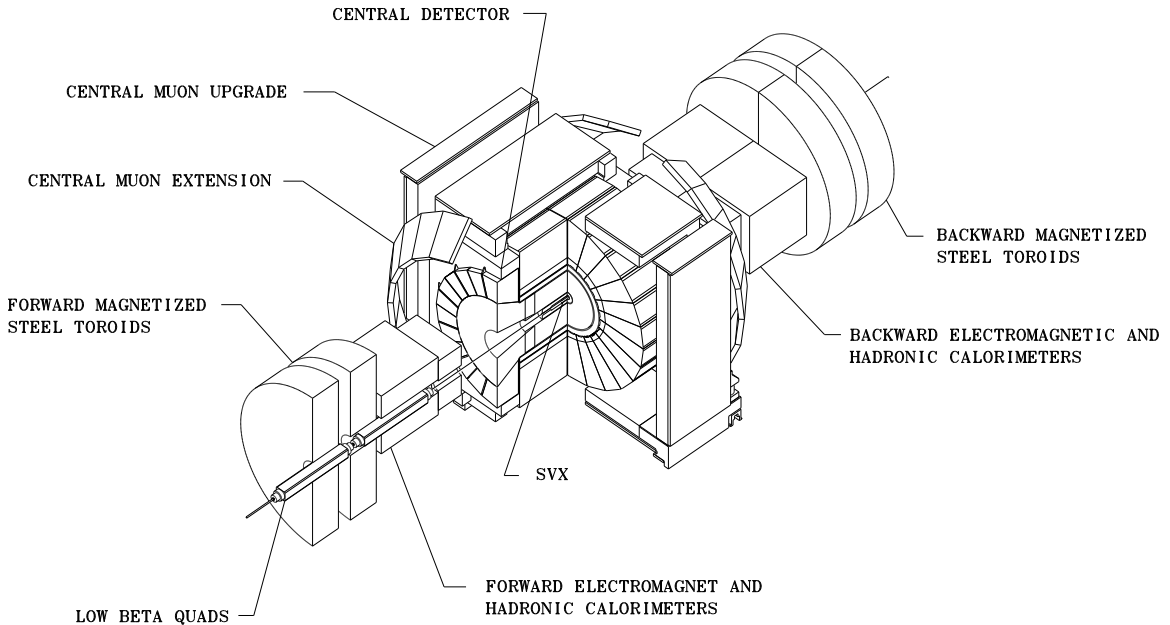


Figure 2.2: An isometric view of three quarters of the CDF detector.

collections of particles that have similar trajectories in  $\eta$ - $\varphi$  space and are typically assumed to originate from a single high energy quark or gluon.

Each of the three main CDF detector regions has an electromagnetic calorimeter; these are the central electromagnetic (CEM), the plug electromagnetic (PEM), and the forward electromagnetic (FEM) calorimeters. Behind the CEM there are two hadronic calorimeters: the central (CHA) and wall hadronic (WHA) calorimeters. The PEM and FEM have a corresponding plug (PHA) and forward hadronic (FHA) calorimeter behind each of them, respectively. Table 2.1 summarizes some selected properties of the CDF calorimeter systems.

Proportional chambers located between the solenoid and the CEM constitute the central preradiator detector, which samples the early  $r$ - $\varphi$  development of electromagnetic showers induced in the material of the superconducting solenoid coils. Other proportional chambers with strip and wire readout are located inside the CEM calorimeter at a depth of  $\sim 6X_0$ , the approximate point where an electromagnetic shower is most fully developed. These central electromagnetic strip detectors measure the positions of showers in both the  $z$  and  $r$ - $\varphi$  views.



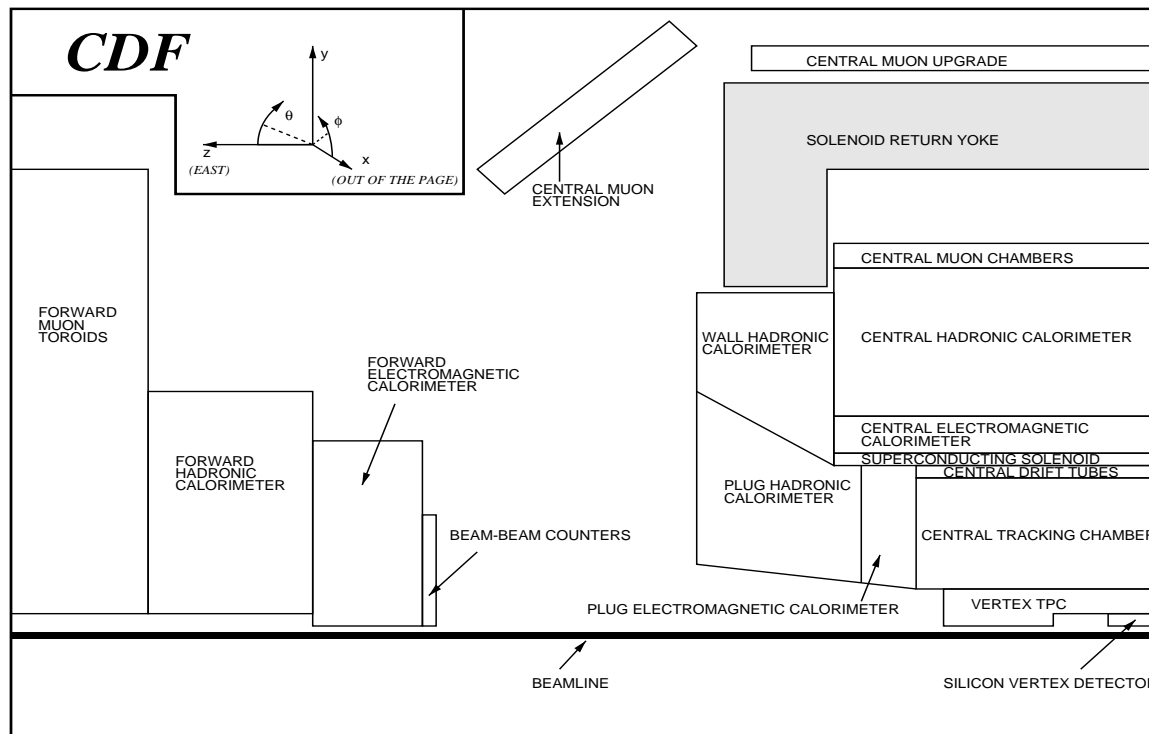


Figure 2.3: A schematic side-elevation view of one quadrant of the CDF detector. The CDF detector, with the exception of the central muon upgrade and extension subsystems, is largely cylindrically symmetric about the interaction region, which is located on the beamline at the right side of the figure.

## 2.3 The Tracking Systems

The reconstruction of exclusive  $B$ -meson decays relies heavily on precise measurements of the daughter particle decay vertices, momenta, and charges. The CDF detector's main tracking capabilities consist of four distinct but complementary tracking subsystems. These systems, listed in order of increasing distance from the interaction region, are the silicon vertex detector, the vertex time projection chamber, the central tracking chamber, and the central drift tube array. Figure 2.3 illustrates the positions of the tracking subsystems, both relative to each other and to the rest of the CDF detector.

### 2.3.1 The Silicon Microstrip Vertex Detector

The silicon microstrip vertex detector (SVX) [104, 105] enables the identification in the  $r$ - $\varphi$  plane of secondary vertices displaced from the  $p\bar{p}$  collision point resulting from the weak

Property	CEM	CHA	WHA	PEM	PHA	FEM	FHA
$ \eta $	0 – 1.1	0 – 0.9	0.7 – 1.3	1.1 – 2.4	1.3 – 2.4	2.2 – 4.2	2.3 – 4.2
$\Delta\eta$	$\sim 0.1$	$\sim 0.1$	$\sim 0.1$	0.09	0.09	0.1	0.1
$\Delta\varphi$	15°	15°	15°	5°	5°	5°	5°
Active	plastic scintillator			gas chambers with cathode pad readout			
Absorber	Pb	Fe	Fe	Pb	Fe	Pb/Sb	Fe
Thickness	18X <sub>0</sub>	4.5λ <sub>0</sub>	4.5λ <sub>0</sub>	18 – 21X <sub>0</sub>	5.7λ <sub>0</sub>	25X <sub>0</sub>	7.7λ <sub>0</sub>

Table 2.1: Selected properties of the CDF calorimeter systems. Shown are the pseudorapidity coverage and segmentation, the azimuthal segmentation, the active medium, the type of absorber, and the thickness in radiation lengths ( $X_0$ ) and interaction lengths ( $\lambda_0$ ) of the electromagnetic and hadronic calorimeters, respectively.

decays of  $b$  quarks. Installed in the CDF detector in 1992, the SVX was the first detector of its kind to be operated successfully in a hadron collider environment. In 1993, a more radiation-hard and low-noise version of the SVX, the SVX' [106], was commissioned for the 1994-1995 Tevatron collider run<sup>2</sup> (refer to Section 3.1). The SVX consists of two identical cylindrical modules, one of which is pictured in Figure 2.4, each comprising four concentric cylindrical layers with radii of 3.0, 4.3, 5.7, and 7.9 cm. The SVX' has the same overall configuration as the SVX, except that the innermost layer has a slightly smaller radius of 2.9 cm. Since the luminous  $p\bar{p}$  interaction region is rather elongated in the  $z$  direction (with a Gaussian distribution having a standard deviation of  $\sigma \sim 30$  cm), approximately 40% of  $p\bar{p}$  collision vertices lie outside the acceptance of the SVX, which has an active length of 51.1 cm.

In both of the SVX barrels, the four layers are each segmented into twelve ‘ladders’ that subtend approximately 30° in azimuth and are oriented parallel to the beam axis. Figure 2.5 depicts a typical ladder situated in the third layer of the SVX. The ladder substrates are fabricated from a light-weight foam (Rohacell) reinforced with strips of carbon fibre. Three single-sided 8.5-cm long silicon microstrip detectors are electrically bonded together with aluminum wire along the  $z$  direction to form a 25.5-cm active silicon region on each ladder

<sup>2</sup>Unless noted otherwise, references to the SVX apply to the SVX' as well.

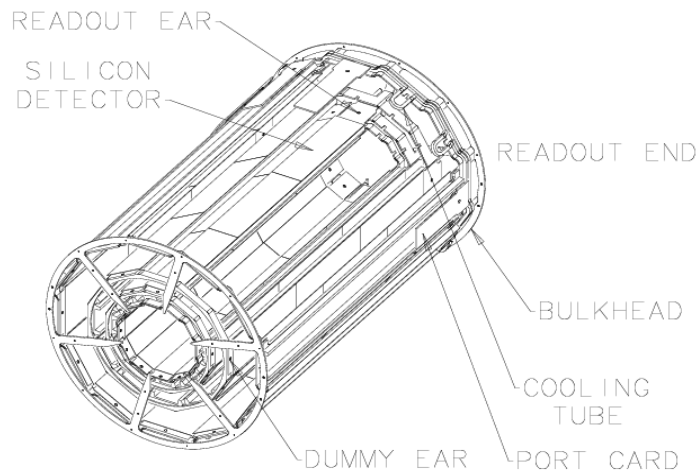


Figure 2.4: Isometric view of one of the two silicon microstrip vertex detector (SVX) barrels. The dummy-ear sides of both barrels are conjoined (with an effective gap of 2.15 cm) at the  $z = 0$  position inside the CDF detector.

module.

Silicon microstrip detectors are a kind of solid ionization chamber in which incident charged particles dislodge electrons via ionization. In their most basic form, the detectors consist of an  $n$ -doped silicon wafer, typically  $300\text{-}\mu\text{m}$  thick, with strips of  $p$ -type material on one side [108]. If a reverse-biased potential is applied to a strip, a  $p$ - $n$  junction diode is set up, and electron-hole pairs created by the passage of a charged particle migrate to their respective electrodes, thereby manifesting an electronic signal that resolves the location of the particle's trajectory as a function of the strip separation, or 'pitch'.

The silicon strip pitch of the inner three SVX layers is  $60\ \mu\text{m}$  and that for the outermost layer is  $55\ \mu\text{m}$ . The average position resolutions for the SVX and the SVX' were measured to be  $13\ \mu\text{m}$  and  $11.6\ \mu\text{m}$ , respectively, and the high transverse momentum (asymptotic) impact parameter resolution was determined to be  $17\ \mu\text{m}$  for the SVX and  $13\ \mu\text{m}$  for the SVX'. Adjacent ladders in a given layer slightly overlap each other to provide full azimuthal coverage; this is achieved with a  $3^\circ$  rotation of the ladders about their major axes. The SVX' has all four of its layers overlapped; however, the innermost layer of the SVX suffers

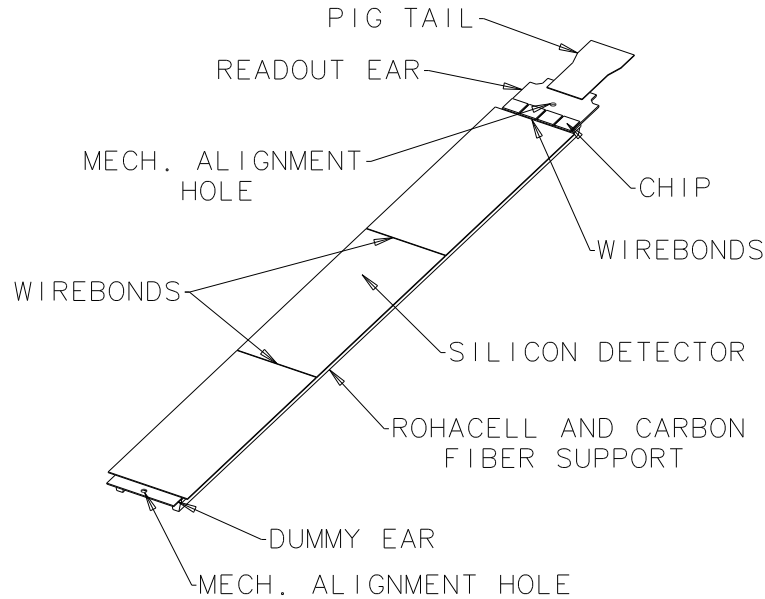


Figure 2.5: Layout of a typical ladder module in the third layer of the SVX. Three single-sided silicon microstrip detectors are wire bonded together to constitute each ladder module.

from a  $1.26^\circ$  gap in  $\varphi$  between adjacent ladder modules.

As shown in Figure 2.5, the outside end of each ladder has a small circuit board that contains the front end readout chips, which each serve 128 channels. Because the ladder widths increase with increasing  $r$ , the number of readout chips on a given ladder module depends upon the layer in question. The innermost layer, for example, has two readout chips per ladder module whereas the outermost layer has six chips per ladder module. The total number of instrumented strips in the SVX is 46 080.

The silicon strips used in the SVX' are AC coupled whereas those for the SVX are DC coupled. The SVX' consequently benefits from a marked reduction in noise compared to the SVX, for which strip-to-strip leakage current variations have to be subtracted by cycling the front end readout chips through two successive charge integrations. An additional advantage of the AC-coupled SVX' design is that the readout chip preamplifiers, which have 40% more gain than their SVX counterparts, will not saturate, even after significant radiation damage has increased the silicon microstrip leakage currents appreciably. The SVX' readout chips were fabricated using radiation hard  $1.2\text{-}\mu\text{m}$  CMOS technology. They therefore have a design absorbed-dose limit of 10 kGy compared with 200 Gy for the SVX,

which uses more conventional 3- $\mu\text{m}$  CMOS electronics [109].

The readout electronics typically generate  $\sim 53.1$  W of heat in each of the two SVX barrels. Cooling pipes transport chilled de-ionized water at a temperature of 13 °C and a flow rate of 10 g/s to the beryllium bulkhead (see Figure 2.4) and the readout circuit boards (see Figure 2.5) to maintain an operating temperature near 20 °C. The cooling circuit runs at a subatmospheric pressure to minimize the potential damage due to a breach in the cooling pipes. Controlling the temperature not only minimizes leakage currents in the silicon microstrips and prevents damage to the front end electronics, but it also discourages thermal gradients in the mechanical support structure that can distort the internal alignment of the SVX.

### 2.3.2 The Vertex Time Projection Chamber

A vertex time projection drift chamber (VTX) surrounds the SVX (refer to Figure 2.3). It was designed to measure the trajectories of charged particles in the  $r$ - $z$  plane in a pseudorapidity range  $|\eta| \lesssim 3.0$ . The VTX is important for the determination of the  $z$  position of the primary vertex and the identification of multiple interactions in the same beam crossing. The VTX resolution of a primary vertex location along the beamline, nominally 2 mm [110], depends on the number of detected tracks originating from that location and the number of primary  $p\bar{p}$  interactions in the event.

The VTX, which extends 132 cm in each  $z$  direction and has a radius of 22 cm, consists of 28 drift modules, each containing two drift regions separated by an aluminum central high voltage grid. Endcaps on each side of the drift modules are azimuthally segmented into octants and are rotated in  $\varphi$  by 15° with respect to adjacent modules (in  $z$ ) to eliminate inefficiencies near module boundaries. Within each octant, 16 or 24 sense wires, depending on the  $z$  position of the module, are oriented tangentially, thereby providing tracking information in the  $r$ - $z$  view. The  $z$  location of a track with respect to a given wire in a given module is determined by the drift time, and the  $r$  information is determined from the radial location of the wire. The electric field is maintained near 1.6 kV/cm and the gas used is a 50:50 admixture of argon and ethane. Figure 2.6 is an event display diagram showing hits from charged particles in two VTX octants. The VTX vertex-finding algorithm has calculated a primary vertex  $z$  position in this event based on a fit to extrapolations of tracks

reconstructed from sense wire hits. The  $z$  vertex position is represented by the seriffed cross in Figure 2.6.

### 2.3.3 The Central Tracking Chamber

The most prominent subsystem in the CDF detector is the central tracking chamber, or CTC. It is the only CDF tracking device that can perform three dimensional momentum and position measurements, both of which are essential to the reconstruction of exclusive  $B$ -meson decays. The CTC, as indicated in Figure 2.3, surrounds the VTX and SVX subsystems and has a coaxial bicylindrical geometry with a 3201.3-mm length (including the endplates), a 2760.0-mm outer diameter, and a 554.0-mm inner diameter. Aluminum is used in the construction of the outer cylinder; carbon fibre reinforced plastic constitutes the inner cylinder wall.

The CTC is a drift chamber that contains 84 layers of 40- $\mu\text{m}$  diameter gold-plated tungsten sense wires arranged into nine ‘superlayers’, five of which have their constituent sense wires oriented parallel to the beam axis (axial superlayers), and four of which have their wires canted at angles of either  $+3^\circ$  or  $-3^\circ$  with respect to the beamline (stereo superlayers). The innermost and outermost sense wires have radii of 309 mm and 1320 mm, respectively. The axial and stereo superlayers alternate with increasing radius and each consists of twelve and six sense wire layers, respectively. The configuration is illustrated in Figure 2.7, which shows the wire slot locations in the aluminum endplates. The majority of the CTC pattern recognition is done using data from the axial layers, which provide tracking information in the  $r$ - $\varphi$  view. The stereo layers furnish tracking information in the  $r$ - $z$  view.

The superlayers are functionally segmented into open drift cells. A drift cell contains a superlayer of (either 12 or 6) sense wires alternating with (either 13 or 7) stainless steel potential wires, which serve to control the gas gain on the sense wires. Two planes of stainless steel field wires on either side of the sense wire superlayers define the fiducial boundaries of each drift cell and control the strength of the electric field in the  $\lesssim 40$ -mm drift regions. The number of cells in each superlayer increases with  $r$  such that the drift distance, which translates into a maximum drift time of  $\sim 800$  ns, is approximately constant for all cells in the CTC. To keep the electric field uniform throughout the fiducial volume

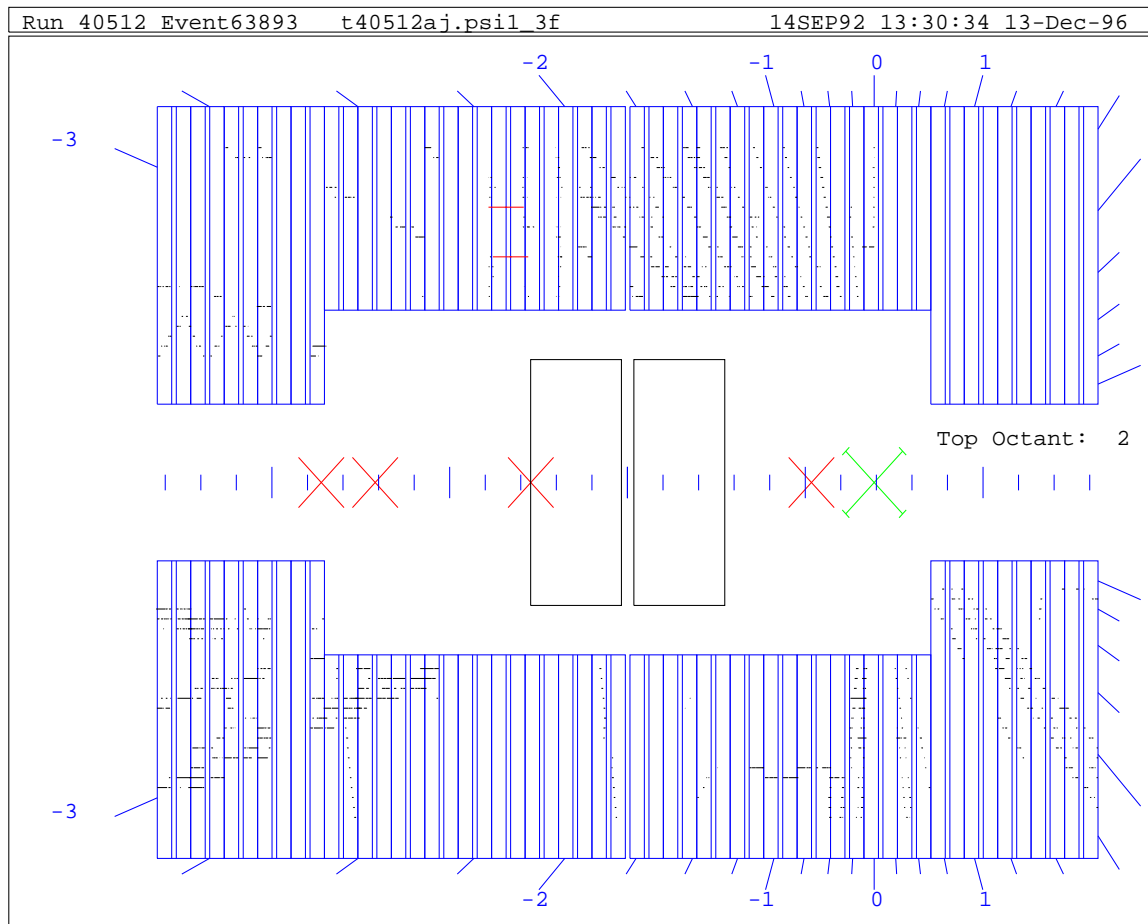


Figure 2.6: Event display of two  $45^\circ$  octants in the vertex time projection chamber (VTX). The beamline runs through the middle of the diagram, across the page. Shown are the 28 drift modules containing hits that form tracks due to the traversal of charged particles from the interaction region. The hits represent the times that the drifting ionization electrons arrive near the sense wires. The crosses along the beamline represent  $z$  vertex candidates found by the VTX software; the single seriffed cross represents an especially high quality vertex that consequently defines the zero location of the event pseudorapidity coordinates, as indicated by the  $\eta$  scale denoted around the outside of the figure. The two rectangles drawn near the geometric centre of the VTX represent active regions of the SVX. This event is a dramatic example of a case where the primary vertex is so distant from  $z = 0$  that the SVX is of little consequence. Also interesting is the helical trajectory of a particle in the upper VTX octant at  $\eta \sim -3.5$ , a result of the large axial magnetic field.

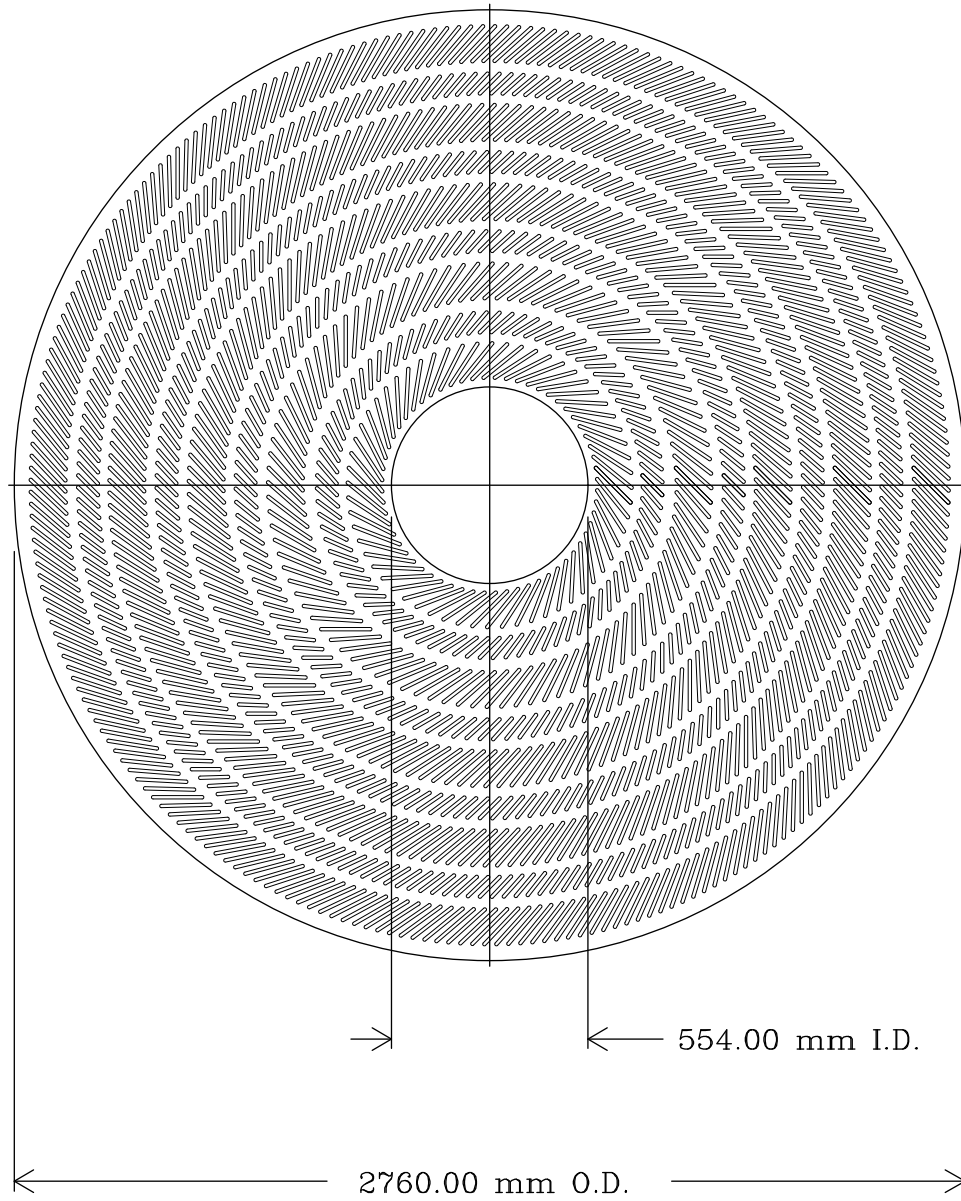


Figure 2.7: One aluminum endplate of the central tracking chamber (CTC), viewed from along the beam axis. The wire slot locations for the alternating axial and stereo superlayers are apparent.



of every drift cell, extra stainless steel shaper and guard wires are located near the cell perimeters, bringing the number of wires in the CTC to a total of 36 504. This translates to a total wire tension of 245 kN and a combined wire length that is in excess of 110 km.

As is evident in Figure 2.7, the CTC drift cells are tilted such that the angle between the radial direction and the electric field direction is approximately  $45^\circ$ . Such a large cant angle is necessary to offset the  $45^\circ$  Lorentz angle, which results from the combined effects of the  $\sim 1.4$ -T magnetic field, the argon-ethane-alcohol gas mixture used (in the proportions 49.6% : 49.6% : 0.8%), and the relatively low  $\sim 1.35$ -kV/cm electric field. The drift trajectories in the CTC are therefore approximately parallel to the azimuthal direction. Every high transverse-momentum track passes close to at least one sense wire in each superlayer.

Preamplifiers mounted on the endplates of the CTC are connected to the sense wires, whose analog signals are amplified further, shaped, and discriminated by circuitry mounted on the solenoid return yoke (see Figure 2.3). The discriminator signals undergo time-to-digital (TDC) conversion in a counting room located at the end of 70 m of flat cable. The 1-ns resolution TDCs can record  $> 7$  hits per wire per event. The CTC double track resolution is  $< 5$  mm due to the approximately 100-ns minimum separation between two resolved hits. The CTC has a single hit resolution of  $< 200 \mu\text{m}$ , and the overall momentum resolution of the combined SVX-CTC system is  $\delta p_T/p_T = \left[ (0.0009 p_T)^2 + (0.0066)^2 \right]^{1/2}$ , where  $p_T$  is the transverse momentum measured in units of GeV/ $c$ . Section 5.2 and Appendix C provide further discussion of the performance of the CTC, and Figure 3.2 contains an event-display diagram of a sample event showing reconstructed CTC track candidates.

### 2.3.4 The Central Drift Tube Array

The central drift tube array, or CDT, is situated at a radius of 1.4 m, between the outer cylinder of the CTC and the inner wall of the solenoid cryostat, as indicated in Figure 2.3. The CDT system consists of stainless steel circular tubes; these are 1.27-cm in diameter, 3-m in length, and 2016 in number. Closely packed into three layers, the tubes are each strung with 50- $\mu\text{m}$  diameter stainless steel anode wires. By virtue of its charge division capability on the anode wires, the CDT can provide tracking information in both the  $r$ - $\varphi$  and  $r$ - $z$  views. For the analysis described in this thesis, CDT tracking information was

not used explicitly in the reconstruction of particle tracks; however, the CDT was used to identify cosmic ray muons as coincident hits with  $\Delta\varphi \sim 180^\circ$ . Cosmic ray muons were used to perform the initial relative alignments of the SVX, VTX, and CTC subsystems within the CDF detector.

## 2.4 The Muon Chambers

The ability to identify muons and their trajectories is essential to the reconstruction of  $J/\psi$  and  $\psi(2S)$  mesons in the dimuon channels. Muon identification can be achieved by exploiting the relatively high muon critical energy<sup>3</sup>, which is several hundred GeV in materials such as iron [30], significantly higher than the critical energy for other ionizing particles. This ability of the muon to penetrate matter thus motivates the location of the muon subsystems in the outer regions of the CDF detector that can only be reached by those charged particles that originate from the interaction region and that penetrate the intervening material. This material, consisting primarily of the calorimeters, serves to filter out the majority of hadrons and electrons before they reach the muon subsystems. Refer to Figure 2.3 for the locations of the three central muon subsystems used in this analysis: the central muon detector (CMU), the central muon upgrade detector (CMP), and the central muon extension (CMX). A map of the  $\eta$ - $\varphi$  muon detection coverage in the central region is shown in Figure 2.8. The forward muon toroid subsystem, shown in Figures 2.2 and 2.3, is not used in this study due to its poor intrinsic momentum resolution and the lack of overlap in acceptance between it and the CTC and SVX tracking systems.

### 2.4.1 The Central Muon Detector

The CMU covers the region  $55^\circ \leq |\theta| \leq 90^\circ$  and resides on the outer edge of the central hadronic calorimeter, 3470 mm from the beam axis, as indicated in Figure 2.9. Each  $12.6^\circ$  azimuthal wedge comprises three modules, each subtending  $4.2^\circ$  in  $\varphi$ . A CMU module, shown in Figure 2.10, consists of four towers, each with four layers of rectangular drift cells. The outermost and second innermost cells in each tower are oriented such that their sense wires lie on a radial that originates from the centre of the CDF detector. The innermost and second outermost drift cells lie on another radial that is offset from the first by 2 mm

---

<sup>3</sup>The muon critical energy is the energy at which losses due to radiation and ionization are equal [30].

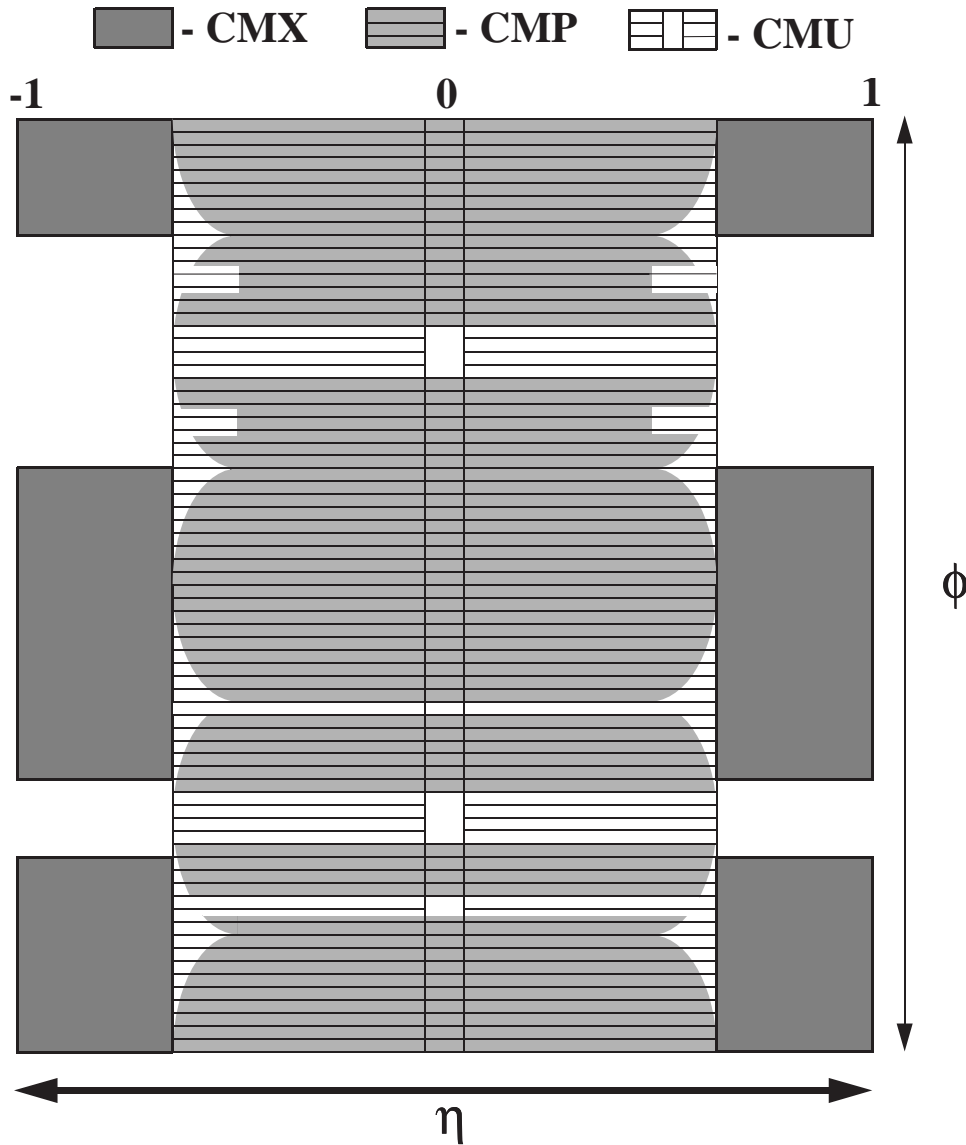


Figure 2.8: Coverage of the central muon subsystems in pseudorapidity ( $\eta$ ) and azimuth ( $\phi$ ) [111]. The lack of CMX coverage at  $\phi \sim 90^\circ$  and  $\phi \sim 270^\circ$  results from the interference due to the Main Ring bypass beampipe and the concrete collision hall floor, respectively.

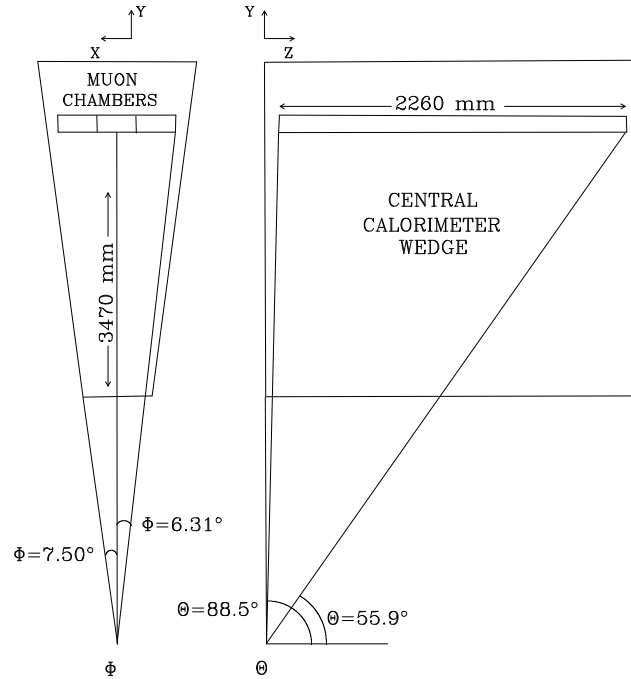


Figure 2.9: The layout of a central muon (CMU) wedge with respect to a central calorimeter wedge in both the azimuthal (left figure) and polar (right figure) views.

at the midpoint (in  $r$ ) of the CMU. The offset cells in each tower resolve the side of the radial, in azimuth, on which the track passed. As indicated in Figure 2.10, the absolute difference in drift electron arrival times for a pair of cells having sense wires on the same radial determines the angle between the candidate muon track and that radial. This angle can be related to the transverse momentum of a muon candidate and is therefore exploited by the trigger system (refer to Section 2.5.1).

A drift cell in the CMU, shown in Figure 2.11, is rectangular with dimensions  $63.5 \text{ mm} \times 26.8 \text{ mm} \times 2261 \text{ mm}$  and has a single  $50\text{-}\mu\text{m}$  stainless steel sense wire strung through its centre. The drift cells are operated in limited streamer mode using a 50:50 admixture of argon and ethane gas, and potentials of  $+3150 \text{ V}$  on the sense wires and  $-2500 \text{ V}$  on the I-beams, which are electrically isolated from the top and bottom aluminum plates by  $0.62 \text{ mm}$  of insulation. The position of a muon candidate track along the sense wire ( $z$ ) direction can be determined with a resolution of  $1.2 \text{ mm}$  using charge division electronics. The position resolution in the drift ( $\varphi$ ) direction is  $250 \mu\text{m}$ .

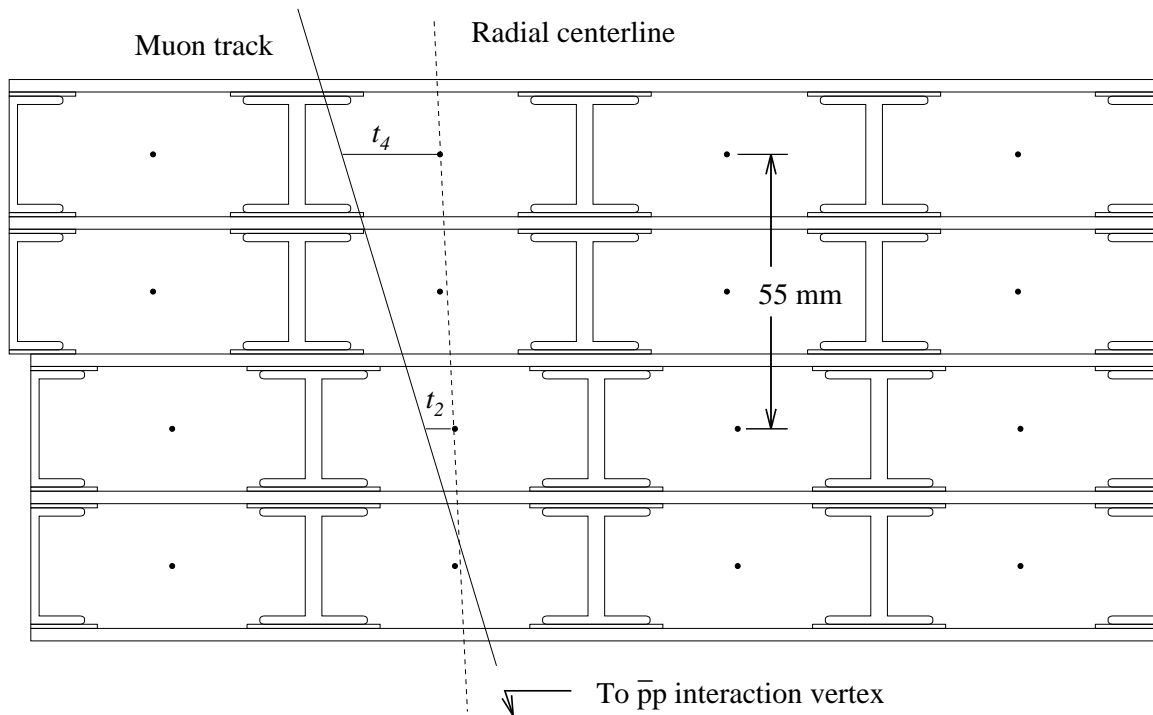


Figure 2.10: Layout of a central muon detector (CMU) module showing the four towers, each with four layers of rectangular drift cells. The outermost and second innermost cells in each tower are oriented such that their sense wires lie on a radial that originates from the geometric centre of the CDF detector. The other two drift cells are offset to determine which side of the radial the track passed. The quantities  $t_2$  and  $t_4$  represent drift electron arrival times; their difference,  $|t_4 - t_2|$ , determines the angle between the candidate muon track and the radial, thus providing a crude but fast measurement of transverse momentum that can be used in a low level trigger. Analogous information from  $t_1$  and  $t_3$  yields a second independent measurement.

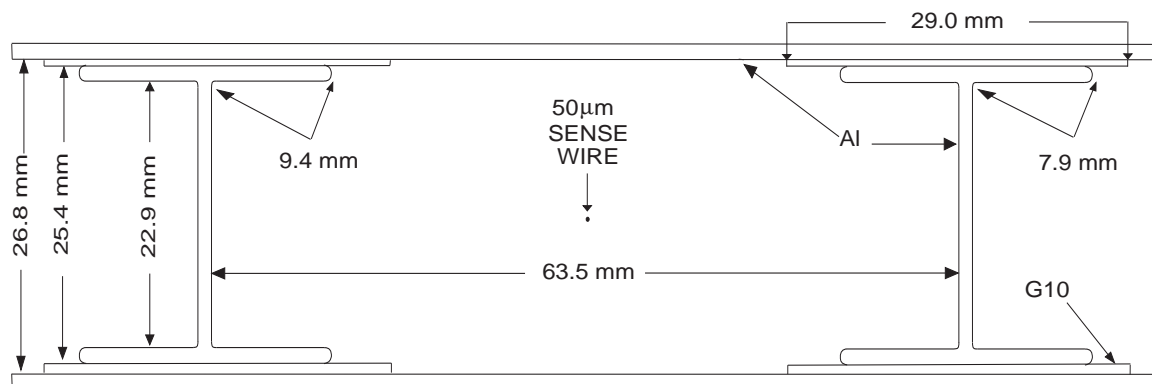


Figure 2.11: Layout of a central muon detector (CMU) drift cell, showing the 0.79-mm aluminum top and bottom plates and the aluminum I-beams that separate adjacent towers.

### 2.4.2 The Central Muon Upgrade Detector

An average of 5.4 pion interaction lengths lies between the CMU and the  $p\bar{p}$  collision region, resulting in approximately 1 in 220 high energy hadrons traversing the calorimeters unchecked. This ‘noninteracting punch-through’ results in an irreducible false muon background rate. The central muon upgrade detector (CMP), shown in Figures 2.2 and 2.3, was commissioned to contend with this punch-through hadron rate [111]. The CMP surrounds the central region of the CDF detector with 630 tons of additional steel. The geometry is box-like, with the return yoke of the solenoid providing the absorption steel on the top and bottom, and two retractable 60-cm thick slabs arranged as vertical walls on each side. The additional absorption material brings the number of pion interaction lengths to 7.8 at  $\theta = 90^\circ$ . Figure 2.8 illustrates the variation in pseudorapidity coverage with azimuth caused by the geometry of the CMP.

The active planes of the CMP consist of four layers of half-cell staggered single-wire drift tubes operating in proportional mode. Each drift cell, of which there are 864 in the CMP, consists of a rectangular extruded aluminum tube 25.4-mm high, 152.4-mm wide, and with a length that depends upon where the tube is mounted. Figure 2.12 is a schematic drawing of the components of a CMP proportional drift cell. The anode, a 50- $\mu\text{m}$  gold-plated tungsten wire, is biased to a potential of +5 600 V, the wide central field-shaping cathode pad is biased to +3 000 V, and the eight narrow field-shaping strips have decrementally decreasing voltages from the centre of the cell out to the edges. The maximum drift time is 1.4  $\mu\text{s}$ .

### 2.4.3 The Central Muon Extension

The central muon extension, or CMX, provides additional pseudorapidity acceptance in the region  $0.65 \leq |\eta| \leq 1.0$ . Shown in Figures 2.2 and 2.3, the CMX modules possess geometries that correspond to sides of the frusta of two cones, each with a base at  $z = 0$  and an axis along either the proton or antiproton direction. The azimuthal coverage of the CMX is not continuous; due to the floor of the collision hall, there is a  $90^\circ$  gap in  $\varphi$  at the bottom of the CDF detector, and, due to the Main Ring bypass beam pipe, there is a  $30^\circ$  gap at the top of the detector. The 1 536 proportional drift cells that constitute the CMX modules are shorter than, but otherwise identical to, those used in the CMP (Figure 2.12). No additional absorber was added between the CMX and the interaction region; however,

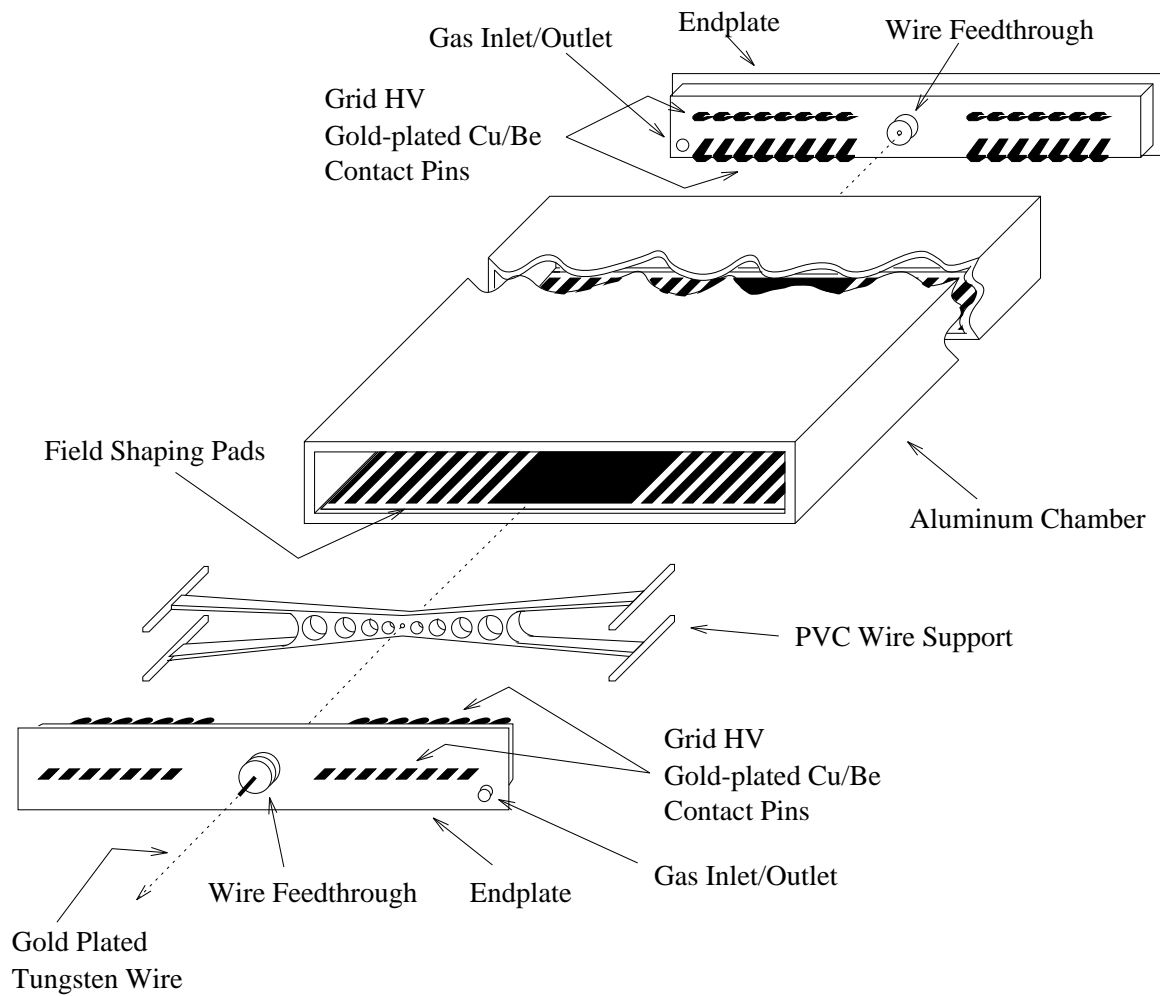


Figure 2.12: Schematic drawing of a proportional drift cell used in both the central muon upgrade detector (CMP) and the central muon extension (CMX) [111].

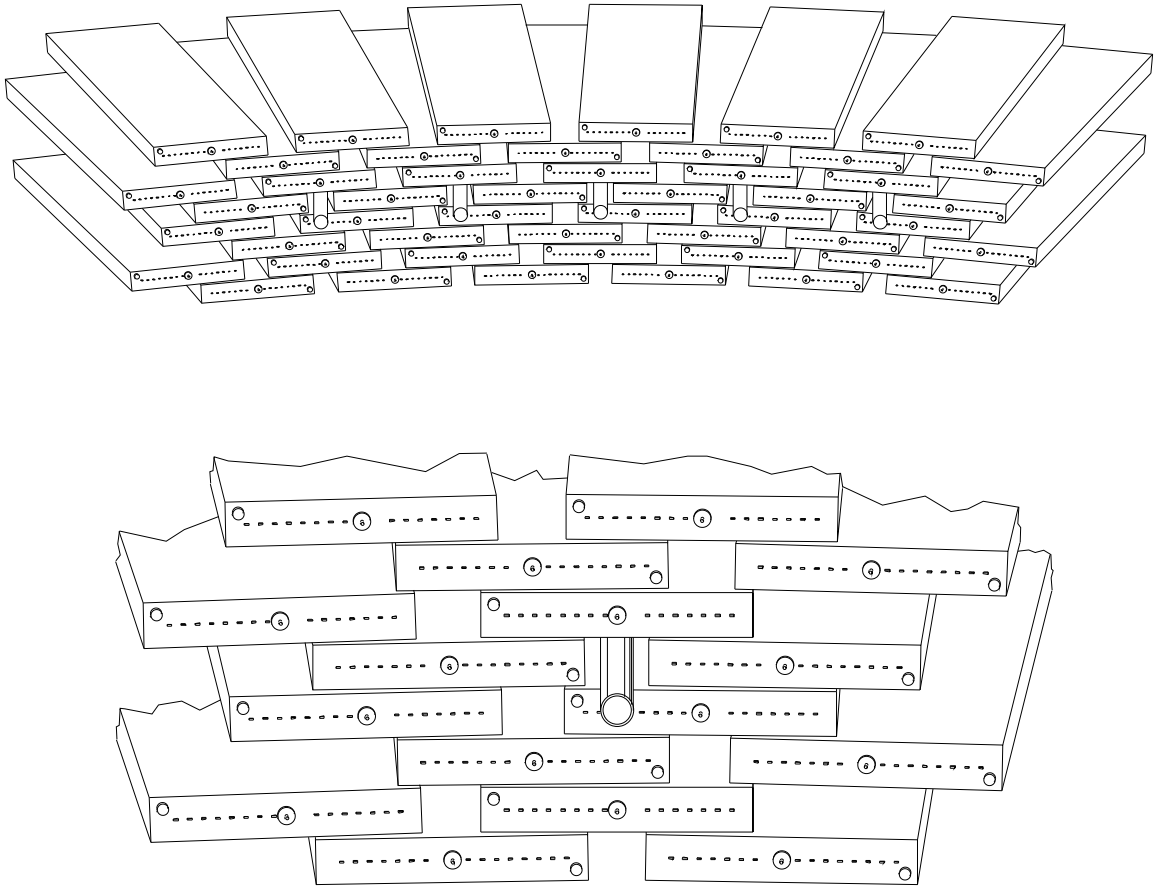


Figure 2.13: Proportional drift cell layout in a  $15^\circ$  module of the central muon extension (CMX) (top figure). Also shown is a close-up view of the staggered cell configuration about one of the threaded rods used to fix the CMX to its support arch (bottom figure) [111].

the smaller polar angle through the hadronic calorimeter and magnet return yoke yields a shielding thickness of 6.2 pion interaction lengths at  $\theta = 55^\circ$ .

The CMX is organized into four stacks, two on the proton side and two on the antiproton side of the CDF detector. Each stack consists of eight modules, which each subtend  $15^\circ$  in azimuth. A module comprises 48 proportional drift cells that are grouped in eight half-cell staggered layers of six tubes each. Refer to Figure 2.13 for an illustration of the interleaved geometry necessary to arrange the rectangular cells along a conical surface. The invisibility of intermodule boundaries is an advantage of this interleaved configuration.

The maximum CMX drift time,  $1.4 \mu\text{s}$ , is such that the spread of arrival times due to background particles is short by comparison. Background rejection and a high speed trigger



are provided by an array of scintillation counters mounted on the inner and outer sides of each CMX module. Four such scintillators, each with its own photomultiplier tube, are located on both sides of every  $15^\circ$  CMX module, for a total of 256 scintillation counters. Background effects are vetoed in the trigger by requiring that both the inner and outer scintillators adjacent to a CMX hit produce pulses that are coincident with the  $p\bar{p}$  beam crossing to within a few nanoseconds.

## 2.5 The Trigger Systems

In the course of data acquisition for this study, proton and antiproton bunch crossings in the Tevatron collider occurred every  $3.5 \mu\text{s}$ , corresponding to a crossing frequency of 286 kHz. With typical instantaneous luminosities of  $\mathcal{L} = 10^{31} \text{ cm}^{-2}\text{s}^{-1}$  and a measured  $p\bar{p}$  total cross section of  $\sigma_{\text{tot}} = 80.03 \pm 2.24 \text{ mb}$  [112] at  $\sqrt{s} = 1.8 \text{ TeV}$ , at least one  $p\bar{p}$  interaction per beam crossing was expected. Moreover, the low signal-to-noise ratio of the  $b\bar{b}$  hadroproduction processes (refer to Section 1.1.3) made the implementation of a trigger system essential.

A CDF event, which amounted to the digitized information from a single beam crossing that could be read out from the CDF detector at a given time, had a data length of  $\sim 165 \text{ kB}$ . Such an event size could only be reliably written out to several 8-mm magnetic tapes at a rate of approximately 10 Hz. This constituted the principal limitation to the CDF data acquisition rate and necessitated a trigger system that could both accommodate the  $p\bar{p}$  interaction rate and select interesting physics events with a  $\sim 30\,000:1$  rejection factor. The CDF trigger [103, 113] consisted of three successive levels, each of which imposed a logical “OR” of a limited number of programmable selection criteria that collectively reduced the data rate exposed to the next higher trigger level. The reduction in the rate presented to the higher trigger levels provided time for more sophisticated analyses of potential events with the accrual of less dead time<sup>4</sup>.

### 2.5.1 Level 1

The Level 1 trigger required less time than the  $3.5\text{-}\mu\text{s}$  beam crossing period to reach a decision on whether or not a given event was suitable for consideration by the higher trigger

---

<sup>4</sup>In this context, ‘dead time’ refers to the amount of time that the CDF detector was unable to consider subsequent  $p\bar{p}$  collisions.

levels; it therefore incurred no dead time. Such speed of operation was achieved by the analog read-out and processing of data from selected detector components with dedicated FASTBUS-based electronics. At an instantaneous luminosity of  $\mathcal{L} = 5 \times 10^{30} \text{ cm}^{-2}\text{s}^{-1}$ , the Level 1 trigger acceptance rate was approximately 1 kHz [38]. Although it could have been configured to base its decisions on information from several different CDF subsystems, the Level 1 trigger primarily used signals from the calorimeters and the muon systems.

The calorimetry component of the Level 1 trigger considered analog signals on dedicated cables from the scintillator photomultiplier tubes in the central calorimeter subsystems and from cathode pads in the plug and forward calorimeter subsystems (refer to Table 2.1). For the purposes of the trigger, the calorimeters were logically segmented into ‘trigger towers’ with  $\Delta\varphi = 15^\circ$  and  $\Delta\eta = 0.2$ . For each subsystem listed in Table 2.1, the individual tower minimum-energy thresholds could be specified to the trigger, which summed the deposited energies, weighted by the polar angle  $\theta$  to determine the transverse energy  $E_T \equiv E \sin\theta$ , for all those trigger towers that were above these thresholds. If the total  $E_T$ , measured in this manner, exceeded a given global threshold, then the Level 1 trigger accepted the event. There was also a similar Level 1 calorimetry trigger that had significantly reduced tower energy thresholds, but was prescaled by a factor of 20 or 40, depending on the data-taking period (Run 1A or Run 1B, respectively; refer to Section 3.1).

The muon component of the Level 1 trigger exploited the relative drift electron arrival times ( $\Delta t$ ) between pairs of drift cell layers in a given CMU module, as described in Section 2.4.1. The two cells constituting each of these pairs were separated in  $r$  by one drift cell, as shown in Figure 2.10. The trigger logic operated on objects, called ‘muon stubs’, that were defined by the existence of any wire pair in a 4-tower  $4.2^\circ$  muon detector module (see Figure 2.10) with a  $\Delta t$  less than a value corresponding to a given minimum transverse momentum ( $p_T$ ) requirement.

Out of a total of seven Level 1 triggers that involved muon candidates, two were directly relevant to this analysis because they specifically identified dimuon candidates in the central region of the CDF detector. One of these dimuon triggers (TWO\_CMU\_3PT3) required that two CMU muon stubs exist, whereas the other (TWO\_CMU\_CMX\_3PT3) required that the two stubs each be in either CMU or CMX modules. In the case of the CMX stubs, the trigger required coincident hits in the CMX scintillators (see Section 2.4.3). The Level 1

system made no further requirements on the positions of the two muon stubs, except for a criterion that they be located in noncontiguous modules. That is, at least one muon module lacking a muon stub must have resided between the two modules where muon stubs were observed. If this was not the case, then the two adjacent stubs were merged into a single muon stub for the purposes of the Level 1 trigger. The minimum  $p_T$  requirement on each stub in these two triggers was nominally 3.3 GeV/ $c$ . Section 4.4 discusses the efficiencies of the Level 1 low- $p_T$  central muon triggers.

### 2.5.2 Level 2

In a  $p\bar{p}$  beam crossing for which the Level 1 trigger did not fire, a timing signal from the Tevatron announcing the occurrence of the next beam crossing would cause the stored signals in the CDF detector to be cleared in preparation for the next crossing. If the Level 1 trigger did fire, then subsequent timing signals were inhibited from clearing information stored in the CDF detector for a period of up to 20  $\mu\text{s}$ , during which the Level 2 trigger made its decision and five disregarded beam crossings could occur. At an instantaneous luminosity of  $\mathcal{L} = 5 \times 10^{30} \text{ cm}^{-2}\text{s}^{-1}$ , the typical Level 2 trigger output rate was approximately 12 Hz [38].

With the increased processing time, the Level 2 trigger system could perform simple tracking calculations and determine basic topological features of the event by considering, with greater sophistication, the same dedicated calorimetry and muon signals used in Level 1. Specifically, expeditious electromagnetic and hadronic transverse-energy clustering was performed at Level 2 by applying ‘seed’ and ‘shoulder’ thresholds to all the calorimeter trigger towers. If a given tower energy exceeded the seed threshold, which is higher than the shoulder threshold, then a cluster was formed. Adjacent trigger towers were iteratively included in this cluster if they both exceeded the shoulder threshold and were not part of another cluster.

High speed track pattern recognition was achieved in Level 2 with the central fast tracker (CFT), a hardware track finder that detected high- $p_T$  charged particles in the CTC (Section 2.3.3). The CFT measured transverse momentum and azimuth, since it only examined hits in the five axial CTC superlayers. For a given traversal of an axial superlayer by a charged particle, the CFT considered two types of timing information: prompt and delayed

hits. Prompt hits, gated  $\leq 80$  ns after the beam crossing time, were due to the short drift times caused by charged particles traversing the plane of sense wires in a superlayer. Pairs of delayed hits, one on each side (in  $\varphi$ ) of a given superlayer, were recorded by a gate that occurred 500-650 ns after the beam crossing. The absolute prompt and delayed drift times provided information on a track's trajectory, whereas the relative drift times furnished measurements of curvature, and hence  $p_T$ . After all the drift hits were recorded, the CFT sought to construct tracks by first examining hits in the outermost superlayer. For each sense wire in the outer layer with a prompt hit, the CFT looked to the inner layers for 'roads', or hit patterns, that matched patterns in a look-up table that had eight  $p_T$  bins and two  $\varphi$  bins, one for each sign of curvature. The  $p_T$  bins ranged<sup>5</sup> from  $\sim 3$  to  $\sim 30$  GeV/ $c$ , and the transverse momentum resolution was  $\delta p_T/p_T \sim 0.035 \times p_T$ , where  $p_T$  is in units of GeV/ $c$ .

The Level 2 trigger system organized the energy clusters, CFT tracks, and muon stubs into clusters called 'physics objects'. These included jets,  $\Sigma E_T$  (total transverse energy), electrons, photons, taus, muons, and neutrinos (whose signature is missing transverse energy,  $\cancel{E}_T$ ). For the majority of the data-taking period, a custom-built 'Jupiter' module accessed the clusters and made a Level 2 decision to accept or reject events. The Jupiter module had two separate processor boards, one that loaded clusters into memory, and another that checked the triggers by imposing several requirements on the physics objects. In the last year of data acquisition, these processors were replaced with commercially available AXP (Alpha) processors manufactured by Digital Equipment Corporation.

All of the dimuon selection triggers at Level 2 imposed a matching criterion between at least one of the two Level 1 muon stubs and a CFT track. Early in the data-taking period, the requirement was that the stub and the extrapolated track have an azimuthal separation in the transverse plane that was  $\leq 15^\circ$ . This criterion was later tightened to  $\Delta\varphi \leq 5^\circ$  to reduce further the trigger rate due to accidental coincidences. The various dimuon Level 2 triggers used in this analysis are listed, along with their prerequisite Level 1 triggers, in Appendix A. Section 4.4 discusses the efficiencies of the Level 2 low- $p_T$  central muon triggers.

---

<sup>5</sup>The CFT  $p_T$ -bin thresholds were changed between Runs 1A and 1B.

### 2.5.3 Level 3

The Level 3 trigger [114] was a flexible, high-level, software-based computer processor ‘farm’ that could reconstruct several events in parallel. When the Level 2 trigger accepted an event, the channels in the CDF detector with valid data were digitized and read out by the data acquisition (DAQ) system. The DAQ electronics subsequently transported the event data to the Level 3 processor farm. Over the course of the data-taking period, both the Level 3 trigger system and the DAQ system (see Section 2.6) underwent several significant changes. Although most of these changes were effected in the interval between the Run 1A and Run 1B collider running periods, not all of them were implemented for physics data taking from the beginning of Run 1B. Unless specifically noted otherwise, the following descriptions of the Level 3 trigger and the DAQ system pertain to the upgraded configurations used for data taking later in Run 1B.

The Level 3 computing farm consisted of 64 commercial processors that were manufactured by Silicon Graphics, Inc. and that ran under the IRIX operating system, a flavour of UNIX. Half of these processors were R3000 Power Servers and half were R4400 Challenge machines. The farm processors received data fragments read out by the DAQ system for a given beam crossing and ‘built’ these fragments into a contiguous event. Prior to the logging of the events to disk or 8-mm magnetic tape, the processors reconstructed and characterized these events for later selection using a configurable trigger table and optimized executables of compiled FORTRAN computer codes. A given event data buffer did not necessarily reside on the same farm computer as the reconstruction executable and processor that were operating on it.

In Run 1A, only 48 R3000 Power Servers were used, and the event fragments were already built into events by the Run 1A DAQ system prior to their reception by the Level 3 farm (refer to Section 2.6). Every processor had two dedicated, but separate, buffers, which each had the capacity to contain an entire event. A separate ‘farm steward’ computer communicated with the rest of the DAQ system, controlled the initiation and cessation of event processing on the farm CPUs<sup>6</sup>, maintained performance statistics of farm activities, and provided Level 3 status information. In the Run 1B trigger system, however, the duties

---

<sup>6</sup>CPU is an acronym for ‘central processing unit’.

of the farm steward were absorbed into other programmes executing on the farm computers.

For the purposes of analyses involving central muons, the Level 3 executables reconstructed muon stubs and CTC tracks using algorithms that were largely identical to those employed in the off-line event reconstruction (refer to Section 3.2); however, because three-dimensional track reconstruction constituted most of the Level 3 execution time, only the faster of two tracking algorithms used in the off-line code was engaged in the trigger. Two Run 1A dimuon triggers were used to form the data samples for the present analysis. One of these, that which contained dimuon candidates from the decay  $J/\psi \rightarrow \mu^+ \mu^-$ , required two oppositely charged muon candidates with a combined invariant mass in the range  $2.8 - 3.4 \text{ GeV}/c^2$ . The other trigger, which accepted dimuon candidates from the decay  $\psi(2S) \rightarrow \mu^+ \mu^-$ , had no opposite-charge requirement and selected dimuon candidates with an invariant mass in the range  $2.8 - 4.0 \text{ GeV}/c^2$ . In Run 1B, both the  $J/\psi$  and  $\psi(2S)$  dimuon modes were accepted by the same trigger, one that imposed no opposite-sign charge requirement and had an invariant mass window of  $2.7 - 4.1 \text{ GeV}/c^2$ .

In addition, the Level 3 dimuon triggers used in this study placed position matching requirements between the muon stubs and their associated CTC tracks. The algorithm extrapolated the CTC track to the appropriate muon subsystem and determined the difference in position between the projected track and the muon stub in both the  $r$ - $\varphi$  plane and the  $z$  direction, correcting for energy loss and multiple scattering as a function of  $p_T$ . The Run 1A  $J/\psi$  tracks were required to match the muon stubs within 4 standard deviations ( $\sigma$ ) of the combined multiple scattering and measurement uncertainties, whereas the  $\psi(2S)$  tracks had a matching requirement of  $\sim 6\sigma$ . The Run 1B Level 3 muon matching requirement was  $\sim 3\sigma$ .

## 2.6 The Data Acquisition System

The data acquisition (DAQ) pipeline, at its lowest, or ‘front end’, level, began with the readout of analog signals from channels in the various subsystems of the CDF detector. In general, these analog pulses were preamplified and transported to an electronics crate on the detector where they underwent further amplification and, depending on the subsystem, pulse shaping and discrimination. Digitization of these analog signals was accomplished

with either analog-to-digital or time-to-digital conversion electronics.

Dedicated signal cables communicated synoptical event information from the front end electronics to the Level 1 (L1) and Level 2 (L2) triggers, as illustrated schematically in Figure 2.14. The Level 1 and Level 2 event acceptance decisions were coordinated by a programmable FASTBUS device known as FRED<sup>7</sup>, which acted as the interface between the trigger and the trigger supervisor board. The trigger supervisor, also a FASTBUS module, initiated and monitored the readout of data from the front end electronics using FASTBUS readout controllers, or FRCs, which were single-width modules that contained MIPS R3000 processors. The FRCs sent their data over a 16-bit parallel scanner bus to six scanner CPUs, or SCPUs. The SCPUs, which were VME<sup>8</sup>-based Motorola 68030 processors running the VxWorks operating system, transported the event fragments to the Level 3 processor nodes via a commercial 256 Mbit/s serial Ultranet hub. The scanner manager, also a VME-based 68030 CPU, used a fibre optic reflective memory network to control the flow of data between the FRCs and the Level 3 trigger system, ensuring that all fragments of a given event were destined for the same Level 3 node. The trigger supervisor interface, also shown in Figure 2.14, facilitated communication between the scanner manager and the trigger supervisor. It consisted of two FRCs that resided in the same crate as the trigger supervisor and were connected to the scanner manager via a scanner bus.

Events accepted by the Level 3 trigger were passed via Ultranet to the consumer server (see Figure 2.14), a process running on a dedicated two-processor Silicon Graphics, Inc. Challenge L machine. The consumers, which received events from the consumer server over ethernet, were diagnostic applications that monitored trigger rates, luminosity conditions, detector performance, and a selected number of known high-rate physics processes. Another consumer, an on-line interactive event display system, provided CDF control-room personnel with graphical physics and detector performance diagnostics (refer to Figures 2.6 and 3.2 for examples of two of the system's displays). Data logger programmes, one for each output data stream, ran on the consumer server machine and wrote accepted events to local disk. The disk-resident data logger events were subsequently written to 8-mm tape by a tape-staging programme that also ran on the consumer server computer.

---

<sup>7</sup>The acronymic or abbreviational origins of FRED are unknown [113].

<sup>8</sup>VME stands for 'Versa Module Eurocard' and is a crate-based electronics package scheme.

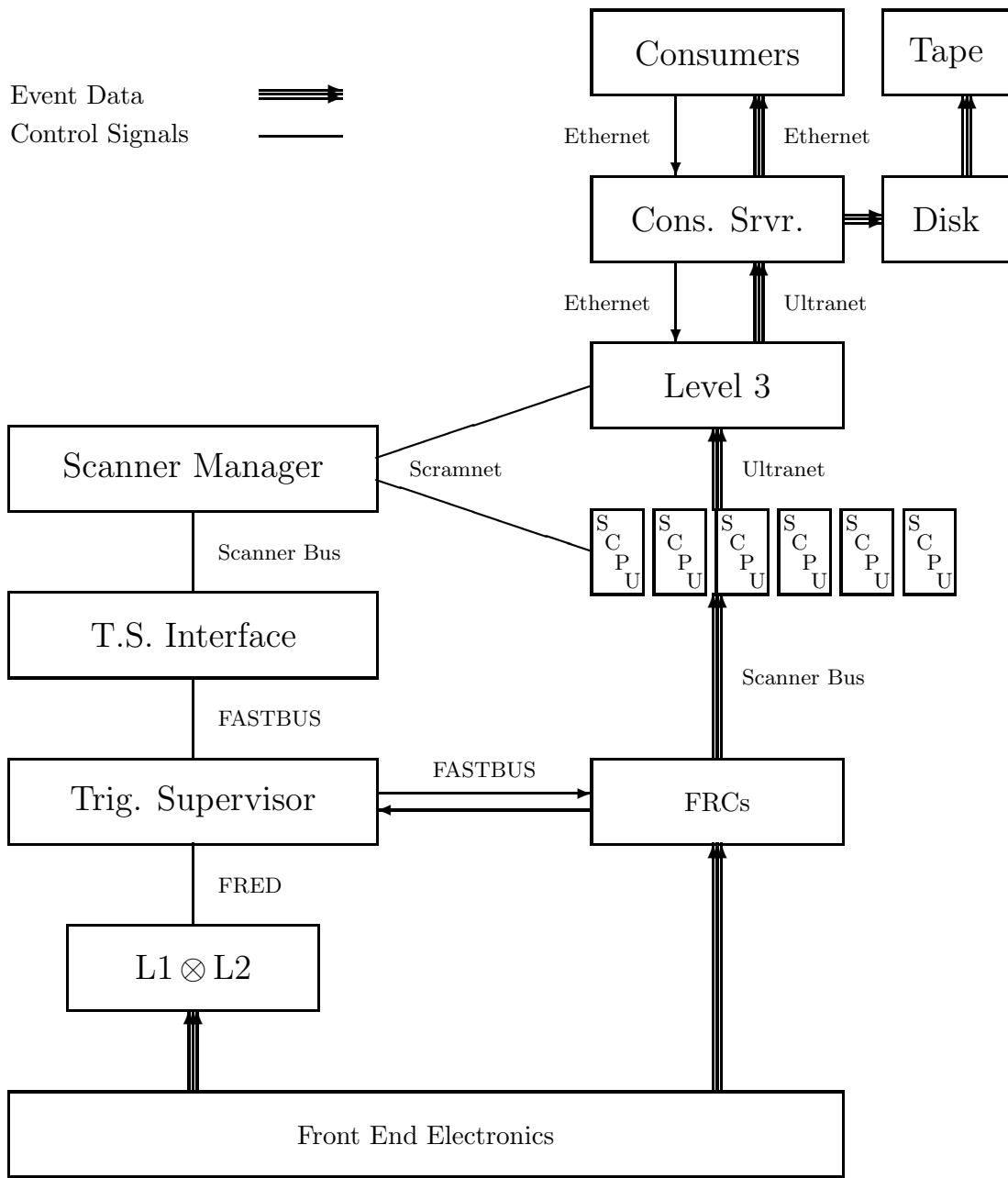


Figure 2.14: A schematic drawing of the principal elements of the CDF data acquisition pipeline [115]. The individual components are described in the text. Scramnet is the fibre optic reflective memory network.



In contrast, the Run 1A DAQ system lacked FRCs, using custom-built scanner modules instead. A hardware event builder [116], rather than SCPUs, constructed complete events and communicated them to the Level 3 trigger. FASTBUS, in lieu of the fibre optic reflective memories, delivered all system control messages, and the rôle of the Run 1B scanner manager was served in Run 1A by a buffer manager running on a MicroVAX II computer.

## Chapter 3

# Selection of Candidate Events

This chapter discusses the means by which charmonia and  $B$ -meson candidates are extracted from the backgrounds that are characteristic of hadron-hadron collision environments. First, the data set is defined. This is followed by a general description of the software machinery used to reduce the data sample. Finally, specific details about the criteria used to identify candidate signal events and reject background sources are presented. The charmonia and  $B$ -meson candidate invariant mass distributions will be presented in Chapters 5 and 6, respectively.

### 3.1 The Data Sample

The experimental data used in this investigation were recorded, using the CDF detector, in the years 1992 through 1995. During this period, the Fermilab Tevatron collided protons with antiprotons at a centre-of-mass energy of  $\sqrt{s} \sim 1.8$  TeV.

The 1992-1995 Tevatron running period, which is generally known as Run 1, comprised two separate data-taking intervals: Run 1A and Run 1B. Run 1A consisted of approximately nine months of physics running, which commenced on 26 August 1992 and ended on 30 May 1993. The data collected during Run 1A correspond to a time-integrated luminosity of  $\int \mathcal{L} dt = (19.5 \pm 1.0) \text{ pb}^{-1}$ .

In the intervening period between Run 1A and Run 1B, the CDF detector underwent several improvements. As described in Chapter 2, the SVX was replaced with the SVX', new trigger requirements and hardware were implemented, and a significantly improved data acquisition system was brought on-line. Most components of the upgraded trigger and

data acquisition hardware were piggybacked onto the existing system to facilitate, if the need arose, the immediate reversion to their analogous Run 1A counterparts. In this way, the AXP Level 2 trigger processors and the upgraded data acquisition system underwent testing early in Run 1B, but were only used for physics data collection several months into the Run 1B Tevatron running period.

Physics-quality data collection in Run 1B began on 18 January 1994 and ended on 24 July 1995. The recorded time-integrated luminosity was  $\int \mathcal{L} dt = (89 \pm 7) \text{ pb}^{-1}$ , yielding a consolidated Run 1 total of  $\int \mathcal{L} dt = (109 \pm 7) \text{ pb}^{-1}$ . It should be noted that some operating conditions were not constant over the course of the Run 1 data-taking period. The temperature and humidity in the collision hall, for example, exhibited a strong seasonal dependence. The CDF solenoid, described in Chapter 2, was operated at slightly different magnetic field strengths (refer to Section 3.3). The most significant operating variations during Run 1, however, were those associated with the performance of the Tevatron accelerator. While the centre-of-mass energy remained constant at 1.8 TeV, the instantaneous luminosity delivered to the  $B\bar{O} p\bar{p}$  interaction region varied from a mean value of  $\mathcal{L} = 3.5 \times 10^{30} \text{ cm}^{-2}\text{s}^{-1}$  in Run 1A to a mean value of  $\mathcal{L} = 8.0 \times 10^{30} \text{ cm}^{-2}\text{s}^{-1}$  in Run 1B. Peak instantaneous luminosities in Run 1B reached figures of  $\mathcal{L} \sim 2.6 \times 10^{31} \text{ cm}^{-2}\text{s}^{-1}$ . Throughout the Run 1 period, the Tevatron experienced several service interruptions due to causes that included power outages, quenching magnets, beam optics adjustments, a liquid  $N_2$  procurement delay, and scheduled maintenance and cost-saving shutdowns.

The present study treated the entire Run 1 data sample. Where necessary, known run-dependent effects were accounted for in the analysis. With these corrections, the data set could be regarded as a single uniform sample.

## 3.2 The Data Reduction Procedure

From the Level 3 trigger system to the final selection at the physics analysis stage, several iterations of data processing and reduction occurred. The same event-driven software paradigm was applied at each of these stages. This uniform software control framework provided a flexible means of combining a virtually unlimited number of independent sub-

programmes, or analysis ‘modules’<sup>1</sup>, into a single executable computer programme. For a given programme, the user could invoke, in any order, any subset of the constituent modules. Events were handled sequentially by this subset of modules, with the output of one subprogramme used as input for the next one in the analysis path. A standard interface was used to modify the adjustable parameters for a given module. Modules also could be configured to function as filters, which would abort the analysis of an event in the middle of processing if that event failed any specified filter criteria. The possible input sources for this analysis framework included disk and magnetic-tape files, on-line event buffers, Monte Carlo generators, and user-written input modules. A single programme could support multiple output streams, and any module could function in several analysis paths with different parameters used in each implementation.

A typical event was first processed by this standard software framework on-line in the Level 3 trigger system (refer to Section 2.5.3). A single optimized computer programme running on a trigger farm node could implement all of the Level 3 triggers and pipe selected events to any of three output streams.

Off-line, events written to 8-mm tape by the data acquisition system (refer to Section 2.6) entered the ‘production and splitting’ farms, which consisted of 64 Silicon Graphics, Inc. and 37 IBM RS6000 computers running the UNIX operating system. The production programmes contained modules that reconstructed higher-level physics objects from low-level detector output data structures, much in the same way as the Level 3 trigger did. Since run-dependent, as opposed to event-dependent, information was known at the off-line production stage, and since execution speed was less critical, the production processes could make use of better calibration and alignment constants, more comprehensive run-condition information, and more sophisticated tracking algorithms than were possible in the Level 3 trigger system. The production farm nodes also ‘split’ events into several data sets defined using physics analysis criteria and typically based on one or more Level 3 triggers. The rate capacity of the production and splitting farm computer system was  $\sim 1.3 \times 10^6$  events/week.

The third principal stage in the data reduction procedure was the application of analysis-specific algorithms to the reconstruction of the candidate physics processes under investigation. In the present study, the existence of similarities in the reconstruction techniques of

---

<sup>1</sup> Analysis modules were typically coded in FORTRAN.

different meson candidates lent itself to a software design philosophy that employed a small number of highly-configurable and reusable analysis modules [117]. For example, it is clear that the reconstruction of the decays  $J/\psi \rightarrow \mu^+ \mu^-$  and  $\psi(2S) \rightarrow \mu^+ \mu^-$  should use identical coding algorithms governed by different kinematic parameters. To this end, a generic ‘dimuon finder’ module was used to reconstruct  $J/\psi$  and dimuon  $\psi(2S)$  meson candidates. A separate ‘two-track finder’ module was used to seek decays of the form  $K^*(892)^0 \rightarrow K^+ \pi^-$  by iterating through charged-track non-muon pair combinations in a given event. Finally, a higher-level ‘charmonium-parent finder’ module could be configured to seek combinations of charmonium candidates, often reconstructed using the ‘dimuon finder’, and either charged tracks in the event or meson objects identified using the ‘two-track finder’.

Particle types, kinematic selection criteria, and constraints used for geometric and kinematic fitting could all be specified to the analysis modules at run time using the standard user interface. Communication between a given module and another module downstream in the analysis path was achieved through data structures identical to those used to represent the event information itself. This enabled the same module to be used more than once, but in different capacities, in a single analysis path.

This modular philosophy was demonstrated by, for example, the reconstruction of the decay  $B^+ \rightarrow \psi(2S) K^+$  via the  $\psi(2S) \rightarrow J/\psi \pi^+ \pi^-$  channel. First, the ‘dimuon finder’ module was used to find  $J/\psi$  candidates in the event. Next, the ‘two-track finder’ module, configured to seek candidate dipions with the expected kinematic criteria, was invoked. The ‘charmonium-parent finder’ module then combined the  $J/\psi$  and dipion candidates into  $\psi(2S)$  candidates, applying the appropriate selection criteria and fit constraints. Further down the analysis chain, the ‘charmonium-parent finder’ module was subsequently reused, with very different operating parameters, to form  $B^+$  meson candidates by constructing combinations of the  $\psi(2S)$  candidates with hitherto-unused tracks in the event. This recursive recycling of modular coding logic enhanced the internal consistency of the analysis.

### 3.3 Magnetic Field Considerations

Since the present branching-fraction study relied heavily on charged-particle trajectory reconstruction, an understanding of the magnetic field conditions for a given event in the

CDF detector was essential, although somewhat less so than for mass measurement analyses. In Run 1A investigations of the  $B_s^0$  meson [118] and  $W^+$  boson [107] masses, the absolute momentum scale was calibrated by using the decays  $J/\psi \rightarrow \mu^+ \mu^-$ ,  $\Upsilon \rightarrow \mu^+ \mu^-$ , and  $Z^0 \rightarrow \mu^+ \mu^-$ . The ensuing nominal magnetic field value used for Run 1A was 1.4127 T. For the Run 1B portion of the data sample, a nominal magnetic field value of 1.4116 T was used; however, this value was corrected on a run-dependent<sup>2</sup> basis using a database of  $\sim 1\,200$  magnetic field measurements performed over the course of Run 1B. These corrections were typically  $\lesssim 0.17\%$  [119], and measurements of the magnetic field in the central detector had uncertainties of  $2 \times 10^{-4}$  T [107]. Local residual magnetic field nonuniformities, both in magnitude and direction, were surveyed in the CDF central tracking volume before the solenoid magnet was installed [120]; these were corrected for in the reconstruction of track helices in both Runs 1A and 1B.

### 3.4 Primary Vertex Considerations

A knowledge of the primary vertex, or point of origin, of the decay process under examination was important to the analysis. Primary vertex information was used in the calculation of primary-secondary decay lengths, momentum-pointing fit constraints, and isolation selection criteria. Two distinct aspects of the primary vertex determination will be discussed here: how the positions of vertices in a given event were measured, and how a single vertex was selected in events where more than one vertex was observed.

The transverse and longitudinal components of the primary vertices were measured in two very different ways. The longitudinal ( $z$ ) coordinate was established on an event-by-event basis using data from the VTX detector (refer to Section 2.3.2), where vertex quality was determined on the basis of the number of VTX hits used to identify the vertex. As the measurement uncertainty calculated by the vertex-finding software was deemed to be unreliable due to the resolution of the VTX subsystem, a fixed uncertainty of  $\sigma_z = 0.3$  cm was assumed for all events. The transverse ( $x$ - $y$ ) coordinates of the primary vertices in an event were typically calculated using the measured run-averaged beam position. The rationale for this was that the transverse beam position typically varied less than  $10\ \mu\text{m}$

---

<sup>2</sup>A ‘run’, in this context, refers to a period of uninterrupted data collection, typically lasting several hours.

in either the  $x$  or  $y$  directions over the course of a single data-taking run and that any event-by-event transverse coordinate measurements would be biased by fluctuating track multiplicities and event topologies in individual events. The slopes and intercepts of the run-averaged beam position were therefore combined with the event-by-event  $z$  locations of the vertices in an event to determine the transverse positions of those vertices. The transverse coordinate measurement uncertainties were fixed to  $(\sigma_x, \sigma_y) = (25, 25) \mu\text{m}$ , corresponding to the observed circular beam spot size in the transverse plane. It should be noted that, in the unusual cases where no run-dependent beam position information or no VTX  $z$ -vertex information was available for a given event, the lacking vertex coordinates were computed using the available SVX and CTC track information for that event.

During the latter stages of Run 1B, when instantaneous luminosities often exceeded those in Run 1A by an order of magnitude, the primary vertex multiplicities also increased dramatically. Whereas in Run 1A the average number of high-quality vertices in a given event was  $\sim 1.6$  with  $\sim 3\%$  of events having at least four such vertices, Run 1B events averaged  $\sim 2.9$  high-quality vertices with  $\sim 5\%$  of events having at least eight such vertices. Once a pair of muon candidates had been identified using the ‘dimuon finder’ machinery described in Section 3.2 (which was a procedure that did not directly employ primary vertex information), the  $z$  coordinates of the two candidates were used to select a single vertex. Specifically, of those vertices possessing the highest quality classification for the given event, the vertex that had the shortest longitudinal displacement from either of the two muon candidates was chosen as the primary vertex corresponding to the muon objects. The position coordinates of muon candidates, as opposed to those of other tracks used in this analysis, were used to select primary vertices because the two muon candidate tracks constituted an unambiguous part of the final state under study.

### 3.5 Track Quality Criteria

The imposition of quality requirements on the tracks used in the analysis was intended to reduce those backgrounds arising from poor track measurements in the CDF detector. Track candidate fits reconstructed for this study were required to have used at least four hits in each of at least two axial CTC superlayers (refer to Section 2.3.3 for a description

of the CTC). These track fits also had to use at least two hits in each of at least two stereo CTC superlayers. No requirement was made on which two of the five axial and four stereo superlayers were to be used in the fit.

In this study, information from the VTX and CTC subsystems was employed in the reconstruction of track paths. For all such tracks, the helical trajectories were extrapolated back into the SVX where associated hits were sought using a road algorithm. If a sufficient number of good SVX hits was found, then the track was refit using all of the relevant VTX, CTC, and SVX information and the resulting track helix was used. Performance disparities in the two silicon microstrip vertex detectors used in Runs 1A and 1B (refer to Section 2.3.1) motivated two different associated SVX hit requirements:  $\geq 3$  hits in the SVX, and  $\geq 2$  hits in the SVX'. Moreover, track fits that made use of SVX information were only considered by this analysis if the SVX  $\chi^2/\text{hit}$ , defined as the increase in the track fit  $\chi^2$  per SVX hit due to the inclusion of SVX hits in the CTC track fit, satisfied the condition  $\chi^2/\text{hit} \leq 6.0$ . This requirement was similar to one used in CDF studies of the top quark [38].

Tracks possessing transverse momenta  $p_T \lesssim 250 \text{ MeV}/c$  were not reconstructed in the production stage of the data reduction process (refer to Section 3.2). Useful measurements of tracks with  $p_T < 250 \text{ MeV}/c$  would have been difficult due to the number of track helices that subtended  $\geq 360^\circ$  in azimuth while inside the CTC ('loopers') and due to the dearth of available hits populating the outer superlayers of the CTC. A study of the low- $p_T$  pattern recognition efficiency (see Appendix C) indicated that a requirement of  $p_T > 400 \text{ MeV}/c$  would ensure that candidate tracks would be in a  $p_T$  region with a relatively constant and measurable tracking efficiency. This  $p_T$  requirement was imposed for all tracks prior to any corrections for multiple-scattering and energy-loss effects.

Similarly, tracks with trajectories at high absolute pseudorapidities tended to deposit fewer hits in the CTC, and therefore were reconstructed less efficiently. Requirements on the radii at which extrapolations of track helices intersected one of the endplate planes of the CTC,  $r_{\text{CTC}}^{\text{exit}}$ , were used to remedy this problem by diminishing the pseudorapidity acceptance. For example, a cut of  $r_{\text{CTC}}^{\text{exit}} > 132.0 \text{ cm}$  on this CTC exit radius would have required that the track in question traverse all nine superlayers of the CTC. The tracking efficiency study outlined in Appendix C, however, showed that a requirement of  $r_{\text{CTC}}^{\text{exit}} > 110.0 \text{ cm}$ , corresponding to the radial position of the outer edge of the second-outermost



axial superlayer, defined a set of tracks with high efficiency while minimizing the reduction in geometric acceptance. This requirement was imposed for all non-muon track candidates after multiple-scattering and energy corrections had been implemented. Muon candidates were not subjected to an  $r_{\text{CTC}}^{\text{exit}}$  cut in order to accept candidates identified by the CMX subsystems, which represented  $\sim 22\%$  of the total central muon fiducial acceptance. Since the muon candidates in all the channels had comparable  $\eta$  distributions, any muon tracking inefficiencies resulting from this lack of a CTC exit radius criterion divided to unity in the final calculations of the ratios of branching fractions.

### 3.6 Optimizing the Kinematic Selection Criteria

The kinematic selection criteria were chosen to achieve accurate and unbiased measurements of the  $B$ -candidate event yields while maximizing both the rejection of the background and the statistical significance of the signal. Wherever possible, uniform criteria were used to reconstruct the different decay modes. This served both to maximize internal consistencies in the study and to reduce the magnitude and number of systematic uncertainties.

In order to minimize any bias caused by fluctuations in the background levels in either the signal or sideband regions of the invariant mass distributions, all of the  $B$ -meson decay modes were used in the determination of the kinematic selection criteria. The figure of merit that was maximized was the signal significance,  $S \equiv \frac{N_s}{\sqrt{N_s + N_b}}$ . The  $N_s$  symbol denotes the number of signal events calculated with a Monte Carlo procedure (refer to Chapter 4) for a given decay mode and a given time-integrated luminosity. The expected number of background events,  $N_b$ , was estimated from the data by extrapolating the background rate in the observed  $B$ -meson invariant mass sidebands to the background yields under the signal regions, defined to lie within three standard deviations of the observed means of the  $B$ -meson resonances. The resultant optimal kinematic selection requirements, which are detailed in the remaining sections of this chapter, varied little within each of the charged and neutral  $B$ -decay mode categories.

The optimum kinematic cuts determined by maximizing  $S$  for each of the decay channels were confirmed by maximizing a different measure of statistical significance derived entirely from the data,  $\frac{N_s}{\sigma(N_s)}$ , where  $\sigma(N_s)$  was taken to be the event-yield uncertainty returned

by the fit of the given invariant mass distribution to a single fixed-width Gaussian signal and a linear background parameterization. Although this latter method was more sensitive to statistical fluctuations, its conclusions were consistent with those of the  $S$ -maximization technique.

### 3.7 Muon Candidate Selection

The minimum transverse momentum required of a muon to traverse the central calorimeters and the solenoid magnet at  $\eta \sim 0$  and reach the CMU subsystem was  $\sim 1.4$  GeV/ $c$ . A raw kinematic requirement of  $p_T > 1.4$  GeV/ $c$  was therefore placed on all muon candidates in the analysis. Because the numerators and denominators in the ratio-of-branching-fraction calculations involved muons with identical selection criteria, there was no need to demand that all candidate muons populate the plateau region of the trigger efficiency parameterizations (refer to Section 4.5.2). As a result, the fact that the lower edge of this  $p_T$  requirement fell in inefficient regions of the measured Level 1 and Level 2  $p_T$ -dependent trigger efficiency distributions was of little consequence. A higher  $p_T$  requirement would have unnecessarily weakened the statistical significance of those  $B$ -meson decays with a  $\psi(2S)$  candidate in the final state.

A major source of muon background was that due to charged kaons and pions decaying to yield muons within the CDF tracking volume. In some cases, the charged kaon or pion tracks were reconstructed in the CTC, and the daughter muons registered stubs in the muon systems. A second major source of muon background was that due to hadronic ‘punch-through’ particles (see Section 2.4.2), namely hadrons that passed through the calorimeters and entered the muon systems.

In order to reduce these backgrounds, a track candidate in the CTC, when extrapolated out to the muon chambers, was required to match the position of a muon stub. This condition was only met if the muon stub and the extrapolated CTC track in question matched within three standard deviations of the multiple-scattering and measurement uncertainties in both the transverse ( $r$ - $\varphi$ ) and longitudinal ( $z$ ) planes. In cases where a CTC track could be extrapolated to stubs in more than one muon subsystem, Boolean “OR” operations were implemented to combine the appropriate matching requirements. In Run 1A, the muon

matching criteria for  $J/\psi$  dimuons had an efficiency of  $(98.66 \pm 0.04)\%$  and increased the  $J/\psi$  signal-to-background ratio from 3.08 to 3.61 in the  $3.0 - 3.2 \text{ GeV}/c^2$  invariant mass interval [121]; comparable effects were expected for Run 1B.

## 3.8 Charmonium Reconstruction

The three charmonium decay modes used in this study were  $J/\psi \rightarrow \mu^+ \mu^-$ ,  $\psi(2S) \rightarrow \mu^+ \mu^-$ , and  $\psi(2S) \rightarrow J/\psi \pi^+ \pi^-$ , where in the latter case the  $J/\psi$  meson was reconstructed in its dimuon mode. These channels were used over other charmonium decay modes because the  $\mu^+ \mu^-$  final state could easily be identified using the CDF trigger system while also making possible the rejection of several background processes. This section describes the selection of charmonium candidates; the resulting inclusive charmonium invariant mass distributions are presented in Section 5.1, where they are used in the determination of certain efficiency corrections.

### 3.8.1 Dimuon Charmonium Decays

Dimuon charmonium candidates were formed using the ‘dimuon finder’ module (see Section 3.2) by considering all the muon candidates in a given event that met the criteria outlined in Section 3.7. The two candidates constituting a muon pair were required to possess charges of opposite sign.

Background contributions were reduced significantly by performing a least-squares fit of the two muon track candidates and applying a ‘vertex constraint’, which forced the two tracks to originate from a common point in space [122]. In this fit, an initial approximation to the track parameters was found, corrected for multiple scattering and  $dE/dx$  (energy-loss) effects, and then adjusted under the vertex constraint so as to minimize the  $\chi^2$ . The confidence level,  $CL(\chi^2)$ , of the fit was required to exceed 0.01.

When  $J/\psi$  and  $\psi(2S)$  candidates were used in the reconstruction of an exclusive  $B$  final state, an additional fit was performed on the dimuon system to improve the invariant-mass resolution of the  $B$  candidate. In this case, the fit was done with the simultaneous application of a vertex constraint and a ‘mass constraint’ [122], which required that the dimuon mass equal the appropriate world average  $J/\psi$  or  $\psi(2S)$  mass of  $3.09688 \text{ GeV}/c^2$  or  $3.68600 \text{ GeV}/c^2$ , respectively [30]. The confidence level of each of these vertex-plus-mass

constrained fits was also required to satisfy the condition  $CL(\chi^2) > 0.01$ .

### 3.8.2 Hadronic Cascade $\psi(2S)$ Decays

Candidates for the decay  $\psi(2S) \rightarrow J/\psi \pi^+ \pi^-$  were chosen by combining  $J/\psi$  dimuons, which were selected as described in Section 3.8.1, with dipions identified using the ‘two-track finder’ module described in Section 3.2. The two pion candidates were required to meet the track quality criteria detailed in Section 3.5, to have charges of opposite sign, and to have an invariant mass, prior to any vertex or vertex-plus-mass constrained fits, in the range  $0.35 < M(\pi^+ \pi^-) < 0.61$  GeV/ $c^2$ . The lower limit of this mass range was motivated by the expected dipion invariant mass distribution for  $\psi(2S)$  decays, discussed in Section 4.2.1. The upper limit corresponded to the maximum kinematically-allowed dipion invariant mass, defined by the  $\psi(2S) - J/\psi$  mass difference with an allowance for measurement uncertainty.

In order to reduce background effects, a vertex-constrained fit was performed on the four-track dimuon-dipion system, with the two candidate muon tracks simultaneously constrained to form an invariant mass equal to the world average  $J/\psi$  mass [30]. The confidence level of this fit was required to exceed 0.01. As in the case of the dimuon charmonia described in Section 3.8.1, when an hadronic cascade decay of the  $\psi(2S)$  meson was used as a daughter process in the reconstruction of another exclusive decay, the four-track system was simultaneously subjected to an additional mass constraint, namely the world average  $\psi(2S)$  mass [30]. Again, the probability of this fit was required to satisfy the criterion  $CL(\chi^2) > 0.01$ .

## 3.9 *B*-Meson Candidate Reconstruction

The reconstruction of the decay modes  $B^+ \rightarrow \psi(2S) K^+$ ,  $B^0 \rightarrow \psi(2S) K^*(892)^0$ ,  $B^+ \rightarrow J/\psi K^+$ , and  $B^0 \rightarrow J/\psi K^*(892)^0$  was achieved by combining one of the three sought-for charmonium meson candidates in a given event with either  $K^+$  or  $K^*(892)^0$  candidate mesons, as appropriate. In spite of the facts that six different decay chains were reconstructed and that the final-state charged-particle track multiplicities forming these chains ranged from three to six tracks, the methods used to identify candidate *B*-meson decays were kept as uniform as possible. This was due in large part to the modularity provided

by the data reduction procedure described in Section 3.2. The following sections describe the selection of kaon candidates, the selection of  $B$ -meson candidates, and the treatment of multiple invariant mass hypotheses.

### 3.9.1 Kaon Candidate Selection Criteria

The CDF detector lacked the ability to differentiate kaon candidates from pion candidates, a fact that necessitated the consideration of all eligible tracks and the assignment of an appropriate kaon or pion mass hypothesis to these tracks. A consequence of these ‘blind’ hypothetical mass assignments was the amassment of significant combinatorial backgrounds. Fortunately, the charged particle inclusive cross section in  $p\bar{p}$  collisions is a rapidly falling function of transverse momentum [123], thus enabling the use of reasonably efficient minimum- $p_T$  criteria to remove a significant fraction of the combinatorial background.

The  $p_T > 400$  MeV/ $c$  cut (see Section 3.5), imposed to avoid low- $p_T$  tracking inefficiencies (see Appendix C), also served to reduce combinatorial backgrounds caused by the lack of particle identification. The optimization scheme described in Section 3.6, however, supported the application of higher  $p_T$  cuts to combat these combinatorial backgrounds. The criteria applied were therefore  $p_T(K^+) > 1.5$  GeV/ $c$  for kaon candidates used in the reconstruction of  $B^+$  candidates and  $p_T(K^*(892)^0) > 2.0$  GeV/ $c$  for the two-track  $K$ - $\pi$  candidates used in the reconstruction of  $B^0$  candidates. Note that the two tracks constituting each  $K^*(892)^0$  candidate did not have individual  $p_T$  cuts imposed on them beyond the universal 400 MeV/ $c$  track quality criterion.

In a given event,  $K^*(892)^0$  candidates were reconstructed by considering all track pairs with charges of opposite sign. For each pair of tracks considered, both mass assignment hypotheses were initially retained. To reduce combinatorial backgrounds further, the invariant mass of each  $K$ - $\pi$  candidate,  $M(K^+\pi^-)$ , was required to fall within a window centred at the world average  $K^*(892)^0$  mass, 896.10 MeV/ $c^2$  [30]. The size of this invariant mass window was 160 MeV/ $c^2$ , a requirement that was estimated to be  $\sim 80.5\%$  efficient under the assumptions that the  $K^*(892)^0$  resonance could be described by a Breit-Wigner [124] line shape with an intrinsic width of  $\Gamma = 50.5$  MeV [30] and that the experimental resolution was significantly less than  $\Gamma$ . Finally, no constrained fits were used to select and reconstruct  $K^*(892)^0$  candidates explicitly, although the two constituent tracks did undergo some ad-

adjustments in subsequent global constrained fits of *B*-meson candidates (see Section 3.9.2). The invariant mass window criterion described above was imposed on the *K*- $\pi$  candidates after they had undergone global constrained fits.

### 3.9.2 *B*-Meson Candidate Selection Criteria

*B* meson candidates were reconstructed by forming combinations of charmonium candidates (*J*/ $\psi$ ,  $\psi(2S)$  dimuon, or  $\psi(2S)$  hadronic cascade modes) with either  $K^+$  or  $K^*(892)^0$  candidates. In a manner similar to that used in the reconstruction of charmonia, a least-squares kinematic fit was performed on the *B* candidate daughter tracks under the constraints that all the tracks originate from a single common secondary vertex and that the charmonium candidates possess an invariant mass equal to the applicable world average mass [30]. It was possible to constrain all the *B* decay daughters to a single decay point because the distances traveled by charmonium and  $K^*(892)^0$  mesons before decaying were negligible compared to the decay vertex resolution of the CDF detector [122].

In the case of *B*-meson reconstruction, a ‘momentum-pointing’ constraint was used in the kinematic fits. This additional constraint required the flight path direction of the *B* candidate to be parallel to its momentum in the transverse (*r*- $\phi$ ) plane. The pointing constraint was not performed in three dimensions due to the large uncertainty on the *z* component of the primary vertex position (refer to Section 3.4). The confidence level of the global least-squares fit of each *B* meson candidate, with vertex-plus-mass and momentum-pointing constraints applied, was required to exceed 0.01.

The kinematic selection optimization, discussed in Section 3.6, resulted in a  $p_T > 6.0$  GeV/*c* transverse momentum requirement for  $B^+$  candidates and a  $p_T > 9.0$  GeV/*c* requirement for  $B^0$  candidates.

Motivated by the understanding that *b* quarks were expected to ‘fragment’ in a way that imparted most of their momentum to the ensuing *B* meson (References [63, 64] and Section 1.2.1), an isolation criterion was imposed on the *B* meson candidates. This requirement was expressed using the variable

$$I_B \equiv \frac{\sum_{i \notin B}^R \vec{p}_i \cdot \hat{p}_B}{|\vec{p}_B|}, \quad (3.1)$$

where  $\vec{p}_B$  was the 3-momentum of the  $B$ -meson candidate and the  $\vec{p}_i$  were the momenta of additional particles, other than those constituting the  $B$  candidate, contained within a cone of radius  $R \equiv \sqrt{(\Delta\varphi)^2 + (\Delta\eta)^2} \leq 1.0$  and with its axis collinear with the  $B$ -candidate 3-momentum direction. In addition, non- $B$  tracks were only included in the sum in Equation 3.1 if their longitudinal displacement parameter,  $z_0$ , lay within 5 cm of the primary vertex location corresponding to the  $B$  candidate in question. This improved the efficiency of the isolation criterion by not discarding  $B$  candidates that were unisolated due to tracks from other primary vertices in the event. Figure 3.1 depicts the distribution of  $I_B$  for candidate  $B^+ \rightarrow J/\psi K^+$  decays, after the combinatorial background under the  $B^+$  decay signal was statistically subtracted using events in the  $J/\psi K^+$  invariant mass sideband regions. The criterion imposed was  $I_B < 7/13$ , which resulted from the optimization procedure described in Section 3.6. Figure 3.1 illustrates that the  $I_B$  requirement was relatively efficient.

The long lifetimes of  $B^+$  and  $B^0$  mesons,  $(1.64 \pm 0.05)$  ps and  $(1.55 \pm 0.05)$  ps [30], respectively, made possible the rejection of background with a cut on the proper decay length,  $c\tau_B$ , defined by

$$c\tau_B \equiv \frac{\vec{p}_T \cdot \vec{x}_T}{p_T^2} m_B, \quad (3.2)$$

where  $\vec{x}_T$  was the distance between the primary and secondary ( $B$ -candidate) vertex, projected onto the transverse plane. The quantity  $m_B$  represented the invariant mass of the candidate  $B$  meson. In the present analysis, a proper decay length requirement of  $c\tau_B > 100 \mu\text{m}$  was imposed on  $B$ -meson candidates.

Figure 3.2 depicts a sample event display of a candidate  $B$ -meson decay that was identified as such by the data reduction algorithms and selection criteria described in this chapter.

### 3.9.3 Multiple Invariant Mass Combinations

Multiple  $B$ -meson candidates that passed all the selection criteria for a given event were a significant source of background. Such additional combinations usually resulted from other tracks that formed a vertex with the two muons in the event and were therefore more prevalent in reconstructions with higher daughter-track multiplicities, such as those involving the  $\psi(2S) \rightarrow J/\psi \pi^+ \pi^-$  mode. Another obvious source of multiple combinations

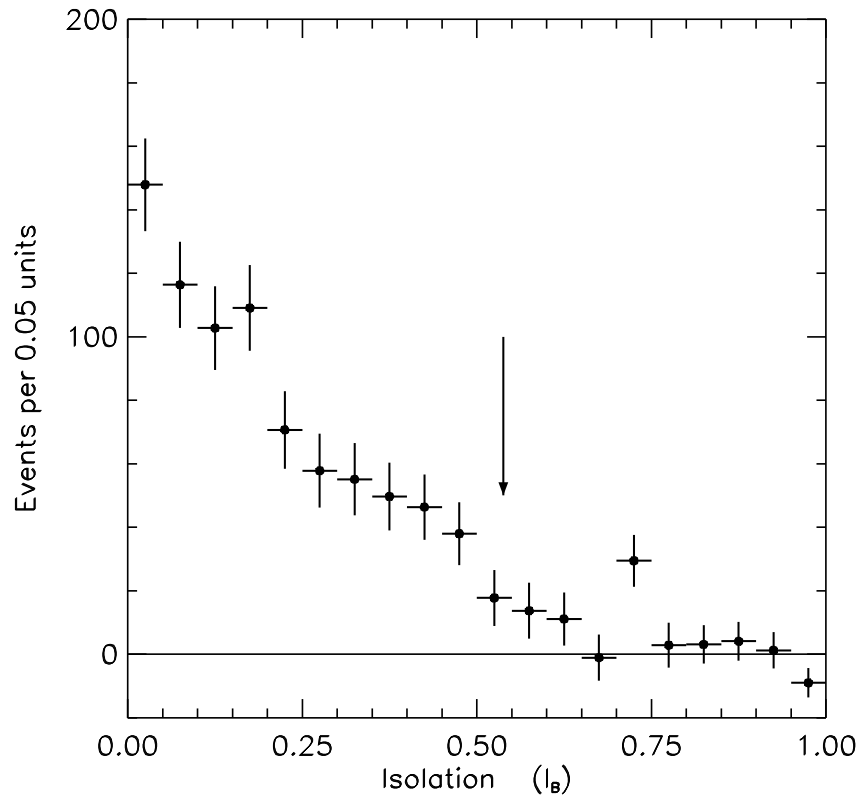


Figure 3.1: The distribution of the isolation variable  $I_B$  for candidate  $B^+ \rightarrow J/\psi K^+$  decays. A background subtraction was performed using the sidebands in the  $J/\psi K^+$  invariant mass distribution. The arrow marks the point below which candidates were accepted.



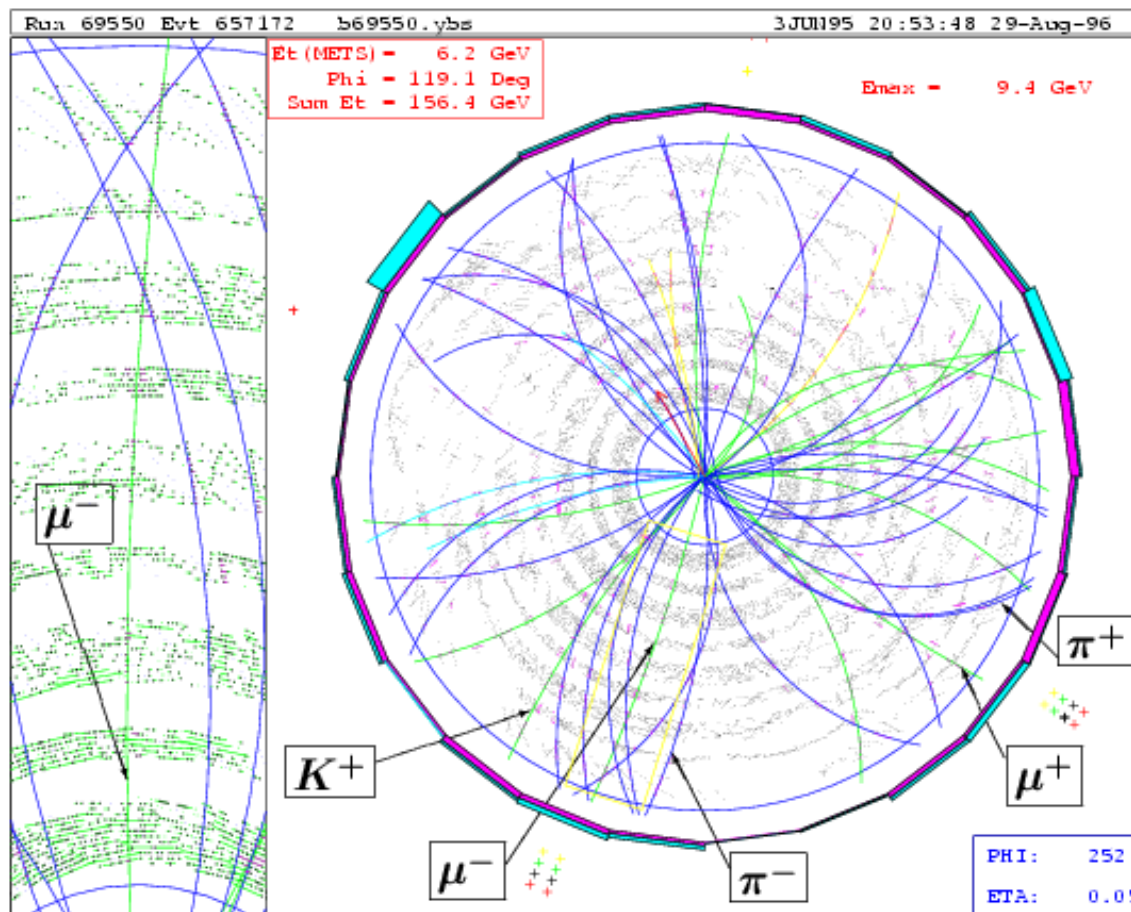


Figure 3.2: A sample event-display diagram of an observed candidate  $B^+$  decay. The view in this figure is similar to that in Figure 2.7. CTC sense wire hits are visible for all nine superlayers, and the transverse projections of the reconstructed candidate track trajectories are indicated by smooth curves. The inner circle denotes the boundary between the CTC and VTX, and the bars outside the CTC represent energy deposition in the  $15^\circ$  central calorimeter wedges. Near the top of the figure are listed the missing transverse energy ( $\cancel{E}_T$ ) and its azimuthal direction, the total transverse energy for the event, and the maximum energy recorded in a single calorimeter wedge. The “+” symbols represent stubs in the central muon chambers. The data reduction algorithms and event selection criteria identified this event as a candidate for the decay  $B^+ \rightarrow \psi(2S) K^+$ , where the  $\psi(2S)$  meson was reconstructed in its  $\psi(2S) \rightarrow J/\psi \pi^+ \pi^-$  mode and the  $J/\psi$  meson was reconstructed in its  $J/\psi \rightarrow \mu^+ \mu^-$  mode. The identified track candidates are indicated in the figure. The azimuth and pseudorapidity coordinates in the bottom right corner are those of the track with the highest  $p_T$ , the  $\mu^-$  candidate, a close-up view of which is illustrated in the left panel of the figure.

was in the case of  $K^*(892)^0$  candidates, where the  $K$ - $\pi$  mass assignment ambiguity and the size of the  $K^*(892)^0$  mass window cut required by the natural width of the  $K^*(892)^0$  meson increased the probability of additional invariant mass combinations in the event.

In the case of the  $K^*(892)^0$  candidates, three treatments of the  $K$ - $\pi$  mass hypothesis ambiguity were considered: (a) random selection of one of the mass hypotheses, (b) selection of the hypothesis with  $M(K^+\pi^-)$  nearest the accepted world average  $K^*(892)^0$  pole value [30], and (c) parameterization of the relative contributions and resolutions of the right and wrong mass assignment hypotheses in the signal region. All of these techniques would have required Monte Carlo calculations.

In this analysis, the last of the above three treatments was adopted in conjunction with a general procedure that made use of the  $\chi^2$  probability of the global constrained least-squares fit,  $CL(\chi^2)$ , to remove multiple combinations. The prescription used was the following:

1. All selection criteria were applied, including the  $M(K^+\pi^-)$  requirement.
2. For a given event, only the candidate possessing the highest global  $CL(\chi^2)$  value returned by the constrained fit was retained.
3. For events where both  $K^*(892)^0$   $K$ - $\pi$  mass hypotheses survived all of the selection criteria, the two  $CL(\chi^2)$  values were often similar. If one of the  $M(K^+\pi^-)$  combinations satisfied the highest- $CL(\chi^2)$  criterion, and a second combination that differed only in the  $K$ - $\pi$  mass assignment existed, then the second entry was also retained.
4. The signal observed in the  $B$  candidate invariant mass distribution of those modes containing a  $K^*(892)^0$  candidate was fit using two Gaussian distributions with their relative widths and amplitudes constrained by ratios determined using the Monte Carlo calculations described in Chapter 4. The constraints are listed in Table 3.1. Refer to Section 6.1 for a synopsis of the  $B$ -meson candidate event yields.

$B$ Mode	$c\bar{c}$ Mode	$\frac{\xi_{WC}}{\xi_{RC}}$	$\frac{\sigma_{WC}}{\sigma_{RC}}$
$B^0 \rightarrow J/\psi K^*(892)^0$	$J/\psi \rightarrow \mu^+ \mu^-$	0.0683	3.623
$B^0 \rightarrow \psi(2S) K^*(892)^0$	$\psi(2S) \rightarrow \mu^+ \mu^-$	0.0456	5.750
$B^0 \rightarrow \psi(2S) K^*(892)^0$	$\psi(2S) \rightarrow J/\psi \pi^+ \pi^-$	0.0429	6.327

Table 3.1: The relative amplitudes ( $\xi$ ) and widths ( $\sigma$ ) of the right ( $RC$ ) and wrong ( $WC$ )  $K$ - $\pi$  combinations, as determined by fits to Monte Carlo invariant mass distributions using double-Gaussian signal parameterizations.

## Chapter 4

# Geometric and Kinematic Acceptance

In branching fraction analyses, a knowledge of the proportion of candidates that go unobserved due to both the fiducial detector geometry and the kinematic selection criteria is essential. Since the data themselves could not be used to determine these acceptances and efficiencies, it was necessary to make use of Monte Carlo [125] calculations.

This chapter describes the Monte Carlo machinery used to generate bottom quarks, hadronize these quarks into  $B$  mesons, decay the  $B$  mesons into final-state particles, simulate the signatures left by the particles in the CDF detector, and simulate the first two levels of the triggers relevant to the study. Neither the underlying event (refer to Equation 1.4) nor multiple  $p\bar{p}$  interactions were modeled in these Monte Carlo studies.

### 4.1 The Monte Carlo Generation of $B$ Mesons

Single  $b$  quarks were generated according to an inclusive transverse momentum ( $k_T(b)$ ) spectrum based on a next-to-leading order QCD calculation [54] that used the Martin-Roberts-Stirling MRSD $\mathcal{O}$  parton distribution functions [126], a renormalization scale of  $\mu = \mu_0 \equiv \sqrt{m_b^2 + k_T^2(b)}$ , and a  $b$ -quark mass of  $m_b = 4.75 \text{ GeV}/c^2$ . Refer to Section 1.1.3 for an account of  $b$ -quark hadroproduction. The  $b$  quarks were produced in the rapidity range  $-1.1 < y_b < 1.1$  with  $k_T(b) > 5.0 \text{ GeV}/c$  and fragmented into  $B$  mesons according to a model that used the Peterson fragmentation function [65] with the Peterson  $\epsilon_b$  parameter defined to be 0.006 [62] (refer to Section 1.2.1). Flavour was conserved in both the production and fragmentation of  $b$  quarks.

## 4.2 The Monte Carlo Decay of $B$ Mesons

Decays of Monte Carlo generated  $B$  mesons into charmonium and kaon final states were performed using a modified version of the CLEO QQ Monte Carlo programme [127]. Properties of the relevant particles, including mass, lifetime, and intrinsic width, were updated in the programme to reflect the current world-average values [30]. For the pseudoscalar  $\rightarrow$  vector + vector decays, the decay helicities were nominally set to the central value of the world-average longitudinal polarization fraction measured for the decay  $B^0 \rightarrow J/\psi K^*(892)^0$ ,  $\Gamma_L/\Gamma = 0.78 \pm 0.07$  [77, 88, 128]. Finally, a customized QQ Monte Carlo matrix element was constructed to model correctly the observed kinematics of the pions in the charmonium decay  $\psi(2S) \rightarrow J/\psi \pi^+ \pi^-$ . The following section describes this customization.

### 4.2.1 The $\psi(2S) \rightarrow J/\psi \pi^+ \pi^-$ Monte Carlo Matrix Element

The dipion kinematics in the decay  $\psi(2S) \rightarrow J/\psi \pi^+ \pi^-$  were studied to search for techniques to remove background efficiently and to ensure that the pion tracks were simulated correctly. Whereas the generated QQ transverse momentum distribution of the dipion system was consistent with that in the data, the simulated QQ dipion invariant mass was not in agreement with the data.

The default QQ Monte Carlo programme determined the kinematics of the  $J/\psi \pi^+ \pi^-$  decay products using pure three-body phase space; however, at the time of the discovery of the  $\psi(2S) \rightarrow J/\psi \pi^+ \pi^-$  decay channel, it was observed that the angular distributions of the pions were isotropic [32]. In subsequent phenomenological investigations of the decay amplitude, the absence of any observed angular correlations made apparent the fact that the amplitude had a strong dependence on the invariant mass of the  $\pi^+ \pi^-$  pair [129, 130, 131].

A set of customized routines was therefore written to model the  $\psi(2S) \rightarrow J/\psi \pi^+ \pi^-$  matrix element in the QQ Monte Carlo programme using the phenomenological prescription. For the purposes of the algorithm, the decay was considered to have the logical form  $\psi(2S) \rightarrow J/\psi \mathcal{P}$ , where  $\mathcal{P}$  was taken to be a dipion pseudostate ( $\mathcal{P} \rightarrow \pi^+ \pi^-$ ). In the first step, the invariant mass of  $\mathcal{P}$  was calculated using the  $\mathcal{P}$  mass distribution [131],

$$\frac{dN}{dm_{\mathcal{P}}} \propto (m_{\mathcal{P}}^2 - 4m_{\pi}^2)^{\frac{5}{2}} \sqrt{(m_{\psi(2S)}^2 - m_{J/\psi}^2 - m_{\mathcal{P}}^2)^2 - 4m_{J/\psi}^2 m_{\mathcal{P}}^2}, \quad (4.1)$$

which is in a form similar to that used in Reference [132]. The mass of the  $\mathcal{P}$  pseudostate

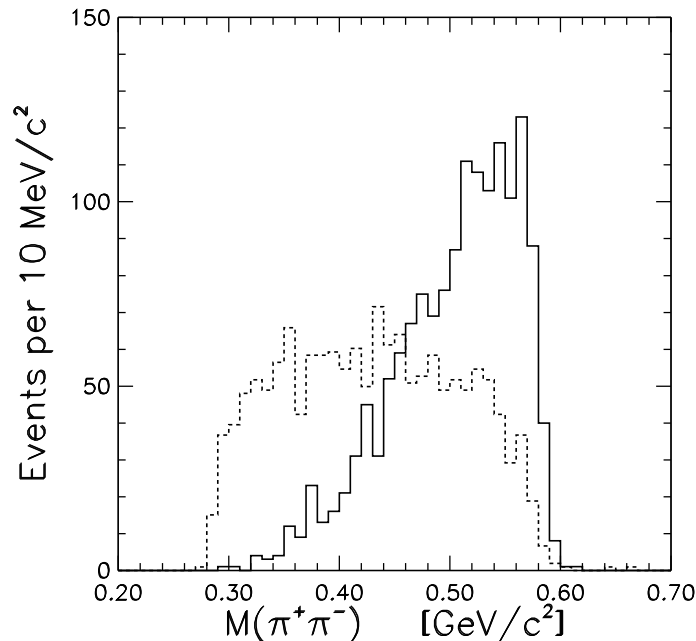


Figure 4.1: The dipion invariant mass distribution calculated using a phenomenologically-prescribed QQ Monte Carlo matrix element (solid histogram). The dashed histogram illustrates the results of a pure phase-space calculation.

was extracted using the Von Neumann acceptance-rejection Monte Carlo method [30]. The second and third steps in the algorithm consisted of decaying, using phase space alone, the modes  $\psi(2S) \rightarrow J/\psi \mathcal{P}$  and  $\mathcal{P} \rightarrow \pi^+ \pi^-$ , respectively. The  $J/\psi \rightarrow \mu^+ \mu^-$  decay was performed using the default QQ matrix element for that decay.

Figure 4.1 illustrates the phenomenologically-inspired and phase-space QQ dipion invariant mass distributions, as determined from Monte Carlo calculations. The correspondence between a parameterization of the phenomenological prediction and the data is pictured in Figure 4.2, where a sideband subtraction was used to remove the background to the  $\psi(2S)$  candidate decays. A recent precision measurement of the  $\psi(2S) \rightarrow J/\psi \pi^+ \pi^-$  branching fraction reports a similar  $M(\pi^+ \pi^-)$  distribution [133]. A conservative cut of  $M(\pi^+ \pi^-) > 0.35 \text{ GeV}/c^2$  (refer to Section 3.8.2) was applied to the dipion candidates prior to the application of any vertex, vertex-plus-mass, or momentum-pointing constrained fits. The  $M(\pi^+ \pi^-)$  requirement was found to be efficient and capable of rejecting a significant number of background candidates.

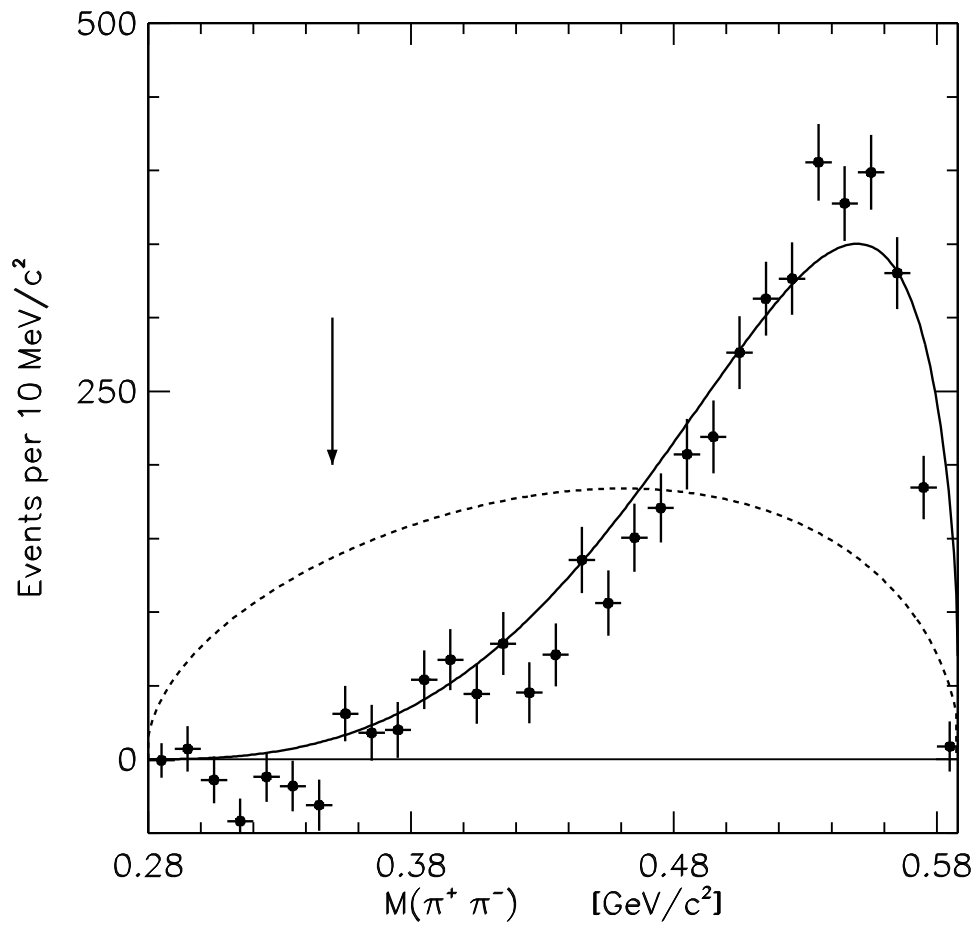


Figure 4.2: The observed background-subtracted distribution of the dipion invariant mass (points) in decays of the form  $\psi(2S) \rightarrow J/\psi \pi^+ \pi^-$ . The arrow indicates where a cut at  $0.35 \text{ GeV}/c^2$  was subsequently imposed. The solid curve represents a phenomenological prediction due to Pham *et al.* [131]; the broken curve describes a pure phase-space parameterization.

### 4.3 Simulation of the Detector Response

Once Monte Carlo  $B$  mesons were generated and decayed into their daughter states, a full Monte Carlo simulation of the CDF detector response was invoked. The simulation produced raw data structures that were in most cases identical to those read out from the DAQ system using collider data (refer to Section 2.6); this enabled the subsequent processing of Monte Carlo events in a manner almost identical to that used for the data. The corrections for local nonuniformities in the magnetic field, described in Section 3.3, however, were switched off at the detector simulation and production (see Section 3.2) processing stages.

As outlined in Section 3.1, the CDF detector geometry changed between Runs 1A and 1B. For the purposes of the detector simulation in the present study, the Run 1B geometry information was used to represent the CDF detector for the entire Run 1 period. Within the Monte Carlo statistics used for this analysis, this assumption appeared to be reasonable for the calculation of relative geometric acceptances and kinematic selection efficiencies.

Greater care was necessary in the characterization of the beam profiles near the primary vertex. The simulated transverse beam profile was tuned to match approximately that observed in the data. The longitudinal beam profile, however, was more important to this study due to its implications for the fiducial SVX acceptance. The  $z$  location of the simulated primary vertex was forced to be distributed according to the sum of two Gaussian probability density functions with means and standard deviations of 2.3 cm and 2.1 cm, and 18.4 cm and 35.6 cm, respectively. The relative normalization of these two Gaussian distributions was approximately 2:3.

The Monte Carlo events were processed by the same production machinery (Section 3.2) used on collider data. This ensured that the data and the Monte Carlo events were both subjected to any biases, should they exist, inherent to the reconstruction algorithms.

### 4.4 Simulation of the Level 1 and 2 Triggers

After the CDF detector response to the Monte Carlo decay fragments had been simulated, the events were passed through a Level 1 and Level 2 dimuon trigger simulation module. (Refer to Sections 2.5.1 and 2.5.2 for descriptions of the Level 1 and Level 2 triggers, respec-



tively.) This module used parameterizations of the measured muon trigger efficiencies to determine the probability that a given candidate dimuon event satisfied the trigger requirement. The Monte Carlo events were then selected using a Monte Carlo procedure based on this probability.

Figure 4.3 illustrates the Level 1 CMU and CMX trigger efficiency parameterizations as functions of muon transverse momentum. These efficiencies were assumed to be functions of  $p_T$  alone and to remain unchanged during the course of Run 1. In the case of the CMX efficiency, the veto scintillation counters (refer to Section 2.4.3) degraded the plateau efficiency uniformly.

The Level 2 dimuon trigger efficiencies were found to depend not only on  $p_T$ , but also on charge, pseudorapidity ( $\eta$ ), azimuth ( $\varphi$ ), and time-integrated luminosity ( $\int \mathcal{L} dt$ ). Due to the geometry of the CTC, positive muon tracks were accepted by the trigger more efficiently than negative tracks. The  $\eta$  dependence of the efficiency was observed to be parabolic due to the increased hit efficiency of higher- $\eta$  tracks<sup>1</sup>. The  $\varphi$  dependence of the efficiency was observed to be sinusoidal due to the offset of the beam from the geometrical centre of the CTC<sup>2</sup>. Finally, the decline in the CTC hit efficiencies as a function of  $\int \mathcal{L} dt$  caused a corresponding degradation in the Level 2 CFT efficiency. This effect also caused an increase in the curvature of the  $\eta$ -dependent efficiency parabola.

Figure 4.4 depicts the Level 2 CMU and CMX trigger efficiency parameterizations as functions of muon transverse momentum. The curves shown are based on  $8.89 \text{ pb}^{-1}$  of positively charged muon candidates that fell in a particular 1B run range (65 001 – 66 000) and the lowest  $p_T$  bin ( $\sim 2.2 \text{ GeV}/c$ ) of the CFT.

Note that the Level 3 dimuon trigger efficiency, which was measured to be  $0.97 \pm 0.02$  and independent of  $p_T$ , was not explicitly simulated in the geometric and kinematic acceptance calculations.

---

<sup>1</sup>Muon tracks with large  $|\eta|$  values deposited more charge on the CTC wires; this increased the pulse height, which in turn enhanced the hit efficiency.

<sup>2</sup>The CFT (Section 2.5.2) did not measure the impact parameter, thereby introducing a false curvature term, which varied with  $\varphi$ .

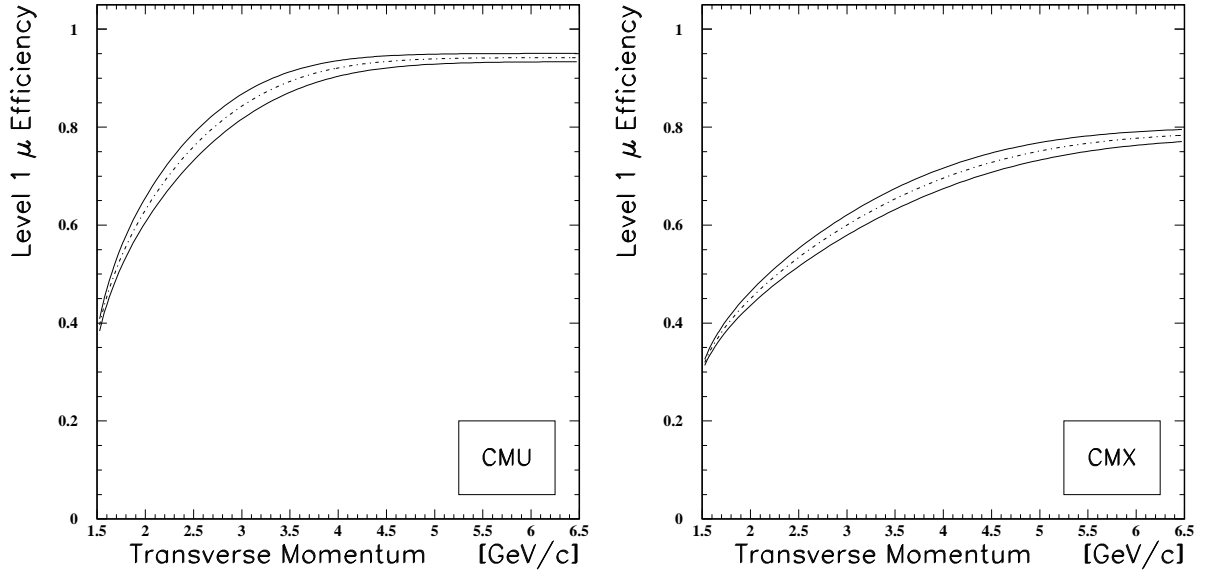


Figure 4.3: The Level 1 low- $p_T$  CMU and CMX trigger efficiency parameterizations. The dashed-dotted curves are the central values and the solid curves represent shifts of the plateau efficiencies and  $p_T$  values by one standard deviation.

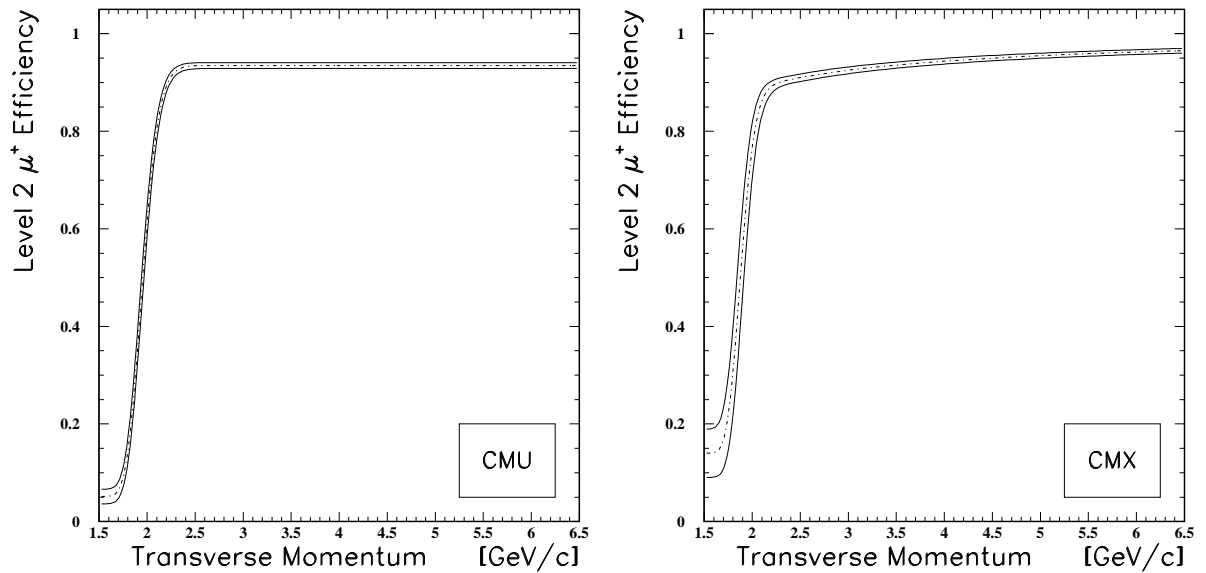


Figure 4.4: The Level 2 low- $p_T$  CMU and CMX trigger efficiency parameterizations for positively charged muons in the 1B run range 65 001 – 66 000 and the lowest- $p_T$  CFT bin. The dashed-dotted curves are the central values and the solid curves represent shifts of the plateau efficiencies and  $p_T$  values by one standard deviation.

$B$ Mode	$c\bar{c}$ Mode	Acceptance
$B^+ \rightarrow J/\psi K^+$	$J/\psi \rightarrow \mu^+ \mu^-$	$0.01920 \pm 0.00025$
$B^+ \rightarrow \psi(2S) K^+$	$\psi(2S) \rightarrow \mu^+ \mu^-$	$0.02183 \pm 0.00027$
$B^+ \rightarrow \psi(2S) K^+$	$\psi(2S) \rightarrow J/\psi \pi^+ \pi^-$	$0.00631 \pm 0.00015$
$B^0 \rightarrow J/\psi K^*(892)^0$	$J/\psi \rightarrow \mu^+ \mu^-$	$0.00777 \pm 0.00016$
$B^0 \rightarrow \psi(2S) K^*(892)^0$	$\psi(2S) \rightarrow \mu^+ \mu^-$	$0.00828 \pm 0.00017$
$B^0 \rightarrow \psi(2S) K^*(892)^0$	$\psi(2S) \rightarrow J/\psi \pi^+ \pi^-$	$0.00385 \pm 0.00011$

Table 4.1: A summary of the absolute products of the geometric and kinematic acceptances, calculated for each decay mode for  $B$  mesons produced with  $k_T(b) > 5.0$  GeV/ $c$  and  $-1.1 < y_b < 1.1$ . The grouping is on the basis of common selection criteria, and the uncertainties given are due to Monte Carlo statistics alone.

## 4.5 The Acceptance Calculations

In the final step of the default Monte Carlo procedure, the events were processed by the same analysis-specific user algorithms used on the collider data. The reconstructed Monte Carlo events were used to estimate the geometric and kinematic acceptances for the decays under study. The products of these quantities are listed in Table 4.1. The Monte Carlo statistical uncertainties on the absolute acceptance values listed in Table 4.1 ranged from 1.2% to 2.9%.

Table 4.2 lists the appropriate relative geometric and kinematic acceptances necessary for the branching-fraction ratio calculations. The syntax in Table 4.2 follows that introduced in Table 1.3, but with particular entries for the two different  $\psi(2S)$  modes. The trends in Table 4.2 are consistent with differences in daughter-track multiplicity and  $c\bar{c}$  meson mass. When the relative acceptance values were used in the branching-fraction calculations, a systematic uncertainty of 3.0% was applied to account for differences between two different CDF detector simulations and between the Run 1A and 1B detector geometries [134]. This systematic uncertainty in the acceptance-measurement method precluded a need for increased Monte Carlo statistics.

Relative Acceptance	$B^+ \rightarrow J/\psi K^+$ $J/\psi \rightarrow \mu^+ \mu^-$	$B^0 \rightarrow J/\psi K^*(892)^0$ $J/\psi \rightarrow \mu^+ \mu^-$	$B^+ \rightarrow \psi(2S) K^+$ $\psi(2S) \rightarrow \mu^+ \mu^-$
$B^0 \rightarrow J/\psi K^*(892)^0$ $J/\psi \rightarrow \mu^+ \mu^-$	$0.405 \pm 0.010$		
$B^+ \rightarrow \psi(2S) K^+$ $\psi(2S) \rightarrow \mu^+ \mu^-$	$1.137 \pm 0.020$	$2.810 \pm 0.068$	
$B^+ \rightarrow \psi(2S) K^+$ $\psi(2S) \rightarrow J/\psi \pi^+ \pi^-$	$0.329 \pm 0.009$	$0.813 \pm 0.025$	$0.289 \pm 0.008$
$B^0 \rightarrow \psi(2S) K^*(892)^0$ $\psi(2S) \rightarrow \mu^+ \mu^-$	$0.431 \pm 0.010$	$1.066 \pm 0.031$	$0.379 \pm 0.009$
$B^0 \rightarrow \psi(2S) K^*(892)^0$ $\psi(2S) \rightarrow J/\psi \pi^+ \pi^-$	$0.201 \pm 0.006$	$0.496 \pm 0.018$	$0.177 \pm 0.006$

Table 4.2: A summary of the relative products of the geometric and kinematic acceptances, calculated for each ratio of decay modes for  $B$  mesons produced with  $k_T(b) > 5.0$  GeV/ $c$  and  $-1.1 < y_b < 1.1$ . The indicated uncertainties represent the Monte Carlo statistics alone.

#### 4.5.1 Differential Production Cross Section of Generated $b$ Quarks

A significant source of systematic uncertainty on the relative acceptance calculations reported in Section 4.5 was that due to the assumed generated  $b$ -quark momentum spectrum. Although the measured  $B$ -meson differential cross section has been observed to have a shape in agreement with theoretical predictions, the absolute rate was near the limits of that predicted by typical variations in the theoretical parameters [92]. An estimate of the acceptance uncertainty due to the calculated  $b$ -quark momentum spectrum was taken by varying the default Monte Carlo generation parameters detailed in Section 4.1 from their nominal values. The  $b$ -quark mass was varied from its central value of  $m_b = 4.75$  GeV/ $c^2$  to 4.50 GeV/ $c^2$  and 5.00 GeV/ $c^2$ , and the renormalization scale was varied from a nominal value of  $\mu = \mu_0$  to  $\mu_0/4$  and  $2\mu_0$ . The effects of these variations on the acceptance ratios were examined, and one half of each maximum deviation was taken as the appropriate systematic uncertainty on the relative acceptance. Table 4.3 summarizes the systematic uncertainties attributed to the generated differential production cross section of the  $b$  quarks.

#### 4.5.2 Trigger Effects

Even though the numerators and denominators of the branching-fraction ratios in Table 1.3 involve muon pairs that originate from common data samples and the  $p_T$  spectra of the  $B^+$

$b$ -Quark Production Spectrum Systematics (%)	$B^+ \rightarrow J/\psi K^+$ $J/\psi \rightarrow \mu^+ \mu^-$	$B^0 \rightarrow J/\psi K^*(892)^0$ $J/\psi \rightarrow \mu^+ \mu^-$	$B^+ \rightarrow \psi(2S) K^+$ $\psi(2S) \rightarrow \mu^+ \mu^-$
$B^0 \rightarrow J/\psi K^*(892)^0$ $J/\psi \rightarrow \mu^+ \mu^-$	4.0		
$B^+ \rightarrow \psi(2S) K^+$ $\psi(2S) \rightarrow \mu^+ \mu^-$	2.4	5.9	
$B^+ \rightarrow \psi(2S) K^+$ $\psi(2S) \rightarrow J/\psi \pi^+ \pi^-$	2.8	5.0	5.5
$B^0 \rightarrow \psi(2S) K^*(892)^0$ $\psi(2S) \rightarrow \mu^+ \mu^-$	5.5	1.9	5.8
$B^0 \rightarrow \psi(2S) K^*(892)^0$ $\psi(2S) \rightarrow J/\psi \pi^+ \pi^-$	6.7	3.4	9.6

Table 4.3: A summary of the systematic uncertainties (expressed in %) on the relative geometric and kinematic acceptance due to variations in the differential production cross section of the generated  $b$  quarks.

and  $B^0$  mesons are expected to be comparable, some care is required due to the possibility of topological effects when considering relative trigger acceptances in branching-fraction ratio studies. In approximately 75% of the selected events, the two muon candidates that were identified as charmonium daughters were also the muon candidates identified by the dimuon trigger system. In most of the remaining events, an additional muon candidate in the event satisfied the dimuon trigger requirements. These ‘volunteers’ were included in the analysis in order to maximize the sensitivity of the data sample.

In order to determine systematic uncertainties on the relative acceptance values that accounted for candidates that were triggered in ways not treated by the dimuon trigger simulation, the relative topology dependence of the unsimulated triggers was investigated by examining some representative yield ratios. Three different topological scenarios with trigger implications were identified as (a) mass-difference effects in ratios involving the dimuon decays of both  $J/\psi$  and  $\psi(2S)$  daughters, (b) polarization effects in ratios involving both  $K^*(892)^0$  and  $K^+$  daughters, and (c) effects in ratios involving both of the aforementioned phenomena. Of the six decay topologies in the analysis, the three with the most populous statistics ( $B^+ \rightarrow J/\psi K^+$ ,  $B^0 \rightarrow J/\psi K^*(892)^0$ , and  $B^+ \rightarrow \psi(2S) K^+$  (dimuonic)) were used to form three yield ratios representing the three topological scenarios described above. The relative yields for these ratios were examined for the full data sample, the subsample

Trigger Systematics (%)	$B^+ \rightarrow J/\psi K^+$ $J/\psi \rightarrow \mu^+ \mu^-$	$B^0 \rightarrow J/\psi K^*(892)^0$ $J/\psi \rightarrow \mu^+ \mu^-$	$B^+ \rightarrow \psi(2S) K^+$ $\psi(2S) \rightarrow \mu^+ \mu^-$
$B^0 \rightarrow J/\psi K^*(892)^0$ $J/\psi \rightarrow \mu^+ \mu^-$	2.0		
$B^+ \rightarrow \psi(2S) K^+$ $\psi(2S) \rightarrow \mu^+ \mu^-$	6.0	7.0	
$B^+ \rightarrow \psi(2S) K^+$ $\psi(2S) \rightarrow J/\psi \pi^+ \pi^-$	2.0	2.0	6.0
$B^0 \rightarrow \psi(2S) K^*(892)^0$ $\psi(2S) \rightarrow \mu^+ \mu^-$	7.0	6.0	2.0
$B^0 \rightarrow \psi(2S) K^*(892)^0$ $\psi(2S) \rightarrow J/\psi \pi^+ \pi^-$	2.0	2.0	7.0

Table 4.4: A summary of the systematic uncertainties (expressed in %) on the relative geometric and kinematic acceptance due to the effects of the dimuon triggers on the relative acceptance ratios.

that passed the dimuon trigger simulation, and the subsample that failed the trigger simulation. Within the available statistics, the yield ratios remained consistent for all three trigger samples. Comparison of the yield ratios between the full sample and the subsample that passed the dimuon trigger simulation suggested a 6% systematic uncertainty for ratios with a dimuon  $\psi(2S)/J/\psi$  mass difference, a 2% uncertainty for ratios with a  $K^*(892)^0/K^+$  polarization difference, and a 7% uncertainty for ratios with both differences. The application of these results to the acceptance ratios is summarized in Table 4.4.

It is useful to investigate the sensitivity of the relative acceptance measurements to uncertainties in the Level 1 and Level 2 CMU and CMX trigger efficiency parameterizations. Table 4.5 details the effects of the one-standard-deviation parameterization shifts, pictured in Figures 4.3 and 4.4, on the relative geometric and kinematic acceptance values. A comparison of Tables 4.2 and 4.5 indicates that, for each ratio of decay-mode acceptances, the effect of varying the trigger efficiency parameterizations is insignificant when compared with the accuracy to which each relative geometric and kinematic acceptance ratio was determined. These variations were therefore not used in the calculation of the systematic uncertainties listed in Table 4.4.

+1 $\sigma$ Trigger Shift -1 $\sigma$ Trigger Shift	$B^+ \rightarrow J/\psi K^+$ $J/\psi \rightarrow \mu^+ \mu^-$	$B^0 \rightarrow J/\psi K^*(892)^0$ $J/\psi \rightarrow \mu^+ \mu^-$	$B^+ \rightarrow \psi(2S) K^+$ $\psi(2S) \rightarrow \mu^+ \mu^-$
$B^0 \rightarrow J/\psi K^*(892)^0$ $J/\psi \rightarrow \mu^+ \mu^-$	0.403 0.409		
$B^+ \rightarrow \psi(2S) K^+$ $\psi(2S) \rightarrow \mu^+ \mu^-$	1.139 1.138	2.814 2.782	
$B^+ \rightarrow \psi(2S) K^+$ $\psi(2S) \rightarrow J/\psi \pi^+ \pi^-$	0.326 0.330	0.808 0.807	0.287 0.290
$B^0 \rightarrow \psi(2S) K^*(892)^0$ $\psi(2S) \rightarrow \mu^+ \mu^-$	0.428 0.435	1.061 1.064	0.376 0.382
$B^0 \rightarrow \psi(2S) K^*(892)^0$ $\psi(2S) \rightarrow J/\psi \pi^+ \pi^-$	0.199 0.202	0.493 0.495	0.175 0.178

Table 4.5: A summary of the effects of +1 $\sigma$  (upper number) and -1 $\sigma$  (lower number) trigger efficiency parameterization shifts on the relative geometric and kinematic acceptance quotients.

### 4.5.3 Helicity Distributions

The longitudinal polarization fractions inherent to the  $B$ -meson decays with vector-vector final states can have implications for the relative acceptance measurements. The systematic uncertainties associated with the longitudinal polarization fractions were estimated by varying the nominal measured world-average  $\Gamma_L/\Gamma$  value for the  $B^0 \rightarrow J/\psi K^*(892)^0$  mode (refer to Reference [77] and Section 4.2) by its standard deviation,  $\pm 0.07$ .

The value of  $\Gamma_L/\Gamma$  has not been measured for the decay  $B^0 \rightarrow \psi(2S) K^*(892)^0$ ; however, it is expected to be similar to that for the  $B^0 \rightarrow J/\psi K^*(892)^0$  mode. Two standard deviations of the world-average  $\Gamma_L/\Gamma$  value for the  $B^0 \rightarrow J/\psi K^*(892)^0$  measurements,  $\pm 0.14$ , were therefore used as the  $\Gamma_L/\Gamma$  variation range for the  $B^0 \rightarrow \psi(2S) K^*(892)^0$  modes. This variation range was applied to each of the  $\psi(2S) K^*(892)^0$  reconstructions, *i.e.*, those involving  $\psi(2S) \rightarrow \mu^+ \mu^-$  and  $\psi(2S) \rightarrow J/\psi \pi^+ \pi^-$  decays.

The consequent systematic uncertainties are summarized in Table 4.6. The ‘absolute’ systematic uncertainties are used in cases where the vector-vector acceptance is considered relative to that for one of the vector-pseudoscalar modes.

$\Gamma_L/\Gamma$ Systematics (%)	$B^0 \rightarrow J/\psi K^*(892)^0$ $J/\psi \rightarrow \mu^+ \mu^-$	Absolute Acceptance
$B^0 \rightarrow J/\psi K^*(892)^0$ $J/\psi \rightarrow \mu^+ \mu^-$		2.0
$B^0 \rightarrow \psi(2S) K^*(892)^0$ $\psi(2S) \rightarrow \mu^+ \mu^-$	4.2	3.3
$B^0 \rightarrow \psi(2S) \bar{K}^*(892)^0$ $\psi(2S) \rightarrow J/\psi \pi^+ \pi^-$	2.2	2.6

Table 4.6: A summary of the systematic uncertainties (expressed in %) on the relative and absolute geometric and kinematic acceptance due to variations in the longitudinal polarization fractions ( $\Gamma_L/\Gamma$ ) of those decays with vector-vector final states. The column on the right lists the systematic uncertainties on the relevant absolute geometric and kinematic acceptance values.



## Chapter 5

# Efficiency Corrections

The topological and candidate-selection similarities amongst the six decay channels in this study afforded the cancelation of several common efficiencies and systematic uncertainties in the branching-fraction ratios. Only those efficiencies that were unique to one of the decay modes in a given ratio or that differed between the channels required careful study. This chapter details the determination of event-yield corrections and their systematic uncertainties due to inefficiencies relevant to the detection and reconstruction of the candidate  $B$ -meson decay modes.

### 5.1 Constrained Fit Confidence Level Criteria

The vertex and vertex-plus-mass constrained fit confidence level criteria imposed on the charmonium and  $B$ -meson event selection were described in Section 3.8. In the present section, several different techniques are used to study the effects of the  $CL(\chi^2)$  criteria on the yield efficiencies.

#### 5.1.1 Dimuon $CL(\chi^2)$ Criteria

In a branching-fraction ratio expression such as the one given in Equation 1.18, most of the dimuon selection criteria, including the  $CL(\chi^2)$  requirements, are expected to divide out of the calculation. It is nevertheless useful to investigate the effects of the dimuon  $CL(\chi^2)$  criteria to test this assumption, examine the background rejection, and test the efficiency measurement techniques.

Figures 5.1 and 5.2 illustrate the distribution of the  $CL(\chi^2)$  variable for vertex con-

strained fits of  $J/\psi$  and  $\psi(2S)$  dimuon candidates, respectively. The shaded histograms consist of like-sign ( $\mu^\pm \mu^\pm$ ) dimuon candidate combinations, normalized to the measured background yield. Dimuon candidates that clearly did not originate from a common vertex are expected to result in constrained fits with low  $CL(\chi^2)$  values, as exemplified by the populous lower  $CL(\chi^2)$  bins in the left-hand plots of Figures 5.1 and 5.2. The relative ‘flatness’ of the  $CL(\chi^2)$  distributions over most of the abscissa suggests that the covariance matrices of the individual candidate track fits are realistic for most vertexing situations.

Figures 5.3 and 5.4 are analogous to Figures 5.1 and 5.2, with the difference that the former are due to fits with simultaneous vertex and mass constraints. Similar conclusions to those for the vertex-constrained fits may be drawn for the vertex-plus-mass constraint  $CL(\chi^2)$  distributions.

The  $CL(\chi^2) > 0.01$  criterion efficiency for vertex-constrained  $J/\psi$  candidate dimuon fits,  $\epsilon_{J/\psi \rightarrow \mu\mu}^v$ , may be calculated directly by examining the effect of the cut on the  $J/\psi$  candidate yield. Figure 5.5 depicts the  $J/\psi$  invariant mass distribution before and after the application of a  $CL(\chi^2) > 0.01$  requirement. Similarly, Figure 5.6 illustrates the analogous  $\psi(2S)$  invariant mass distributions used in the calculation of  $\epsilon_{\psi(2S) \rightarrow \mu\mu}^v$ .

An alternate method to measure the charmonium event yields is available by constructing normalized invariant mass distributions. Figures 5.7 and 5.8 depict the normalized invariant mass distributions, or ‘pulls’, before and after the  $CL(\chi^2)$  criterion was imposed, for the  $J/\psi$  and  $\psi(2S)$  dimuon candidate distributions, respectively. Note that the widths of the Gaussian signals exceed unity in both cases, indicating some underestimation of the track helix uncertainties. The distributions in Figures 5.7 and 5.8 may also be used to estimate  $\epsilon_{J/\psi \rightarrow \mu\mu}^v$  and  $\epsilon_{\psi(2S) \rightarrow \mu\mu}^v$ .

The extra inefficiency arising from the additional constraint to the appropriate world average charmonium mass,  $\epsilon^m$ , may be estimated from the normalized invariant mass distributions. By relating the peak area obtained with a double-Gaussian fit in a  $\pm 2.58$  standard deviation window about the mean of the normalized invariant mass signal (with the  $CL(\chi^2) > 0.01$  criterion on the vertex-only constrained fit already applied) to the entire signal fit area, the efficiency of an additional mass-constraint  $CL(\chi^2) > 0.01$  requirement can be computed. The right-hand plots in Figures 5.7 and 5.8 were used in this way to measure  $\epsilon_{J/\psi \rightarrow \mu\mu}^m$  and  $\epsilon_{\psi(2S) \rightarrow \mu\mu}^m$ , respectively.

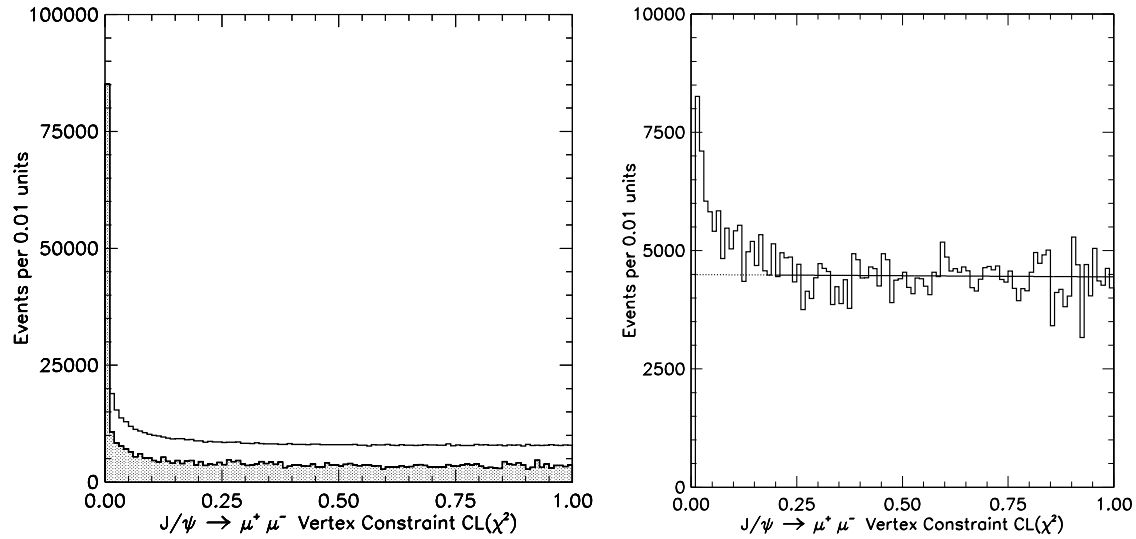


Figure 5.1: The  $CL(\chi^2)$  distribution of the vertex-constrained  $J/\psi$  dimuon fit. The unshaded histogram in the left plot contains the combined signal and background events; the shaded histogram in the left plot represents the like-sign dimuon ( $\mu^\pm \mu^\pm$ ) candidates, normalized to the background yield. The right plot is the difference of the two histograms in the left plot.

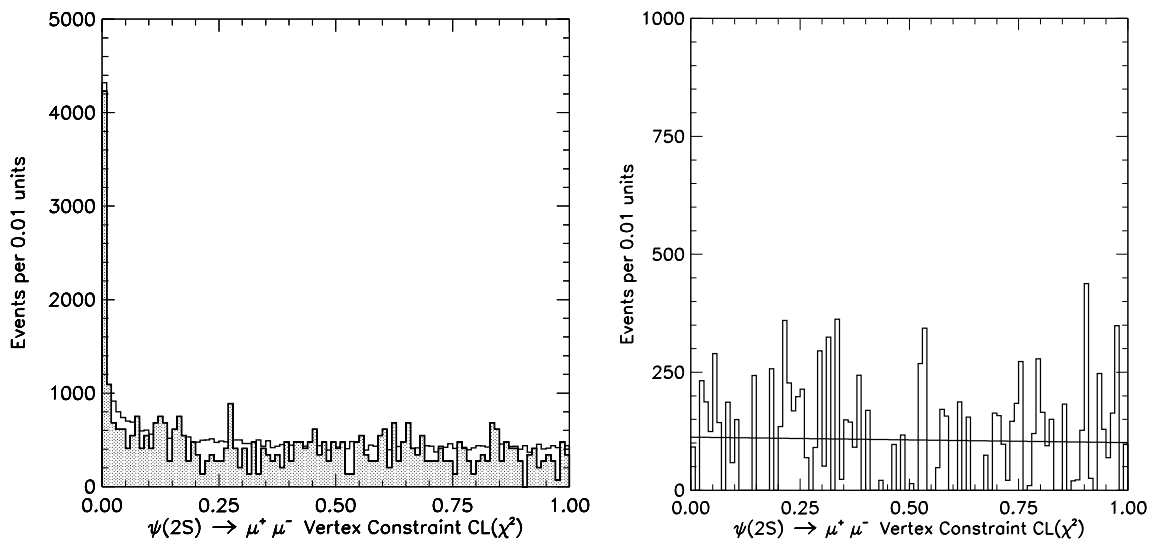


Figure 5.2: The  $CL(\chi^2)$  distribution of the vertex-constrained  $\psi(2S)$  dimuon fit. The unshaded histogram in the left plot contains the combined signal and background events; the shaded histogram in the left plot represents the like-sign dimuon ( $\mu^\pm \mu^\pm$ ) candidates, normalized to the background yield. The right plot is the difference of the two histograms in the left plot.

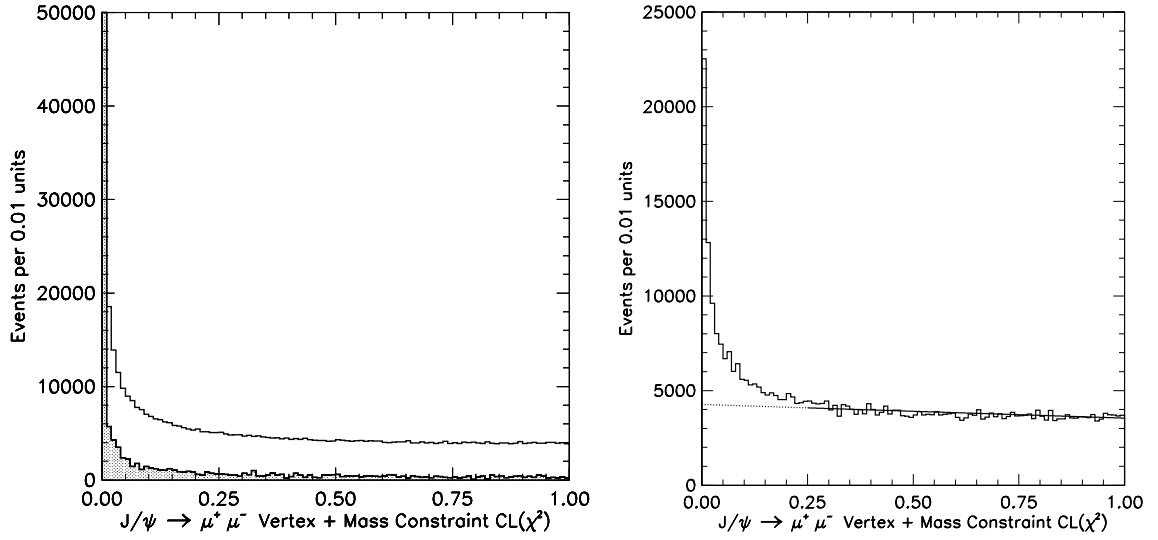


Figure 5.3: The  $CL(\chi^2)$  distribution of the vertex-plus-mass-constrained  $J/\psi$  dimuon fit. The unshaded histogram in the left plot contains the combined signal and background events; the shaded histogram in the left plot represents the like-sign dimuon ( $\mu^\pm \mu^\pm$ ) candidates normalized to the background yield. The right plot is the difference of the two histograms in the left plot.

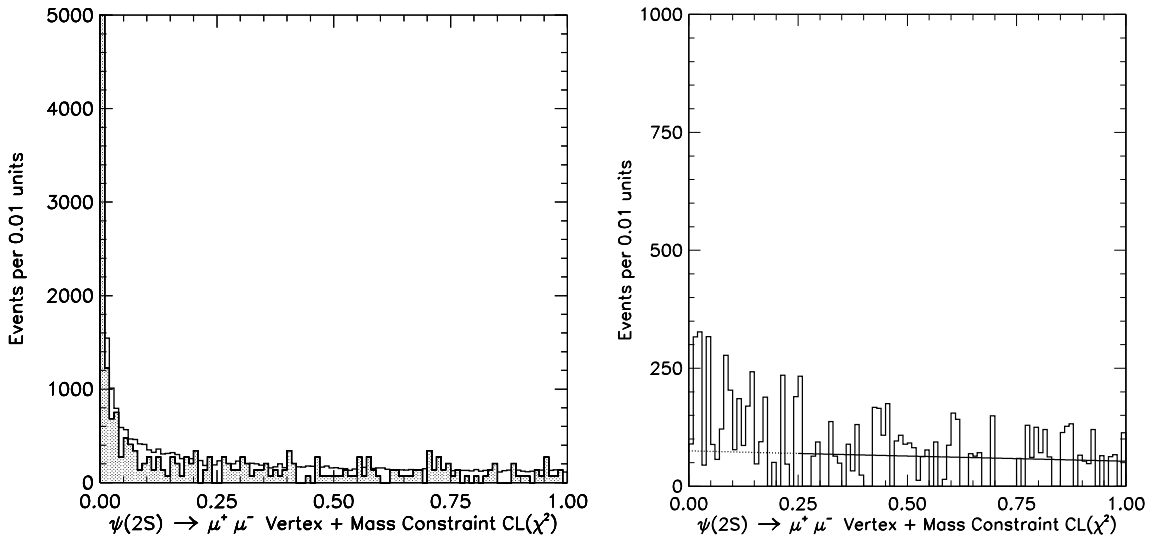


Figure 5.4: The  $CL(\chi^2)$  distribution of the vertex-plus-mass-constrained  $\psi(2S)$  dimuon fit. The unshaded histogram in the left plot contains the combined signal and background events; the shaded histogram in the left plot represents the like-sign dimuon ( $\mu^\pm \mu^\pm$ ) candidates normalized to the background yield. The right plot is the difference of the two histograms in the left plot.

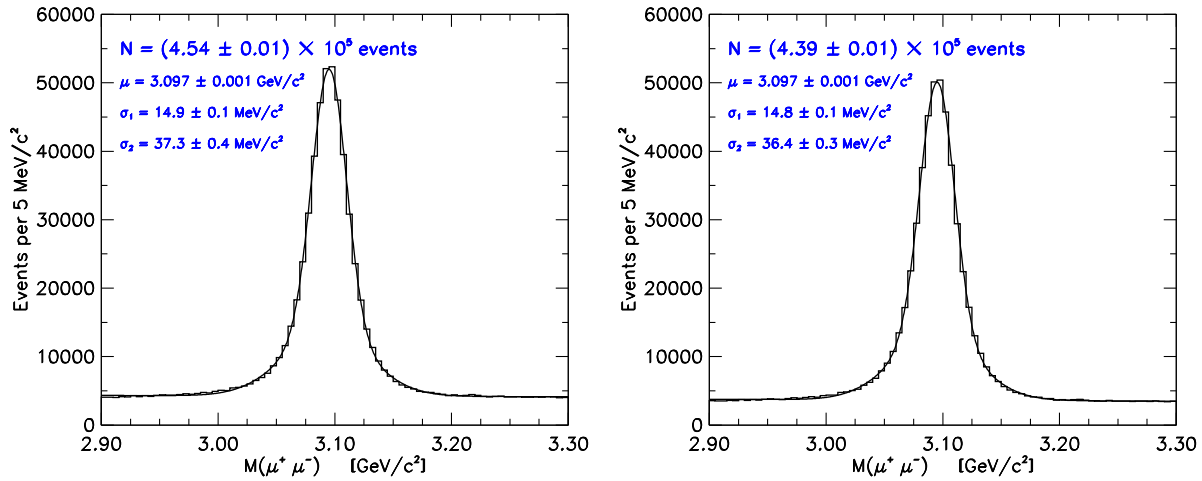


Figure 5.5: The  $J/\psi$  dimuon candidate invariant mass distribution before (left) and after (right) a vertex-constraint criterion of  $CL(\chi^2) > 0.01$  was applied. The fit is to a double Gaussian signal with linear amplitudes and a linear background term.

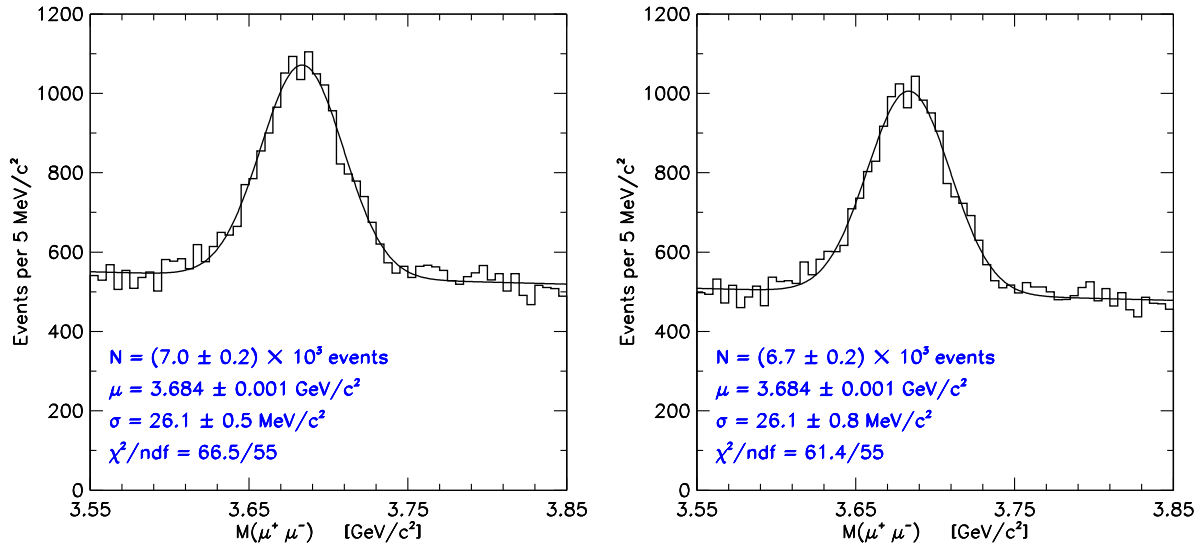


Figure 5.6: The  $\psi(2S)$  dimuon candidate invariant mass distribution before (left) and after (right) a vertex-constraint criterion of  $CL(\chi^2) > 0.01$  was applied. The fit is to a Gaussian signal and a linear background term. A requirement of  $p_T > 2.5$  GeV/c was imposed on each muon candidate to control the background.

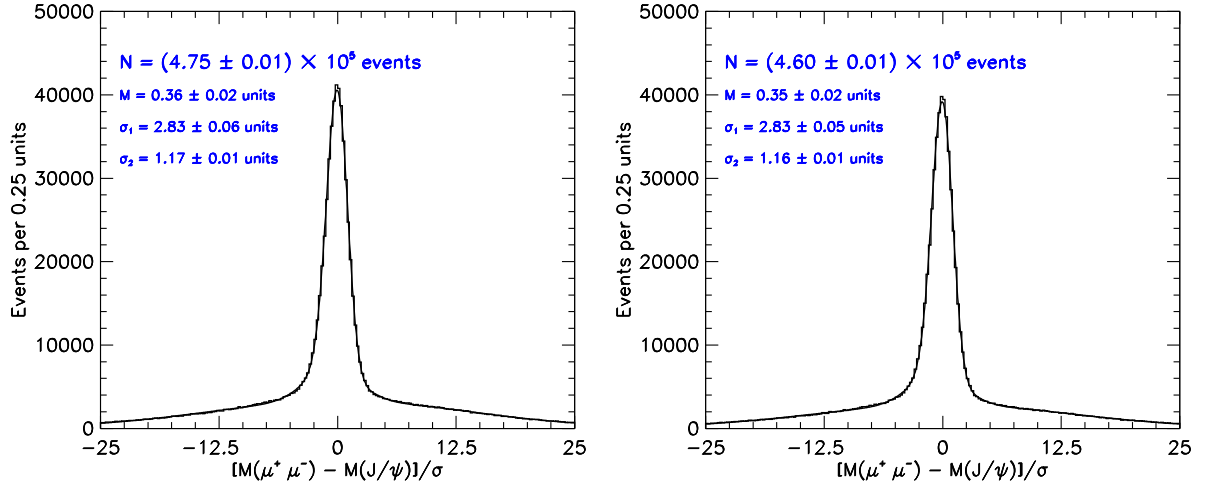


Figure 5.7: The  $J/\psi$  dimuon normalized candidate invariant mass distribution before (left) and after (right) a vertex-constraint criterion of  $CL(\chi^2) > 0.01$  was applied. The fit is to a double Gaussian signal with linear amplitudes and a Gaussian background term.

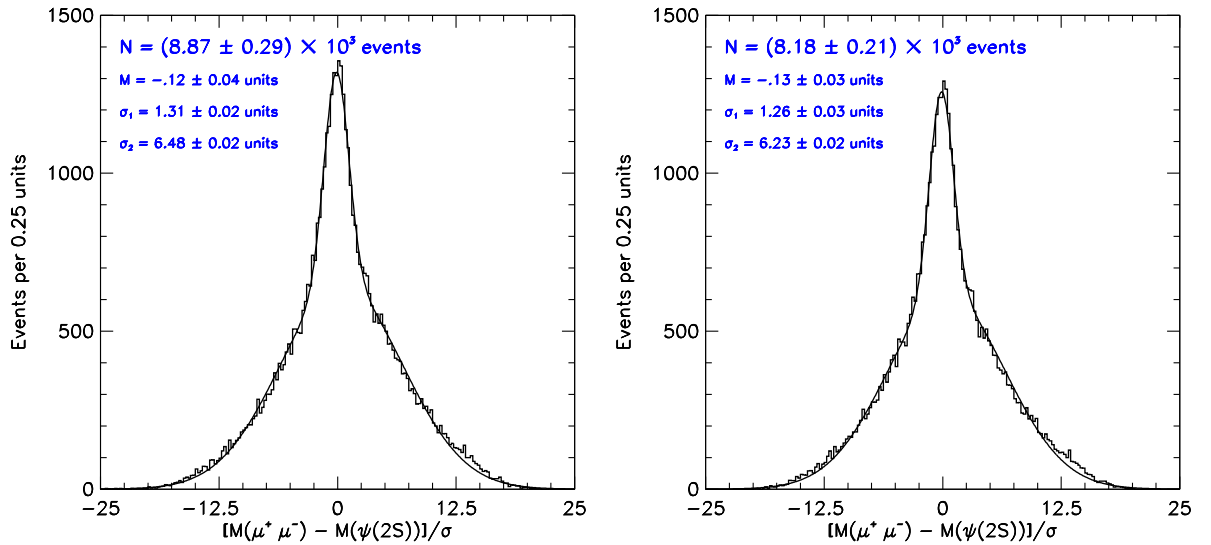


Figure 5.8: The  $\psi(2S)$  dimuon normalized candidate invariant mass distribution before (left) and after (right) a vertex-constraint criterion of  $CL(\chi^2) > 0.01$  was applied. The fit is to a Gaussian signal and a Gaussian background term. A requirement of  $p_T > 2.5$  GeV/ $c$  was imposed on each muon candidate to control the background.

Efficiency	Technique	Measurement
$\epsilon_{J/\psi \rightarrow \mu\mu}^v$	mass	$0.966 \pm 0.003$
$\epsilon_{J/\psi \rightarrow \mu\mu}^v$	normalized mass	$0.969 \pm 0.004$
$\epsilon_{\psi(2S) \rightarrow \mu\mu}^v$	mass	$0.956 \pm 0.036$
$\epsilon_{\psi(2S) \rightarrow \mu\mu}^v$	normalized mass	$0.922 \pm 0.039$
$\epsilon_{\mu\mu}^v$	weighted mean	$0.967 \pm 0.003$
$\epsilon_{J/\psi \rightarrow \mu\mu}^m$	normalized mass	$0.963 \pm 0.002$
$\epsilon_{\psi(2S) \rightarrow \mu\mu}^m$	normalized mass	$0.958 \pm 0.035$
$\epsilon_{\mu\mu}^m$	weighted mean	$0.963 \pm 0.002$

Table 5.1: Dimuon vertex and vertex-plus-mass  $CL(\chi^2) > 0.01$  criterion efficiency summary. The quantities  $\epsilon_{\mu\mu}^v$  and  $\epsilon_{\mu\mu}^m$  were computed by performing a weighted mean of the measured values.

Table 5.1 presents a summary of the various  $CL(\chi^2)$  criterion efficiencies measured in this section. As expected, the various measurements, using either  $J/\psi$  or  $\psi(2S)$  dimuon reconstructions, are largely mutually consistent, thereby supporting the assumption that dimuon  $CL(\chi^2)$  selection effects divide out of the branching-fraction ratio calculations. The average vertex and mass constraint requirements were measured to be  $\epsilon_{\mu\mu}^v = 0.967 \pm 0.003$  and  $\epsilon_{\mu\mu}^m = 0.963 \pm 0.002$ , respectively.

### 5.1.2 Dipion $CL(\chi^2)$ Criteria

Unlike in the dimuon cases, charmonium reconstructions performed via the decay  $\psi(2S) \rightarrow J/\psi \pi^+ \pi^-$  did not necessarily have  $CL(\chi^2)$  requirement efficiencies that divided out of the branching-fraction ratios. The vertex and vertex-plus-mass  $CL(\chi^2)$  cut efficiencies for this hadronic-cascade charmonium mode were taken to be factorizable according to the expressions  $\epsilon_{\psi(2S) \rightarrow J/\psi \pi \pi}^v = \epsilon_{\mu\mu}^v \cdot \epsilon_{\pi\pi}^v$  and  $\epsilon_{\psi(2S) \rightarrow J/\psi \pi \pi}^m = \epsilon_{\mu\mu}^m \cdot \epsilon_{\pi\pi}^m$ , respectively. The fact that the  $J/\psi$  dimuon candidate was first vertex-plus-mass constrained separately, before the  $\pi^+ \pi^-$  candidates were included in the fit, permitted this factorization of  $CL(\chi^2)$  cut efficiencies. The principal advantage of factorizing the efficiency in this way is that the dimuon efficiency factors,  $\epsilon_{\mu\mu}^v$  and  $\epsilon_{\mu\mu}^m$ , can still divide to unity in the branching-fraction

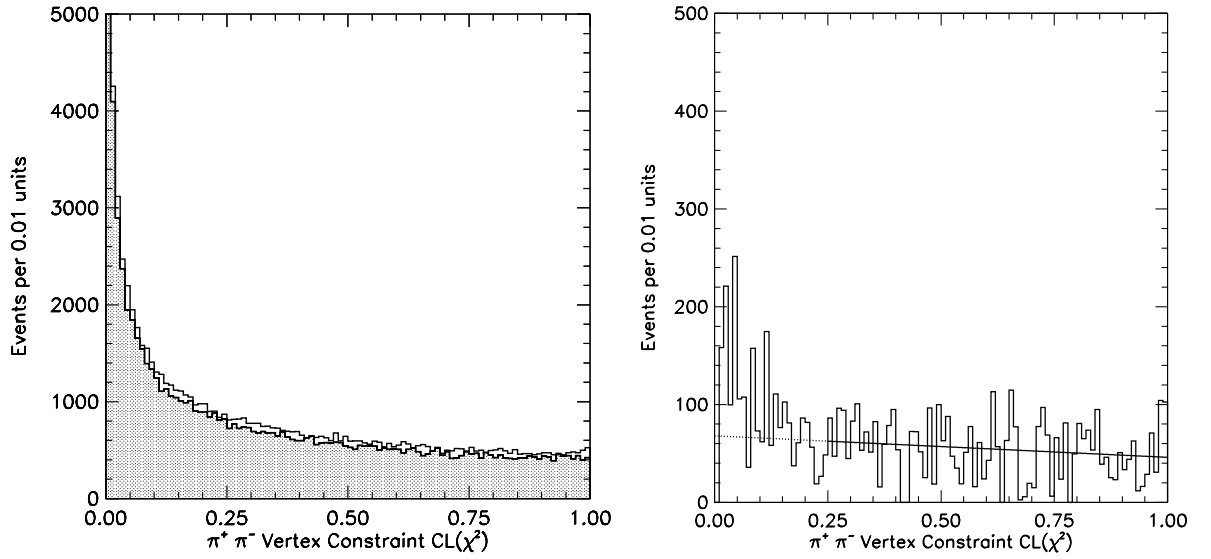


Figure 5.9: The  $CL(\chi^2)$  distribution of the vertex-constrained  $\pi^+ \pi^-$  fit. The unshaded histogram in the left plot contains the combined signal and background events; the shaded histogram in the left plot represents the like-sign dipion ( $\pi^\pm \pi^\pm$ ) candidates normalized to the background yield. The right plot is the difference of the two histograms in the left plot.

ratio expressions.

Figure 5.9 illustrates the distribution of the  $CL(\chi^2)$  variable for vertex-constrained fits of  $J/\psi \pi^+ \pi^-$  candidates performed after vertex-plus-mass constrained fits (and the corresponding  $CL(\chi^2)$  criteria) were applied to the  $J/\psi$  dimuon candidates alone. The shaded histogram was created from like-sign-pion ( $J/\psi \pi^\pm \pi^\pm$ ) candidate combinations, normalized to the measured background yield. The features in Figure 5.9 are similar to those observed in Figures 5.1 and 5.2 in Section 5.1.1.

Figures 5.10 and 5.11 respectively depict the  $J/\psi \pi^+ \pi^-$  invariant mass and normalized invariant mass distributions before and after the additional  $CL(\chi^2) > 0.01$  criterion was applied to the  $\pi^+ \pi^-$  vertex-constrained fit quality. The techniques used to measure the  $\epsilon_{\pi\pi}^v$  and  $\epsilon_{\pi\pi}^m$  efficiencies were similar to those described in Section 5.1.1. Table 5.2 summarizes the  $\epsilon_{\pi\pi}^v$  and  $\epsilon_{\pi\pi}^m$  results. The uncertainties on the efficiencies were estimated by conservatively combining in quadrature the yield uncertainties before and after the  $CL(\chi^2) > 0.01$  criterion was imposed.



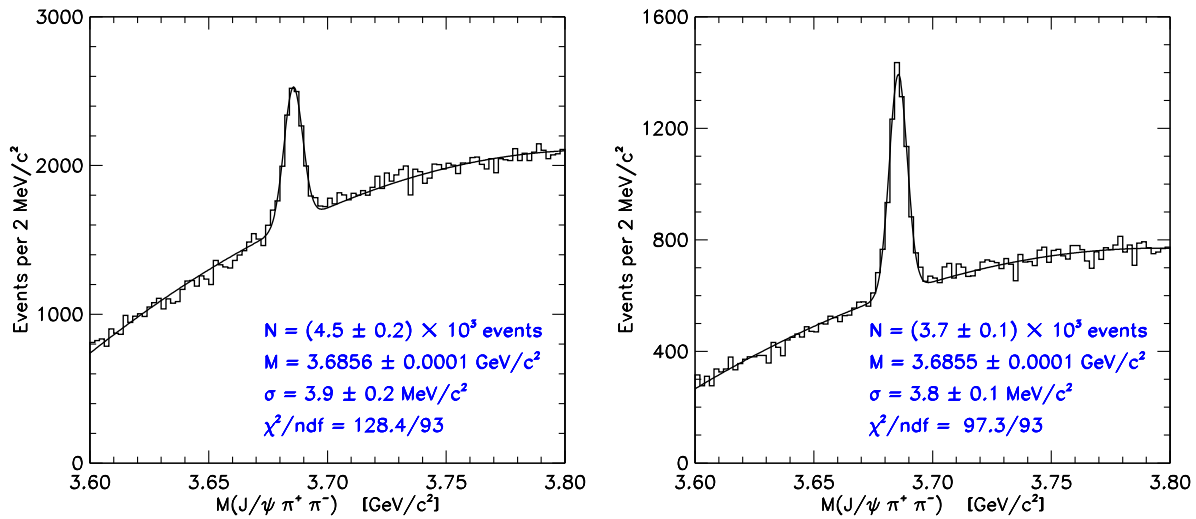


Figure 5.10: The  $J/\psi \pi^+ \pi^-$  candidate invariant mass distribution before (left) and after (right) a vertex-constraint criterion of  $CL(\chi^2) > 0.01$  was applied. The fit is to a Gaussian signal and a cubic polynomial background term.

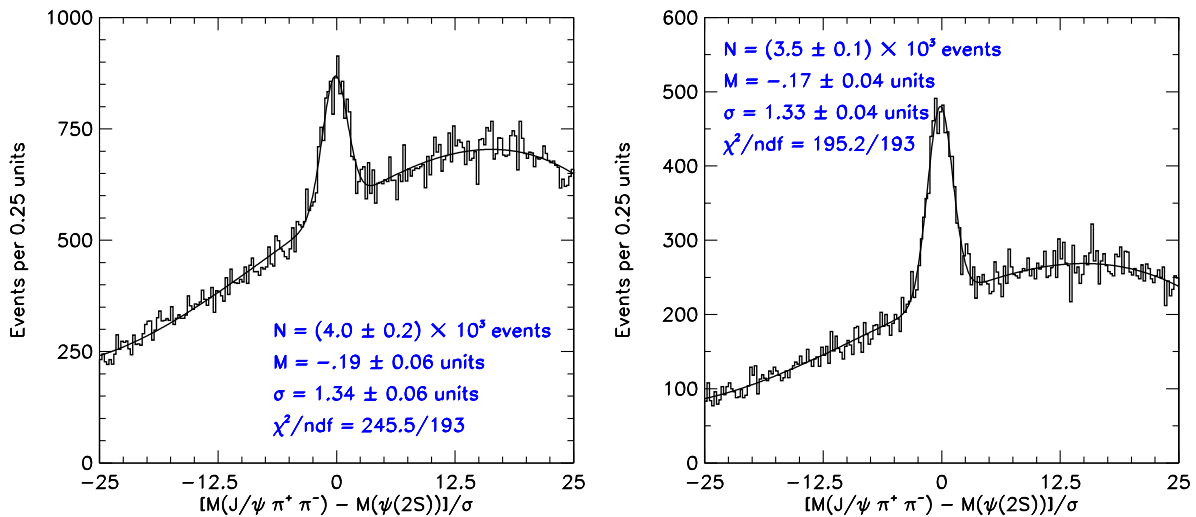


Figure 5.11: The  $J/\psi \pi^+ \pi^-$  normalized candidate invariant mass distribution before (left) and after (right) a vertex-constraint criterion of  $CL(\chi^2) > 0.01$  was applied. The fit is to a Gaussian signal and a cubic polynomial background term.

Efficiency	Technique	Measurement
$\epsilon_{\pi\pi}^v$	mass	$0.816 \pm 0.039$
$\epsilon_{\pi\pi}^v$	normalized mass	$0.858 \pm 0.045$
$\epsilon_{\pi\pi}^v$	weighted mean	$0.834 \pm 0.039$
$\epsilon_{\pi\pi}^m$	normalized mass	$0.945 \pm 0.031$

Table 5.2: Dipion vertex and vertex-plus-mass  $CL(\chi^2) > 0.01$  criterion efficiency summary.

### 5.1.3 $B$ -Meson $CL(\chi^2)$ Criteria

The efficiency of the vertex and momentum-pointing  $CL(\chi^2) > 0.01$  criterion on the candidate  $B$  decays was expected to be similar to those calculated for the inclusive charmonium reconstructions. In practice, limited statistics made it difficult to examine the effects of  $CL(\chi^2)$  requirements on ‘global’ vertex-constrained fits of  $B$ -meson candidates. To accommodate any possible noncancellation of the global  $B$   $CL(\chi^2)$  cut efficiencies for a given ratio of branching fractions, a systematic uncertainty of 2.0% was assigned on each ratio. This systematic uncertainty was estimated by taking the standard deviation of the measured  $\epsilon^v$  and  $\epsilon^m$  values in Table 5.1.

## 5.2 Tracking Efficiencies

An advantage of measuring ratios of branching fractions was that the tracking efficiencies largely divided out of the calculations. Such was the case for ratios involving the dimuonic charmonium modes and like species of strange meson in both numerator and denominator. Ratios of branching fractions involving the decay  $\psi(2S) \rightarrow J/\psi \pi^+ \pi^-$  and unlike kaon species of the form  $K^*(892)^0/K^+$ , however, possessed residual dipion and single-pion tracking efficiency factors, respectively.

Over the course of the entire Run 1 period, several known effects with potential implications for tracking performance were noted: the instantaneous luminosity varied by amounts in excess of an order of magnitude (refer to Section 3.1), the propensity for multiple primary vertices in a given event increased, the Tevatron beam optics were modified, the wire geometry in the CTC was altered by gravity-induced sagging, and the electrostatic and

gas-quality characteristics of the CTC changed.

Motivated not only by the requirements of the present ratio-of-branching-fraction analysis, but also by the needs of other CDF analyses that made use of low momentum tracking information, a detailed study [135] of single- and double-track CTC pattern recognition efficiencies was conducted. Appendix C summarizes the methodology and results of the pattern recognition efficiency measurements. The single-pion pattern recognition efficiency was measured to be  $0.928 \pm 0.020$  for  $p_T > 0.4$  GeV/ $c$  and  $r_{\text{CTC}}^{\text{exit}} > 110$  cm. The double-pion efficiency was measured to be  $0.881 \pm 0.043$ , also for  $p_T > 0.4$  GeV/ $c$  and  $r_{\text{CTC}}^{\text{exit}} > 110$  cm.

### 5.3 Proper Decay Length Criteria

In this analysis, both the numerator and the denominator in each ratio of branching fractions contained  $B^+$  or  $B^0$  meson candidates. The measured world-average proper decay lengths ( $c\tau_B$ ) of  $B^+$  and  $B^0$  mesons are  $(492 \pm 18)$   $\mu\text{m}$  and  $(465 \pm 15)$   $\mu\text{m}$  [30], respectively. The fact that the accepted lifetimes for the two  $B$ -meson flavours were mutually consistent lead to the expectation that the  $c\tau_B > 100$   $\mu\text{m}$  criterion (refer to Section 3.9.2) efficiencies would be similar for all the modes. The world-average  $B$  lifetimes, however, were short enough that the efficiency of a 100- $\mu\text{m}$  proper decay length cut was potentially sensitive to the resolution of the  $c\tau_B$  measurement itself, which, in turn, was sensitive to the momentum and vertex resolution of the final-state tracks. Here the different decay topologies could play a measurable rôle in the efficiency, owing to the  $c\tau_B$  resolution dependence on the multiplicity of candidate tracks that made use of SVX (Section 2.3.1) tracking information.

The sideband regions of the  $B$ -meson candidate invariant mass distributions were expected to be populated primarily by prompt, *i.e.*, low proper-decay-length, processes. The regions  $5.145 - 5.220$  GeV/ $c^2$  and  $5.340 - 5.415$  GeV/ $c^2$ , with the kinematic selection criteria relaxed to enhance the statistics, were therefore used to examine the  $c\tau_B$  resolution as a function of the number of daughter-candidate tracks with SVX hit information used in their fits. The results for the  $B^+$  and  $B^0$  decay modes are given in Tables 5.3 and 5.4, respectively.

The relative frequencies of occurrence of the different SVX multiplicity possibilities were estimated for each decay mode with a Monte Carlo calculation (described in Chapter 4), for

Number of tracks with SVX hits	$B^+ \rightarrow J/\psi K^+$ $J/\psi \rightarrow \mu^+ \mu^-$	$B^+ \rightarrow \psi(2S) K^+$ $\psi(2S) \rightarrow \mu^+ \mu^-$	$B^+ \rightarrow \psi(2S) K^+$ $\psi(2S) \rightarrow J/\psi \pi^+ \pi^-$ $J/\psi \rightarrow \mu^+ \mu^-$
0	$575 \pm 6$	$783 \pm 49$	$520 \pm 26$
1	$171 \pm 4$	$181 \pm 1$	$189 \pm 35$
2	$94 \pm 1$	$99 \pm 3$	$243 \pm 122$
3	$57 \pm 1$	$52 \pm 1$	$55 \pm 9$
4			$78 \pm 10$
5			$49 \pm 2$

Table 5.3: Sideband  $c\tau_B$  resolutions, measured in units of  $\mu\text{m}$ , for each  $B^+$  decay mode and SVX track multiplicity.

Number of tracks with SVX hits	$B^0 \rightarrow J/\psi K^*(892)^0$ $J/\psi \rightarrow \mu^+ \mu^-$ $K^*(892)^0 \rightarrow K^+ \pi^-$	$B^0 \rightarrow \psi(2S) K^*(892)^0$ $\psi(2S) \rightarrow \mu^+ \mu^-$ $K^*(892)^0 \rightarrow K^+ \pi^-$	$B^0 \rightarrow \psi(2S) K^*(892)^0$ $\psi(2S) \rightarrow J/\psi \pi^+ \pi^-$ $J/\psi \rightarrow \mu^+ \mu^-$ $K^*(892)^0 \rightarrow K^+ \pi^-$
0	$591 \pm 3$	$762 \pm 22$	$584 \pm 13$
1	$202 \pm 3$	$210 \pm 7$	$291 \pm 52$
2	$117 \pm 1$	$102 \pm 3$	$168 \pm 21$
3	$68 \pm 1$	$68 \pm 1$	$74 \pm 8$
4	$49 \pm 1$	$56 \pm 1$	$61 \pm 4$
5			$59 \pm 2$
6			$48 \pm 1$

Table 5.4: Sideband  $c\tau_B$  resolutions, measured in units of  $\mu\text{m}$ , for each  $B^0$  decay mode and SVX track multiplicity.

$B$ Mode	$c\bar{c}$ Mode	Central	$-1\sigma$	$+1\sigma$	Efficiency
$B^+ \rightarrow J/\psi K^+$	$J/\psi \rightarrow \mu^+ \mu^-$	.753	.741	.764	$.753 \pm .012$
$B^+ \rightarrow \psi(2S) K^+$	$\psi(2S) \rightarrow \mu^+ \mu^-$	.738	.726	.748	$.738 \pm .013$
$B^+ \rightarrow \psi(2S) K^+$	$\psi(2S) \rightarrow J/\psi \pi^+ \pi^-$	.762	.750	.774	$.762 \pm .012$
$B^0 \rightarrow J/\psi K^*(892)^0$	$J/\psi \rightarrow \mu^+ \mu^-$	.755	.742	.766	$.755 \pm .013$
$B^0 \rightarrow \psi(2S) K^*(892)^0$	$\psi(2S) \rightarrow \mu^+ \mu^-$	.749	.736	.760	$.749 \pm .013$
$B^0 \rightarrow \psi(2S) K^*(892)^0$	$\psi(2S) \rightarrow J/\psi \pi^+ \pi^-$	.761	.748	.773	$.761 \pm .013$

Table 5.5: Measured  $c\tau_B$  cut efficiencies in the  $B^+$  and  $B^0$  decay modes, showing the effects of variations of the world-average  $B$  lifetimes by their standard deviations.

which the detector simulation had been tuned on data to determine the SVX hit efficiencies and hit association characteristics. The measured  $c\tau_B$  resolutions in Tables 5.3 and 5.4 were then convolved with  $c\tau_B$  distributions that used the world average  $B^+$  and  $B^0$  proper lifetimes [30] in their decay constants, respectively. A toy Monte Carlo programme was employed to perform  $10^5$  convolutions for each decay, and the resolution contributions from the various SVX track multiplicities were administered according to weighting probabilities determined by the relative frequencies calculated from the Monte Carlo samples. The procedure was then repeated for the world-average  $c\tau_B$  values shifted high and low by their standard deviations ( $\sigma$ ) [30]. The results of these shifts, along with the central values, are listed in Table 5.5. The systematic uncertainties on the efficiency values correspond to the maximum efficiency deviations observed in the  $-1\sigma$  and  $+1\sigma$  studies. As expected, the measured  $c\tau_B$  efficiencies were similar, with all values near 0.75. The small efficiency differences amongst the various channels were consistent with differences in the daughter-track multiplicities.

## 5.4 $B$ -Candidate Isolation Criterion

The  $B$ -meson candidate isolation criterion,  $I_B = \frac{\sum_{i \notin B}^R \vec{p}_i \cdot \hat{p}_B}{|\vec{p}_B|} < \frac{7}{13}$ , was defined and described in Section 3.9.2. This requirement rejected significant contributions of background to the  $B$ -candidate signals, namely backgrounds arising from invariant mass combinations

<i>B</i> Mode	<i>c</i> $\bar{c}$ Mode	Efficiency
$B^+ \rightarrow J/\psi K^+$	$J/\psi \rightarrow \mu^+ \mu^-$	$0.900 \pm 0.063$
$B^+ \rightarrow \psi(2S) K^+$	$\psi(2S) \rightarrow \mu^+ \mu^-$	$1.000^{+0.000}_{-0.300}$
$B^+ \rightarrow \psi(2S) K^+$	$\psi(2S) \rightarrow J/\psi \pi^+ \pi^-$	$1.000^{+0.000}_{-0.294}$
$B^0 \rightarrow J/\psi K^*(892)^0$	$J/\psi \rightarrow \mu^+ \mu^-$	$0.937^{+0.063}_{-0.092}$
$B^0 \rightarrow \psi(2S) K^*(892)^0$	$\psi(2S) \rightarrow \mu^+ \mu^-$	n/a
$B^0 \rightarrow \psi(2S) K^*(892)^0$	$\psi(2S) \rightarrow J/\psi \pi^+ \pi^-$	$0.907^{+0.093}_{-0.268}$
Combined-Channel Measurement		$0.928 \pm 0.054$

Table 5.6: Measured isolation criterion efficiencies in the  $B^+$  and  $B^0$  decay modes. The domination of background in the  $B^0 \rightarrow \psi(2S) K^*(892)^0$ ,  $\psi(2S) \rightarrow \mu^+ \mu^-$  decay-chain reconstruction prevented an individual measurement; however, the invariant mass distributions for all six modes were used to compute the combined efficiency in the bottom row.

of the dimuon candidates with non- $B$  tracks from the underlying event (which is represented by  $X$  in Equation 1.4). The large  $\eta$ - $\varphi$  cone radius and the stipulation that the non- $B$  tracks that contribute to the summation in the isolation expression be consistent with having originated from the same primary vertex as the  $B$  candidate suggested that the isolation criterion would be relatively efficient, as exemplified in Figure 3.1. Investigations of  $B$ -meson isolation requirements indicate that the efficiencies of these criteria are largely independent of the type of  $B$  decay mode and the  $p_T$  of the  $B$  candidate [136].

As a consistency test of the observation [136] that the  $B$ -candidate isolation criterion was independent of decay topology (therefore obviating a need for individual efficiencies in the branching-fraction ratio calculations), the effective efficiency of the isolation requirement was examined for each of the six  $B$ -meson reconstructions investigated in this study. Table 5.6 lists the efficiencies, which were measured by comparing the appropriate candidate yields after and before the isolation criterion was imposed. The combined efficiency of the isolation requirement was found to be  $0.928 \pm 0.054$  and the efficiencies for the individual topologies were observed to be mutually consistent.

Decay Mode	Branching Fraction
$J/\psi \rightarrow \mu^+ \mu^-$	$(6.01 \pm 0.19) \times 10^{-2}$
$\psi(2S) \rightarrow \mu^+ \mu^-$	$(8.5 \pm 0.7) \times 10^{-3}$
$\psi(2S) \rightarrow J/\psi \pi^+ \pi^-$	$(3.07 \pm 0.19) \times 10^{-1}$
$K^*(892)^0 \rightarrow K^+ \pi^-$	$2/3$

Table 5.7: Branching fractions of the daughter meson decay modes that were reconstructed in the present analysis. For the charmonia, the world-average branching fractions were used, with the assumption of lepton universality in the  $\mathcal{B}(\psi(2S) \rightarrow \mu^+ \mu^-)$  case [30]. The  $K^*(892)^0$  branching fraction was based on isospin symmetry.

## 5.5 Daughter Branching Fractions

Depending on the ratio of  $B$ -meson branching fractions being calculated in this study, different combinations of daughter branching fractions did not divide out of the calculation. These quantities are listed in Table 5.7. The charmonium branching fractions were taken to be the most recent accepted world-average values [30]; however, the  $\mathcal{B}(J/\psi \rightarrow \mu^+ \mu^-)$  average did not take into account the measurement reported in Reference [137]. For the value of  $\mathcal{B}(\psi(2S) \rightarrow \mu^+ \mu^-)$ , the world average for  $\mathcal{B}(\psi(2S) \rightarrow e^+ e^-)$ , which has a significantly smaller uncertainty, was used under the assumption of lepton universality. The  $\mathcal{B}(K^*(892)^0 \rightarrow K^+ \pi^-)$  value is based on isospin symmetry. The uncertainties on the world-average charmonium branching fractions constitute the largest contributions to the total systematic uncertainties in the present analysis.

## Chapter 6

# Branching Fraction Measurements

### 6.1 $B$ -Meson Candidate Event Yields

The  $B$ -meson candidate event yields in this study were computed by fitting binned invariant mass distributions to signal and background lineshapes using a maximum log-likelihood technique. In order to avoid any contributions of partially reconstructed  $B$  mesons to the lower-sideband fit region, invariant masses  $< 5.15 \text{ GeV}/c^2$  were excluded from all the fits. Figure 6.1 features the observed  $B^+ \rightarrow J/\psi K^+ (J/\psi \rightarrow \mu^+ \mu^-)$  invariant mass distribution. Figure 6.2 illustrates the analogous  $B^+ \rightarrow \psi(2S) K^+$  invariant mass distributions, with both the  $\psi(2S) \rightarrow \mu^+ \mu^-$  and  $\psi(2S) \rightarrow J/\psi \pi^+ \pi^-$  charmonium daughter modes.

The fits for the  $B^0$  candidate event yields embodied the relative double-Gaussian parameterizations described in Table 3.1 in Section 3.9.3. Figure 6.3 shows the  $J/\psi K^*(892)^0 (J/\psi \rightarrow \mu^+ \mu^-)$  invariant mass distribution, whereas Figure 6.4 presents both the  $\psi(2S) \rightarrow \mu^+ \mu^-$  and  $\psi(2S) \rightarrow J/\psi \pi^+ \pi^-$  reconstructed  $\psi(2S) K^*(892)^0$  invariant mass distributions.

The event yields and their statistical uncertainties are summarized in Table 6.1. The relative yields of those final states with  $\psi(2S)$  candidates are consistent with expectations from the acceptance and efficiency measurements. An uncertainty of 4.0% was assigned on the branching-fraction ratios to account for differences in the event yields due to different fitting intervals and different right-mass-combination counting techniques in the  $K^*(892)^0$  modes. The fit interval was varied from  $5.1 - 5.6 \text{ GeV}/c^2$  to  $5.2 - 5.6 \text{ GeV}/c^2$  and an algorithm that selected  $K^+ \pi^-$  combinations nearest the world-average  $K^*(892)^0$  pole mass [30] were used in lieu of the default techniques (fitting over the interval  $5.15 - 5.6 \text{ GeV}/c^2$  and using the double-Gaussian method) to estimate this systematic uncertainty.



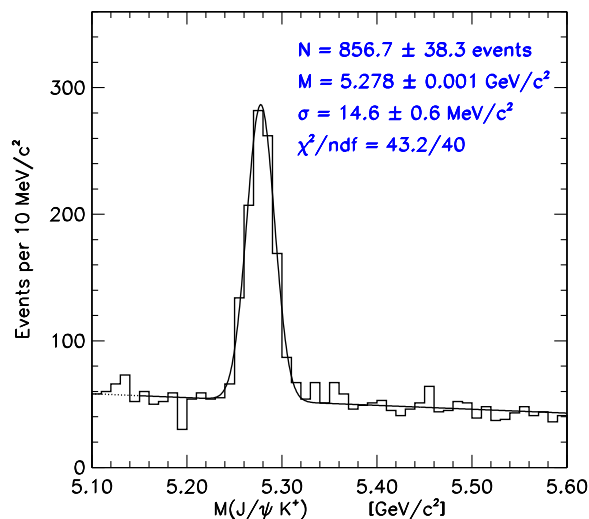


Figure 6.1: The  $J/\psi K^+$  invariant mass distribution. The fit is to a Gaussian signal lineshape and a linear background parameterization.

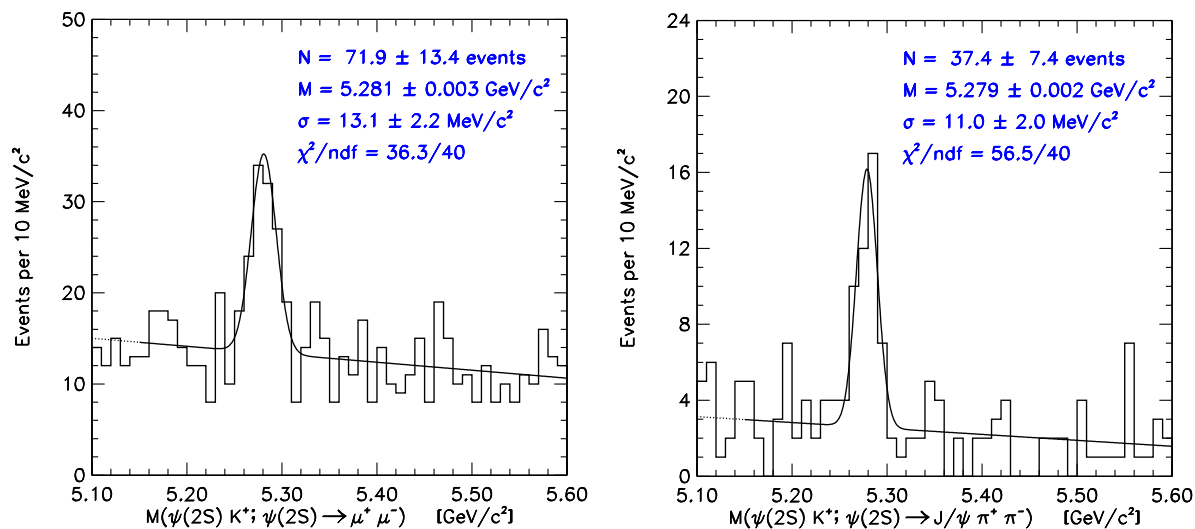


Figure 6.2: The  $\psi(2S) K^+$  invariant mass distributions using the  $\psi(2S) \rightarrow \mu^+ \mu^-$  (left plot) and  $\psi(2S) \rightarrow J/\psi \pi^+ \pi^-$  (right plot) modes. Each fit is to a Gaussian signal lineshape and a linear background parameterization.

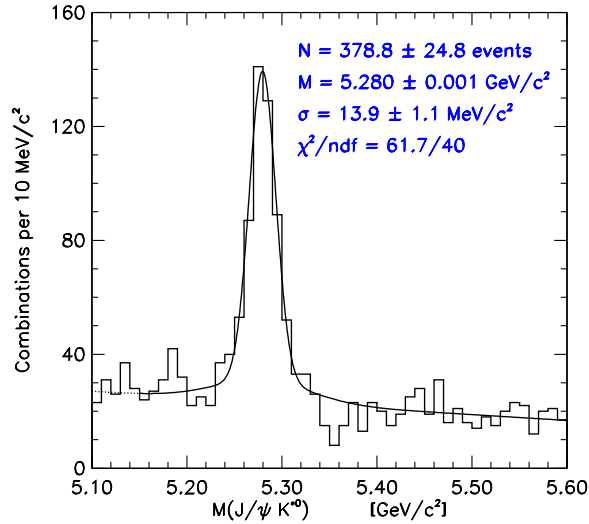


Figure 6.3: The  $J/\psi K^*(892)^0$  invariant mass distribution. The fit is to a double Gaussian signal lineshape and a linear background parameterization. The indicated fit parameters describe the Gaussian distribution of those combinations with correct  $K$ - $\pi$  mass hypotheses.

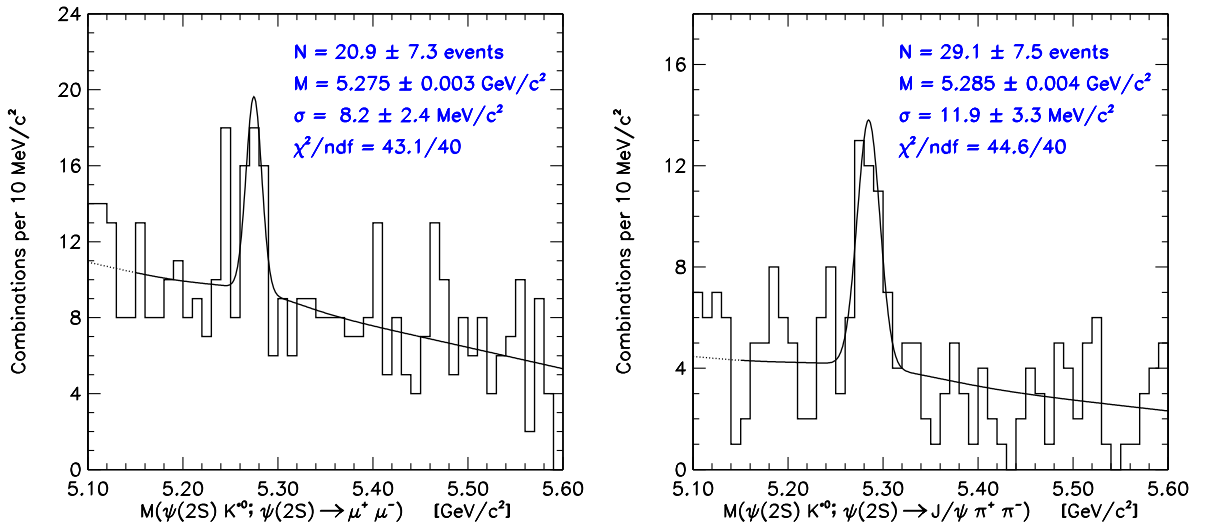


Figure 6.4: The  $\psi(2S) K^*(892)^0$  invariant mass distributions using the  $\psi(2S) \rightarrow \mu^+ \mu^-$  (left plot) and  $\psi(2S) \rightarrow J/\psi \pi^+ \pi^-$  (right plot) modes. Each fit is to a double Gaussian signal lineshape and a linear background parameterization. The indicated fit parameters describe the Gaussian distribution of those combinations with correct  $K$ - $\pi$  mass hypotheses.

$B$ Mode	$c\bar{c}$ Mode	Event Yield
$B^+ \rightarrow J/\psi K^+$	$J/\psi \rightarrow \mu^+ \mu^-$	$856.7 \pm 38.3$
$B^+ \rightarrow \psi(2S) K^+$	$\psi(2S) \rightarrow \mu^+ \mu^-$	$71.9 \pm 13.4$
$B^+ \rightarrow \psi(2S) K^+$	$\psi(2S) \rightarrow J/\psi \pi^+ \pi^-$	$37.4 \pm 7.4$
$B^0 \rightarrow J/\psi K^*(892)^0$	$J/\psi \rightarrow \mu^+ \mu^-$	$378.8 \pm 24.8$
$B^0 \rightarrow \psi(2S) K^*(892)^0$	$\psi(2S) \rightarrow \mu^+ \mu^-$	$20.9 \pm 7.3$
$B^0 \rightarrow \psi(2S) K^*(892)^0$	$\psi(2S) \rightarrow J/\psi \pi^+ \pi^-$	$29.1 \pm 7.5$

Table 6.1: Summary of  $B$ -meson candidate event yields. The indicated uncertainties are statistical only.

## 6.2 Sample Branching-Fraction Ratio Calculation

The event yields, relative geometric and kinematic acceptances, efficiencies, daughter-meson branching fractions, and systematic uncertainties were combined into the calculations of the ratios of branching fractions. An example of the calculation of the ratio  $R_{J/\psi K^*(892)^0}^{\psi(2S) K^+}$  in Table 1.3 can be illustrated by expanding the form of the expression in Equation 1.18 to treat both of the  $\psi(2S)$  daughter reconstructions:

$$\frac{\mathcal{B}(B^+ \rightarrow \psi(2S) K^+)}{\mathcal{B}(B^0 \rightarrow J/\psi K^*(892)^0)} = \frac{N(B^+ \rightarrow \psi(2S) K^+, \psi(2S) \rightarrow \mu^+ \mu^-) + N(B^+ \rightarrow \psi(2S) K^+, \psi(2S) \rightarrow J/\psi \pi^+ \pi^-)}{N(B^0 \rightarrow J/\psi K^*(892)^0, J/\psi \rightarrow \mu^+ \mu^-)} \times \frac{\varepsilon^{\text{tot}}(B^0 \rightarrow J/\psi K^*(892)^0, J/\psi \rightarrow \mu^+ \mu^-)}{\varepsilon^{\text{tot}}(B^+ \rightarrow \psi(2S) K^+, \psi(2S) \rightarrow \mu^+ \mu^-) + \varepsilon^{\text{tot}}(B^+ \rightarrow \psi(2S) K^+, \psi(2S) \rightarrow J/\psi \pi^+ \pi^-)}, \quad (6.1)$$

where the  $N$  symbols represent the event yields and the  $\varepsilon^{\text{tot}}$  quantities represent products of absolute geometric and kinematic acceptances, efficiencies, and daughter-meson branching fractions<sup>1</sup>. Resolving the expression in Equation 6.1 into the relevant measured factors gives the form

$$\frac{\mathcal{B}(B^+ \rightarrow \psi(2S) K^+)}{\mathcal{B}(B^0 \rightarrow J/\psi K^*(892)^0)} = \frac{N(B^+ \rightarrow \psi(2S) K^+, \psi(2S) \rightarrow \mu^+ \mu^-) + N(B^+ \rightarrow \psi(2S) K^+, \psi(2S) \rightarrow J/\psi \pi^+ \pi^-)}{N(B^0 \rightarrow J/\psi K^*(892)^0, J/\psi \rightarrow \mu^+ \mu^-)} \times \quad (6.2)$$

<sup>1</sup>The method of combining the results from the two  $\psi(2S)$  channels was motivated by the low efficiencies involved in identifying candidate events, thereby requiring the use of Poisson probability distributions.

$$\begin{aligned}
& \varepsilon_{\pi}^{\text{trk}} \cdot \varepsilon^{c\tau}(B^0 \rightarrow J/\psi K^*(892)^0) \cdot \mathcal{B}(K^*(892)^0 \rightarrow K^+ \pi^-) \times \\
& \left[ \frac{\mathcal{A}(B^+ \rightarrow \psi(2S) K^+, \psi(2S) \rightarrow \mu^+ \mu^-)}{\mathcal{A}(B^0 \rightarrow J/\psi K^*(892)^0)} \cdot \varepsilon^{c\tau}(B^+ \rightarrow \psi(2S) K^+, \psi(2S) \rightarrow \mu^+ \mu^-) \right. \\
& \times \frac{\mathcal{B}(\psi(2S) \rightarrow \mu^+ \mu^-)}{\mathcal{B}(J/\psi \rightarrow \mu^+ \mu^-)} \quad + \quad \frac{\mathcal{A}(B^+ \rightarrow \psi(2S) K^+, \psi(2S) \rightarrow J/\psi \pi^+ \pi^-)}{\mathcal{A}(B^0 \rightarrow J/\psi K^*(892)^0)} \\
& \left. \times \varepsilon^{c\tau}(B^+ \rightarrow \psi(2S) K^+, \psi(2S) \rightarrow J/\psi \pi^+ \pi^-) \cdot \varepsilon_{\pi\pi}^{\text{v}} \cdot \varepsilon_{\pi\pi}^{\text{m}} \cdot \varepsilon_{\pi\pi}^{\text{trk}} \cdot \mathcal{B}(\psi(2S) \rightarrow J/\psi \pi^+ \pi^-) \right]^{-1},
\end{aligned}$$

where  $\varepsilon_{\pi}^{\text{trk}}$  represents the single-pion pattern recognition efficiency (refer to Section 5.2 and Appendix C),  $\varepsilon^{c\tau}$  represents the proper-decay-length requirement efficiencies (refer to Section 5.3), the quantities  $\mathcal{A}$  represent the geometric and kinematic acceptances,  $\varepsilon_{\pi\pi}^{\text{v}}$  and  $\varepsilon_{\pi\pi}^{\text{m}}$  represent the  $CL(\chi^2)$  requirement efficiencies (refer to Section 5.1.2), and  $\varepsilon_{\pi\pi}^{\text{trk}}$  represents the double-pion pattern recognition efficiency (refer to Section 5.2). The numerical ingredients entering into the calculation of Equation 6.2 are listed in Table 6.2.

### 6.3 Branching-Fraction Ratio Results

The results for the ratios of the four  $B$ -meson final states are presented in Table 6.3. Where appropriate, the  $\psi(2S) \rightarrow \mu^+ \mu^-$  and  $\psi(2S) \rightarrow J/\psi \pi^+ \pi^-$  contributions were consolidated to produce single measurements using approaches similar to that of the sample calculation in Section 6.2. In ratios that contained unlike species of  $B$  meson in the numerator and denominator, the equality  $f_u = f_d$  was assumed (refer to Section 1.3). It is interesting to note from Table 6.3 that  $R_{J/\psi K^+}^{\psi(2S) K^+} \sim R_{J/\psi K^*(892)^0}^{\psi(2S) K^*(892)^0}$ , which suggests that the flavour of the light spectator quark (refer to Figure 1.3) has little effect on the decay width.

Figure 6.5 compares the measured branching-fraction ratios with predictions derived using two different factorization approaches. As discussed in Section 1.2.3, several factors divide out of the theoretical expressions for the decay-rate ratios, including the CKM elements and the parameter  $a_2$  in Equation 1.15. The Neubert *et al.* [138] predictions used the same form factors as BSW [73, 74], which were calculated using a relativistic harmonic oscillator potential model; however, whereas the BSW form factors were given a single-pole dependence on  $q^2$  in References [73, 74], the Neubert *et al.* [138] predictions were based on most of the form factors having a dipole behaviour. As mentioned in Section 1.2.4, the

Quantity	Value
$N(B^+ \rightarrow \psi(2S) K^+, \psi(2S) \rightarrow \mu^+ \mu^-)$	$71.9 \pm 13.4$
$N(B^+ \rightarrow \psi(2S) K^+, \psi(2S) \rightarrow J/\psi \pi^+ \pi^-)$	$37.4 \pm 7.4$
$N(B^0 \rightarrow J/\psi K^*(892)^0, J/\psi \rightarrow \mu^+ \mu^-)$	$378.8 \pm 24.8$
$\frac{\mathcal{A}(B^+ \rightarrow \psi(2S) K^+, \psi(2S) \rightarrow \mu^+ \mu^-)}{\mathcal{A}(B^0 \rightarrow J/\psi K^*(892)^0)}$	$2.810 \pm 0.068$
$\frac{\mathcal{A}(B^+ \rightarrow \psi(2S) K^+, \psi(2S) \rightarrow J/\psi \pi^+ \pi^-)}{\mathcal{A}(B^0 \rightarrow J/\psi K^*(892)^0)}$	$0.813 \pm 0.025$
$\varepsilon^{c\tau}(B^+ \rightarrow \psi(2S) K^+, \psi(2S) \rightarrow \mu^+ \mu^-)$	$0.738 \pm 0.013$
$\varepsilon^{c\tau}(B^+ \rightarrow \psi(2S) K^+, \psi(2S) \rightarrow J/\psi \pi^+ \pi^-)$	$0.762 \pm 0.012$
$\varepsilon^{c\tau}(B^0 \rightarrow J/\psi K^*(892)^0)$	$0.755 \pm .013$
$\varepsilon_{\pi}^{\text{trk}}$	$0.928 \pm 0.020$
$\varepsilon_{\pi\pi}^{\text{trk}}$	$0.881 \pm 0.043$
$\varepsilon_{\pi\pi}^{\text{v}}$	$0.834 \pm 0.039$
$\varepsilon_{\pi\pi}^{\text{m}}$	$0.945 \pm 0.031$
$\mathcal{B}(\psi(2S) \rightarrow \mu^+ \mu^-)$	$(8.5 \pm 0.7) \times 10^{-3}$
$\mathcal{B}(\psi(2S) \rightarrow J/\psi \pi^+ \pi^-)$	$(3.07 \pm 0.19) \times 10^{-1}$
$\mathcal{B}(J/\psi \rightarrow \mu^+ \mu^-)$	$(6.01 \pm 0.19) \times 10^{-2}$
$\mathcal{B}(K^*(892)^0 \rightarrow K^+ \pi^-)$	$2/3$
$b$ -Quark Production Spectrum Systematics	5.9%, 5.0%
Trigger Systematics	7.0%, 2.0%
Helicity Systematic	2.0%
Simulation Systematic	3.0%
Fitting Procedure Systematic	4.0%
Global $CL(\chi^2)$ Systematic	2.0%

Table 6.2: Summary of event yields, geometric and kinematic acceptances, efficiencies, daughter-meson branching fractions, and systematic uncertainties used in the sample calculation of  $R_{J/\psi K^*(892)^0}^{\psi(2S) K^+}$  by way of Equation 6.2.

Branching-Fraction Ratio	Measurement
$R_{J/\psi K^+}^{J/\psi K^*(892)^0}$	$1.76 \pm 0.14[\text{stat}] \pm 0.15[\text{syst}]$
$R_{J/\psi K^+}^{\psi(2S) K^+}$	$0.558 \pm 0.082[\text{stat}] \pm 0.056[\text{syst}]$
$R_{J/\psi K^+}^{\psi(2S) K^*(892)^0}$	$0.908 \pm 0.194[\text{stat}] \pm 0.100[\text{syst}]$
$R_{J/\psi K^*(892)^0}^{\psi(2S) K^+}$	$0.317 \pm 0.049[\text{stat}] \pm 0.036[\text{syst}]$
$R_{J/\psi K^*(892)^0}^{\psi(2S) K^*(892)^0}$	$0.515 \pm 0.113[\text{stat}] \pm 0.052[\text{syst}]$
$R_{\psi(2S) K^+}^{\psi(2S) K^*(892)^0}$	$1.62 \pm 0.41[\text{stat}] \pm 0.19[\text{syst}]$

Table 6.3: The branching-fraction ratios measured for the various  $B$ -meson final states, corresponding to the elements of Table 1.3. Note that the ratios containing  $\psi(2S)$  mesons are composed of contributions from two separate  $B$ -meson reconstructions. The first uncertainties are statistical and the second are systematic.

Deandrea *et al.* [81] predictions employed monopole form factors that were derived from  $D$ -meson decay measurements.

Inspection of Figure 6.5 indicates that neither of the two phenomenological approaches is discounted by the data. The agreement between prediction and data, however, is favoured somewhat in the Neubert *et al.* [138] case, for which all but one of the predictions are consistent with the measured ratios to within one standard deviation. The Deandrea *et al.* [81] predictions are only consistent within one standard deviation of the measured values for the last two ratios in Figure 6.5; in the first four entries, the Deandrea *et al.* predictions agree with the data within two standard deviations. Note that Deandrea *et al.* predict a somewhat lower  $B^+ \rightarrow \psi(2S) K^+$  rate, which accounts for much of the observed difference.

Although the consistency between data and prediction in Figure 6.5 does not constitute proof for the validity of the factorization *Ansatz* in colour-suppressed  $B$ -meson decays, the data do appear to favour the approach where the majority of the form factors have a dipole dependence in  $q^2$  and where semileptonic  $D$ -meson measurements were not used to estimate the heavy-to-light form factors.

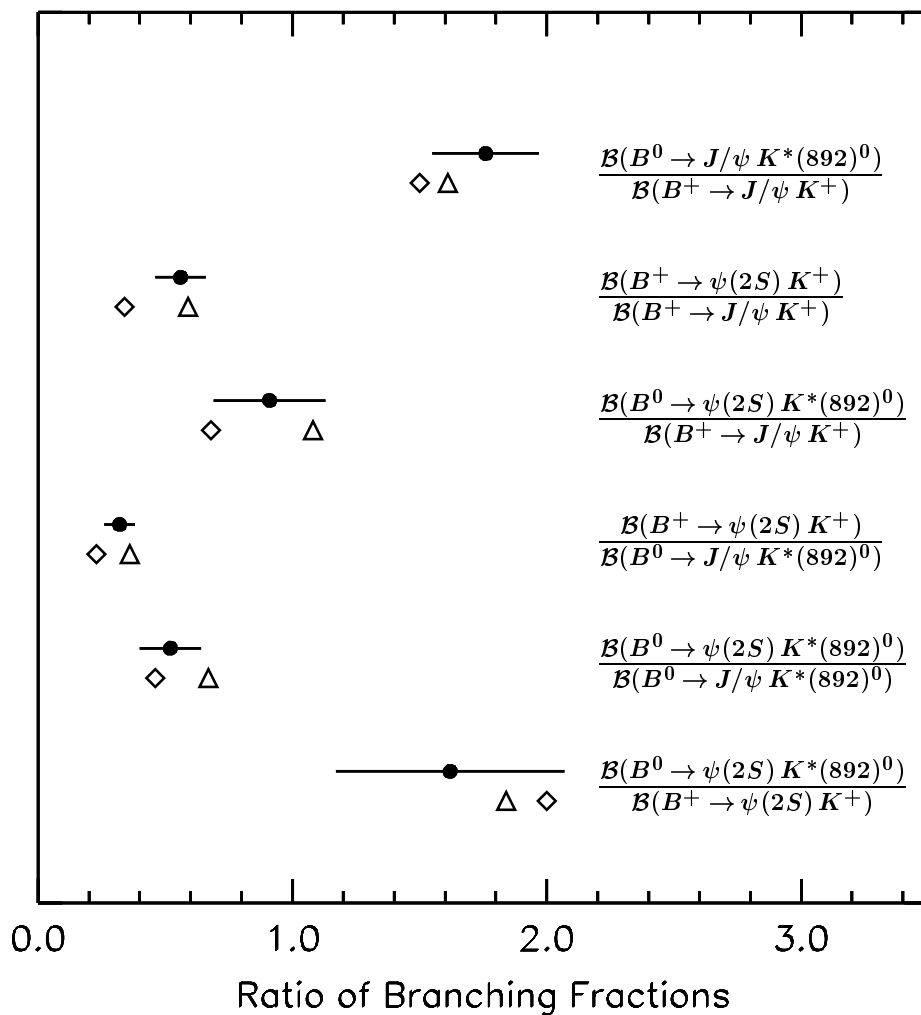


Figure 6.5: Comparison of the measured branching-fraction ratios (filled circles) with theoretical predictions by Neubert *et al.* [138] (triangles) and Deandrea *et al.* [81] (diamonds). The CDF measurements were taken from Table 6.3, with the statistical and systematic uncertainties combined in quadrature. In ratios involving both  $B^+$  and  $B^0$  mesons,  $f_u = f_d$  was assumed.

## 6.4 Derived Absolute Branching-Fraction Results

The measured ratios of branching fractions listed in Table 6.3 were used to extract absolute branching fractions for three of the four final states by employing the world average value for  $\mathcal{B}(B^+ \rightarrow J/\psi K^+)$ , which is the best measured quantity<sup>2</sup>. The technique of normalizing to a single world-average branching fraction was adopted in the present study for several reasons: a weighted-mean approach would have required a more complicated method of combining correlated systematic uncertainties, the world-average values for those modes other than  $B^+ \rightarrow J/\psi K^+$  had comparatively large uncertainties, no previous measurements using the CDF data sample were used in the determination of the world average value of  $\mathcal{B}(B^+ \rightarrow J/\psi K^+)$ , and the extracted absolute branching-fraction results derived using a single world-average normalization could be updated easily with subsequent improvements to the world-average value of  $\mathcal{B}(B^+ \rightarrow J/\psi K^+)$ .

The world-average value [30]

$$\mathcal{B}(B^+ \rightarrow J/\psi K^+) = (1.01 \pm 0.14) \times 10^{-3} \quad (6.3)$$

was therefore used with the first three entries in Table 6.3 to compute the derived absolute branching fractions listed in Table 6.4. The calculations of the ‘branching fraction’ uncertainties for the two modes involving  $\psi(2S)$  daughters assumed that the world-average charmonium branching-fraction uncertainties were independent of the uncertainty in Equation 6.3; this was the most conservative assumption.

The derived absolute branching fractions for the decays  $B^+ \rightarrow \psi(2S) K^+$  and  $B^0 \rightarrow \psi(2S) K^*(892)^0$  are compared with measurements and limits from  $e^+ e^-$  colliders in Figure 6.6. These results are the world’s most precise measurements of these branching fractions. In the case of the mode  $B^+ \rightarrow \psi(2S) K^+$ , the result from the present study is consistent within one standard deviation of the measurement reported by the CLEO II collaboration[139], but is only marginally consistent with the measurement reported by the ARGUS collaboration [140]. For the  $B^0 \rightarrow \psi(2S) K^*(892)^0$  channel, the CDF result is seen to be consistent with the previous measurement and limits<sup>3</sup>.

---

<sup>2</sup>The structure of the matrix in Table 1.3, however, suggested that an alternate approach could have been effected by performing weighted averages of multiple ratio measurements and normalizing to world-average values for the modes other than the one for which an absolute value was to be derived. This approach was



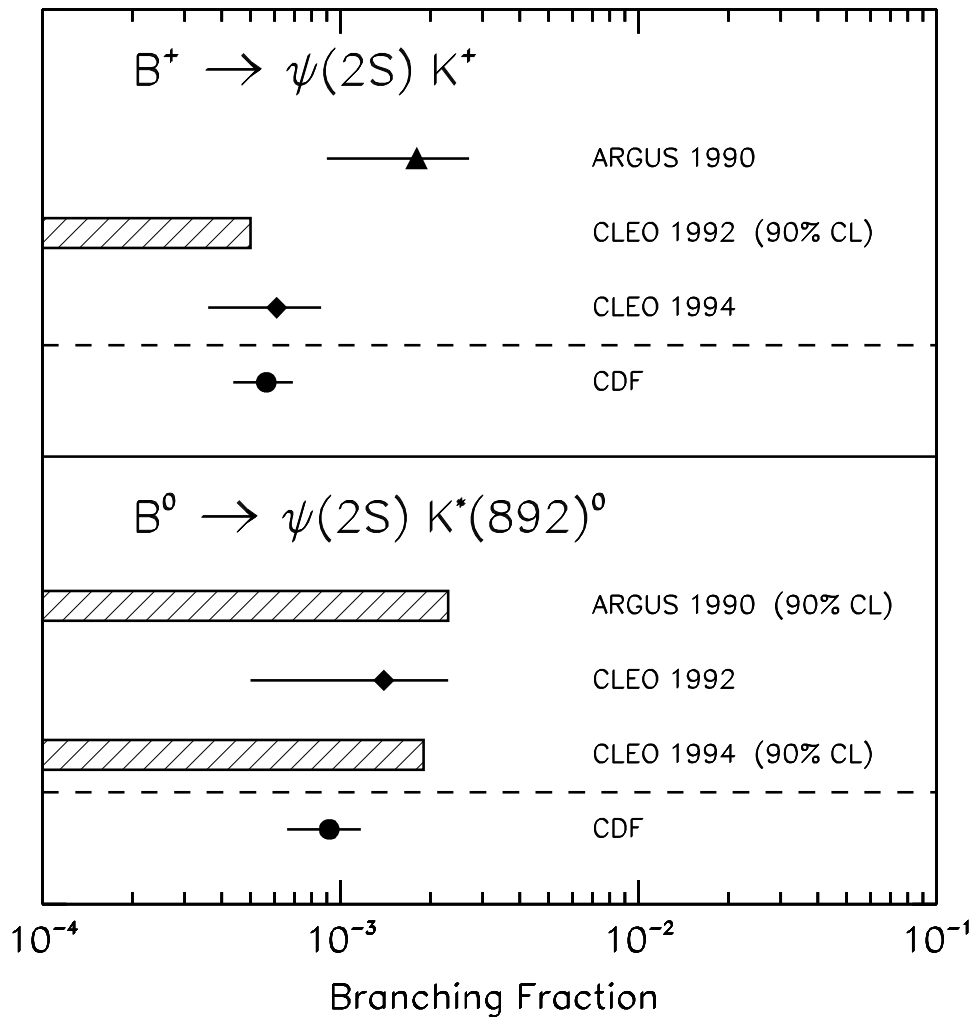


Figure 6.6: A comparison of the derived CDF  $\mathcal{B}(B^+ \rightarrow \psi(2S) K^+)$  and  $\mathcal{B}(B^0 \rightarrow \psi(2S) K^*(892)^0)$  absolute branching fractions with measurements and limits from the ARGUS [140], CLEO [142], and CLEO II [139] experiments. The hatched bars denote 90% CL upper limits and the error bars represent the statistical, systematic, and branching-fraction uncertainties added in quadrature.

Branching Fraction ( $\mathcal{B}$ )	CDF Measurement [ $\times 10^{-3}$ ]	PDG [ $\times 10^{-3}$ ]
$B^0 \rightarrow J/\psi K^*(892)^0$	$1.78 \pm 0.14[\text{stat}] \pm 0.29[\text{syst}]$	$1.49 \pm 0.22$
$B^+ \rightarrow \psi(2S) K^+$	$0.56 \pm 0.08[\text{stat}] \pm 0.10[\text{syst}]$	$0.69 \pm 0.31$
$B^0 \rightarrow \psi(2S) K^*(892)^0$	$0.92 \pm 0.20[\text{stat}] \pm 0.16[\text{syst}]$	$1.4 \pm 0.9$

Table 6.4: The derived CDF absolute branching fractions calculated by relating the entries in Table 6.3 to the world-average value in Equation 6.3. The first uncertainties are statistical and the second are systematic (including the uncertainty in Equation 6.3 and, if applicable, the uncertainties in the world-average values of the charmonium branching fractions [30]). The right column lists the previous world-average values compiled by the Particle Data Group (PDG) [30].

The derived absolute  $B \rightarrow \psi(2S)$  branching fractions may also be compared against the predictions detailed in Table 1.2, as is illustrated in Figure 6.7. Whereas the less recent Deshpande and Trampetic [71] predictions do not lie within one standard deviation of the measured CDF values, the Deandrea *et al.* [81] and Cheng *et al.* [86] predictions are consistent with the measurements. The general agreement amongst the measurements and predictions in Figure 6.7 is relatively good in spite of the large model dependencies and uncertainties in the predicted values.

---

taken in References [93, 121].

<sup>3</sup>The reversion of the CLEO result from a measurement to a limit (refer to Figure 6.6) has been attributed to statistical effects [141].

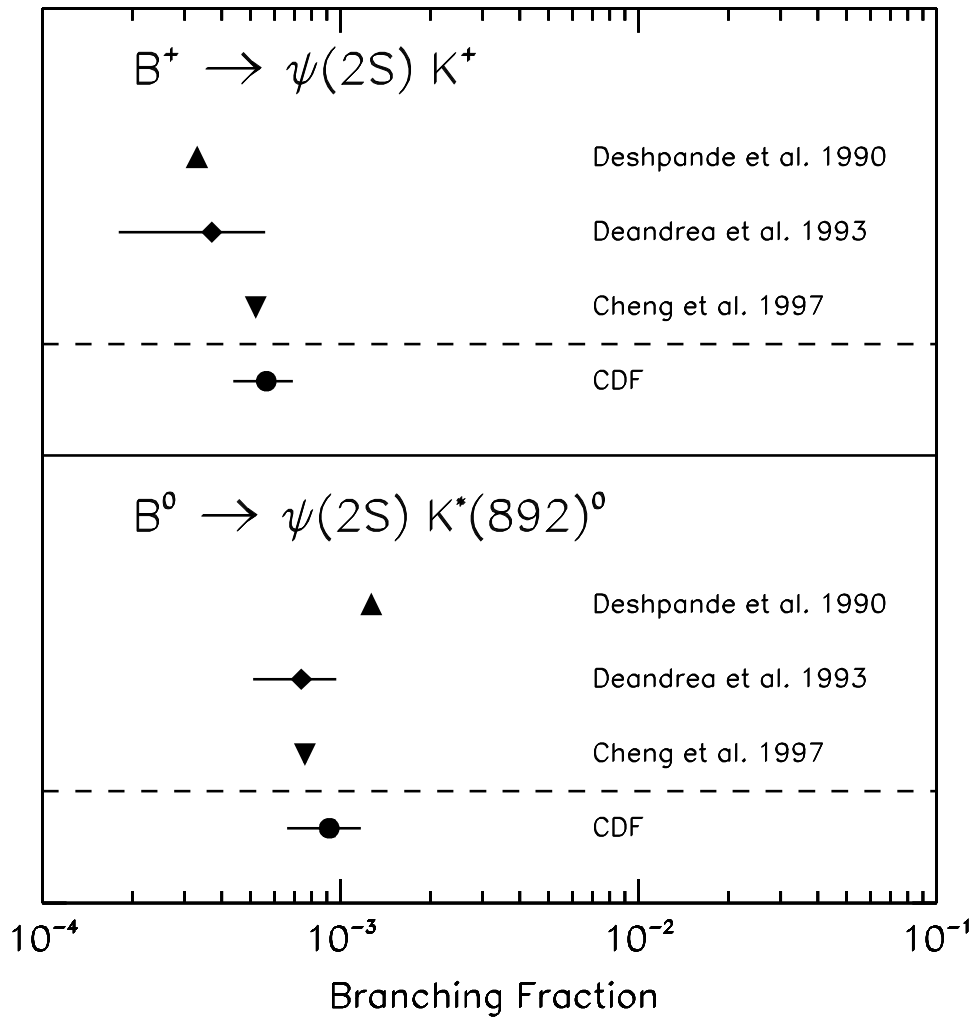


Figure 6.7: A comparison of the derived CDF  $\mathcal{B}(B^+ \rightarrow \psi(2S) K^+)$  and  $\mathcal{B}(B^0 \rightarrow \psi(2S) K^*(892)^0)$  absolute branching fractions with theoretical predictions due to Deshpande and Trampetic [71], Deandrea *et al.* [81], and Cheng *et al.* [86]. The error bars in the Deandrea *et al.* results represent only the uncertainties on the experimental inputs to their form factor estimations.

## Chapter 7

# Conclusions

Exclusive nonleptonic decays of  $B$  mesons into strange mesons and  $J/\psi$  or  $\psi(2S)$  mesons were studied using the CDF detector to observe a sample corresponding to  $\int \mathcal{L} dt = (109 \pm 7) \text{ pb}^{-1}$  of 1.8-TeV proton-antiproton collisions produced by the Fermilab Tevatron collider. The investigated decays were

$$B^+ \rightarrow J/\psi K^+$$

$$B^0 \rightarrow J/\psi K^*(892)^0$$

$$B^+ \rightarrow \psi(2S) K^+$$

$$B^0 \rightarrow \psi(2S) K^*(892)^0,$$

which were reconstructed via the daughter meson decay modes

$$J/\psi \rightarrow \mu^+ \mu^-$$

$$\psi(2S) \rightarrow \mu^+ \mu^-$$

$$\psi(2S) \rightarrow J/\psi \pi^+ \pi^-$$

$$K^*(892)^0 \rightarrow K^+ \pi^-.$$

With statistical significances of  $\sim 5$  and  $\sim 3$  standard deviations, respectively, the observations of the decay modes  $B^+ \rightarrow \psi(2S) K^+$  and  $B^0 \rightarrow \psi(2S) K^*(892)^0$  constituted the first measurements of these processes in a hadron collider environment and amounted to the world's largest recorded sample of these decays.

## 7.1 Branching Fraction Measurements

Several similarities between the decay modes were exploited to make possible the precise measurement of the relative branching fractions between the  $B$ -meson decay modes studied. The calculated relative geometric and kinematic acceptances, measured efficiency corrections, observed yields, world-average daughter-meson branching fractions, and systematic uncertainties were used to compute the ratios of branching fractions. For ratios that involved both  $B^+$  and  $B^0$  mesons, equal production rates were assumed for both meson types. The measured ratios are

$$\frac{\mathcal{B}(B^0 \rightarrow J/\psi K^*(892)^0)}{\mathcal{B}(B^+ \rightarrow J/\psi K^+)} = 1.76 \pm 0.14[\text{stat}] \pm 0.15[\text{syst}] \quad (7.1)$$

$$\frac{\mathcal{B}(B^+ \rightarrow \psi(2S) K^+)}{\mathcal{B}(B^+ \rightarrow J/\psi K^+)} = 0.558 \pm 0.082[\text{stat}] \pm 0.056[\text{syst}] \quad (7.2)$$

$$\frac{\mathcal{B}(B^0 \rightarrow \psi(2S) K^*(892)^0)}{\mathcal{B}(B^+ \rightarrow J/\psi K^+)} = 0.908 \pm 0.194[\text{stat}] \pm 0.100[\text{syst}] \quad (7.3)$$

$$\frac{\mathcal{B}(B^+ \rightarrow \psi(2S) K^+)}{\mathcal{B}(B^0 \rightarrow J/\psi K^*(892)^0)} = 0.317 \pm 0.049[\text{stat}] \pm 0.036[\text{syst}] \quad (7.4)$$

$$\frac{\mathcal{B}(B^0 \rightarrow \psi(2S) K^*(892)^0)}{\mathcal{B}(B^0 \rightarrow J/\psi K^*(892)^0)} = 0.515 \pm 0.113[\text{stat}] \pm 0.052[\text{syst}] \quad (7.5)$$

$$\frac{\mathcal{B}(B^0 \rightarrow \psi(2S) K^*(892)^0)}{\mathcal{B}(B^+ \rightarrow \psi(2S) K^+)} = 1.62 \pm 0.41[\text{stat}] \pm 0.19[\text{syst}], \quad (7.6)$$

where the first uncertainties are statistical and the second are systematic.

The branching-fraction ratio measurements were compared with two different sets of theoretical predictions that each employed the factorization *Ansatz*, but that used form factors derived in different ways with different parameterizations in  $q^2$ . All of the predictions were consistent with the measured ratios to within two standard deviations, thereby supporting, but not proving, the applicability of the factorization *Ansatz* to colour-suppressed  $B \rightarrow \psi K$  decays.

Of the two sets of predictions, one was consistent with the measurements to within

one standard deviation for all but one of the six branching-fraction ratios. This set of predictions, due to Neubert *et al.* [138], assumed a dipole behaviour for the majority of the form factors, which were calculated from solutions to a relativistic harmonic oscillator potential model [73, 74]. The somewhat less-favoured set of predictions assumed single-pole form factors that were estimated from measurements of semileptonic  $D$ -meson (heavy-to-light) decays [81].

Relative branching-fraction measurements were combined with the world-average branching fraction for the decay  $B^+ \rightarrow J/\psi K^+$  [30],  $(1.01 \pm 0.14) \times 10^{-3}$ , to extract the following absolute branching fractions:

$$\mathcal{B}(B^0 \rightarrow J/\psi K^*(892)^0) = (1.78 \pm 0.14[\text{stat}] \pm 0.29[\text{syst}]) \times 10^{-3}$$

$$\mathcal{B}(B^+ \rightarrow \psi(2S) K^+) = (0.56 \pm 0.08[\text{stat}] \pm 0.10[\text{syst}]) \times 10^{-3}$$

$$\mathcal{B}(B^0 \rightarrow \psi(2S) K^*(892)^0) = (0.92 \pm 0.20[\text{stat}] \pm 0.16[\text{syst}]) \times 10^{-3},$$

where the first uncertainties are statistical and the second are systematic. The derived absolute branching fractions for the two  $B$ -meson decays to  $\psi(2S)$  final states were shown to be consistent with both recent measurements and limits at  $e^+e^-$  colliders and recent phenomenological predictions.

The branching-fraction measurements reported here are consistent with the world-average values compiled by the Particle Data Group [30] (refer to Table 6.4). The measured branching fractions that involve  $\psi(2S)$  final states constitute the world's most precise measurements of these quantities.

## 7.2 Future Prospects

Using the same data sample as that described in the present study, measurements of several other similar exclusive  $B$ -meson decay processes are feasible. These processes include the analogous decays  $B^0 \rightarrow J/\psi K^0$ ,  $B^0 \rightarrow \psi(2S) K^0$ ,  $B^+ \rightarrow J/\psi K^*(892)^+$ , and  $B^+ \rightarrow \psi(2S) K^*(892)^+$ , which, when combined with the results of the present work, could yield a measurement of the ratio of fragmentation fractions,  $f_u/f_d$ . Decays of the  $B_s^0$  meson into  $c\bar{c}$  final states,  $B_s^0 \rightarrow J/\psi \phi(1020)$  and  $B_s^0 \rightarrow \psi(2S) \phi(1020)$ , also have similar topologies and reconstruction techniques. Relative branching fractions of some of these modes were

reported for Run 1A data [143, 93]. Other recent work [128] also used the Run 1A data set to measure the longitudinal polarization fractions in the decays  $B^0 \rightarrow J/\psi K^*(892)^0$  and  $B_s^0 \rightarrow J/\psi \phi(1020)$ , a study that can be extended to use the full Run 1 sample and to measure  $\Gamma_L/\Gamma$  for the other vector-vector decays mentioned above. In particular, improved measurements of the quantity  $\frac{\Gamma_L}{\Gamma}(B^0 \rightarrow J/\psi K^*(892)^0)$  are needed for comparison with measurements from  $e^+e^-$  colliders [30, 144]. Finally, the large samples of  $\psi(2S) \rightarrow J/\psi \pi^+ \pi^-$  and  $\psi(2S) \rightarrow \mu^+ \mu^-$  decays in Run 1 (refer to Chapter 5) could be used to measure the relative branching fraction between the two charmonium modes, thereby reducing the total systematic uncertainty of the  $B$ -meson results reported in this dissertation.

The Fermilab Tevatron is currently being upgraded with a ‘Main Injector’ to operate at a centre-of-mass energy of  $\sqrt{s} = 2.0$  TeV with instantaneous luminosities of up to  $2 \times 10^{32} \text{ cm}^{-2}\text{s}^{-1}$ . Scheduled to begin in 1999, the next run of the Tevatron (Run 2) is expected to accumulate a data sample with time-integrated luminosity  $\int \mathcal{L} dt = 2 \text{ fb}^{-1}$ , a twenty-fold increase over that for the sample used in this study. Commensurate with the improvements to the Tevatron, the CDF detector is being rebuilt into the upgraded ‘CDF II’ detector [145]. The tracking systems will have redesigned and integrated silicon and drift-chamber detectors with improvements in the combined pattern recognition, momentum resolution, and pseudorapidity coverage. The muon systems will be extended to cover nearly all angles in azimuth and pseudorapidities in the range  $|\eta| \leq 2.0$ . The data acquisition system is expected to handle 132-ns bunch crossings, and the trigger will have no dead time with the added improvements of tracking information at Level 1, impact parameter discrimination at Level 2, and 300-Hz operation at Level 3. The CDF II and Tevatron upgrades are expected to augment significantly both the scope and reach of inquiry into the properties and interactions of the bottom quark well into the next millennium.

# Appendix A

## Level 2 Dimuon Triggers

This appendix describes the Level 2 dimuon triggers that were used to construct the data samples studied for this analysis. Refer to Section 2.5.2 for a description of the Level 2 system. For each Level 2 trigger, the associated Level 1 prerequisite dimuon trigger is given. A description of the Run 1A and Run 1B running periods is given in Section 3.1.

### A.1 Run 1A Level 2 Dimuon Triggers

1. `TWO_CMU_ONE_CFT`: Two CMU Level 2 muon clusters are necessary, with one of the clusters required to match a CFT track. The Level 1 prerequisite trigger is `TWO_CMU_3PT3`. This trigger is dynamically prescaled.
2. `CMX_ONE_CMU_CFT`: One CMX Level 2 muon cluster and one CMU Level 2 muon cluster are necessary, with the CMU cluster required to match a CFT track. The Level 1 prerequisite trigger is `TWO_CMU_CMX_3PT3`. This trigger is dynamically prescaled.
3. `CMU_OR_CMX_ONE_CMX_CFT`: Either two CMX Level 2 muon clusters or both a CMU cluster and a CMX cluster are necessary, with a CMX cluster required to match a CFT track. The Level 1 prerequisite trigger is `TWO_CMU_CMX_3PT3`. This trigger is dynamically prescaled.

### A.2 Run 1B Level 2 Dimuon Triggers

1. `TWO_CMU_TWO_CFT`: Two CMU Level 2 muon clusters are necessary, with each cluster required to match a CFT track. The Level 1 prerequisite trigger is `TWO_CMU_3PT3`.



This trigger is not prescaled, and the two muon clusters are required to be in non-contiguous modules. If one cluster is in the  $+z$  region of the CDF detector and the other cluster is in the  $-z$  region, then the two clusters are required to have different  $\varphi$  values.

2. `CMX_CMU_TWO_CFT`: One CMU Level 2 muon cluster and one CMX Level 2 muon cluster are necessary, with each cluster required to match a CFT track. The Level 1 prerequisite trigger is `TWO_CMU_CMX_3PT3`. This trigger is dynamically prescaled.
3. `TWO_CMX_TWO_CFT`: Two CMX Level 2 muon clusters are necessary, with each cluster required to match a CFT track. The Level 1 prerequisite trigger is `TWO_CMU_CMX_3PT3`. This trigger is dynamically prescaled, and, if both CMX muon clusters are in the same hemisphere (in  $z$ ) of the CDF detector, then they are required to be separated by at least one wedge.
4. `TWO_CMU_ONE_CFT_6TOW`: Two adjacent CMU Level 2 muon stubs, which together form a single cluster that spans six or more calorimeter trigger towers, are necessary. The single cluster is required to match a CFT track, and the Level 1 prerequisite trigger is `TWO_CMU_3PT3`. This trigger is dynamically prescaled and is intended to offset losses due to the discontinuities imposed in the `TWO_CMU_TWO_CFT` trigger.

## Appendix B

# CDF Track Characterization

This appendix introduces the mathematical formulation [122, 146], adapted for use in the present study, that describes helical trajectories of charged particles in the CDF detector. Five parameters are used to define a track's helix: the curvature,  $c$ ; the azimuthal angle,  $\varphi_0$ , at the point of closest approach to  $(x, y) = (0, 0)$ ; the cotangent of the polar angle,  $\cot \theta$ ; the impact parameter with respect to  $(x, y) = (0, 0)$ ,  $d_0$ ; and the local  $z$  coordinate with respect to  $(x, y) = (0, 0)$ ,  $z_0$ . In Section B.1, the global coordinates of a particle's trajectory are derived from the track helical parameters; in Section B.2, a method to derive the track helix using only point-of-origin and momentum information is outlined.

### B.1 Global Coordinates from the Track Helix

The curvature of a track is defined as

$$c \equiv \frac{Q}{2r_0}, \quad (\text{B.1})$$

where  $r_0$  is the radius of curvature and  $Q$  denotes the sign of the electric charge of the particle. It is assumed here that  $|Q| = 1$ .

In order to determine the global coordinates of a track in the CDF detector, the azimuthal deflection of the particle's momentum,  $\Delta\varphi$ , is defined as

$$\Delta\varphi \equiv \frac{sQ}{r_0}, \quad (\text{B.2})$$

where  $s$  is the arc length of the helix, projected onto the transverse  $(x, y)$  plane. By substitution of Equation B.1 into Equation B.2, the global azimuthal angle,  $\varphi$ , is defined in

radians as

$$\varphi \equiv (\Delta\varphi + \varphi_0) \bmod 2\pi = (2cs + \varphi_0) \bmod 2\pi. \quad (\text{B.3})$$

If the coordinates  $(x_0, y_0)$  define the transverse location of the centre of the track helix, then the global transverse coordinates of the helix are

$$\begin{aligned} x &= x_0 + r_0 Q \sin \varphi \\ y &= y_0 - r_0 Q \cos \varphi. \end{aligned} \quad (\text{B.4})$$

The same form as that in Equation B.4 may be used to calculate the coordinates of the point in the track trajectory that is nearest, in the transverse plane, to the geometric centre of the detector,  $(x', y')$ :

$$\begin{aligned} x' &= x_0 + r_0 Q \sin \varphi_0 \\ y' &= y_0 - r_0 Q \cos \varphi_0. \end{aligned} \quad (\text{B.5})$$

Since the magnitude of the impact parameter,  $|d_0|$ , is defined as  $|d_0| \equiv \left| \sqrt{x_0^2 + y_0^2} - r_0 \right|$ , and its sign is defined as

$$\frac{d_0}{|d_0|} \equiv \frac{Q \left( \sqrt{x_0^2 + y_0^2} - r_0 \right)}{\left| \sqrt{x_0^2 + y_0^2} - r_0 \right|}, \quad (\text{B.6})$$

the coordinates  $(x', y')$  may also be written as

$$\begin{aligned} x' &= -d_0 \sin \varphi_0 \\ y' &= d_0 \cos \varphi_0. \end{aligned} \quad (\text{B.7})$$

Solving for  $(x_0, y_0)$  in Equations B.5 and B.7 yields

$$\begin{aligned} x_0 &= -(r_0 Q + d_0) \sin \varphi_0 \\ y_0 &= (r_0 Q + d_0) \cos \varphi_0. \end{aligned} \quad (\text{B.8})$$

Substitution of Equation B.8 into Equation B.4, and translation of the  $z_0$  helix parameter into its analogous global coordinate, furnishes the following expressions for a track's global

coordinates:

$$\begin{aligned}
 x &= r_0 Q \sin \varphi - (r_0 Q + d_0) \sin \varphi_0 \\
 y &= -r_0 Q \cos \varphi + (r_0 Q + d_0) \cos \varphi_0 \\
 z &= z_0 + s \cot \theta.
 \end{aligned}
 \tag{B.9}$$

## B.2 Helix from Momentum and Point of Origin

In studies that involved the embedding of Monte Carlo generated particle tracks into actual data events, a transformation from momentum, electric charge, and spatial-origin coordinates to local helical parameter coordinates was necessary. The transformations used, as well as any assumptions made, are detailed in the following.

The curvature parameter was calculated with the formula

$$c = \frac{(1.49898 \times 10^{-3}) Q B}{p_T}, \tag{B.10}$$

where  $B$  is the magnetic field in units of Tesla and  $p_T$  is the transverse momentum,  $p_T \equiv |\vec{p}| \sin \theta$ , in units of GeV/ $c$ .

The azimuth parameter was determined with the expression

$$\varphi_0 = \begin{cases} \arccos\left(\frac{p_x}{p_T}\right) & \text{if } p_y > 0 \\ 2\pi - \arccos\left(\frac{p_x}{p_T}\right) & \text{if } p_y \leq 0 \end{cases}, \tag{B.11}$$

where  $p_x$  and  $p_y$  are the  $x$  and  $y$  components of the momentum vector, respectively, and an approximation<sup>1</sup> that  $\varphi_0 = \varphi$  is assumed.

The cotangent of the polar angle was simply computed using

$$\cot \theta = \frac{p_z}{p_T}, \tag{B.12}$$

where  $p_z$  is the  $z$  component of the momentum vector.

The calculation of the impact parameter,  $d_0$ , required care to avoid a numerical instability. The impact parameter may be defined as

$$d_0 \equiv Q(\xi - r_0), \tag{B.13}$$

---

<sup>1</sup>The stated approximation is justified in track embedding studies where only a subset of the Monte Carlo tracks generated for a given event is considered and there is therefore no need to preserve the precise kinematics of the parent particle.

where  $\xi \equiv \sqrt{x_0^2 + y_0^2}$ . In practice, Equation B.13 is difficult to calculate since  $|d_0| \ll \xi$ . This was remedied by rewriting Equation B.13 in the form [146]

$$d_0 = Q(\xi - r_0) = \frac{Q(\xi - r_0)(\xi + r_0)/r_0}{(\xi + r_0)/r_0}. \quad (\text{B.14})$$

The coordinates  $(x'', y'')$  were defined to represent the displacement of the track's point of origin. A substitution of an analogous form of Equation B.4 was made to convert Equation B.14 to the form

$$d_0 = \frac{Q[(x'')^2 + (y'')^2] + 2r_0[y'' \cos \varphi_0 - x'' \sin \varphi_0]}{r_0 + \sqrt{(x'' - r_0 Q \sin \varphi_0)^2 + (y'' + r_0 Q \cos \varphi_0)^2}}. \quad (\text{B.15})$$

Further substitution using Equation B.1 yielded the practical form

$$d_0 = \frac{2c[(x'')^2 + (y'')^2] + 2[y'' \cos \varphi_0 - x'' \sin \varphi_0]}{1 + 2cQ\sqrt{(x'' - r_0 Q \sin \varphi_0)^2 + (y'' + r_0 Q \cos \varphi_0)^2}}. \quad (\text{B.16})$$

Following the same justification as that used in the  $\varphi_0 = \varphi$  assumption in Equation B.11, the value of  $z_0$ , which according to Equation B.9 is  $z_0 = z'' - s \cot \theta$ , was approximated as

$$z_0 = z''. \quad (\text{B.17})$$

## Appendix C

# Pattern Recognition Efficiencies

This appendix summarizes a study [135] of the single- and double-track pion pattern recognition efficiencies in the CDF central tracking chamber (CTC) over the course of the Run 1 data-taking period.

### C.1 Data Sample

The sample used in this efficiency study consisted of  $\sim 36\,000$  raw dimuon events from 40 data-taking runs, 10 from Run 1A and 30 from Run 1B. The runs represented in this sample are detailed in Table C.1.

The four loose run-range bins in Table C.1 are delimited by the changeover period between Runs 1A and 1B, a major reorientation of the Tevatron beam optics, and a prolonged shutdown of the collider, respectively. The left side of Figure C.1 illustrates the instantaneous luminosity profile of  $\sim 530\,000$   $B^+ \rightarrow J/\psi K^+$  candidates, including background, and clearly features the natural divisions between the four run bins. Portrayed on the right side of Figure C.1 is the profile of the event sample used in the present efficiency study.

### C.2 Track Embedding Procedure

The crux of this study was the embedding of hits representing two Monte-Carlo-generated pions into raw data events.  $B^+$  mesons were generated in a manner similar to that described in Section 4.1. The CLEO qq programme [127] was used, as in Section 4.2, to decay the  $B^+$  mesons in the chain  $B^+ \rightarrow \psi(2S) K^+$ ,  $\psi(2S) \rightarrow J/\psi \pi^+ \pi^-$ , and  $J/\psi \rightarrow \mu^+ \mu^-$ . The dipion invariant mass distribution was generated according to the customized matrix

Experiment	Run 1A	Run 1B		
Run Range	40 100–47 835	Low 55 242–60 900	Medium 60 901–67 390	High 67 391–71 023
R	40 512	55 571	61 024	68 040
u	41 085	56 002	61 548	68 206
n	42 030	57 006	63 171	68 517
	43 016	57 513	63 502	68 758
N	44 366	58 093	64 041	69 036
u	45 047	58 564	65 004	69 550
m	46 031	59 042	65 560	69 809
b	46 519	59 517	66 020	70 019
e	47 008	60 004	66 539	70 559
r	47 552	60 597	66 615	71 013
$\int \mathcal{L} dt$ [ $\text{pb}^{-1}$ ]	20.90	9.46	47.08	35.41

Table C.1: A list of runs representing four logical run-range divisions of the Run 1 data-taking period. Each of these four divisions contributed  $\sim 9000$  events to the sample. The bottom row of the table lists the time-integrated luminosities represented by the various run-range bins.

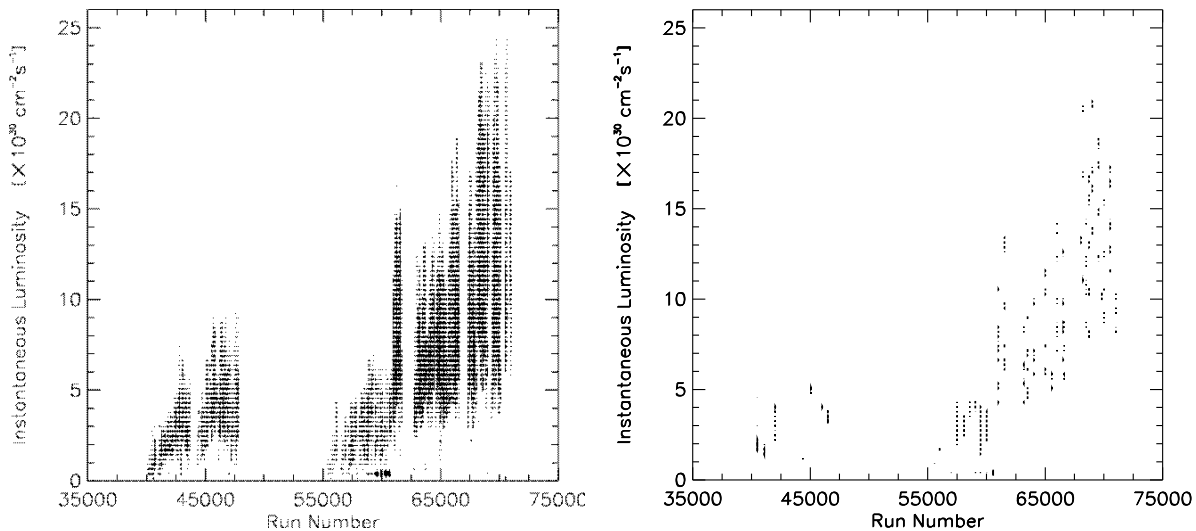


Figure C.1: Instantaneous luminosity vs. run number profile for (left)  $\sim 530\,000$   $B^+ \rightarrow J/\psi K^+$  candidates and that for (right)  $\sim 36\,000$  raw dimuon events used in the present efficiency study.

element described in Section 4.2.1. For events where the  $\pi^+$  and  $K^+$  particles each passed a  $p_T > 250$  MeV/ $c$  transverse momentum requirement, the 3-momentum and charge of the two pions in the decay chain were extracted from the CLEO QQ output and stored for use in the embedding stage.

The curvature ( $c$ ), azimuth ( $\varphi_0$ ), and polar angle ( $\cot \theta$ ) helical parameters of the tracks to be embedded were derived from the 3-momentum and charge information furnished in the Monte Carlo track generation stage. The impact ( $d_0$ ) and longitudinal displacement ( $z_0$ ) helical parameters were calculated with additional information on the primary vertex location of the particular event into which the tracks were to be embedded. Appendix B describes the method by which the track helices were determined.

Once all five helical parameters for each of the two pion tracks were known, a set of routines [147] was used to embed hits into the CTC and VTX data structures. The values of the embedded parameters were recorded for later comparisons, and the full default production executable package (described in Section 3.2) was used to reconstruct the tracks in the events.

In order to determine the wire hit efficiencies to use in the embedding software, the mean numbers of hits used by the reconstructed track fits in each CTC superlayer were examined, as functions of instantaneous luminosity, for both embedded and data tracks. Figures C.2 and C.3 show the mean numbers of hits per superlayer used in fits of tracks embedded with 100% wire hit efficiencies, as functions of instantaneous luminosity, for the axial and stereo superlayers, respectively.

The mean numbers of hits per superlayer used in the embedded track fits were tuned to match those observed in data by iteratively adjusting the superlayer-by-superlayer wire hit efficiencies in the embedding routines. Table C.2 summarizes the reduced wire efficiencies calculated using this technique.

It is evident from Figures C.2 and C.3 that there was negligible sensitivity to the charge of the embedded track. Consequently, the wire efficiencies featured in Table C.2 were applied to both positively and negatively charged tracks. Within the axial and stereo superlayer categories in Table C.2, the wire efficiencies were observed to diminish monotonically from the outer to the inner superlayers. Due to the geometry of the CTC and the  $p_T$  distribution of charged tracks [123], increased charged-track occupancies near the inner-superlayer radii



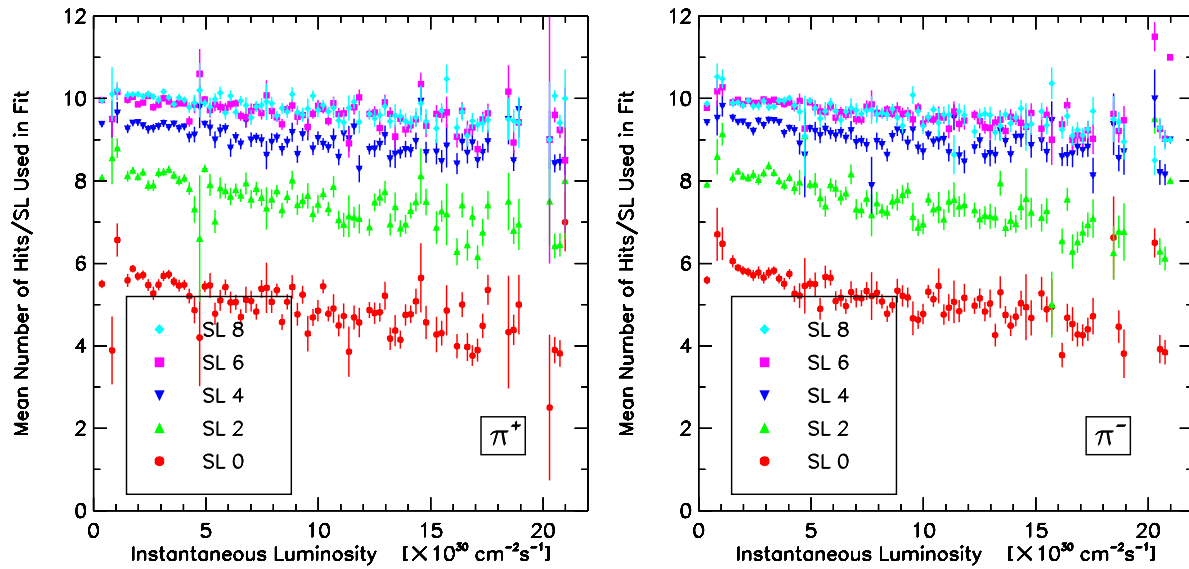


Figure C.2: The mean number of hits per axial superlayer used in fits of  $\pi^+$  (left) and  $\pi^-$  (right) tracks embedded with uniform 100% wire hit efficiencies, as a function of instantaneous luminosity.

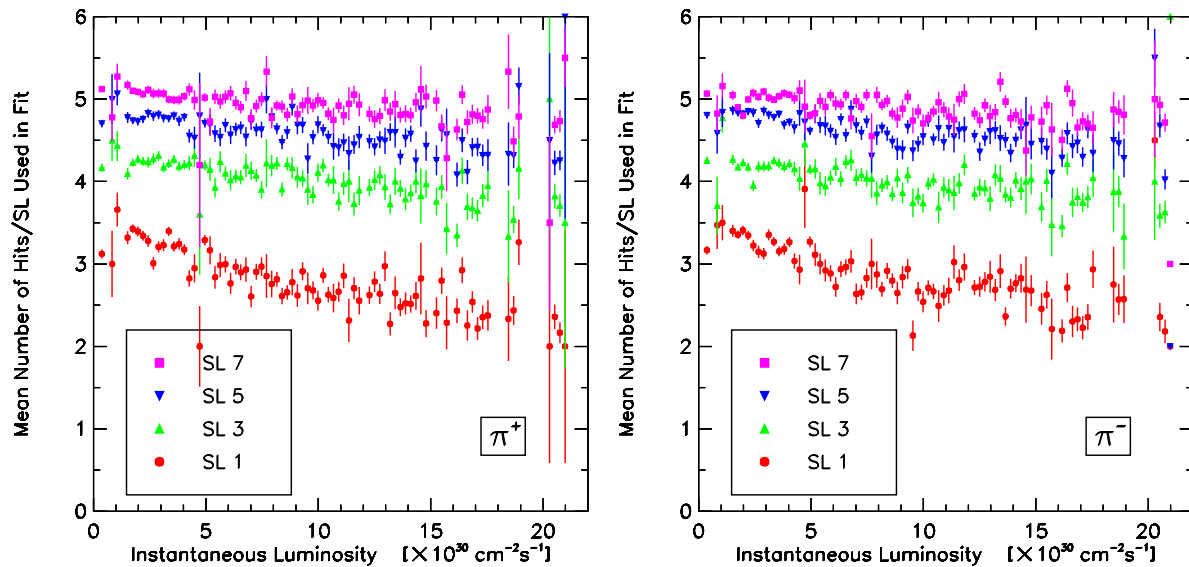


Figure C.3: The mean number of hits per stereo superlayer used in fits of  $\pi^+$  (left) and  $\pi^-$  (right) tracks embedded with uniform 100% wire hit efficiencies, as a function of instantaneous luminosity.

Axial Superlayer	Stereo Superlayer	Wire Numbers	Wire Efficiency
8		72 – 83	1.00
	7	66 – 71	0.99
6		54 – 65	1.00
	5	48 – 53	0.96
4		36 – 47	0.97
	3	30 – 35	0.89
2		18 – 29	0.80
	1	12 – 17	0.82
0		0 – 11	0.74

Table C.2: The wire efficiencies used to embed hits in the 9 CTC superlayers. These were calculated by tuning the mean number of fitted hits per superlayer to match in embedded and data samples.

accounted for the bulk of the observed relative trends in the superlayer-dependent wire efficiencies.

### C.3 Definition of a “Found” Track or Track Pair

The technique used to identify a “found” track attempted to account for interparameter correlations in the reconstructed helices. Specifically, for a given Monte Carlo track with embedded helical parameter vector  $\alpha$ , where  $\alpha_i \in (\cot \theta, c, z_0, d_0, \varphi_0)$ , each reconstructed track in the event,  $\hat{\alpha}$ , that shared the same sign of curvature with  $\alpha$ , was used to calculate a matching  $\chi^2$  quantity via the expression [30]

$$\chi^2 \equiv (\alpha - \hat{\alpha})^T \hat{V}^{-1} (\alpha - \hat{\alpha}), \quad (\text{C.1})$$

where the matrix  $\hat{V}$  was the  $5 \times 5$  covariance matrix of the reconstructed track helix. For each embedded track charge, the reconstructed track in the event that formed the lowest matching  $\chi^2$  value with the embedded track,  $\chi_{\min}^2$ , was retained for consideration as a “found” track.

There was some speculation about the relative effects of the stereo and axial contributions to inefficiencies in the CTC. Tracks were initially identified in the CTC by seeking segments in the axial superlayers and forming 2-dimensional track objects in the  $r$ - $\varphi$  view. Stereo reconstruction then took place to form 3-dimensional tracks, using the information

from the stereo superlayers and from the VTX, which provided the initial information on the  $z_0$  helix parameter of the tracks. It was therefore predicted that, under increased instantaneous luminosity conditions that precipitated higher primary vertex multiplicities in the VTX, the reliability of the  $z_0$  determination, and hence the stereo reconstruction efficiency, would suffer. Occupancy-related luminosity-dependent efficiency losses in the inner CTC superlayers were also expected to afflict the stereo more than the axial reconstruction because of the lesser number of superlayers and wires per superlayer in the stereo view (refer to Section 2.3.3 for a description of the CTC).

The foregoing considerations about axial and stereo contributions to tracking performance motivated the construction of an axial-only matching  $\chi^2$  quantity. Specifically, the vector  $\alpha$  in Equation C.1 was modified such that  $\alpha_i \in (c, d_0, \varphi_0)$  and the matrix  $\hat{V}$  became the corresponding  $3 \times 3$  track parameter covariance matrix.

In the case of 3-dimensional track matching, a reconstructed track was designated as “found” if its matching  $\chi^2$  value satisfied the criterion

$$\chi_{\min}^2 < 500.$$

The analogous criterion in the case of 2-dimensional axial-only matching was

$$\chi_{\min}^2 < 300.$$

The efficacy of these cuts in discriminating between the embedded track and other tracks in the event is exemplified in Figure C.4, which plots the minimum matching  $\chi^2$ ,  $\chi_{\min}^2$ , versus the next-to-minimum matching  $\chi^2$ ,  $\chi_{\text{next}}^2$ , for the 3-dimensional case. Figure C.4 furnishes two useful observations: first, the matching  $\chi^2$  selection criteria, indicated by the horizontal lines, were relatively efficient at determining the distinction between the found track and any other track in the event; and second, the majority of events where an embedded track was not found at all had  $\chi_{\min}^2 \sim \chi_{\text{next}}^2$ , as expected.

The  $p_T$  dependence of tracks that passed and failed the “found”-track identification criteria is pictured in Figure C.5, this time for 2-dimensional matching. These plots indicate that any inefficiencies in the  $\chi_{\min}^2$  matching criteria were largely confined to embedded tracks with extremely low  $p_T$ . These figures also suggest that the majority of embedded tracks that failed to be “found” had low  $p_T$ .

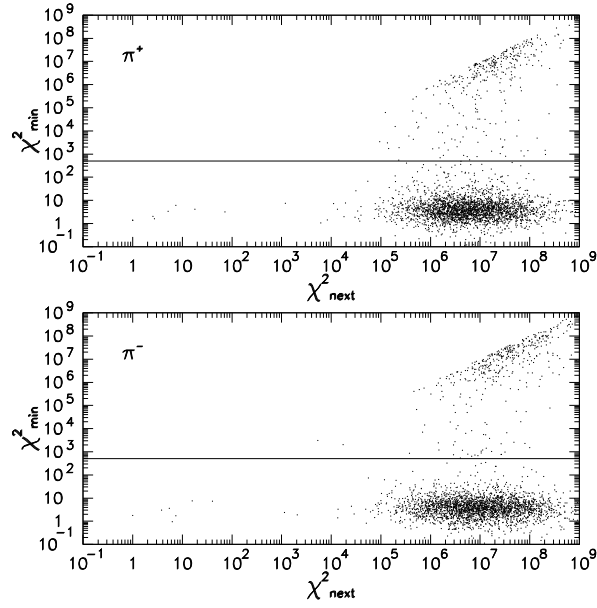


Figure C.4: The minimum 3-dimensional matching  $\chi^2$ ,  $\chi_{\min}^2$ , plotted against the 3-dimensional next-to-minimum matching  $\chi^2$ ,  $\chi_{\text{next}}^2$ , for 3 000 embedded  $\pi^+$  mesons (top) and  $\pi^-$  mesons (bottom). The horizontal line designates the selection criterion,  $\chi_{\min}^2 < 500$ .

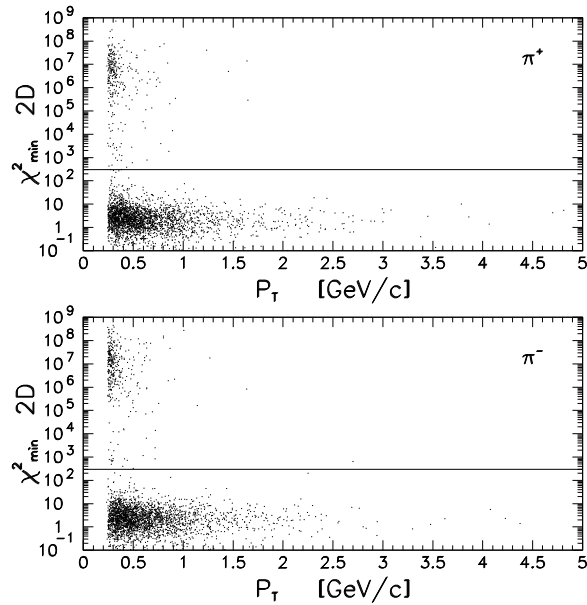


Figure C.5: The minimum 2-dimensional matching  $\chi^2$ ,  $\chi_{\min}^2$ , plotted against the embedded track transverse momentum,  $p_T$ , for 3 000 embedded  $\pi^+$  mesons (top) and  $\pi^-$  mesons (bottom). The horizontal line designates the selection criterion,  $\chi_{\min}^2 < 300$ .

The embedding of both  $\pi^+$  and  $\pi^-$  mesons into the same event enabled the determination of a “found” track pair. A track pair was considered to be “found” if, in the case of 3-dimensional track matching,

$$\max\left(\chi_{\min}^2[\pi^+], \chi_{\min}^2[\pi^-]\right) < 500$$

and, in the case of 2-dimensional track matching,

$$\max\left(\chi_{\min}^2[\pi^+], \chi_{\min}^2[\pi^-]\right) < 300.$$

## C.4 Pattern Recognition Efficiency

### C.4.1 Definition

The single- and double-track CTC pattern recognition efficiencies may be expressed as a function of one of several observables. Equation C.2 defines the bin-by-bin pattern recognition efficiency for a given bin,  $\Delta\xi$ , in an observable  $\xi$ :

$$\varepsilon(\Delta\xi) \equiv \frac{\int_{\Delta\xi} N_{\text{found}}(\xi) d\xi}{\int_{\Delta\xi} [N_{\text{found}}(\xi) + N_{\overline{\text{found}}}(\xi)] d\xi} \Bigg|_{\substack{p_T > p_T^{\min} \\ r_{\text{CTC}}^{\text{exit}} > (r_{\text{CTC}}^{\text{exit}})^{\min}}}. \quad (\text{C.2})$$

The  $N_{\text{found}}(\xi)$  symbol represents the number of tracks (or track pairs) at a given value of  $\xi$  that are identified as “found” according to the criteria discussed in Section C.3. The  $N_{\overline{\text{found}}}(\xi)$  symbol represents the corresponding “found”-track (or track pair) failures, and the quantity  $r_{\text{CTC}}^{\text{exit}}$  is the CTC exit radius, or the radius at which tracks intersect one of the two endplate planes of the CTC. Note that the  $p_T$  or  $r_{\text{CTC}}^{\text{exit}}$  requirements in Equation C.2 are not applied when  $\xi \equiv p_T$  or  $\xi \equiv r_{\text{CTC}}^{\text{exit}}$ , respectively. Also, when paired track efficiencies are determined as a function of  $p_T$ ,  $\xi \equiv \min(p_T[\pi^+], p_T[\pi^-])$  in Equation C.2.

An aggregate pattern recognition efficiency may be calculated in terms of  $\xi \equiv p_T$ , for  $p_T > p_T^{\min}$ , as

$$\varepsilon(p_T > p_T^{\min}) \equiv \frac{\sum_{p_T > p_T^{\min}} N_{\text{found}}(\Delta p_T)}{\sum_{p_T > p_T^{\min}} [N_{\text{found}}(\Delta p_T) + N_{\overline{\text{found}}}(\Delta p_T)]} \Bigg|_{r_{\text{CTC}}^{\text{exit}} > (r_{\text{CTC}}^{\text{exit}})^{\min}}, \quad (\text{C.3})$$

with binomial statistics used to compute the statistical uncertainty on  $\varepsilon$ .

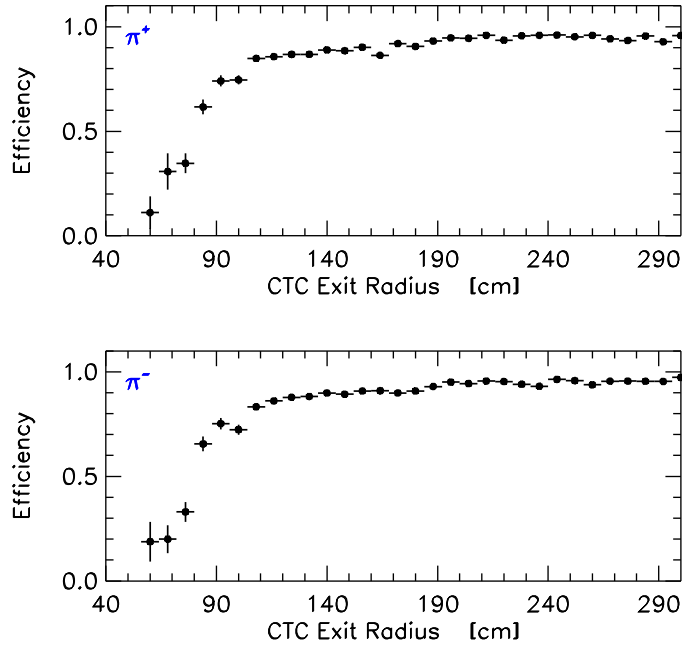


Figure C.6: The efficiency dependence on the CTC exit radius for  $\pi^+$  (top) and  $\pi^-$  (bottom) tracks.

#### C.4.2 Efficiency Dependence on Kinematic Observables

Employing the definition described in Equation C.2, the pattern recognition efficiency was studied for tracks in several different kinematic observables. Unless noted otherwise,  $p_T^{\min} \equiv 0.4 \text{ GeV}/c$  in Equation C.2.

Figure C.6 depicts the efficiency dependence on  $r_{\text{CTC}}^{\text{exit}}$  for both  $\pi^+$  and  $\pi^-$  tracks with no  $(r_{\text{CTC}}^{\text{exit}})^{\min}$  criterion. The shape of the turn-on motivated the use of a  $(r_{\text{CTC}}^{\text{exit}})^{\min}$  criterion less than the often-used 132-cm one, which is conservative and corresponds to the outer edge of superlayer 8. Figure C.6 suggests that a conservative criterion of  $(r_{\text{CTC}}^{\text{exit}})^{\min} = 110 \text{ cm}$  was appropriate for the provision of reliable tracking efficiency information for muon tracks, without any significant compromise in the CMX acceptance. The remaining figures in this appendix (except the left side of Figure C.13) have been prepared using  $(r_{\text{CTC}}^{\text{exit}})^{\min} = 110 \text{ cm}$ , which corresponds to a radius just outside the outer edge of superlayer 6.

Figure C.7 presents an example of the  $p_T$ -dependent pattern recognition efficiencies for single  $\pi^+$  and  $\pi^-$  tracks and  $\pi^+\pi^-$  track pairs. The data points were calculated using Equation C.2 with  $p_T^{\min} = 0$  and  $(r_{\text{CTC}}^{\text{exit}})^{\min} = 110 \text{ cm}$ . The indicated aggregate efficiencies

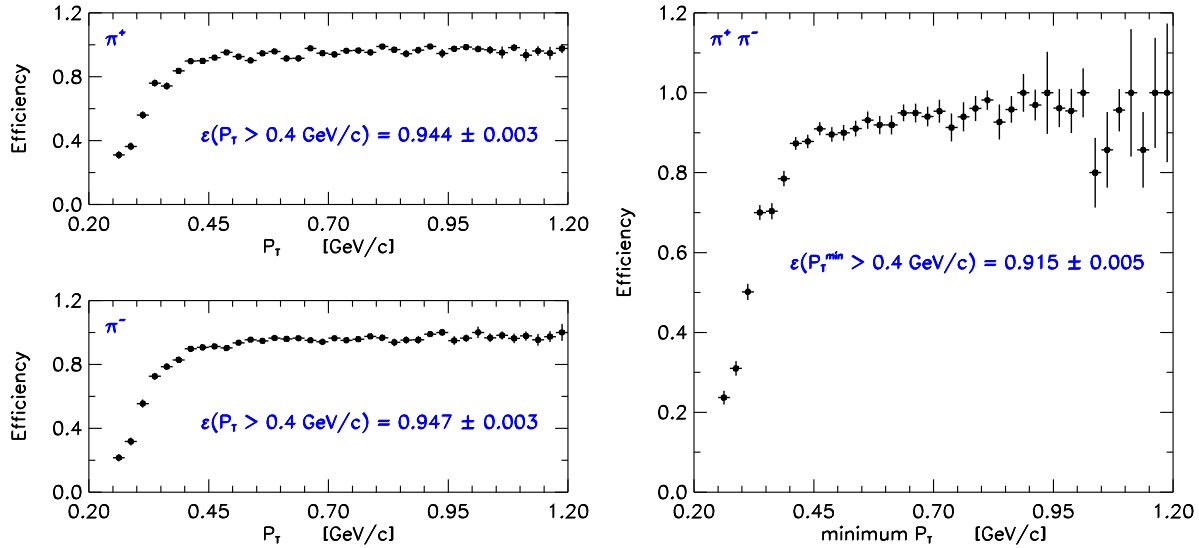


Figure C.7: An example of the efficiency dependence on transverse momentum for single tracks (left) and track pairs (right), in this case for the Run 1B “Low” run-range sample. The indicated measured aggregate efficiencies represent this run range alone; the uncertainties are statistical.

were calculated using Equation C.3, but with  $p_T^{\min} = 0.4$  GeV/c; the uncertainties are statistical only. Note that the product of the two single-track efficiencies,  $0.894 \pm 0.004$ , differs from the two-track efficiency by  $\sim 3.3$  standard deviations, indicating that the pattern recognition efficiencies for two tracks in a single event are correlated. This observation is discussed further in Section C.4.3.

### C.4.3 Efficiency Dependence on Occupancy-Related Observables

The effects of CTC occupancy on the pattern recognition efficiency were traditionally contemplated in terms of instantaneous luminosity dependence. Figure C.8 shows plots of the single- and two-track efficiencies as functions of instantaneous luminosity.

For a given event, the instantaneous luminosity was only indirectly related to the true track occupancy in the CTC fiducial volume. A more direct measure of occupancy is provided by the multiplicity of high-quality primary vertices in an event. In Figure C.9, the single- and two-track efficiencies as functions of the number of Class-12 vertices<sup>1</sup> are

<sup>1</sup>The highest quality  $z$  vertex identifiable using the VTX was deemed a ‘Class-12’ vertex. Class-12 vertices were defined as such when the number of associated hits in the VTX exceeded 180.

illustrated. Note that the efficiency dependence on primary vertex multiplicity is greater than that on instantaneous luminosity by more than a factor of two.

It is useful to examine the efficiency dependence on variables that are considered to be even more correlated than primary vertex multiplicity with the true occupancy of the CTC. An example of one of these is the total number of fitted CTC tracks in each event. In spite of the fact that the CTC track fits themselves used primary  $z$ -vertex information, the CTC track multiplicity was expected to be more correlated with the CTC occupancy because the track multiplicity was measured in the CTC itself and, for example, would be largely independent of those primary vertices that represented tracks at high absolute pseudorapidities, outside the fiducial acceptance of the CTC. Figure C.10 portrays the single- and double-track efficiencies as functions of the number of CTC tracks. Although the distributions are limited by poor statistics at low and high multiplicities, the efficiencies exhibit a significant dependence on CTC track multiplicity.

The correlation between the pattern recognition efficiencies of two tracks in a given event was discussed briefly in Section C.4.2. Figure C.11 compares the efficiency of a track pair,  $\varepsilon(\pi^+ \pi^-)$ , with the efficiency product of two individual tracks,  $\varepsilon(\pi^+) \varepsilon(\pi^-)$ , as a function of Class-12 primary vertex multiplicity. For the purposes of this figure, a more restrictive  $p_T(\pi^\pm) > 0.5$  GeV/ $c$  criterion was imposed to reduce the tracking differences between positively and negatively charged tracks; the exit radius cut, however, was kept at  $r_{\text{CTC}}^{\text{exit}} > 110$  cm. The central values of the  $\varepsilon(\pi^+ \pi^-)$  measurements were consistently greater than those for the  $\varepsilon(\pi^+) \varepsilon(\pi^-)$  measurements, but the two quantities were only statistically inconsistent (by at least one standard deviation) in events with only one or two Class-12 primary vertices. In spite of the fact that the events with only one or two Class-12 vertices constituted a major fraction of the total number of events in the sample, the degree of correlation between two tracks in a single event, while interesting, was unobservable when systematic uncertainties were considered.

#### C.4.4 Time-Dependent Effects

Section 5.2 mentioned several time-dependent factors that may have been detrimental to the CTC tracking efficiencies in Run 1. Time-dependent effects can be organized into two broad categories: effects due to occupancy and those due to aging and other sources. Although



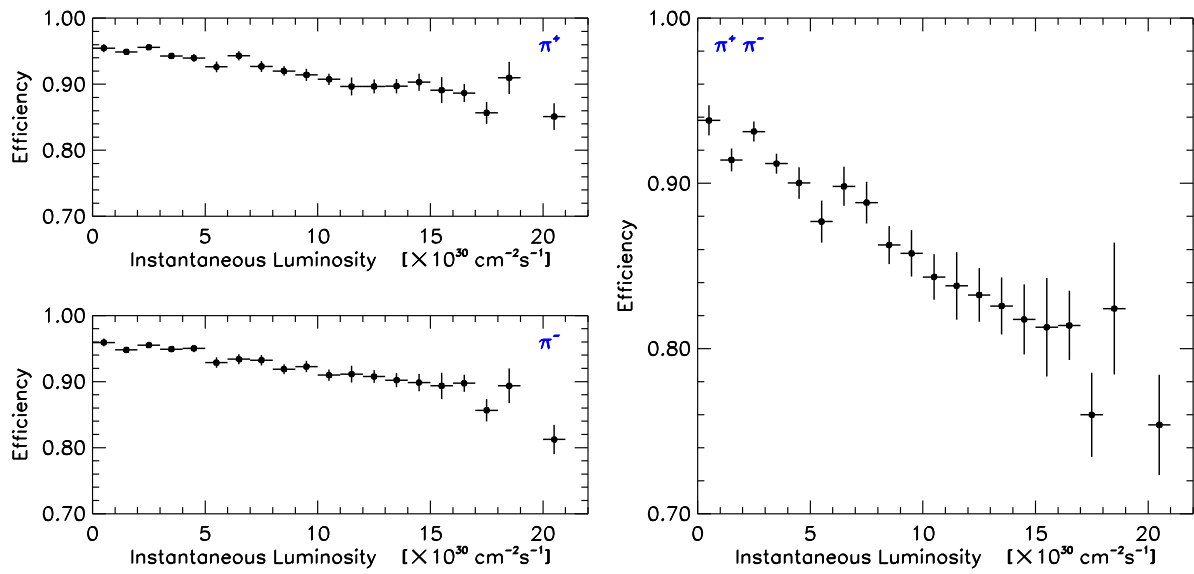


Figure C.8: The efficiency dependence on instantaneous luminosity for single tracks (left) and track pairs (right).

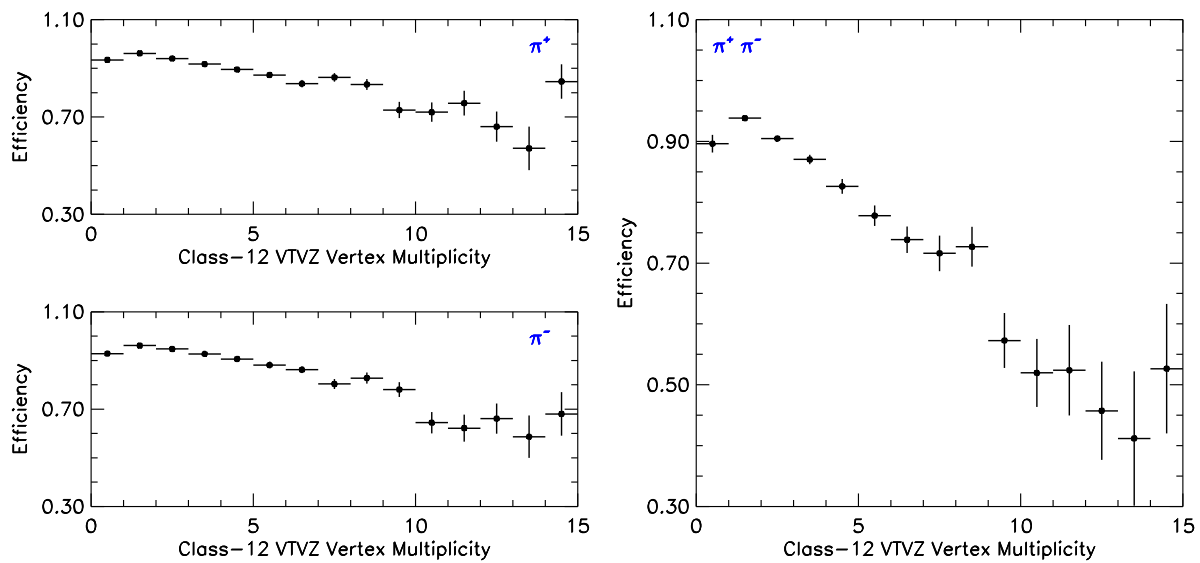


Figure C.9: The efficiency dependence on multiplicity of Class-12 (high-quality) vertices for single tracks (left) and track pairs (right).

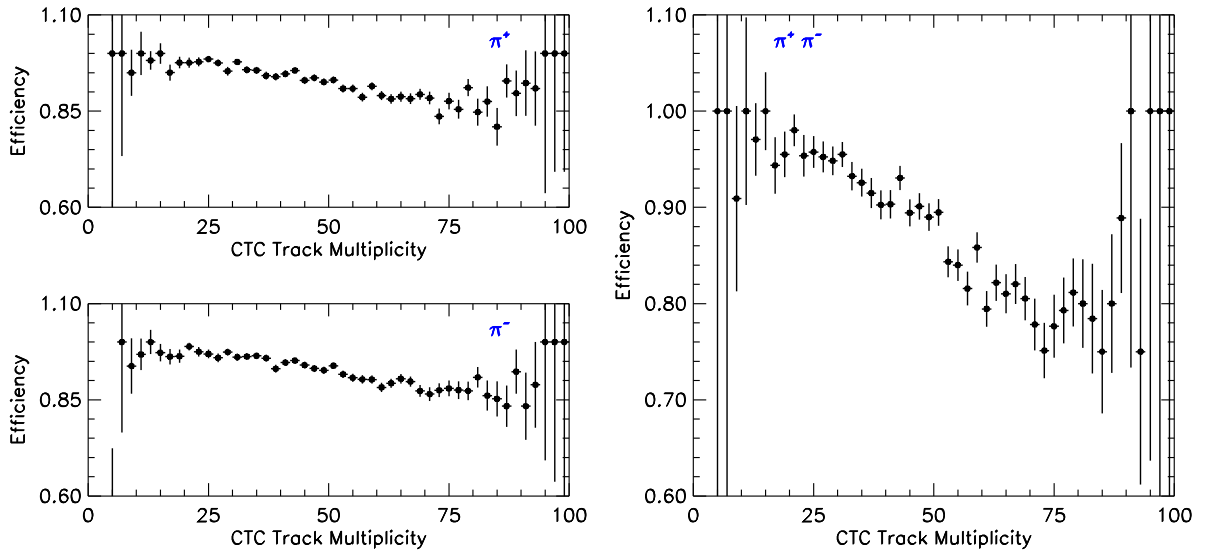


Figure C.10: The efficiency dependence on multiplicity of CTC tracks for single tracks (left) and track pairs (right).

the time dependence of the latter category is typically studied in terms of run number, time-integrated luminosity is a more meaningful quantity for this purpose.

It is apparent from the results presented in Section C.4.3 that the CTC pattern recognition efficiencies depended strongly on the occupancy conditions inside the CTC. The results from Section C.4.3 also suggest that variables similar to primary-vertex and CTC-track multiplicity be used to constrain occupancy levels in studies of run-dependent aging effects in the CTC.

As outlined in Section C.2, hits were embedded into the CTC with wire efficiencies that were tuned from the data. The embedding techniques used in this study therefore did account for some time-dependent performance effects (in addition to occupancy), to the extent that the wire efficiencies used in the embedding were derived from data quantities (the numbers of used hits per superlayer) that were expected to be sensitive to time-dependent performance effects in the CTC. It is important to note, however, that the present study cannot be expected to resolve *a posteriori* any time-dependencies that affected the embedded hits directly, since the wire efficiencies were calculated using run-averaged effects and were administered uniformly for all the events in the sample. It should be emphasized that, with the exception of the embedded hits, this technique can potentially resolve all other

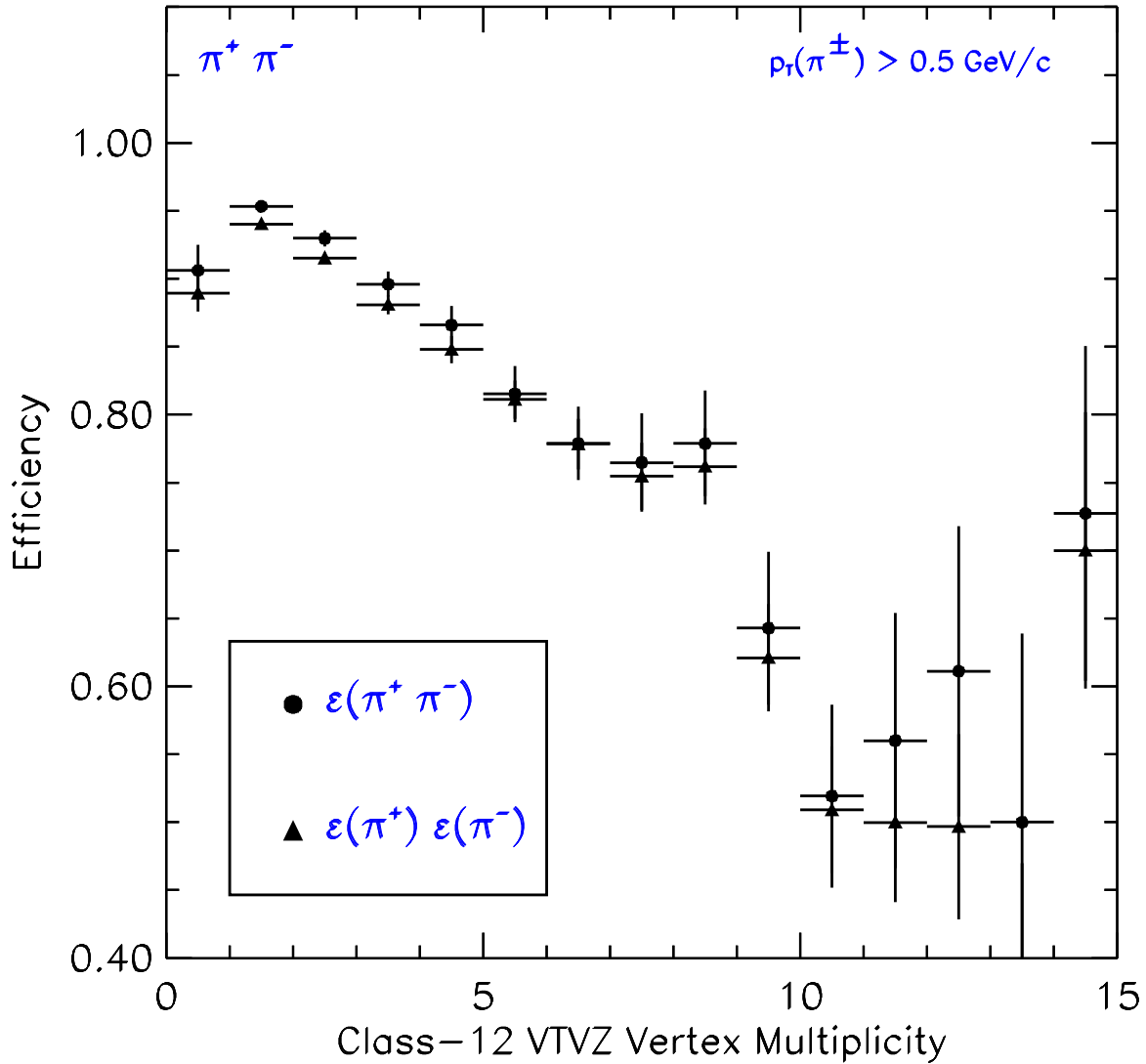


Figure C.11: A comparison of the two-track efficiency and the product of single-track efficiencies, as a function of primary vertex multiplicity. A tighter  $p_T(\pi^\pm) > 0.5 \text{ GeV}/c$  criterion was imposed to reduce the tracking differences between positively and negatively charged tracks, but the exit radius cut was kept at  $r_{\text{CTC}}^{\text{exit}} > 110 \text{ cm}$ . The indicated uncertainties are statistical only.

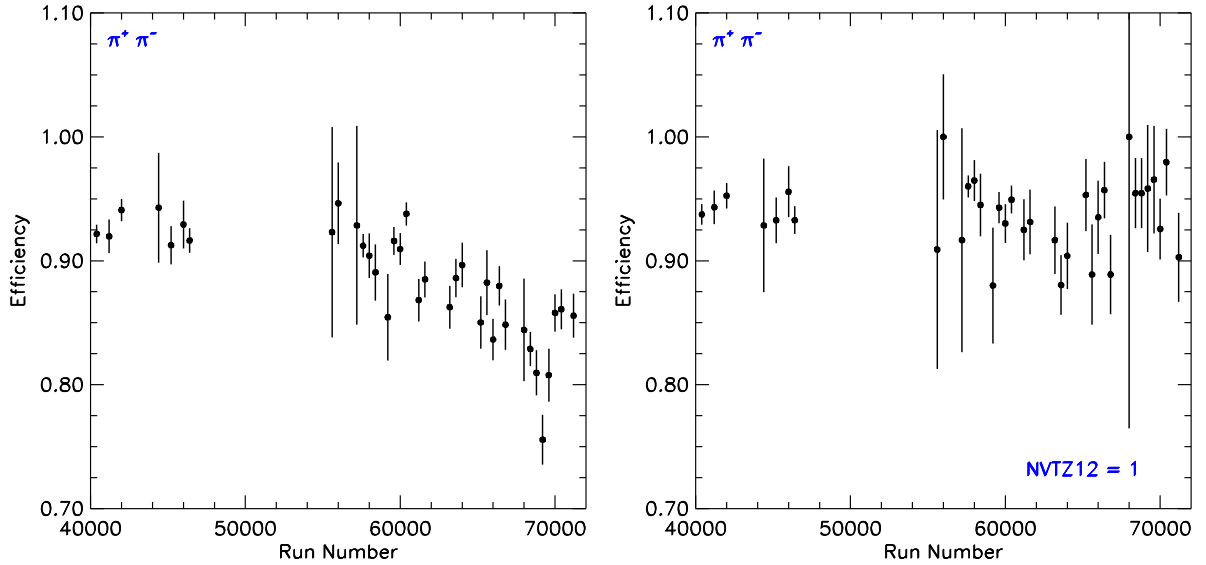


Figure C.12: The dipion efficiency dependence on run number for all Class-12 primary vertex multiplicities (left) and for one and only one Class-12 primary vertex (right).

time-dependent effects in each of the  $\sim 36\,000$  events.

Figure C.12 illustrates the dependence of the pattern recognition efficiency on run number. For the case where all primary vertex multiplicities are permitted, a negative slope in the distribution is discernible. When the efficiency is examined in events with only one Class-12 vertex, the slope is observed to vanish within the available statistics. The trends in Figure C.12 are consistent with the expectations of this embedding technique and the conclusion that the most pernicious effect on the pattern recognition is one of occupancy.

#### C.4.5 Stereo Efficiency

Pursuant to the discussion in Section C.3 about relative stereo and axial contributions to the tracking inefficiency, a *stereo* pattern recognition efficiency was defined, also using Equation C.2, but with the denominator populated by the subsample of events that satisfied the 2-dimensional axial-only matching criteria. In this expression of the stereo efficiency,  $N_{\text{found}}$  represented the number of events that, in addition to meeting the axial-only criterion, satisfied the 3-dimensional matching requirement. Figure C.13 shows plots of the stereo pattern recognition efficiency as a function of two kinematic observables: the CTC exit radius,  $r_{\text{CTC}}^{\text{exit}}$ , and the transverse momentum,  $p_{\text{T}}$ . The stereo efficiency in Figure C.13 was

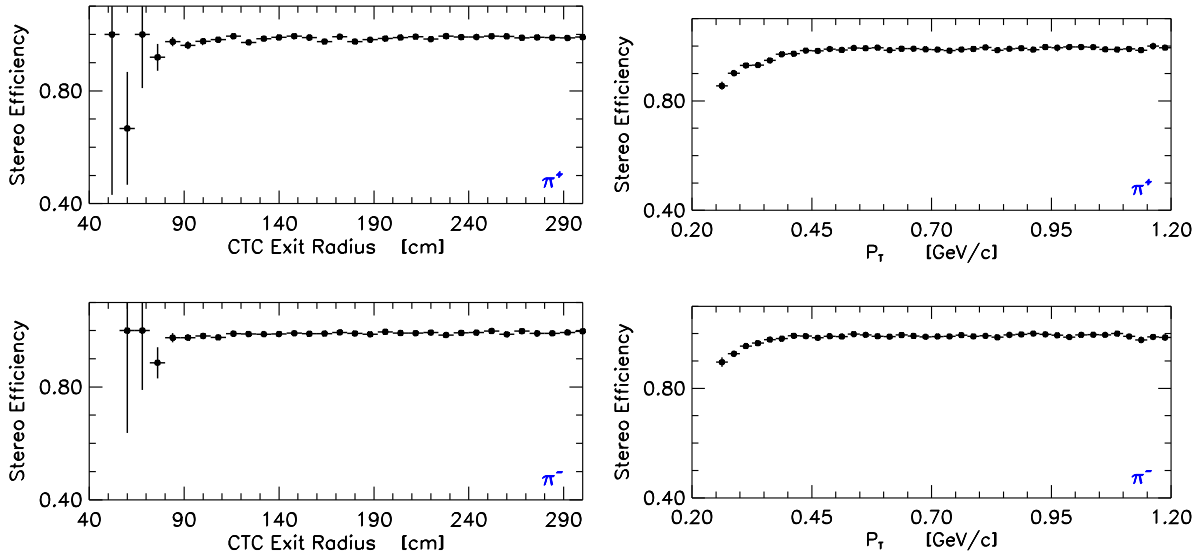


Figure C.13: The stereo pattern recognition efficiency for  $\pi^+$  (top) and  $\pi^-$  (bottom) tracks as a function of two kinematic observables: (left) the CTC exit radius,  $r_{\text{CTC}}^{\text{exit}}$ , and (right) the transverse momentum,  $p_T$ .

observed to remain constant near 100% in  $r_{\text{CTC}}^{\text{exit}}$ , but to diminish appreciably in  $p_T$  for  $p_T < 0.4$  GeV/c. The dependence of the stereo pattern recognition efficiency on occupancy-related observables is illustrated in Figure C.14, which features plots of the stereo efficiency as a function of the primary-vertex and CTC-track multiplicities. The stereo pattern recognition efficiency appears to drop by  $\sim 10\%$  with increasing primary-vertex multiplicity and by  $\sim 5\%$  with increasing CTC-track multiplicity. No significant differences in stereo efficiencies between  $\pi^+$  and  $\pi^-$  tracks are apparent in Figures C.13 and C.14.

## C.5 Results

Single- and double-track pattern recognition efficiencies were calculated for each of the four run-number bins using Equation C.3 with  $p_T^{\text{min}} = 0.4$  GeV/c. Tables C.3 and C.4 list the results of these calculations for  $r_{\text{CTC}}^{\text{exit}} > 110$  cm with 3-dimensional and 2-dimensional matching criteria, respectively. Similarly, Tables C.6 and C.7 list the results of the calculations for  $r_{\text{CTC}}^{\text{exit}} > 132$  cm with 3-dimensional and 2-dimensional matching criteria, respectively. Tables C.5 and C.8 summarize the aggregate Run 1 single- and double-track pattern recognition efficiencies for  $r_{\text{CTC}}^{\text{exit}} > 110$  cm and  $r_{\text{CTC}}^{\text{exit}} > 132$  cm, respectively. The totals

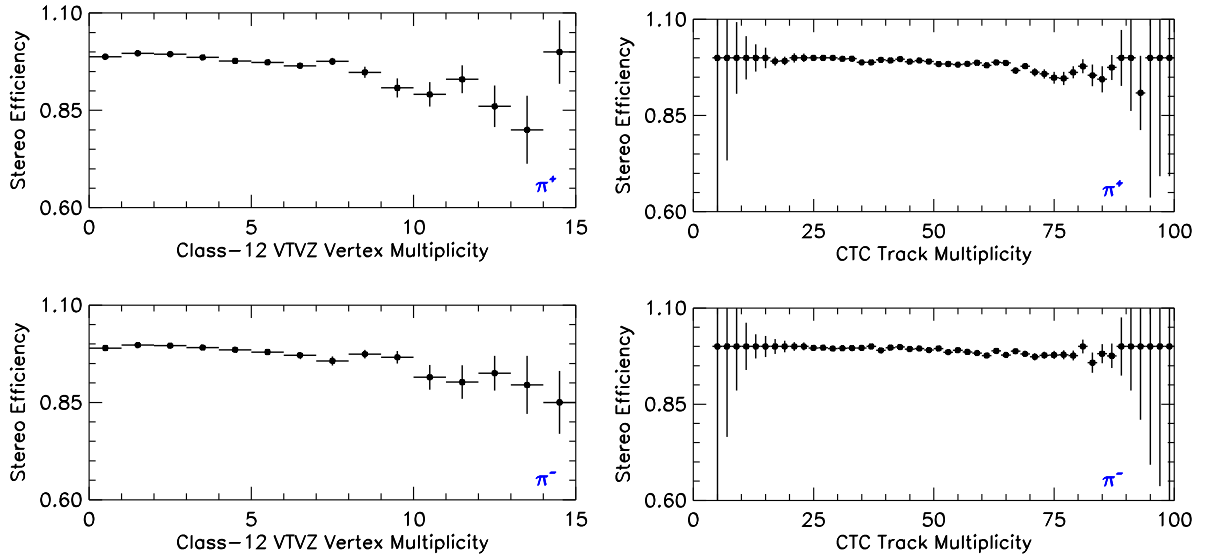


Figure C.14: The stereo pattern recognition efficiency for  $\pi^+$  (top) and  $\pi^-$  (bottom) tracks as a function of two occupancy-related observables: (left) the Class-12 VTVZ primary vertex multiplicity and (right) the CTC track multiplicity.

were computed by calculating mean values weighted in time-integrated luminosity (refer to Table C.1) and statistical uncertainty. For each aggregate efficiency, the mean statistical uncertainty was added in quadrature with the systematic uncertainty, which was taken to be equal to the maximum difference between the tracking efficiencies calculated with full (100%) wire hit efficiencies and those calculated with reduced wire hit efficiencies.

## C.6 Conclusions

This study of Run 1A and 1B single- and double-track pattern recognition efficiencies yielded several qualitative and quantitative conclusions:

1. To model accurately the CTC performance in Run 1, it was necessary to employ reduced wire hit efficiencies in the track embedding procedure.
2. Throughout this study,  $\pi^+$  and  $\pi^-$  tracks were treated separately. Within the statistical uncertainties alone, no significant differences between efficiencies for positively and negatively charged tracks were observed.
3. A CTC track exit radius criterion of  $r_{\text{CTC}}^{\text{exit}} > 110$  cm ensured that the track was in

3-D Efficiency		$\varepsilon(\pi^+)$	$\varepsilon(\pi^-)$	$\varepsilon(\pi^+ \pi^-)$
Run 1A		$.952 \pm .003 \pm .017$	$.956 \pm .003 \pm .018$	$.924 \pm .004 \pm .029$
Run 1B	Low	$.944 \pm .003 \pm .016$	$.947 \pm .003 \pm .014$	$.915 \pm .005 \pm .023$
	Medium	$.921 \pm .004 \pm .023$	$.923 \pm .003 \pm .023$	$.869 \pm .006 \pm .036$
	High	$.899 \pm .004 \pm .030$	$.900 \pm .004 \pm .026$	$.827 \pm .006 \pm .043$

Table C.3: The single- and double-track 3-dimensional pattern recognition efficiencies measured in the four run-number bins for tracks with  $p_T > 0.4$  GeV/c and  $r_{\text{CTC}}^{\text{exit}} > 110$  cm. The first uncertainties shown are statistical and the second are systematic.

2-D Efficiency		$\varepsilon(\pi^+)$	$\varepsilon(\pi^-)$	$\varepsilon(\pi^+ \pi^-)$
Run 1A		$.957 \pm .003 \pm .017$	$.960 \pm .003 \pm .017$	$.931 \pm .004 \pm .030$
Run 1B	Low	$.949 \pm .003 \pm .016$	$.952 \pm .003 \pm .013$	$.922 \pm .005 \pm .023$
	Medium	$.933 \pm .003 \pm .021$	$.931 \pm .003 \pm .020$	$.883 \pm .005 \pm .035$
	High	$.918 \pm .004 \pm .025$	$.916 \pm .004 \pm .019$	$.858 \pm .006 \pm .035$

Table C.4: The single- and double-track 2-dimensional pattern recognition efficiencies measured in the four run-number bins for tracks with  $p_T > 0.4$  GeV/c and  $r_{\text{CTC}}^{\text{exit}} > 110$  cm. The first uncertainties shown are statistical and the second are systematic.

Aggregate Efficiency	Matching	$\varepsilon(\pi^+)$	$\varepsilon(\pi^-)$	$\varepsilon(\pi^+ \pi^-)$
Run 1B only	3-D	$.917 \pm .030$	$.920 \pm .026$	$.860 \pm .043$
	2-D	$.931 \pm .025$	$.930 \pm .020$	$.880 \pm .035$
Runs 1A + 1B	3-D	$.927 \pm .030$	$.928 \pm .026$	$.881 \pm .043$
	2-D	$.937 \pm .025$	$.936 \pm .020$	$.895 \pm .035$

Table C.5: The total Run 1B and 1A + 1B single- and double-track pattern recognition efficiencies, each calculated by combining the relevant run-number bins into a single mean, weighted by the appropriate statistical uncertainties and time-integrated luminosities. Values are given for both the 3-dimensional and 2-dimensional matching techniques for tracks with  $p_T > 0.4$  GeV/c and  $r_{\text{CTC}}^{\text{exit}} > 110$  cm, and the uncertainties are quadratic sums of the statistical and systematic components.

3-D Efficiency		$\varepsilon(\pi^+)$	$\varepsilon(\pi^-)$	$\varepsilon(\pi^+ \pi^-)$
Run 1A		$.959 \pm .003 \pm .015$	$.961 \pm .003 \pm .016$	$.937 \pm .004 \pm .028$
Run 1B	Low	$.951 \pm .003 \pm .013$	$.952 \pm .003 \pm .014$	$.929 \pm .005 \pm .024$
	Medium	$.929 \pm .004 \pm .021$	$.931 \pm .003 \pm .021$	$.887 \pm .006 \pm .032$
	High	$.906 \pm .004 \pm .029$	$.907 \pm .004 \pm .023$	$.849 \pm .007 \pm .040$

Table C.6: The single- and double-track 3-dimensional pattern recognition efficiencies measured in the four run-number bins for tracks with  $p_T > 0.4$  GeV/c and  $r_{\text{CTC}}^{\text{exit}} > 132$  cm. The first uncertainties shown are statistical and the second are systematic.

2-D Efficiency		$\varepsilon(\pi^+)$	$\varepsilon(\pi^-)$	$\varepsilon(\pi^+ \pi^-)$
Run 1A		$.963 \pm .003 \pm .015$	$.964 \pm .003 \pm .016$	$.944 \pm .004 \pm .027$
Run 1B	Low	$.955 \pm .003 \pm .014$	$.957 \pm .003 \pm .012$	$.937 \pm .004 \pm .021$
	Medium	$.942 \pm .003 \pm .017$	$.938 \pm .003 \pm .019$	$.900 \pm .005 \pm .032$
	High	$.926 \pm .004 \pm .022$	$.923 \pm .004 \pm .016$	$.881 \pm .006 \pm .031$

Table C.7: The single- and double-track 2-dimensional pattern recognition efficiencies measured in the four run-number bins for tracks with  $p_T > 0.4$  GeV/ $c$  and  $r_{\text{CTC}}^{\text{exit}} > 132$  cm. The first uncertainties shown are statistical and the second are systematic.

Aggregate Efficiency	Matching	$\varepsilon(\pi^+)$	$\varepsilon(\pi^-)$	$\varepsilon(\pi^+ \pi^-)$
Run 1B only	3-D	$.925 \pm .029$	$.927 \pm .023$	$.882 \pm .040$
	2-D	$.939 \pm .022$	$.936 \pm .019$	$.901 \pm .032$
Runs 1A + 1B	3-D	$.934 \pm .029$	$.935 \pm .023$	$.901 \pm .040$
	2-D	$.944 \pm .022$	$.942 \pm .019$	$.913 \pm .032$

Table C.8: The total Run 1B and 1A + 1B single- and double-track pattern recognition efficiencies, each calculated by combining the relevant run-number bins into a single mean, weighted by the appropriate statistical uncertainties and time-integrated luminosities. Values are given for both the 3-dimensional and 2-dimensional matching techniques for tracks with  $p_T > 0.4$  GeV/ $c$  and  $r_{\text{CTC}}^{\text{exit}} > 132$  cm, and the uncertainties are quadratic sums of the statistical and systematic components.



a region of well-understood pattern recognition efficiency without undue compromise to the CTC and CMX fiducial acceptance (refer to Section C.4.2).

4. The deleterious effects of CTC occupancy on the pattern recognition constituted the principal source of tracking inefficiency in Run 1.
5. The pattern recognition efficiencies were studied for single and double tracks as a function of three occupancy-related observables, which were, in order of increasing correlation with the true CTC occupancy, the instantaneous luminosity, the multiplicity of high-quality primary vertices, and the multiplicity of reconstructed tracks in the CTC (refer to Section C.4.3). It was recommended that investigations of non-occupancy time-dependent effects be performed with constraints using variables that were as closely correlated with the CTC occupancy as possible.
6. The pattern recognition efficiencies of two tracks within a single event were correlated, a conclusion that followed from the observation that these efficiencies were driven by the event-by-event track-multiplicity environment conditions inside the CTC. In the context of primary-vertex multiplicity, the intertrack correlations were only statistically significant at low primary-vertex multiplicities. Any double-track correlations became insignificant when systematic uncertainties were included in the efficiency measurements.
7. CTC tracking performance in the stereo view alone appeared to contribute little to the observed pattern recognition inefficiencies. The stereo efficiencies possessed a weak dependence on occupancy and a strong dependence on  $p_T$  in the region  $p_T < 0.4$  GeV/ $c$ , which lay outside the practical kinematic range of this investigation (refer to Section C.4.5).
8. Single- and double-track efficiencies were calculated in 2 dimensions (axial-only) and 3 dimensions (axial and stereo) in four run-range bins spanning the Run 1A and 1B data-taking periods. Measurements were presented for tracks with  $p_T > 0.4$  GeV/ $c$  and either  $r_{\text{CTC}}^{\text{exit}} > 110$  cm or  $r_{\text{CTC}}^{\text{exit}} > 132$  cm. Aggregate Run 1 single- and double-track 3-dimensional and 2-dimensional pattern recognition efficiency measurements

were also computed for both the  $r_{\text{CTC}}^{\text{exit}} > 110\text{-cm}$  and  $r_{\text{CTC}}^{\text{exit}} > 132\text{-cm}$  selection criteria. Refer to Tables C.3, C.4, C.5, C.6, C.7, and C.8 in Section C.5.

9. The total 3-dimensional Run 1A + 1B single-track efficiency for  $p_{\text{T}} > 0.4 \text{ GeV}/c$  and  $r_{\text{CTC}}^{\text{exit}} > 110 \text{ cm}$  was measured to be  $0.928 \pm 0.020$ .
10. The total 3-dimensional Run 1A + 1B double-track efficiency for  $p_{\text{T}} > 0.4 \text{ GeV}/c$  and  $r_{\text{CTC}}^{\text{exit}} > 110 \text{ cm}$  was measured to be  $0.881 \pm 0.043$ .

## Appendix D

# The CDF Collaboration

F. Abe,<sup>17</sup> H. Akimoto,<sup>39</sup> A. Akopian,<sup>31</sup> M. G. Albrow,<sup>7</sup> A. Amadon,<sup>5</sup> S. R. Amendolia,<sup>27</sup> D. Amidei,<sup>20</sup> J. Antos,<sup>33</sup> S. Aota,<sup>37</sup> G. Apollinari,<sup>31</sup> T. Arisawa,<sup>39</sup> T. Asakawa,<sup>37</sup> W. Ashmanskas,<sup>18</sup> M. Atac,<sup>7</sup> P. Azzi-Bacchetta,<sup>25</sup> N. Bacchetta,<sup>25</sup> S. Bagdasarov,<sup>31</sup> M. W. Bailey,<sup>22</sup> P. de Barbaro,<sup>30</sup> A. Barbaro-Galtieri,<sup>18</sup> V. E. Barnes,<sup>29</sup> B. A. Barnett,<sup>15</sup> M. Barone,<sup>9</sup> G. Bauer,<sup>19</sup> T. Baumann,<sup>11</sup> F. Bedeschi,<sup>27</sup> S. Behrends,<sup>3</sup> S. Belforte,<sup>27</sup> G. Bellettini,<sup>27</sup> J. Bellinger,<sup>40</sup> D. Benjamin,<sup>35</sup> J. Bensinger,<sup>3</sup> A. Beretvas,<sup>7</sup> J. P. Berge,<sup>7</sup> J. Berryhill,<sup>5</sup> S. Bertolucci,<sup>9</sup> S. Bettelli,<sup>27</sup> B. Bevensee,<sup>26</sup> A. Bhatti,<sup>31</sup> K. Biery,<sup>7</sup> C. Bigongiari,<sup>27</sup> M. Binkley,<sup>7</sup> D. Bisello,<sup>25</sup> R. E. Blair,<sup>1</sup> C. Blocker,<sup>3</sup> S. Blusk,<sup>30</sup> A. Bodek,<sup>30</sup> W. Bokhari,<sup>26</sup> G. Bolla,<sup>29</sup> Y. Bonushkin,<sup>4</sup> D. Bortoletto,<sup>29</sup> J. Boudreau,<sup>28</sup> L. Breccia,<sup>2</sup> C. Bromberg,<sup>21</sup> N. Bruner,<sup>22</sup> R. Brunetti,<sup>2</sup> E. Buckley-Geer,<sup>7</sup> H. S. Budd,<sup>30</sup> K. Burkett,<sup>20</sup> G. Busetto,<sup>25</sup> A. Byon-Wagner,<sup>7</sup> K. L. Byrum,<sup>1</sup> M. Campbell,<sup>20</sup> A. Caner,<sup>27</sup> W. Carithers,<sup>18</sup> D. Carlsmith,<sup>40</sup> J. Cassada,<sup>30</sup> A. Castro,<sup>25</sup> D. Cauz,<sup>36</sup> A. Cerri,<sup>27</sup> P. S. Chang,<sup>33</sup> P. T. Chang,<sup>33</sup> H. Y. Chao,<sup>33</sup> J. Chapman,<sup>20</sup> M. -T. Cheng,<sup>33</sup> M. Chertok,<sup>34</sup> G. Chiarelli,<sup>27</sup> C. N. Chiou,<sup>33</sup> L. Christofek,<sup>13</sup> M. L. Chu,<sup>33</sup> S. Cihangir,<sup>7</sup> A. G. Clark,<sup>10</sup> M. Cobal,<sup>27</sup> E. Cocca,<sup>27</sup> M. Contreras,<sup>5</sup> J. Conway,<sup>32</sup> J. Cooper,<sup>7</sup> M. Cordelli,<sup>9</sup> D. Costanzo,<sup>27</sup> C. Couyoumtzelis,<sup>10</sup> D. Cronin-Hennessy,<sup>6</sup> R. Culbertson,<sup>5</sup> D. Dagenhart,<sup>38</sup> T. Daniels,<sup>19</sup> F. DeJongh,<sup>7</sup> S. Dell’Agnello,<sup>9</sup> M. Dell’Orso,<sup>27</sup> R. Demina,<sup>7</sup> L. Demortier,<sup>31</sup> M. Deninno,<sup>2</sup> P. F. Derwent,<sup>7</sup> T. Devlin,<sup>32</sup> J. R. Dittmann,<sup>6</sup> S. Donati,<sup>27</sup> J. Done,<sup>34</sup> T. Dorigo,<sup>25</sup> N. Eddy,<sup>20</sup> K. Einsweiler,<sup>18</sup> J. E. Elias,<sup>7</sup> R. Ely,<sup>18</sup> E. Engels, Jr.,<sup>28</sup> D. Errede,<sup>13</sup> S. Errede,<sup>13</sup> Q. Fan,<sup>30</sup> R. G. Feild,<sup>41</sup> Z. Feng,<sup>15</sup> C. Ferretti,<sup>27</sup> I. Fiori,<sup>2</sup> B. Flaughner,<sup>7</sup>

G. W. Foster,<sup>7</sup> M. Franklin,<sup>11</sup> J. Freeman,<sup>7</sup> J. Friedman,<sup>19</sup> H. Frisch,<sup>5</sup> Y. Fukui,<sup>17</sup>  
 S. Galeotti,<sup>27</sup> M. Gallinaro,<sup>26</sup> O. Ganel,<sup>35</sup> M. Garcia-Sciveres,<sup>18</sup> A. F. Garfinkel,<sup>29</sup>  
 C. Gay,<sup>41</sup> S. Geer,<sup>7</sup> D. W. Gerdes,<sup>15</sup> P. Giannetti,<sup>27</sup> N. Giokaris,<sup>31</sup> P. Giromini,<sup>9</sup>  
 G. Giusti,<sup>27</sup> M. Gold,<sup>22</sup> A. Gordon,<sup>11</sup> A. T. Goshaw,<sup>6</sup> Y. Gotra,<sup>25</sup> K. Goulios,<sup>31</sup>  
 H. Grassmann,<sup>36</sup> L. Groer,<sup>32</sup> C. Grosso-Pilcher,<sup>5</sup> G. Guillian,<sup>20</sup> J. Guimaraes da Costa,<sup>15</sup>  
 R. S. Guo,<sup>33</sup> C. Haber,<sup>18</sup> E. Hafen,<sup>19</sup> S. R. Hahn,<sup>7</sup> R. Hamilton,<sup>11</sup> T. Handa,<sup>12</sup>  
 R. Handler,<sup>40</sup> F. Happacher,<sup>9</sup> K. Hara,<sup>37</sup> A. D. Hardman,<sup>29</sup> R. M. Harris,<sup>7</sup> F. Hartmann,<sup>16</sup>  
 J. Hauser,<sup>4</sup> E. Hayashi,<sup>37</sup> J. Heinrich,<sup>26</sup> W. Hao,<sup>35</sup> B. Hinrichsen,<sup>14</sup> K. D. Hoffman,<sup>29</sup>  
 M. Hohlmann,<sup>5</sup> C. Holck,<sup>26</sup> R. Hollebeck,<sup>26</sup> L. Holloway,<sup>13</sup> Z. Huang,<sup>20</sup> B. T. Huffman,<sup>28</sup>  
 R. Hughes,<sup>23</sup> J. Huston,<sup>21</sup> J. Huth,<sup>11</sup> H. Ikeda,<sup>37</sup> M. Incagli,<sup>27</sup> J. Incandela,<sup>7</sup> G. Introzzi,<sup>27</sup>  
 J. Iwai,<sup>39</sup> Y. Iwata,<sup>12</sup> E. James,<sup>20</sup> H. Jensen,<sup>7</sup> U. Joshi,<sup>7</sup> E. Kajfasz,<sup>25</sup> H. Kambara,<sup>10</sup>  
 T. Kamon,<sup>34</sup> T. Kaneko,<sup>37</sup> K. Karr,<sup>38</sup> H. Kasha,<sup>41</sup> Y. Kato,<sup>24</sup> T. A. Keaffaber,<sup>29</sup>  
 K. Kelley,<sup>19</sup> R. D. Kennedy,<sup>7</sup> R. Kephart,<sup>7</sup> D. Kestenbaum,<sup>11</sup> D. Khazins,<sup>6</sup> T. Kikuchi,<sup>37</sup>  
 B. J. Kim,<sup>27</sup> H. S. Kim,<sup>14</sup> S. H. Kim,<sup>37</sup> Y. K. Kim,<sup>18</sup> L. Kirsch,<sup>3</sup> S. Klimenko,<sup>8</sup>  
 D. Knoblauch,<sup>16</sup> P. Koehn,<sup>23</sup> A. Königeter,<sup>16</sup> K. Kondo,<sup>37</sup> J. Konigsberg,<sup>8</sup> K. Kordas,<sup>14</sup>  
 A. Korytov,<sup>8</sup> E. Kovacs,<sup>1</sup> W. Kowald,<sup>6</sup> J. Kroll,<sup>26</sup> M. Kruse,<sup>30</sup> S. E. Kuhlmann,<sup>1</sup>  
 E. Kuns,<sup>32</sup> K. Kurino,<sup>12</sup> T. Kuwabara,<sup>37</sup> A. T. Laasanen,<sup>29</sup> I. Nakano,<sup>12</sup> S. Lami,<sup>27</sup>  
 S. Lammel,<sup>7</sup> J. I. Lamoureux,<sup>3</sup> M. Lancaster,<sup>18</sup> M. Lanzoni,<sup>27</sup> G. Latino,<sup>27</sup> T. LeCompte,<sup>1</sup>  
 S. Leone,<sup>27</sup> J. D. Lewis,<sup>7</sup> P. Limon,<sup>7</sup> M. Lindgren,<sup>4</sup> T. M. Liss,<sup>13</sup> J. B. Liu,<sup>30</sup>  
 Y. C. Liu,<sup>33</sup> N. Lockyer,<sup>26</sup> O. Long,<sup>26</sup> C. Loomis,<sup>32</sup> M. Loreti,<sup>25</sup> D. Lucchesi,<sup>27</sup>  
 P. Lukens,<sup>7</sup> S. Lusin,<sup>40</sup> J. Lys,<sup>18</sup> K. Maeshima,<sup>7</sup> P. Maksimovic,<sup>19</sup> M. Mangano,<sup>27</sup>  
 M. Mariotti,<sup>25</sup> J. P. Marriner,<sup>7</sup> A. Martin,<sup>41</sup> J. A. J. Matthews,<sup>22</sup> P. Mazzanti,<sup>2</sup>  
 P. McIntyre,<sup>34</sup> P. Melese,<sup>31</sup> M. Menguzzato,<sup>25</sup> A. Menzione,<sup>27</sup> E. Meschi,<sup>27</sup> S. Metzler,<sup>26</sup>  
 C. Miao,<sup>20</sup> T. Miao,<sup>7</sup> G. Michail,<sup>11</sup> R. Miller,<sup>21</sup> H. Minato,<sup>37</sup> S. Miscetti,<sup>9</sup> M. Mishina,<sup>17</sup>  
 S. Miyashita,<sup>37</sup> N. Moggi,<sup>27</sup> E. Moore,<sup>22</sup> Y. Morita,<sup>17</sup> A. Mukherjee,<sup>7</sup> T. Muller,<sup>16</sup>  
 P. Murat,<sup>27</sup> S. Murgia,<sup>21</sup> H. Nakada,<sup>37</sup> I. Nakano,<sup>12</sup> C. Nelson,<sup>7</sup> D. Neuberger,<sup>16</sup> C. Newman-  
 Holmes,<sup>7</sup> C.-Y. P. Ngan,<sup>19</sup> L. Nodulman,<sup>1</sup> S. H. Oh,<sup>6</sup> T. Ohmoto,<sup>12</sup> T. Ohsugi,<sup>12</sup>  
 R. Oishi,<sup>37</sup> M. Okabe,<sup>37</sup> T. Okusawa,<sup>24</sup> J. Olsen,<sup>40</sup> C. Pagliarone,<sup>27</sup> R. Paoletti,<sup>27</sup>  
 V. Papadimitriou,<sup>35</sup> S. P. Pappas,<sup>41</sup> N. Parashar,<sup>27</sup> A. Parri,<sup>9</sup> J. Patrick,<sup>7</sup> G. Pauletta,<sup>36</sup>  
 M. Paulini,<sup>18</sup> A. Perazzo,<sup>27</sup> L. Pescara,<sup>25</sup> M. D. Peters,<sup>18</sup> T. J. Phillips,<sup>6</sup> G. Piacentino,<sup>27</sup>  
 M. Pillai,<sup>30</sup> K. T. Pitts,<sup>7</sup> R. Plunkett,<sup>7</sup> L. Pondrom,<sup>40</sup> J. Proudfoot,<sup>1</sup> F. Ptohos,<sup>11</sup>

G. Punzi,<sup>27</sup> K. Ragan,<sup>14</sup> D. Reher,<sup>18</sup> M. Reischl,<sup>16</sup> A. Ribon,<sup>25</sup> F. Rimondi,<sup>2</sup> L. Ristori,<sup>27</sup> W. J. Robertson,<sup>6</sup> T. Rodrigo,<sup>27</sup> S. Rolli,<sup>38</sup> L. Rosenson,<sup>19</sup> R. Roser,<sup>13</sup> T. Saab,<sup>14</sup> W. K. Sakumoto,<sup>30</sup> D. Saltzberg,<sup>4</sup> A. Sansoni,<sup>9</sup> L. Santi,<sup>36</sup> H. Sato,<sup>37</sup> P. Schlabach,<sup>7</sup> E. E. Schmidt,<sup>7</sup> M. P. Schmidt,<sup>41</sup> A. Scott,<sup>4</sup> A. Scribano,<sup>27</sup> S. Segler,<sup>7</sup> S. Seidel,<sup>22</sup> Y. Seiya,<sup>37</sup> F. Semeria,<sup>2</sup> G. Sganos,<sup>14</sup> T. Shah,<sup>19</sup> M. D. Shapiro,<sup>18</sup> N. M. Shaw,<sup>29</sup> P. F. Shepard,<sup>28</sup> T. Shibayama,<sup>37</sup> M. Shimojima,<sup>37</sup> M. Shochet,<sup>5</sup> J. Siegrist,<sup>18</sup> A. Sill,<sup>35</sup> P. Sinervo,<sup>14</sup> P. Singh,<sup>13</sup> K. Sliwa,<sup>38</sup> C. Smith,<sup>15</sup> F. D. Snider,<sup>15</sup> J. Spalding,<sup>7</sup> T. Speer,<sup>10</sup> P. Sphicas,<sup>19</sup> F. Spinella,<sup>27</sup> M. Spiropulu,<sup>11</sup> L. Spiegel,<sup>7</sup> L. Stanco,<sup>25</sup> J. Steele,<sup>40</sup> A. Stefanini,<sup>27</sup> R. Ströhmer,<sup>7a</sup> J. Strologas,<sup>13</sup> F. Strumia,<sup>10</sup> D. Stuart,<sup>7</sup> K. Sumorok,<sup>19</sup> J. Suzuki,<sup>37</sup> T. Suzuki,<sup>37</sup> T. Takahashi,<sup>24</sup> T. Takano,<sup>24</sup> R. Takashima,<sup>12</sup> K. Takikawa,<sup>37</sup> M. Tanaka,<sup>37</sup> B. Tannenbaum,<sup>22</sup> F. Tartarelli,<sup>27</sup> W. Taylor,<sup>14</sup> M. Tecchio,<sup>20</sup> P. K. Teng,<sup>33</sup> Y. Teramoto,<sup>24</sup> K. Terashi,<sup>37</sup> S. Tether,<sup>19</sup> D. Theriot,<sup>7</sup> T. L. Thomas,<sup>22</sup> R. Thurman-Keup,<sup>1</sup> M. Timko,<sup>38</sup> P. Tipton,<sup>30</sup> A. Titov,<sup>31</sup> S. Tkaczyk,<sup>7</sup> D. Toback,<sup>5</sup> K. Tollefson,<sup>19</sup> A. Tollestrup,<sup>7</sup> H. Toyoda,<sup>24</sup> W. Trischuk,<sup>14</sup> J. F. de Troconiz,<sup>11</sup> S. Truitt,<sup>20</sup> J. Tseng,<sup>19</sup> N. Turini,<sup>27</sup> T. Uchida,<sup>37</sup> F. Ukegawa,<sup>26</sup> S. C. van den Brink,<sup>28</sup> S. Vejcik, III,<sup>20</sup> G. Velev,<sup>27</sup> R. Vidal,<sup>7</sup> R. Vilar,<sup>7a</sup> D. Vucinic,<sup>19</sup> R. G. Wagner,<sup>1</sup> R. L. Wagner,<sup>7</sup> J. Wahl,<sup>5</sup> N. B. Wallace,<sup>27</sup> A. M. Walsh,<sup>32</sup> C. Wang,<sup>6</sup> C. H. Wang,<sup>33</sup> M. J. Wang,<sup>33</sup> A. Warburton,<sup>14</sup> T. Watanabe,<sup>37</sup> T. Watts,<sup>32</sup> R. Webb,<sup>34</sup> C. Wei,<sup>6</sup> H. Wenzel,<sup>16</sup> W. C. Wester, III,<sup>7</sup> A. B. Wicklund,<sup>1</sup> E. Wicklund,<sup>7</sup> R. Wilkinson,<sup>26</sup> H. H. Williams,<sup>26</sup> P. Wilson,<sup>5</sup> B. L. Winer,<sup>23</sup> D. Winn,<sup>20</sup> D. Wolinski,<sup>20</sup> J. Wolinski,<sup>21</sup> S. Worm,<sup>22</sup> X. Wu,<sup>10</sup> J. Wyss,<sup>27</sup> A. Yagil,<sup>7</sup> W. Yao,<sup>18</sup> K. Yasuoka,<sup>37</sup> G. P. Yeh,<sup>7</sup> P. Yeh,<sup>33</sup> J. Yoh,<sup>7</sup> C. Yosef,<sup>21</sup> T. Yoshida,<sup>24</sup> I. Yu,<sup>7</sup> A. Zanetti,<sup>36</sup> F. Zetti,<sup>27</sup> and S. Zucchelli<sup>2</sup>

(CDF Collaboration)

<sup>1</sup> *Argonne National Laboratory, Argonne, Illinois 60439*

<sup>2</sup> *Istituto Nazionale di Fisica Nucleare, University of Bologna, I-40127 Bologna, Italy*

<sup>3</sup> *Brandeis University, Waltham, Massachusetts 02254*

<sup>4</sup> *University of California at Los Angeles, Los Angeles, California 90024*

<sup>5</sup> *University of Chicago, Chicago, Illinois 60637*

<sup>6</sup> *Duke University, Durham, North Carolina 27708*

- <sup>7</sup> *Fermi National Accelerator Laboratory, Batavia, Illinois 60510*
- <sup>8</sup> *University of Florida, Gainesville, FL 32611*
- <sup>9</sup> *Laboratori Nazionali di Frascati, Istituto Nazionale di Fisica Nucleare, I-00044 Frascati, Italy*
- <sup>10</sup> *University of Geneva, CH-1211 Geneva 4, Switzerland*
- <sup>11</sup> *Harvard University, Cambridge, Massachusetts 02138*
- <sup>12</sup> *Hiroshima University, Higashi-Hiroshima 724, Japan*
- <sup>13</sup> *University of Illinois, Urbana, Illinois 61801*
- <sup>14</sup> *Institute of Particle Physics, McGill University, Montreal H3A 2T8, and University of Toronto, Toronto M5S 1A7, Canada*
- <sup>15</sup> *The Johns Hopkins University, Baltimore, Maryland 21218*
- <sup>16</sup> *Institut für Experimentelle Kernphysik, Universität Karlsruhe, 76128 Karlsruhe, Germany*
- <sup>17</sup> *National Laboratory for High Energy Physics (KEK), Tsukuba, Ibaraki 305, Japan*
- <sup>18</sup> *Ernest Orlando Lawrence Berkeley National Laboratory, Berkeley, California 94720*
- <sup>19</sup> *Massachusetts Institute of Technology, Cambridge, Massachusetts 02139*
- <sup>20</sup> *University of Michigan, Ann Arbor, Michigan 48109*
- <sup>21</sup> *Michigan State University, East Lansing, Michigan 48824*
- <sup>22</sup> *University of New Mexico, Albuquerque, New Mexico 87131*
- <sup>23</sup> *The Ohio State University, Columbus, OH 43210*
- <sup>24</sup> *Osaka City University, Osaka 588, Japan*
- <sup>25</sup> *Università di Padova, Istituto Nazionale di Fisica Nucleare, Sezione di Padova, I-36132 Padova, Italy*
- <sup>26</sup> *University of Pennsylvania, Philadelphia, Pennsylvania 19104*
- <sup>27</sup> *Istituto Nazionale di Fisica Nucleare, University and Scuola Normale Superiore of Pisa, I-56100 Pisa, Italy*
- <sup>28</sup> *University of Pittsburgh, Pittsburgh, Pennsylvania 15260*
- <sup>29</sup> *Purdue University, West Lafayette, Indiana 47907*
- <sup>30</sup> *University of Rochester, Rochester, New York 14627*
- <sup>31</sup> *Rockefeller University, New York, New York 10021*
- <sup>32</sup> *Rutgers University, Piscataway, New Jersey 08855*
- <sup>33</sup> *Academia Sinica, Taipei, Taiwan 11530, Republic of China*
- <sup>34</sup> *Texas A&M University, College Station, Texas 77843*
- <sup>35</sup> *Texas Tech University, Lubbock, Texas 79409*
- <sup>36</sup> *Istituto Nazionale di Fisica Nucleare, University of Trieste/ Udine, Italy*

<sup>37</sup> *University of Tsukuba, Tsukuba, Ibaraki 315, Japan*

<sup>38</sup> *Tufts University, Medford, Massachusetts 02155*

<sup>39</sup> *Waseda University, Tokyo 169, Japan*

<sup>40</sup> *University of Wisconsin, Madison, Wisconsin 53706*

<sup>41</sup> *Yale University, New Haven, Connecticut 06520*

# Bibliography

- [1] E. Rutherford, “The Scattering of  $\alpha$  and  $\beta$  Particles by Matter and the Structure of the Atom,” *Phil. Mag.* **21**, (1911): 669-88.
- [2] H. Becquerel, “Sur les radiations invisibles émises par les corps phosphorescents,” *Compt. Ren.* **122**, (1896): 501-3; *idem*, “Sur quelques propriétés nouvelles des radiations invisibles émises par divers corps phosphorescents,” *ibid.* **122**, (1896): 559-64; *idem*, “Sur les propriétés différentes des radiations invisibles émises par les sels d’uranium, et du rayonnement de la paroi anticathodique d’un tube de Crookes,” *ibid.* **122**, (1896): 762-7; *idem*, “Émission de radiations nouvelles par l’uranium métallique,” *ibid.* **122**, (1896): 1086-8.
- [3] J. Chadwick and E. S. Bieler, “The Collisions of  $\alpha$  Particles with Hydrogen Nuclei,” *Phil. Mag.* **42**, (1921): 923-40.
- [4] E. Rutherford, “Collision of  $\alpha$  Particles with Light Atoms. IV. An Anomalous Effect in Nitrogen,” *Phil. Mag.* **37**, (1919): 581-7.
- [5] J. Chadwick, “Possible Existence of a Neutron,” *Nature* **129**, (1932): 312.
- [6] H. Yukawa, “On the Interaction of Elementary Particles. I.,” *Proc. Phys.-Math. Soc. Jap.* **17**, (1935): 48-57.
- [7] D. H. Perkins, “Nuclear Disintegration by Meson Capture,” *Nature* **159**, (1947): 126-7; G. P. S. Occhialini and C. F. Powell, “Nuclear Disintegrations Produced by Slow Charged Particles of Small Mass,” *ibid.* **159**, (1947) 186-90.
- [8] S. H. Neddermeyer and C. D. Anderson, “Note on the Nature of Cosmic-Ray Particles,” *Phys. Rev.* **51**, (1937): 884-6.



- [9] A. Pais, "Some Remarks on the  $V$ -Particles," *Phys. Rev.* **86**, (1952): 663-72.
- [10] For a review, see R. N. Cahn and G. Goldhaber, *The Experimental Foundations of Particle Physics*, Cambridge University Press, Cambridge: 1989.
- [11] M. Gell-Mann, "The Eightfold Way: A Theory of Strong Interaction Symmetry," CTSL-20, Caltech, (1961), unpublished. Reprinted in: M. Gell-Mann and Y. Ne'eman, "The Eightfold Way: A Review – With Collection of Reprints," *Frontiers in Physics*, ed. D. Pines, W. A. Benjamin, Inc., New York and Amsterdam: 1964.
- [12] Y. Ne'eman, "Derivations of Strong Interactions from a Gauge Invariance," *Nucl. Phys.* **26**, (1961): 222-9.
- [13] S. Sakata, "On a Composite Model for the New Particles," *Progr. of Theor. Phys.* **16**, (1956): 686-8.
- [14] M. Gell-Mann, "A Schematic Model of Baryons and Mesons," *Phys. Lett.* **8**, (1964): 214-5.
- [15] G. Zweig, "An  $SU(3)$  Model for Strong Interaction Symmetry and its Breaking I," CERN-8182-TH-401, CERN preprint, (1964), unpublished; *idem*, "An  $SU(3)$  Model for Strong Interaction Symmetry and its Breaking II," CERN-8419-TH-412, CERN preprint, (1964), unpublished. Reprinted in "Developments in the Quark Theory of Hadrons," *A Reprint Collection V.1: 1964-1978*, eds. D. B. Lichtenberg and S. P. Rosen, Hadronic Press, Inc., Massachusetts: 1980.
- [16] E. D. Bloom *et al.*, "High-Energy Inelastic  $e$ - $p$  Scattering at  $6^\circ$  and  $10^\circ$ ," *Phys. Rev. Lett.* **23**, (1969): 930-4; M. Breidenbach *et al.*, "Observed Behavior of Highly Inelastic Electron-Proton Scattering," *ibid.* **23**, (1969): 935-9; G. Miller *et al.*, "Inelastic Electron-Proton Scattering at Large Momentum Transfers and the Inelastic Structure Functions of the Proton," *Phys. Rev. D* **5**, (1972): 528-44.
- [17] J. D. Bjorken, "Asymptotic Sum Rules at Infinite Momentum," *Phys. Rev.* **179**, (1969): 1547-53; J. D. Bjorken and E. A. Paschos, "Inelastic Electron-Proton and  $\gamma$ -Proton Scattering and the Structure of the Nucleon," *ibid.* **185**, (1969): 1975-82.

- [18] R. P. Feynman, "Very High-Energy Collisions of Hadrons," *Phys. Rev. Lett.* **23**, (1969): 1415-7.
- [19] R. F. Schwitters *et al.*, "Azimuthal Asymmetry in Inclusive Hadron Production by  $e^+ e^-$  Annihilation," *Phys. Rev. Lett.* **35**, (1975): 1320-2.
- [20] H. L. Anderson *et al.*, "Total Cross Sections of Negative Pions in Hydrogen," *Phys. Rev.* **85**, (1952): 934-5; *idem*, "Total Cross Sections of Positive Pions in Hydrogen," *ibid.* **85**, (1952) : 936.
- [21] W. Pauli, "Über den Einfluß der Geschwindigkeitsabhängigkeit der Elektronenmasse auf den Zeemaneffekt," *Z. Phys.* **31**, (1925): 373-85; *idem*, "Über den Zusammenhang des Abschlusses der Elektronengruppen im Atom mit der Komplexstruktur der Spektren," *ibid.* **31**, (1925): 765-83.
- [22] E. Fermi, "Sulla quantizzazione del gas perfetto monoatomico," *Rend. Lincei* **3**, (1926): 145-9; *idem*, "Zur Quantelung des idealen einatomigen Gases," *Z. Phys.* **36**, (1926): 902-12; P. A. M. Dirac, "On the Theory of Quantum Mechanics," *Proc. Roy. Soc.* **A112**, (1926): 661-77.
- [23] O. W. Greenberg, "Spin and Unitary-Spin Independence in a Paraquark Model of Baryons and Mesons," *Phys. Rev. Lett.* **13**, (1964): 598-602; M. Y. Han and Y. Nambu, "Three-Triplet Model with Double SU(3) Symmetry," *Phys. Rev.* **139**, (1965): B1006-10; N. N. Bogolyubov *et al.*, "On the Composite Models in Theories of Elementary Particles," preprint JINR-D-1968, (1965), unpublished; O. W. Greenberg and D. Zwanziger, "Saturation in Triplet Models of Hadrons," *Phys. Rev.* **150**, (1966): 1177-80.
- [24] S. Weinberg, "Non-Abelian Gauge Theories of the Strong Interactions," *Phys. Rev. Lett.* **31**, (1973): 494-7.
- [25] H. Fritzsch, M. Gell-Mann, and H. Leutwyler, "Advantages of the Color Octet Gluon Picture," *Phys. Lett.* **47B**, (1973): 365-8.
- [26] D. J. Gross and F. Wilczek, "Asymptotically Free Gauge Theories I," *Phys. Rev. D* **8**, (1973): 3633-52.

- [27] G. Hanson *et al.* (Mark I Collaboration), “Evidence for Jet Structure in Hadron Production by  $e^+ e^-$  Annihilation,” *Phys. Rev. Lett.* **35**, (1975): 1609-12.
- [28] D. P. Barber *et al.* (MARK-J Collaboration), “Discovery of Three-Jet Events and a Test of Quantum Chromodynamics at PETRA,” *Phys. Rev. Lett.* **43**, (1979): 830-3; R. Brandelik *et al.* (TASSO Collaboration), “Evidence for Planar Events in  $e^+ e^-$  Annihilation at High Energies,” *Phys. Lett.* **86B**, (1979): 243-9; C. Berger *et al.* (PLUTO Collaboration), “Evidence for Gluon Bremsstrahlung in  $e^+ e^-$  Annihilations at High Energies,” *ibid.* **86B**, (1979): 418-25; W. Bartel *et al.* (JADE Collaboration), “Observation of Planar Three-Jet Events in  $e^+ e^-$  Annihilation and Evidence for Gluon Bremsstrahlung,” *ibid.* **91B**, (1980): 142-7.
- [29] J.-E. Augustin *et al.* (Mark I Collaboration), “Discovery of a Narrow Resonance in  $e^+ e^-$  Annihilation,” *Phys. Rev. Lett.* **33**, (1974): 1406-8; J. J. Aubert *et al.*, “Experimental Observation of a Heavy Particle  $J$ ,” *ibid.* **33**, (1974): 1404-6; C. Bacci *et al.*, “Preliminary Result of Frascati (ADONE) on the Nature of a New 3.1-GeV Particle Produced in  $e^+ e^-$  Annihilation,” *ibid.* **33**, (1974): 1408-10.
- [30] R. M. Barnett *et al.* (Particle Data Group), “Review of Particle Physics,” *Phys. Rev. D* **54**, (1996): 1-720, and 1997 off-year partial update for the 1998 edition (URL: <http://pdg.lbl.gov>).
- [31] G. S. Abrams *et al.* (Mark I Collaboration), “Discovery of a Second Narrow Resonance in  $e^+ e^-$  Annihilation,” *Phys. Rev. Lett.* **33**, (1974): 1453-5.
- [32] G. S. Abrams *et al.* (Mark I Collaboration), “Decay of  $\psi(3684)$  into  $\psi(3095)$ ,” *Phys. Rev. Lett.* **34**, (1975): 1181-3.
- [33] S. L. Glashow, J. Iliopoulos, and I. Maiani, “Weak Interactions with Lepton-Hadron Symmetry,” *Phys. Rev. D* **2**, (1970): 1285-92.
- [34] M. L. Perl *et al.* (Mark I Collaboration), “Evidence for Anomalous Lepton Production in  $e^+ e^-$  Annihilation,” *Phys. Rev. Lett.* **35**, (1975): 1489-92; *idem*, “Properties of Anomalous  $e\mu$  Events Produced in  $e^+ e^-$  Annihilation,” *Phys. Lett.* **63B**, (1976): 466-70.

- [35] S. W. Herb *et al.*, “Observation of a Dimuon Resonance at 9.5 GeV in 400-GeV Proton-Nucleus Collisions,” *Phys. Rev. Lett.* **39**, (1977): 252-5.
- [36] W. R. Innes *et al.*, “Observation of Structure in the  $\Upsilon$  Region,” *Phys. Rev. Lett.* **39**, (1977): 1240-2; *erratum, ibid.* **39**, (1977): 1640; C. Berger *et al.* (PLUTO Collaboration), “Observation of a Narrow Resonance Formed in  $e^+e^-$  Annihilation at 9.46 GeV,” *Phys. Lett.* **76B**, (1978): 243-5; J. K. Bienlein *et al.*, “Observation of a Narrow Resonance at 10.02 GeV in  $e^+e^-$  Annihilations,” *Phys. Lett.* **78B**, (1978): 360-3.
- [37] W. Bartel *et al.* (JADE Collaboration), “A Measurement of the Electroweak Induced Charge Asymmetry in  $e^+e^- \rightarrow b\bar{b}$ ,” *Phys. Lett.* **B146**, (1984): 437-42.
- [38] F. Abe *et al.* (CDF Collaboration), “Evidence for Top Quark Production in  $\bar{p}p$  Collisions at  $\sqrt{s} = 1.8$  TeV,” *Phys. Rev. D* **50**, (1994): 2966-3026; *idem*, *Phys. Rev. Lett.* **73**, (1994): 225-31.
- [39] F. Abe *et al.* (CDF Collaboration), “Observation of Top Quark Production in  $\bar{p}p$  Collisions with the Collider Detector at Fermilab,” *Phys. Rev. Lett.* **74**, (1995): 2626-31.
- [40] S. Abachi *et al.* (DØ Collaboration), “Observation of the Top Quark,” *Phys. Rev. Lett.* **74**, (1995): 2632-7.
- [41] E. J. Konopinski and H. M. Mahmoud, “The Universal Fermi Interaction,” *Phys. Rev.* **92**, (1953): 1045-9; K. Nishijima, “Vanishing of the Neutrino Rest Mass,” *Phys. Rev.* **108**, (1957): 907-8.
- [42] N. Cabibbo, “Unitarity Symmetry and Leptonic Decays,” *Phys. Rev. Lett.* **10**, (1963): 531-3.
- [43] M. Kobayashi and T. Maskawa, “ $CP$ -Violation in the Renormalizable Theory of Weak Interaction,” *Prog. Theor. Phys.* **49**, (1973): 652-7.
- [44] C. S. Wu *et al.*, “Experimental Test of Parity Conservation in Beta Decay,” *Phys. Rev.* **105**, (1957): 1413-5; R. L. Garwin, L. M. Lederman, and M. Weinrich, “Observations

- of the Failure of Conservation of Parity and Charge Conjugation in Meson Decays: the Magnetic Moment of the Free Muon,” *ibid.* **105**, (1957): 1415-7.
- [45] H. Galić *et al.* (Particle Data Group), “Current Experiments in Particle Physics,” LBL-91 Revised, UC-414, September (1996).
- [46] E. Fermi, “Versuch einer Theorie der  $\beta$ -Strahlen. I,” *Z. Phys.* **88**, (1934): 161-77; *idem*, “Tentativo di una teoria dei raggi,” *Nuovo Cim.* **11**, (1934): 1-19; R. P. Feynman and M. Gell-Mann, “Theory of the Fermi Interaction,” *Phys. Rev.* **109**, (1958): 193-8.
- [47] J. J. Sakurai, “Mass Reversal and Weak Interactions,” *Nuovo Cim.* **7**, (1958): 649-60.
- [48] D. H. Perkins, *Introduction to High Energy Physics*, 3<sup>rd</sup> ed., Addison-Wesley, Menlo Park, California: 1987.
- [49] S. L. Glashow, “Partial-Symmetries of Weak Interactions,” *Nucl. Phys.* **22**, (1961): 579-88; S. Weinberg, “A Model of Leptons,” *Phys. Rev. Lett.* **19**, (1967): 1264-6; A. Salam, “Weak and Electromagnetic Interactions,” in *Elementary Particle Theory*, ed. N. Svartholm, Almqvist and Wiksells, Stockholm: 1968, pp. 367-77; R. N. Cahn, “The Eighteen Arbitrary Parameters of the Standard Model in Your Everyday Life,” *Rev. Mod. Phys.* **68**, (1996): 951-9.
- [50] P. W. Higgs, “Broken Symmetries and the Masses of Gauge Bosons,” *Phys. Rev. Lett.* **13**, (1964): 508-9; *idem*, “Spontaneous Symmetry Breakdown without Massless Bosons,” *Phys. Rev.* **145**, (1966): 1156-63.
- [51] G. 't Hooft, “Renormalization of Massless Yang-Mills Fields,” *Nucl. Phys.* **B33**, (1971): 173-99; *idem*, “Renormalizable Lagrangians for Massive Yang-Mills Fields,” *ibid.* **B35**, (1971): 167-88; G. 't Hooft and M. Veltman, “Regularization and Renormalization of Gauge Fields,” *ibid.* **B44**, (1972): 189-213; *idem*, “Combinatorics of Gauge Fields,” *ibid.* **B50**, (1972): 318-53.
- [52] F. J. Hasert *et al.*, “Observation of Neutrino-Like Interactions without Muon or Electron in the Gargamelle Neutrino Experiment,” *Phys. Lett.* **45B**, (1973): 138-40.

- [53] G. Arnison *et al.* (UA1 Collaboration), “Experimental Observation of Isolated Large Transverse Energy Electrons with Associated Missing Energy at  $\sqrt{s} = 540$  GeV,” *Phys. Lett.* **122B**, (1983): 103-16; M. Banner *et al.* (UA2 Collaboration), “Observation of Single Isolated Electrons of High Transverse Momentum in Events with Missing Transverse Energy at the CERN  $\bar{p}p$  Collider,” *ibid.* **122B**, (1983): 476-85; G. Arnison *et al.* (UA1 Collaboration), “Experimental Observation of Lepton Pairs of Invariant Mass Around  $95 \text{ GeV}/c^2$  at the CERN SPS Collider,” *ibid.* **126B**, (1983): 398-410; B. Bagnaia *et al.* (UA2 Collaboration), “Evidence for  $Z^0 \rightarrow e^+ e^-$  at the CERN  $\bar{p}p$  Collider,” *ibid.* **129B**, (1983): 130-40.
- [54] P. Nason, S. Dawson, and R. K. Ellis, “The Total Cross Section for the Production of Heavy Quarks in Hadronic Collisions,” *Nucl. Phys.* **B303**, (1988): 607-33; *idem*, “The One Particle Inclusive Differential Cross Section for Heavy Quark Production in Hadronic Collisions,” *ibid.* **B327**, (1989): 49-92; *erratum, ibid.* **B335**, (1990): 260.
- [55] N. Ellis and A. Kernan, “Heavy Quark Production at the CERN  $p\bar{p}$  Collider,” *Phys. Rep.* **195**, (1990): 23-125.
- [56] M. Luke and M. J. Savage, “Extracting  $|V_{bc}|$ ,  $m_c$  and  $m_b$  from Inclusive  $D$  and  $B$  Decays,” *Phys. Lett.* **B321**, (1994): 88-94.
- [57] A. S. Schwarz, “Heavy Flavour Physics at Colliders with Silicon Strip Vertex Detectors,” *Phys. Rep.* **238**, (1994): 1-133.
- [58] C. Bebek *et al.* (CLEO Collaboration), “Evidence for New-Flavor Production at the  $\Upsilon(4S)$ ,” *Phys. Rev. Lett.* **46**, (1981): 84-7; K. Chadwick *et al.* (CLEO Collaboration), “Decay of  $b$ -Flavored Hadrons to Single-Muon and Dimuon Final States,” *ibid.* **46**, (1981): 88-91.
- [59] H. Fritzsch, “How to Discover the  $B$  Mesons,” *Phys. Lett.* **86B**, (1979): 343-6; *idem*, “Seeing the  $B$  Mesons in Hadronic Collisions,” *ibid.* **86B**, (1979): 164-6.
- [60] M. B. Wise, “An Estimate of  $J/\psi$  Production in  $B$  Decays,” *Phys. Lett.* **89B**, (1980): 229-31; T. A. de Grand and D. Toussant, “The Decay of  $b$  Quarks into  $\psi$ 's,” *ibid.* **89B**,

- (1980): 256-8; J. H. Kühn, S. Nussinov, and R. Rückl, “Charmonium Production in  $B$ -Decays,” *Z. Phys. C* **5**, (1980): 117-20.
- [61] S. Behrends *et al.* (CLEO Collaboration), “Observation of Exclusive Decay Modes of  $b$ -Flavored Mesons,” *Phys. Rev. Lett.* **50**, (1983): 881-4.
- [62] J. Chrin, “Upon the Determination of Heavy Quark Fragmentation Functions in  $e^+e^-$  Annihilation,” *Z. Phys. C* **36**, (1987): 163-71.
- [63] M. Suzuki, “Fifth Quark and Dimuon Production by Neutrinos,” *Phys. Lett.* **68B**, (1977): 164-8.
- [64] J. D. Bjorken, “Properties of Hadron Distributions in Reactions Containing Very Heavy Quarks,” *Phys. Rev. D* **17**, (1978): 171-3.
- [65] C. Peterson, D. Schlatter, I. Schmitt, and P. M. Zerwas, “Scaling Violations in Inclusive  $e^+e^-$  Annihilation Spectra,” *Phys. Rev. D* **27**, (1983): 105-11.
- [66] M. Wirbel, “Description of Weak Decays of  $D$  and  $B$  Mesons,” *Prog. Part. Nucl. Phys.* **21**, (1988): 33-98.
- [67] G. Sterman *et al.* (CTEQ Collaboration), “Handbook of Perturbative QCD,” *Rev. Mod. Phys.* **67**, (1995): 157-248.
- [68] M. Alston *et al.*, “Resonance in the  $K$ - $\pi$  System,” *Phys. Rev. Lett.* **6**, (1961): 300-2.
- [69] W. Chinowsky *et al.*, “On the Spin of the  $K^*$  Resonance,” *Phys. Rev. Lett.* **9**, (1962): 330-2.
- [70] M. Gourdin, A. N. Kamal, and X. Y. Pham, “Difficulties in Explaining Recent Data on  $B \rightarrow J/\psi + K(K^*)$  Decays with Commonly Used Form Factors within the Factorization Approach,” *Phys. Rev. Lett.* **73**, (1994): 3355-8; M. Gourdin, Y. Y. Keum, and X. Y. Pham, “Factorization and  $SU(2)$  Heavy Flavour Symmetry for  $B$ -Meson Decays Producing Charmonium,” *Phys. Rev. D* **52**, (1995): 1597-613.
- [71] N. G. Deshpande and J. Trampetic, “Estimate of Exclusive  $B$  Decays into Charmonia and  $K$  and  $K^*$  Mesons,” *Phys. Rev. D* **41**, (1990): 986-7.

- [72] M. R. Ahmady and D. Liu, “Non-Leptonic  $B$  Decays into  $K$ -Resonances,” *Phys. Lett.* **B324**, (1994): 231-5.
- [73] M. Wirbel, B. Stech, and M. Bauer, “Exclusive Semileptonic Decays of Heavy Mesons,” *Z. Phys. C* **29**, (1985): 637-42.
- [74] M. Bauer, B. Stech, and M. Wirbel, “Exclusive Non-Leptonic Decays of  $D$ -,  $D_s$ - and  $B$ -Mesons,” *Z. Phys. C* **34**, (1987): 103-15.
- [75] M. Wirbel and Y.-L. Wu, “ $D$  and  $D^*$  Production in Inclusive  $B$  Decays,” *Phys. Lett.* **B228**, (1989): 430-4.
- [76] V. Barger and R. Phillips, *Collider Physics*, Addison-Wesley, New York: 1987.
- [77] T. E. Browder, K. Honscheid, and D. Pedrini, “Nonleptonic Decays and Lifetimes of Charm and Beauty Particles,” *Ann. Rev. Nucl. Part. Sci.* **46**, (1996): 395-469.
- [78] M. Gourdin, A. N. Kamal, Y. Y. Keum, and X. Y. Pham, “On the Determination of  $a_1$  and  $a_2$  from Hadronic Two Body  $B$  Decays,” *Phys. Lett.* **B333**, (1994): 507-13.
- [79] M. Neubert, “A New Look at Hadronic  $B$  Decays,” CERN-TH/97-169, hep-ph/9707368, to appear in *Proceedings of the High Energy Physics Euroconference on Quantum Chromodynamics, Montpellier, France, 3-9 July 1997*.
- [80] N. Isgur and M. B. Wise, “Weak Decays of Heavy Mesons in the Static Quark Approximation,” *Phys. Lett.* **B232**, (1989): 113-7; *idem*, “Weak Transition Form Factors between Heavy Mesons,” *ibid.* **B237**, (1990): 527-30; M. E. Luke, “Effects of Sub-leading Operators in the Heavy Quark Effective Theory,” *ibid.* **B252**, (1990): 447-55.
- [81] A. Deandrea, N. Di Bartolomeo, R. Gatto, and G. Nardulli, “Two Body Non-Leptonic Decays of  $B$  and  $B_s$  Mesons,” *Phys. Lett.* **B318**, (1993): 549-58; R. Casalbuoni *et al.*, “Effective Lagrangian for Heavy and Light Mesons,” *ibid.* **B299**, (1993): 139-50.
- [82] R. Aleksan *et al.*, “Critical Analysis of Theoretical Estimates for  $B$ -to-Light-Meson Form Factors and  $B \rightarrow \psi K(K^*)$  Data using Factorization,” *Phys. Rev. D* **51**, (1995): 6235-52.



- [83] A. N. Kamal and T. N. Pham, “Cabibbo-Favored Hadronic Two-Body  $B$  Decays,” *Phys. Rev. D* **50**, (1994): 395-401.
- [84] I. Bigi *et al.*, “Non-Leptonic Decays of Beauty Hadrons – From Phenomenology to Theory,” in *B Decays*, Revised 2<sup>nd</sup> ed., ed. S. Stone, World Scientific, Singapore: 1994, pp. 132-57.
- [85] A. N. Kamal and A. B. Santra, “Probing Factorization in the Color-Suppressed Decay  $B \rightarrow \psi(2S) + K(K^*)$ ,” *Phys. Rev. D* **51**, (1995): 1415-8.
- [86] H.-Y. Cheng, “Nonfactorizable Contributions to Nonleptonic Weak Decays of Heavy Mesons,” *Phys. Lett.* **B335**, (1994): 428-35; *idem*, “Can  $B \rightarrow J/\psi K(K^*)$  Decays be Described by Factorization?” *ibid.* **B395**, (1997): 345-54; H.-Y. Cheng, C.-Y. Cheung, and C.-W. Hwang, “Mesonic Form Factors and the Isgur-Wise Function on the Light Front,” *Phys. Rev. D* **55**, (1997): 1559-77.
- [87] J. M. Soares, “‘Nonfactorizable’ Terms in Hadronic  $B$ -Meson Weak Decays,” *Phys. Rev. D* **51**, (1995): 3518-24.
- [88] A. N. Kamal *et al.*, “Nonfactorization in Hadronic Two-Body Cabibbo-Favored Decays of  $D^0$  and  $D^+$ ,” *Phys. Rev. D* **53**, (1996): 2506-15; A. N. Kamal and A. B. Santra, “Nonfactorization and Color-Suppressed  $B \rightarrow \psi(\psi') + K(K^*)$  Decays,” *Z. Phys. C* **72**, (1996): 91-7.
- [89] F. M. Al-Shamali and A. N. Kamal, “Nonfactorization and Final State Interactions in  $(B, B_s) \rightarrow \psi P$  and  $\psi V$  Decays,” University of Alberta Preprint Thy-09-97, hep-ph/9705465, August 1997.
- [90] M. Neubert and B. Stech, “Non-Leptonic Weak Decays of  $B$  Mesons,” to appear in *Heavy Flavours*, Revised 2<sup>nd</sup> ed., eds. A. J. Buras and M. Lindner, World Scientific, Singapore, hep-ph/9705292, CERN-TH/97-99.
- [91] A. Warburton (representing the CDF Collaboration), “Branching Fractions of  $B^+ \rightarrow \psi(2S) K^+$  and  $B^0 \rightarrow \psi(2S) K^{*0}$  Decays at CDF,” FERMILAB-Conf-96/160-E, contributed paper to the XXVIII<sup>th</sup> International Conference on High Energy Physics (ICHEP96), Warsaw, Poland (July 1996).

- [92] F. Abe *et al.* (CDF Collaboration), “Measurement of the  $B$  Meson Differential Cross Section  $d\sigma/dp_T$  in  $p\bar{p}$  Collisions at  $\sqrt{s} = 1.8$  TeV,” *Phys. Rev. Lett.* **75**, (1995): 1451-5.
- [93] F. Abe *et al.* (CDF Collaboration), “Ratios of Bottom Meson Branching Fractions Involving  $J/\psi$  Mesons and Determination of  $b$  Quark Fragmentation Fractions,” *Phys. Rev. D* **54**, (1996): 6596-609.
- [94] B. Barish *et al.* (CLEO Collaboration), “Measurement of the  $\bar{B} \rightarrow D^* \ell \bar{\nu}$  Branching Fractions and  $|V_{cb}|$ ,” *Phys. Rev. D* **51**, (1995): 1014-33.
- [95] J. D. Cockroft and E. T. S. Walton, “Artificial Production of Fast Protons,” *Nature* **129**, (1932): 242; *idem*, “Disintegration of Lithium by Swift Protons,” *Nature* **129**, (1932): 649.
- [96] J. R. Sanford, “The Fermi National Accelerator Laboratory,” *Ann. Rev. Nucl. Sci.* **26**, (1976): 151-98. Note that several parameters described in this article have changed since its publication. These include the ion species produced in the Cockroft-Walton preaccelerator (previously protons) and the energy achieved by the Linac (previously 200 MeV).
- [97] L. M. Lederman, “The Tevatron,” *Scientific American*, (March 1991): 48-55.
- [98] E. M. McMillan, “The Synchrotron – A Proposed High Energy Particle Accelerator,” *Phys. Rev.* **68**, (1945): 143-4.
- [99] R. Palmer and A. V. Tollestrup, “Superconducting Magnet Technology for Accelerators,” *Ann. Rev. Nucl. Part. Sci.* **34**, (1984): 247-84.
- [100] R. R. Wilson, “The Tevatron,” *Physics Today* **30**, (October 1977): 23-30.
- [101] G. Carron *et al.*, “Stochastic Cooling Tests in ICE,” *Phys. Lett.* **77B**, (1978): 353-4; D. Möhl, G. Petrucci, L. Thorndahl, and S. van der Meer, “Physics and Technique of Stochastic Cooling,” *Phys. Rep.* **58**, (1980): 73-119; S. van der Meer, “Stochastic Cooling in the CERN Antiproton Accumulator,” *IEEE Trans. Nucl. Sci.* **28**, (1981): 1994-8.

- [102] A. G. Ruggiero, "The Fermilab Tevatron I Debuncher Ring," *IEEE Trans. Nucl. Sci.* **30**, (1983): 2478-80; B. Autin, J. Marriner, A. Ruggiero, and K. Takayama, "Fast Betatron Cooling in the Debuncher Ring for the Fermilab Tevatron I Project," *IEEE Trans. Nucl. Sci.* **30**, (1983): 2593-95.
- [103] F. Abe *et al.* (CDF Collaboration), "The CDF Detector: An Overview," *Nucl. Instr. and Meth. A* **271**, (1988): 387-403. The references listed in this article describe in some detail several subsystems of the CDF detector.
- [104] S. Tkaczyk *et al.*, "The CDF Silicon Vertex Detector," *Nucl. Instr. and Meth. A* **342**, (1994): 240-50.
- [105] D. Amidei *et al.*, "The Silicon Vertex Detector of the Collider Detector at Fermilab," *Nucl. Instr. and Meth. A* **350**, (1994): 73-130.
- [106] P. Azzi *et al.*, "SVX', the New CDF Silicon Vertex Detector," *Nucl. Instr. and Meth. A* **360**, (1995): 137-40.
- [107] F. Abe *et al.* (CDF Collaboration), "Measurement of the  $W$  Boson Mass," *Phys. Rev. D* **52**, (1995): 4784-827.
- [108] K. Kleinknecht, *Detectors for Particle Radiation*, Cambridge University Press, Cambridge: 1986.
- [109] S. A. Kleinfelder *et al.*, "A Flexible 128 Channel Silicon Strip Detector Instrumentation Integrated Circuit with Sparse Data Readout," *IEEE Trans. Nucl. Sci.* **35**, (1988): 171-5.
- [110] B. T. Huffman, University of Pittsburgh, private communication.
- [111] J. D. Lewis *et al.*, "The 1992 CDF Muon System Upgrade," CDF Internal Note CDF/PUB/MUON/PUBLIC/2858 (1995), to be submitted to *Nucl. Instr. and Meth. A*.
- [112] F. Abe *et al.* (CDF Collaboration), "Measurement of the Antiproton-Proton Total Cross Section at  $\sqrt{s} = 546$  and 1800 GeV," *Phys. Rev. D* **50**, (1994): 5550-61.

- [113] D. Amidei *et al.*, “The CDF Trigger,” *Nucl. Instr. and Meth. A* **265**, (1988): 326-35.  
Note that this article describes an early version of the CDF trigger; however, several of the aspects mentioned persist in more recent CDF trigger configurations.
- [114] J. T. Carroll *et al.*, “The CDF Level 3 Trigger,” *Nucl. Instr. and Meth. A* **300**, (1991): 552-67. Note that this article describes an early version of the CDF Level 3 trigger, one that used Motorola 68020 processors. Although several important details have since changed, the design philosophy and the interaction with the DAQ system are rather similar to recent versions of the Level 3 trigger system.
- [115] Adapted, with permission, from a figure by K. Biery, Fermi National Accelerator Laboratory.
- [116] P. K. Sinervo, K. J. Ragan, A. W. Booth, and T. M. Shaw, “Fast Data Acquisition with the CDF Event Builder,” *IEEE Trans. Nucl. Sci.* **36**, (1989): 440-5; T. M. Shaw *et al.*, “Architecture and Development of the CDF Hardware Event Builder,” *IEEE Trans. Nucl. Sci.* **36**, (1989): 765-9.
- [117] Some of the analysis codes used in the reconstruction of meson candidates in this study were adapted from routines prepared by G. S. Sganos.
- [118] F. Abe *et al.* (CDF Collaboration), “Measurement of the Mass of the  $B_s^0$  Meson,” *Phys. Rev. D* **53**, (1996): 3496-505.
- [119] F. Abe *et al.* (CDF Collaboration), “Observation of  $\Lambda_b^0 \rightarrow J/\psi \Lambda$  at the Fermilab Proton-Antiproton Collider,” *Phys. Rev. D* **55**, (1997): 1142-52.
- [120] C. Newman-Holmes, E. E. Schmidt, and R. Yamada, “Measurement of the Magnetic Field of the CDF Magnet,” *Nucl. Instr. and Meth. A* **274**, (1989): 443-51.
- [121] G. S. Sganos, Ph.D. Thesis, University of Toronto, 1996.
- [122] J. P. Marriner, “Secondary Vertex Fit with (optional) Mass Constraints and (optional) Pointing Constraints,” CDF Internal Note CDF/DOC/SEC\_VTX/PUBLIC/1996 (1993), unpublished.

- [123] F. Abe *et al.* (CDF Collaboration), “Transverse-Momentum Distributions of Charged Particles Produced in  $\bar{p}p$  Interactions at  $\sqrt{s} = 630$  and 1800 GeV,” *Phys. Rev. Lett.* **61**, (1988): 1819-22.
- [124] G. Breit and E. Wigner, “Capture of Slow Neutrons,” *Phys. Rev.* **49**, (1936): 519-31.
- [125] F. James, “Monte Carlo Theory and Practice,” *Rep. Prog. Phys.* **43**, (1980): 1145-89.
- [126] A. D. Martin, W. J. Stirling, and R. G. Roberts, “New Information on Parton Distributions,” *Phys. Rev. D* **47**, (1993): 867-82.
- [127] P. Avery, K. Read, and G. Trahern, “QQ: A Monte Carlo Generator,” Internal Software Note CSN-212, Cornell University, (1985), unpublished.
- [128] F. Abe *et al.* (CDF Collaboration), “Measurement of the Polarization in the Decays  $B_d \rightarrow J/\psi K^{*0}$  and  $B_s \rightarrow J/\psi \phi$ ,” *Phys. Rev. Lett.* **75**, (1995): 3068-72.
- [129] J. Schwinger, K. A. Milton, W.-Y. Tsai, and L. L. DeRaad Jr., “Pion Spectrum in Decay of  $\psi'(3.7)$  to  $\psi(3.1)$ ,” *Proc. Nat. Acad. Sci. USA* **72**, (1975): 4216-7.
- [130] L. S. Brown and R. N. Cahn, “Chiral Symmetry and  $\psi' \rightarrow \psi \pi \pi$  Decay,” *Phys. Rev. Lett.* **35**, (1975): 1-4; R. N. Cahn, “Angular Distributions in the Decay  $\psi' \rightarrow \psi \pi \pi$ ,” *Phys. Rev. D* **12**, (1975): 3559-63.
- [131] T. N. Pham, B. Pire, and T. N. Truong, “Two-Pion Spectrum and Angular Distribution in  $\psi' \rightarrow \psi + 2\pi$  Decays,” *Phys. Lett.* **61B**, (1976): 183-6.
- [132] D. Coffman *et al.* (Mark III Collaboration), “Direct Measurement of the  $J/\psi$  Leptonic Branching Fraction,” *Phys. Rev. Lett.* **68**, (1992): 282-5; *erratum, ibid.* **69**, (1992): 3689.
- [133] T. A. Armstrong *et al.* (Fermilab E760 Collaboration), “Measurement of the Branching Ratios  $\psi' \rightarrow e^+ e^-$ ,  $\psi' \rightarrow J/\psi \pi^+ \pi^-$ ,  $\psi' \rightarrow J/\psi \eta$ ,” *Phys. Rev. D* **55**, (1997): 1153-8.
- [134] S. D. Metzler and B. T. Huffman, “Measurement of  $\mathcal{B}(B^+ \rightarrow J/\psi \pi^+)/\mathcal{B}(B^+ \rightarrow J/\psi K^+)$  and  $\mathcal{B}(B_c^+ \rightarrow J/\psi \pi^+)/\mathcal{B}(B_c^+ \rightarrow J/\psi K^+)$ ,” CDF Internal Note CDF/ANAL/BOTTOM/CDFR/3541 (1996), unpublished.

- [135] A. Warburton, “Run 1A and 1B Low- $p_T$  Single- and Double-Track CTC Pattern Recognition Efficiencies,” CDF Internal Note CDF/ANAL/BOTTOM/CDFR/4139 (1997), unpublished.
- [136] K. Kelley, B. Mattingly, and P. Sphicas, “A Study of the Isolation of  $B$ -Mesons,” MIT/CDF Internal Note CDF/ANAL/BOTTOM/CDFR/2765 (1994), unpublished; G. Bauer, J. Friedman, K. Kelley, T. Shah, and P. Sphicas, “A Study of the Isolation of  $B$ -Mesons Part II,” MIT/CDF Internal Note CDF/ANAL/BOTTOM/CDFR/3684 (1996), unpublished.
- [137] J. Z. Bai *et al.* (BES Collaboration), “Precision Measurement of  $J/\psi$  Leptonic Branching Fraction,” BIHEP-EPI-96-01, (1996), submitted to *Phys. Rev. D*.
- [138] M. Neubert, V. Rieckert, B. Stech, and Q. P. Xu, “Exclusive Weak Decays of  $B$ -Mesons,” in *Heavy Flavours*, eds. A. J. Buras and M. Lindner, World Scientific, Singapore: 1992, pp. 286-333.
- [139] M. S. Alam *et al.* (CLEO II Collaboration), “Exclusive Hadronic  $B$  Decays to Charm and Charmonium Final States,” *Phys. Rev. D* **50**, (1994): 43-68.
- [140] H. Albrecht *et al.* (ARGUS Collaboration), “Exclusive Hadronic Decays of  $B$  Mesons,” *Z. Phys. C* **48**, (1990): 543-51.
- [141] D. L. Kreinick, Cornell University, private communication.
- [142] D. Bortoletto *et al.* (CLEO Collaboration), “Inclusive and Exclusive Decays of  $B$  Mesons to Final States Including Charm and Charmonium Mesons,” *Phys. Rev. D* **45**, (1992): 21-35.
- [143] F. Abe *et al.* (CDF Collaboration), “Reconstruction of  $B^0 \rightarrow J/\psi K_S^*$  and Measurement of Ratios of Branching Ratios Involving  $B \rightarrow J/\psi K^*$  and  $B^+ \rightarrow J/\psi K^+$ ,” *Phys. Rev. Lett.* **76**, (1996): 2015-20.
- [144] C. P. Jessop *et al.* (CLEO II Collaboration), “Measurement of the Decay Amplitudes and Branching Fractions of  $B \rightarrow J/\psi K^*$  and  $B \rightarrow J/\psi K$  Decays,” *Phys. Rev. Lett.* **79**, (1997): 4533-7.

- [145] R. Blair *et al.* (CDF II Collaboration), “The CDF II Detector Technical Design Report,” FERMILAB-Pub-96/390-E, (November 1996).
- [146] J. B. González-Atavales, Ph.D. Dissertation, University of Pennsylvania, 1996.
- [147] The hit embedding machinery was originally coded by A. Mukherjee, Fermi National Accelerator Laboratory.